



AxIrO₃ (A = Li, Na or H) for the electrochemical storage and conversion of energy

Paul-Emile Pearce

► To cite this version:

Paul-Emile Pearce. AxIrO₃ (A = Li, Na or H) for the electrochemical storage and conversion of energy. Chemical Physics [physics.chem-ph]. Sorbonne Université, 2019. English. NNT : 2019SORUS313 . tel-02862134

HAL Id: tel-02862134

<https://theses.hal.science/tel-02862134>

Submitted on 9 Jun 2020

HAL is a multi-disciplinary open access archive for the deposit and dissemination of scientific research documents, whether they are published or not. The documents may come from teaching and research institutions in France or abroad, or from public or private research centers.

L'archive ouverte pluridisciplinaire **HAL**, est destinée au dépôt et à la diffusion de documents scientifiques de niveau recherche, publiés ou non, émanant des établissements d'enseignement et de recherche français ou étrangers, des laboratoires publics ou privés.



COLLÈGE
DE FRANCE
— 1530 —



Sorbonne Université

Ecole doctorale 397

Collège de France : Chaire de Chimie du Solide et Energie

$A_x\text{IrO}_3$ ($A = \text{Li}, \text{Na}$ ou H) pour le stockage et la conversion électrochimique de l'énergie

Par Paul-Emile Pearce

Thèse de doctorat de Physique et Chimie des Matériaux

Dirigée par Jean-Marie Tarascon et Gwenaëlle Rousse

Présentée et soutenue publiquement le 8 octobre 2019

Devant un jury composé de :

Dr. Alain Demourgues	Directeur de recherche, ICMCB, Bordeaux	Rapporteur
Prof. Lorenzo Stievano	Professeur, ICGM, Montpellier	Rapporteur
Dr. Valérie Pralong	Directrice de recherche, CRISMAT, Caen	Examinatrice
Dr. David Portehault	Chargé de recherche, LCMCP, Paris	Examineur
Prof. Dominique Larcher	Professeur, LRCS, Amiens	Examineur
Prof. Jean-Marie Tarascon	Professeur, Collège de France, Paris	Directeur
Dr. Gwenaëlle Rousse	Enseignante-Chercheuse, Sorbonne Université	Directrice
Dr. Alexis Grimaud	Chargé de recherche, Collège de France, Paris	Invité du jury



Except where otherwise noted, this work is licensed under
<http://creativecommons.org/licenses/by-nc-nd/3.0/>



COLLÈGE
DE FRANCE
—1530—



Sorbonne Université

Doctoral School 397

Collège de France : Chaire de Chimie du Solide et Energie

$A_x\text{IrO}_3$ ($A = \text{Li}, \text{Na}$ or H) for the electrochemical storage and conversion of energy

By Paul-Emile Pearce

PhD thesis of Physics and Chemistry of Materials

Supervised by Jean-Marie Tarascon and Gwenaëlle Rousse

Presented and defended publicly on October the 8th 2019

In front of the following jury :

Dr. Alain Demourgues	Research Director, ICMCB, Bordeaux	Referee
Prof. Lorenzo Stievano	Professor, ICGM, Montpellier	Referee
Dr. Valérie Pralong	Research Director, CRISMAT, Caen	Examiner
Dr. David Portehault	Research Scientist, LCMCP, Paris	Examiner
Prof. Dominique Larcher	Professor, LRCS, Amiens	Examiner
Prof. Jean-Marie Tarascon	Professor, Collège de France, Paris	Supervisor
Dr. Gwenaëlle Rousse	Associate Professor, Sorbonne University	Supervisor
Dr. Alexis Grimaud	Research Scientist, Collège de France, Paris	Invited member



Except where otherwise noted, this work is licensed under
<http://creativecommons.org/licenses/by-nc-nd/3.0/>

Acknowledgements

I am immensely grateful to Jean-Marie Tarascon for giving me the opportunity to be a part of this amazing lab in such a prestigious place as the Collège de France. His fierce dedication to science, to his students and to the exploration of fundamental questions is truly awesome. I have learned tremendously from working with and around him.

I have been lucky to share an office with Gwenaëlle Rousse whose joyfulness knows no end and whose laughter is so contagious and uplifting. She has been a great teacher and helped further my understanding of crystallography and diffraction techniques which compose a great deal of my work.

I would like to acknowledge the great help of Alexis Grimaud and his mentorship. You are just as impressive as Jean-Marie in your dedication to science and your students and I feel fortunate to have worked with you during such an exciting time for catalysis.

This work could not have been carried out without the Collège de France and the funding from the European Research Council (ERC) (FP/2014)/ERC Grant-Project 670116-ARPEMA.

I would like to express my sincere appreciation and gratitude to Chunzhen Yang and Gaurav Assat for their collaborations, their valuable input and their help during the past two years. This thesis would not be the same without you.

When I first arrived in this lab, Arnaud Perez really took the time and had the patience to show me around, give me tips and tricks for making batteries, plotting data efficiently and so much more and for this I am grateful.

I have had the great pleasure of spending these few years working with Daniel Alves Dalla Corte who has truly inspired me. He has the special ability of being unconditionally kind and patient with everyone in addition to being creative,

resourceful, organized and willing. He has been greatly supportive and has become a true friend. Thanks for everything Dani.

There are of course others which have contributed to the good mood and sound scientific discussions such as Sujoy Saha, Pierre Lemaire, Nicolas Dubouis, Antonella Iadecola, Boris Mirvaux, Ignacio Blázquez Alcover, Quentin Jacquet, Romain Dugas, Florent Lepoivre, Sathiya Mariyappan and Jessica Duvoisin.

I am grateful to Lorenzo Stievano and Alain Demourgues for accepting the role of referee of this thesis and of course to Valérie Pralong, Dominique Larcher and David Portehault for agreeing to be part of the jury. I thank all of them for taking the time out of their summers to read my thesis and can only hope they found it worthy of their efforts.

Finally, I cannot begin to express my gratitude to my family, my friends and my amazing companion Julie who supported me during these three years. Thank you so much for being there in both joyful and difficult times.

Summary

Acknowledgements.....	iii
Summary.....	v
General introduction	1
Chapter I. Introduction to battery technologies	4
Prequel to the Li based energy storage technologies	5
I-1 Lithium batteries	6
I-2 Li-ion batteries (LIBs).....	9
I-3 Improving the capacity of LIBs.....	11
I-4 Outgrowing classical cationic redox	13
I-5 Origin of performance decay in Li-rich layered oxides	18
I-6 Origin of anionic redox	19
I-7 Na-ion batteries (NIBs)	22
Conclusion	24
Chapter II. Structural and electronic implications of delithiation for the β -Li ₂ IrO ₃	26
II-1 Introduction.....	27
II-2 Synthesis and structure	28
II-2-a Synthesis	28
II-2-b Structural characterization	30

II-3 Electrochemical performances	33
II-4 Determining anionic and cationic participation during delithiation	38
II-4-a X-ray Absorption Near Edge Structure (XANES).....	38
II-4-b Hard X-ray Photoelectron Spectroscopy (HAXPES)	42
II-5 Structural evolution during cycling.....	46
II-5-a Synchrotron X-ray diffraction (SXRd)	46
II-5-b Neutron powder diffraction	48
II-5-c Extended X-ray absorption fine structure (EXAFS).....	55
Conclusion	59
Chapter III. IrO ₃ as a Na ⁺ host with an active oxygen network	61
Introduction.....	62
III-1 Synthesis	63
III-2 Structural Characterization	64
III-3 Electrochemical behavior	67
III-4 Anionic redox activity	69
III-5 <i>Operando</i> XRD.....	70
III-6 Long term cycling.....	76
III-7 Thermal stability	77
Conclusion	79

Chapter IV. A protonated iridium oxide catalyst for water oxidation in acidic media	81
Introduction.....	82
IV-1 Synthesis and characterization	83
IV-1-a Ion exchange.....	83
IV-1-b Chemical composition.....	83
IV-1-c Structural characterization.....	85
IV-1-d Particle morphology	87
IV-1-e Ir oxidation state.....	87
IV-1-f Proton insertion.....	88
IV-2 The oxygen evolution reaction	92
IV-2-a Electrochemical performance.....	93
IV-2-b Stability during OER.....	94
IV-2-c <i>Operando</i> XRD – β -H ₂ IrO ₃	96
IV-2-d Charge compensation during OER	97
IV-3 Reactivity of lithiated intermediates in acidic media	98
IV-3-a Sample preparation.....	98
IV-3-b <i>Ex situ</i> characterization	99
IV-3-c On-line Mass spectrometry	101
IV-3-d Stability	102

IV-3-e Operando XRD – β -Li ₂ IrO ₃	103
IV-4 Proton insertion as charge compensation for stable OER catalysis	104
IV-5 Conclusion.....	106
General conclusions.....	108
Appendix.....	112
Appendix – Chapter II.....	112
Methods.....	112
Figures.....	114
Appendix – Chapter III	122
Methods.....	122
Figures.....	124
Appendix – Chapter IV	130
Methods.....	130
Figures.....	133
References.....	142

General introduction

Producing clean and renewable energy is key to mitigating global warming and the energy crisis to come. Large efforts are invested in the development of technologies such as photovoltaics and wind turbines which allow the conversion of solar and wind energy to electricity. These technologies are intermittent in nature, therefore their integration to the grid is challenging. In order to alleviate this issue, energy storage systems must be developed in parallel. One technology which is gaining much traction thanks to its versatility and diminishing costs is the Li-ion battery (LIB). The ability to store large amounts of energy and have reasonable power capabilities is a great advantage for grid applications. Furthermore, this enables isolated power systems which rely on solar panels or wind turbines but do not have access to the grid.

In addition to solving issues concerning energy production for grid applications, the transportation sector is one of the main greenhouse gas emitters and most of the world population relies on the use internal combustion engines for individual transportation or freight forwarding. Developing alternatives to fossil fuels for locomotion is crucial for the transition to a greener planet. Although electric cars predate the internal combustion engine, their development was close to inexistent during most of the 20th century due to the availability, high energy density and ease of use of oil. In the past decade however, hybrid and fully electric vehicles have seen their way to the market and prices are dropping as the advances in battery technologies continue.

Although the energy density and reliability of LIBs have greatly improved since their commercialization in 1991 by Sony, today's requirements are still not met and further improvements are needed. Furthermore, major concerns about the limited abundance of Li have driven the development of alternative battery technologies with namely the Na-ion technology. While it has not reached the maturity of the LIBs, there have been considerable improvements in the materials used for such sodium based systems. These developments have led to the launch of a French startup called Tiamat in 2018 which commercializes the first industrial grade 18650 Na-ion cells.

One emerging paradigm for the development of new high energy density positive electrode materials for battery technologies is the participation of lattice oxygen in the

redox processes during insertion and extraction of alkali ions in a certain family of oxides. This allows materials which exhibit such activity to increase their reversible capacity at high voltage, thus increasing their energy density. However, this usually comes at a price on the cycle life and severe performance decay is observed. While the first chapter will go further into details on this subject, the aim of this thesis is to study the structural and electronic implications of anionic redox in a model iridate host, IrO_3 , for Li^+ and Na^+ ions. The use of cutting edge analytical techniques such as synchrotron X-ray and neutron powder diffraction (NPD) as well as X-ray absorption or photoemission spectroscopies are instrumental to probe the different aspects of such a subtle process. A firm understanding of the structural and electronic repercussions of lattice oxygen oxidation should help the scientific community in finding solutions and making these materials industrially viable.

While battery technologies are promising energy storage systems and have become dominant in transportation and portable electronics, tomorrow's energy landscape will most likely be composed of a variety of different technologies, one of which will be hydrogen fuel cells. Indeed, using hydrogen as a fuel and controlling its recombination with oxygen to form water while delivering large amounts of energy seems like an ideal solution. However, considerable efforts have been deployed to develop efficient systems capable of producing hydrogen from water using only renewable energies but advances have been scarce in the past few decades. One major roadblock is the sluggish kinetics of the oxygen evolution reaction (OER) - counter reaction to the evolution of hydrogen - which translates to large energy penalties. The production of hydrogen can be carried out in both acidic and alkaline environments but the lowest overpotentials are obtained at very low pH. In these harsh conditions, OER catalyst materials which are composed of transition metal oxides generally dissolve during anodic polarization. The best materials today are composed of Iridium and Ruthenium with the latter being less stable and the former less active. The iridate described in this thesis presents interesting properties for OER catalysis. Indeed, its ability to uptake and deliver protons has brought new insight into the charge compensation mechanism of a long suspected hydrous iridium oxide. Furthermore, the ability to form IrO_3 by oxidation of the $\beta\text{-Li}_2\text{IrO}_3$ in organic media has enabled the study of a high valence iridate suspected of being the active intermediate during OER catalysis on the surface of oxides. It is important to continue the search for highly efficient

catalysts capable of lowering the high overpotentials encountered during the water splitting reaction in order to make the technology viable.

The focus of this thesis is the study of oxygen redox in the bulk of the hyperhoneycomb IrO_3 host material during insertion and extraction of Li and Na as well as on the surface of the protonated phase in acidic media. The fields concerned by this work are the Li- and Na-ion battery technologies and the electrocatalysis of the water oxidation reaction. This manuscript is divided into four chapters not including this short general introduction.

The first chapter will briefly explain the working principle of alkali ion batteries, the different host materials and their evolution during the past three decades. In the same chapter, the recent observation of a new solid state redox mechanism coined anionic redox will be explained which will introduce the following work.

The second chapter will present the study performed on the $\beta\text{-Li}_2\text{IrO}_3$ phase, namely its synthesis, structural characterization, electrochemical performances, structural transitions during charge and the participation of both Iridium and Oxygen to the de/lithiation process.

The third chapter will discuss the synthesis and characterization of the $\beta\text{-Na}_{1.7}\text{IrO}_3$ phase obtained electrochemically by sodiation of the delithiated IrO_3 . The structural evolution during charge and discharge are determined and the oxygen lattice is shown to participate in the desodiation process.

The fourth chapter will present the synthesis and characterization of a protonated crystalline phase obtained by cation exchange of $\beta\text{-Li}_2\text{IrO}_3$ in 1M H_2SO_4 . The proton extraction/insertion capabilities of this new phase are assessed and its activity as OER catalyst is evaluated. The structural and electronic changes occurring during OER are characterized by *operando* X-ray diffraction and X-ray absorption spectroscopy. The reactivity of IrO_3 in acidic media is evaluated and a charge compensation mechanism is described in order to rationalize the observations.

Finally, some general conclusions will complete this thesis with a few directions for future research in both the field of battery and the field of electrocatalysis.

Chapter I. Introduction to battery technologies

Prequel to the Li based energy storage technologies

Batteries date back to the 18th century with the first electrochemical primary battery being developed by Alessandro Volta in 1799-1800.¹ He first described this electrochemical cell in a letter as composed of alternating discs of different conducting metals such as Zinc (Zn) and Copper (Cu) each separated by cloth soaked in a solution of salt water and which produces electricity without having to charge it (as opposed to the Leyden jar, antique capacitor technology of the time). In his letter, he often compares his device to the torpedo fish or the electric eel and therefore expresses his will to call it the “*organe électrique artificiel*” (artificial electric organ). However, it is most known by the name of voltaic pile in reference to him and to the device which is nothing more than a pile of metallic discs and cloth. Since then, electrochemical storage systems have greatly evolved and have become crucial to the positive transition of societies energy landscape to a more sustainable future. These evolutions have been marked by the fundamental understanding of the redox reactions taking place in such electrochemical cells and to both intentional and serendipitous breakthroughs throughout the past two hundred years.

One of the pivotal events which has enabled the development of today’s high capacity electrochemical storage technologies was the discovery of Lithium by Johan August Arfwedson and Jöns Jakob Berzelius in 1817-1818² which was later isolated by William Thomas Brande in 1821 and who described it at the time as “a brilliant white and highly combustible metallic substance”. Interestingly, he also states that “Pure lithia is very soluble in water, and its solution tastes acrid like other fixed alcalis” which illustrates the lack of personal safety considerations of the time.³ It was later understood that its flammability was due to its reactivity towards the ambient moisture which produced hydrogen gas. Indeed, its electrochemical potential was determined by Gilbert Lewis and Frederick Keyes in 1913 and found to be “the highest electrode potential hitherto measured”,⁴ attributing it the highest reducing power of all elements. Note the use of the Nernst–Lewis–Latimer convention (commonly referred to as the American convention) which defines the potential as that of the half reaction measured against a standard hydrogen electrode (SHE) which sign depends on the setup of the measurement as opposed to the Gibbs–Ostwald–Stockholm convention (commonly referred to as the European convention) which will be used in this thesis and that considers the potential

as that of the electrode which is invariant in sign.⁵ In the European convention, a reducing agent has a lower potential than an oxidizing agent, hence the potential of lithium is given as -3.04 V vs SHE. In addition to this incredibly low potential of -3.04 V versus the standard hydrogen electrode, it is the lightest solid element under standard conditions giving it the highest specific energy of all alkali metals. Higher specific energies can be attained by divalent and trivalent elements such as Beryllium or Aluminum but issues of toxicity (for Beryllium), solvation and diffusion arise which make them, as we will see, more difficult to use for industrial energy storage applications.

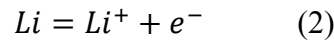
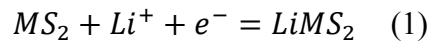
Before the discovery and the isolation of Lithium, the English scientist Sir Humphry Davy had managed to isolate sodium which was described by Jules Verne's emblematic character – Captain Nemo in *20,000 Leagues Under the Sea* – as “the most electromotive element of all”. While this is not true for sodium, it is more so the case for lithium which has driven intense academic and industrial research efforts for the past fifty years. In any case, this incredible foresight from a science fiction author of the 19th century is quite remarkable.

I-1 Lithium batteries

Owing to its light weight (6.94 g/mol), low potential (-3.04 V vs SHE) and high theoretical capacity (3862 mA·h/g), lithium was early on believed to have great potential for primary and secondary (rechargeable) battery systems but its reactivity was both the motivation and the roadblock. Finding a stable electrolyte was an arduous task and one that took over 20 years between the 50's and the 70's and was started by the seminal work of Harris and his thesis called “Electrochemical studies in cyclic esters”.⁶ His study of the transport properties of different ions in organic solvents paved the way to the finding “stable” electrolytes for Li metal plating which in turn would enable the development of energy storage systems. It was later understood that the aforementioned solvent's stability was in fact the result of a parasitic reaction. Indeed, in contact with lithium some organic solvents such as carbonates would react and form a passivation layer which would act as an ionic conductor and an electronic insulator, thus limiting further degradation of the electrolyte. This complex layer was coined by Peled as the “solid electrolyte interphase” (SEI).⁷ It is on account of this SEI that primary systems

using lithium as negative electrode were able to display long shelf lives of 10 years or more.⁸

Secondary batteries were developed in the late 70's early 80's with the increasing understanding of insertion chemistry thanks to researchers such as Stanley M. Whittingham and John B. Goodenough and the discovery of Li hosts such as the layered structure of sulfides (TiS_2 , ZrS_2 , MoS_2 ...), selenides (TiSe_2 , ZrSe_2 , MoSe_2 ...) ⁹ and lithiated oxides (Li_xWO_3 , LCO ...) ^{10,11} which could reversibly uptake/deliver Li^+ ions following the half reaction (1) and serve as positive electrodes in cells using Li metal (2) as negative electrode and an organic electrolyte (Figure I.1). This attracted much attention and craze over the possibility of making high energy density rechargeable lithium batteries. However, due to the fact that a battery is a closed system in which the consumption of the electrolyte by the parasitic reaction leading to the formation of the SEI over several plating/stripping cycles strongly hindered the development of these rechargeable systems. In addition, the SEI leads to inhomogeneous nucleation of lithium metal and the formation of preferential growth sites which in turn leads to the formation of Li filaments called “dendrites” as represented in Figure I.1 bottom panel. These dendrites can cross the separator and create short circuits which often lead to thermal runaway and, due to the volatile and flammable nature of the organic solvents used, to an explosion. While some companies still pursued the Li metal battery technology, the commercialization in 1988 by Moli Energy of a system based on MoS_2 as the positive electrode and using Li metal as the negative electrode which led to a massive recall of cell phones in Japan due to numerous fire incidents marked the end of the infatuation with Li metal negative electrodes.



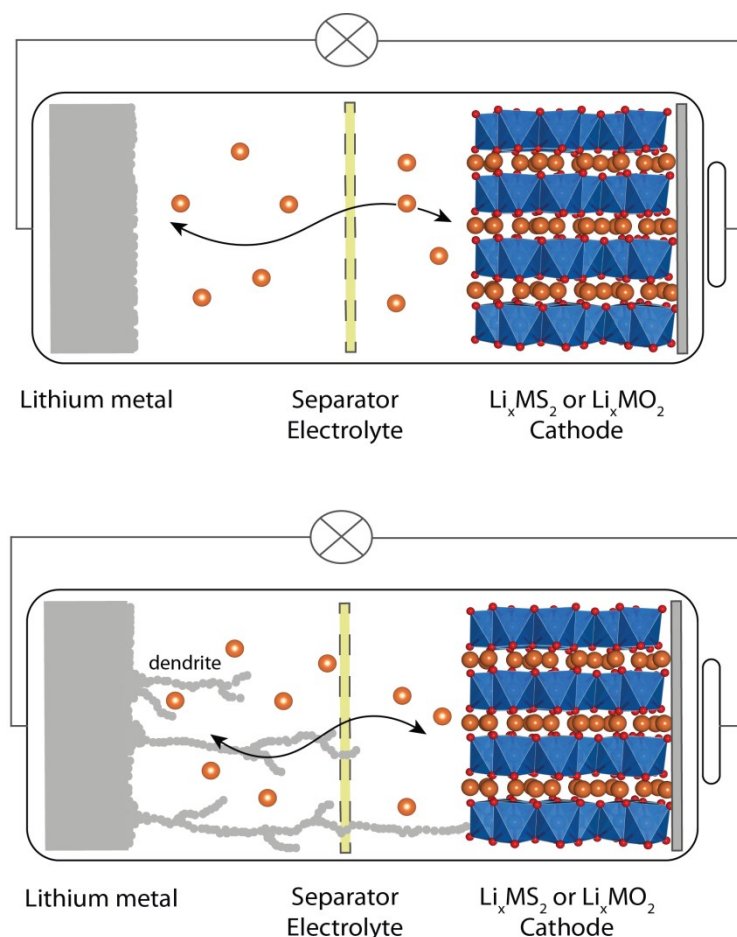


Figure I.1 (Top) Schematic of a Lithium battery with on the left the metallic lithium negative electrode, on the right the transition metal (TM) sulfide of oxide layered material and the separator with electrolyte between the two. In this simplified schematic view, only the Li⁺ cations are shown in the electrolyte but there is also the solvent molecules and the counter ions. (Bottom) Schematic representation of a cell after charging and the formation of dendrites which cross the separator to reach the cathode.

A few years later, a solid polymer electrolyte based system using Li metal as anode was commercialized but the technology was reserved for niche application such as stationary energy storage for telecommunication companies. Recently, Paris has been the testing grounds for this technology in shared vehicles called “Autolib” which are developed by Bolloré under the name BlueCar. This technology requires heating the cells around 60°C in order to improve Li⁺ diffusion within the polymer membrane and to maintain the proper management of dendritic growth. While this is acceptable for shared cars and public transportation applications it is poorly adapted to individual car ownership. The test was a success in terms of proving the technology viability but

unforeseen costs and underuse by the public far below the expectations led to a substantial debt and brought the project to an early grave in August 2018.

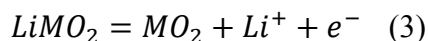
Academic and industrial research efforts are still deployed today in order to find solutions to the inherent risks of using lithium metal as a negative electrode but no mature technology is expected in the next few years. The most promising lead is the all solid state batteries which are very similar to the lithium metal polymer systems but with an inorganic electrolyte instead of the organic polymer. However, interfacial issues arise from the volume variations of both the lithium negative electrode and the insertion cathode. Due to the inherent risks of using lithium metal as anode, another promising technology surfaced near the end of the 80's which led the revolution of the LIBs.

I-2 Li-ion batteries (LIBs)

During the 80's the concept of lithium rocking chair batteries was developed which are known today as LIBs. The first mention of such systems was made D. Murphy and B. Scrosati in the late 1970's where the authors explain that the use of insertion materials, or host materials, for both the positive and the negative electrodes could solve the issues concerning the cycling of Li metal anodes.^{12,13} Shortly after, examples of such systems using LiWO_2 as negative electrode and positive electrodes composed of TiS_2 , WO_3 or NbS_2 were demonstrated¹⁴ but owing to the necessity to prelithiate the negative electrode prior to assembling the final cell and the poor diffusion of Li^+ into these hosts, they were considered too costly and inefficient.

Layered structures such as the sulfides are uncommon in oxides due to the high electronegativity of oxygen and the important coulombic repulsions ensuing between the negatively charged layers. Nevertheless, it is possible to obtain layered structures in oxides with alkali ions in between the MO_2 sheets, thus screening the negative charges. The discovery in 1980 by John Goodenough of LiCoO_2 ¹⁰ (LCO) and the subsequent discovery of several other LiMO_2 compounds with $M = \text{V}, \text{Cr}, \text{Ni}$ ¹⁵ and Mn which could reversibly release and uptake lithium into their structure (3) was key to the development of today's LIBs. The idea to use these lithiated compounds as the initial source of Lithium was presented by Auborn and Barberio in 1987 when they demonstrated the possibility of using as synthesized LCO as positive electrode and MoO_2 or WO_2 as

negative electrode without any prior steps.¹⁶ However, the overall capacity of such systems was not competitive due to the heavy TM ions in both electrodes.



The best negative intercalation electrode material was quickly understood to be graphite due to its relatively high capacity (372 mA·h/g), fast ion transport, low weight, low volume expansion during lithiation and reduction potential very close to that of lithium metal plating. Another good anode material is lithium titanate which was reported to have no strain induced by lithiation or delithiation.¹⁷ However, while its relatively high working potential (1.55 V vs Li) makes it very stable with respect to the carbonate electrolyte solution, it also lowers the overall tension of the battery which is a high price to pay. Similarly to lithium metal, a stable SEI can be formed on the surface of carbonaceous anodes, protecting the electrolyte from further degradation. However, lithium intercalation into graphite is accompanied by co-intercalation of propylene carbonate (PC), most commonly used electrolyte during that period, which led to exfoliation of the graphene sheets and loss of performances. It wasn't until discovering that the addition of ethylene carbonate (EC) into the electrolyte largely diminished this detrimental co-intercalation that practical applications became a reality. The first paper to evidence the beneficial effect of EC was published in 1990¹⁸ and the first commercialized cells were brought to market in 1991 by Sony which used graphite as negative electrode, LCO as positive electrode and an EC containing electrolyte.

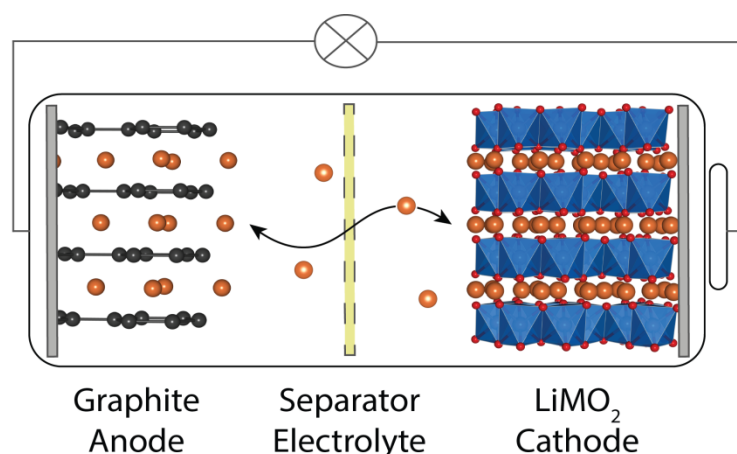


Figure I.2 « Rocking chair » or Li-ion battery (LIB) with two intercalation compounds at each electrode. The negative electrode is graphite and the positive electrode is a lithiated TM oxide. On charge, under potential or current control, Li^+ is extracted from the positive electrode commonly called cathode in the battery field and flow through the electrolyte to the negative electrode, commonly called anode. On discharge, the reverse reaction occurs spontaneously and Li^+ flows from the anode to the cathode through the electrolyte while electrons flow through the outer circuit creating a current.

Although the first commercialized LIB used LCO as cathode material, the high price and toxicity of Co were very early on a concern for commercialization and research was focused on finding materials with cheaper TM. Two main oxide families were pursued : the spinel LiMn_2O_4 ¹⁹ and the olivine LiFePO_4 .²⁰ While much research has been carried out on these two structures with different TM compositions, the focus of this thesis lies with the evolution of the layered oxide family derived from LCO.

I-3 Improving the capacity of LIBs

As explained above, the cost and toxicity of cobalt was a real driving force for researchers to find materials that could attain performances similar to or better than LCO using more environmental friendly and earth abundant elements. Furthermore, only ~50% of the theoretical capacity (135 $\text{mA}\cdot\text{h/g}$ out of 275 $\text{mA}\cdot\text{h/g}$) of LCO can be cycled reversibly which represents a significant amount of inactive capacity. Thus, LiNiO_2 (LNO) appeared to be advantageous as nickel is cheaper than cobalt, the working potential of LNO is slightly below that of LCO leading to less reactivity towards anodic decomposition of electrolyte and it has a higher capacity (> 150 $\text{mA}\cdot\text{h/g}$). However, it

was quickly shown that the thermal instability of Li_xNiO_2 presented major safety drawbacks, making its implementation unwise.²¹ Nevertheless, cation substitutions such as $\text{LiNi}_{(1-x)}\text{Co}_x\text{O}_2$ decreased the thermal instability while slightly increasing the capacity compared to LCO ($\sim 140 \text{ mA}\cdot\text{h/g}$). The best thermal stability was demonstrated by LiMn_2O_4 ²¹ and although this is not a layered compound it suggested that Mn could be a good substitution element for improving safety but also cost and toxicity. In addition, the demonstration of a cyclable LiMnO_2 ²² and the feasibility of a solid solution of composition $\text{Li}(\text{Ni}_{(1-x-y)}\text{Mn}_x\text{Co}_y)\text{O}_2$ ²³ with varying performances depending on the values of x and y opened the door to a proliferation of papers on a variety of possible combinations in order to obtain the highest performances with the lowest costs. Other cations were investigated such as Al^{3+} , Ti^{4+} and Mg^{2+} and others;^{24–26} however, due to the extensive research on the subject we will focus on the family of oxides called NMC for Nickel-Manganese-Cobalt.

In 2001, T. Ohzuku and Y. Makimura reported the now well known “NMC 111” which has equal parts of each TM and can attain a reversible capacity of $150 \text{ mA}\cdot\text{h/g}$ with a cutoff voltage of 4.2 V vs Li.²⁷ During that same year, J. Dahn’s group published a paper on $\text{Li}[\text{Ni}_x\text{Co}_{(1-2x)}\text{Mn}_x]\text{O}_2$ for which $x = 1/4$ and $3/8$ which stated that capacities of $160 \text{ mA}\cdot\text{h/g}$ and $150 \text{ mA}\cdot\text{h/g}$ respectively could be obtained with a cutoff potential of 4.4 V .²⁸ For $x = 3/8$, if the high voltage limit was reduced to 4.2 V , the reversible capacity was closer to LCO with $136 \text{ mA}\cdot\text{h/g}$. However, they measured the stability of each compound at different states of charge and compared with LCO. It was found that both materials performed better and presented definite advantages with respect to safety in addition to those in terms of cost and toxicity brought by Mn. It is today’s understanding that the capacity of these materials is mainly brought by Ni and to a lesser extent to Co which rather brings rate capability by improving electronic conductivity and that Mn has a stabilizing effect with respect to thermal decomposition.^{29,30} While the presence of Ni in the Li interlayer in non-stoichiometric $\text{Li}_{1-x}\text{Ni}_{1+x}\text{O}_2$ but also at high states of charge due to cation migrations in LNO was determined to be the cause of capacity fading observed in these cathode materials,³¹ it seems substitution by Co and Mn hinders this degradation path. Thus, one of the best performing electrodes used today for EV applications is the NMC materials but large efforts are invested in increasing the amount of Ni in order to increase the capacity while avoiding the thermal instability and capacity fading of pure LNO. Today’s market for EV applications is for

the most part composed of NMC 111 and 532 but higher Ni content materials such as 622 and to a lesser extent 811 capable of delivering as much as 200 mA·h/g are seeing their way to the market as well and seem to be the most promising cathode materials for EVs in the near future.^{29,32}

I-4 Outgrowing classical cationic redox

As we have seen in previous sections, the energy density of cathode materials has improved during the past decade and devices are becoming increasingly reliable. Nevertheless, it seems we are approaching the limits of the best known materials and innovations that disrupt the field are needed. In recent years, such a paradigm shift has occurred with the discovery of what is now well established as anionic redox. It all started with Amatucci *et al.* showing that full delithiation of LCO to obtain CoO₂ was possible but that Co was only partially oxidized in the fully delithiated compound.³³ It was quickly hypothesized that oxygen must also be, in some part, capable of being oxidized during delithiation.^{34,35} Evidence of O-O distance shortening in LCO at high states of charge further suggested that oxidation of the lattice oxygen was a relevant charge compensation mechanism during delithiation.³⁶ However, it wasn't until the discovery of a new family of oxides with surprising energy densities known today as Li-rich NMC that this theory really started making sense.

These Li-rich materials of composition Li_{1+x}M_{1-x}O₂ with $x \leq 1/3$ ($M = \text{Ni, Mn and/or Co}$), also written Li₂MO₃ for $x = 1/3$, can be obtained by substituting the TM from LiMO₂ for additional Li in the TM layers. Such systems, with $M = \text{Ru or Mo}$, were studied early on by James and Goodenough in 1988 as cathode materials due to their structural similarities with the LiMO₂ phases.^{37,38} Indeed, Li₂MO₃ compounds can adopt a rocksalt derived layered structure in which Li₃ and LiM₂ sheets are alternated and separated from each other by O layers. Due to the size difference between Li and the TM, a specific ordering can be achieved describing a honeycomb motif. While these compounds intuitively could attain higher capacities thanks to the increased Li/TM ratio, the limitation was thought to come from the highest oxidation state of the TM. It wasn't until the successful cycling of Li₂MnO₃ in which Mn is in octahedral coordination with a +IV oxidation state and for which the +V state is unlikely, that questions about the origin of the high capacity of this material started arising. The capacity and cyclability

was initially thought to be due to the loss of Li_2O from the structure at high potential and the formation of a biphasic system with LiMnO_2 which was redox active and stabilized by the presence of Li_2MnO_3 domains.³⁰ This was the beginning of a new wave of materials research which aimed at developing composite materials of composition $x\text{Li}_2\text{MnO}_3-(1-x)\text{LiMO}_2$ with $M = \text{Ni}, \text{Mn}, \text{Co}$ and other TMs which were later understood to be solid solution compounds.

Indeed, in 2002, Dahn and coworkers described the synthesis of a family of compounds of composition $\text{Li}[\text{Ni}_x\text{Li}_{1/3-2x/3}\text{Mn}_{2/3-x/3}]\text{O}_2$ with $x = 1/2, 5/12, 1/3, 1/4$ and $1/6$ with intriguing electrochemical properties. It is important to bear in mind that in all the compounds, Mn is maintained in the +IV state whereas Ni is either in +II or +III state and is the only redox active TM. When limiting the potential window between 2.0 V and 4.0 V, the voltage composition curve shows a smooth plateau on charge and discharge with no significant polarization, capacities close to the theoretical values and good reversibility are obtained. Surprisingly, when the upper cutoff voltage is increased to 4.8 V, a second smooth voltage plateau is observed on charge with a slope-like discharge with a large irreversible capacity. X-ray diffraction allowed to determine that the irreversible capacity loss was due to the loss of oxygen from the structure.^{39,40} While this irreversible loss of oxygen was cause for concern, the reversible capacities could attain $230 \text{ mA}\cdot\text{h/g}$ with a voltage window between 2.0 V and 4.8 V. Further substitution of Mn by some amount of Co led to what are now known as the Li-rich oxides which can deliver up to $270 \text{ mA}\cdot\text{h/g}$ (Figure I.3).^{41,42}

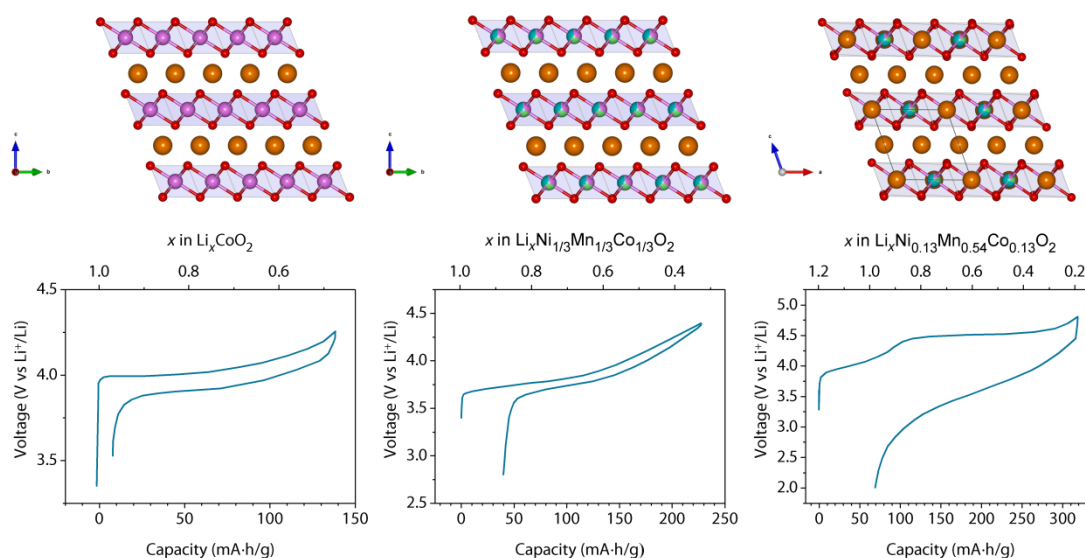


Figure I.3 Evolution of Layered oxide cathode materials structure/composition and their electrochemical behavior. a) LCO composed of alternating layers of Co (pink) and Li (orange) separated by layers of oxygen (red). The electrochemistry is very reversible and stable. b) NMC 111 with a structure similar to LCO with partial substitution of Co for Ni (green) and Mn (blue). The electrochemistry is quite similar between the different NMC materials although capacities vary (extracted from Deng et al. 2010⁴³). c) Li-rich NMC in which the TM are partially substituted for Li resulting in a honeycomb motif. The electrochemistry is characteristic of Li-rich compounds with two distinct plateaus on the first charge and a slope discharge⁴⁴.

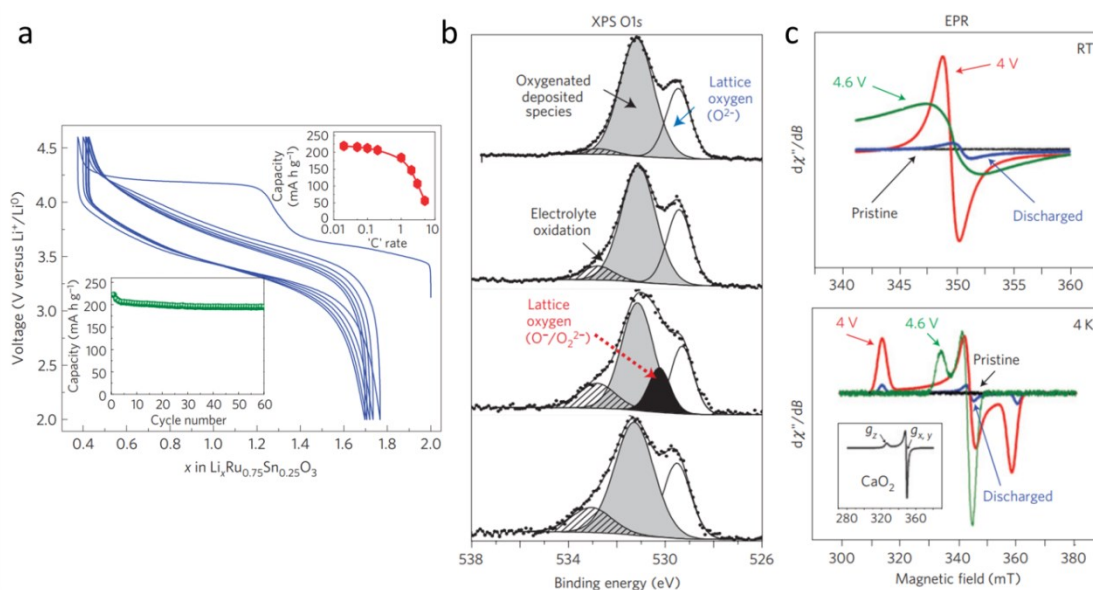


Figure I.4 Reversible anionic redox evidenced by XPS and EPR in $\text{Li}_2\text{Ru}_{1-y}\text{Sn}_y\text{O}_3$. a) Voltage composition curve for $\text{Li}_2\text{Ru}_{0.75}\text{Sn}_{0.25}\text{O}_3$ showing a staircase profile on first charge followed by an S-shaped discharge which is retained on subsequent charge/discharge cycles. b) XPS O 1s spectra at different states of charge and discharge with from top de bottom : pristine, charged to 4.0 V, charged to 4.6 V and after full discharge back to 2.0 V. The different signals obtained by deconvolution of the signal are explained on the figure. c) EPR spectra at room temperature (top) and at 4 K (bottom) showing the appearance of a sharp signal at full charge signifying the presence of paramagnetic electrons on oxygen and therefore of oxidized species. Reproduced from Sathiya *et al.*, *Nature Materials* (2013).

While several hypotheses on the origin of the extra capacity were stipulated during the following years (TM over-oxidation, loss of Li_2O or O_2 accompanied by the formation of spinel-like phase on the surface, Li/H ion exchange...), it wasn't until 2013 that a solid explanation could be demonstrated through the study of model materials such as $\text{Li}_2\text{Ru}_{1-y}\text{M}_y\text{O}_3$ ($y = 0-1$) with $M = \text{Sn}, \text{Ti}, \text{Mn}$.⁴⁵⁻⁴⁷ Indeed, these compounds adopt a similar layered structure to the Li-rich NMC with honeycomb layers of LiM_2 alternated with pure Li layers in a dense stacking of oxygen. Their advantage is their simplicity with regards to the redox active species and their similar electrochemical behavior to the Li-rich NMC materials, namely the first charge composed of two well defined voltage plateaus followed by an S shaped discharge after the second plateau leading to slope-like subsequent charge/discharge cycles. Indeed, in $\text{Li}_2\text{Ru}_{1-y}\text{Sn}_y\text{O}_3$, only Ru is a redox active cation and its oxidation which can be followed either by X-ray photoemission spectroscopy (XPS)^{45,48} or by X-ray absorption near edge structure

(XANES).⁴⁹ However, the first signs of anionic redox were detected by electron paramagnetic resonance spectroscopy (EPR) and XPS on the O 1s level (see Figure I.4). The appearance of a new component around 531 eV on the second plateau was assigned to an oxidized lattice oxygen O^- environment which was supported by density functional theory (DFT) calculations.^{45,47,48} These oxidized oxygens were suspected to form “peroxo-like” species with shortened O-O distances however, due to the lack of long range ordering they could not be evidenced by XRD. It wasn't until their detection by XPS and their visualization by transmission electron microscopy (TEM) and (NPD) in α - Li_2IrO_3 that this was confirmed (see Figure I.5).⁵⁰ Finally it was concluded that oxygen redox could bring additional capacity which brought new hope to the field of materials research for higher energy density cathode materials.³⁰

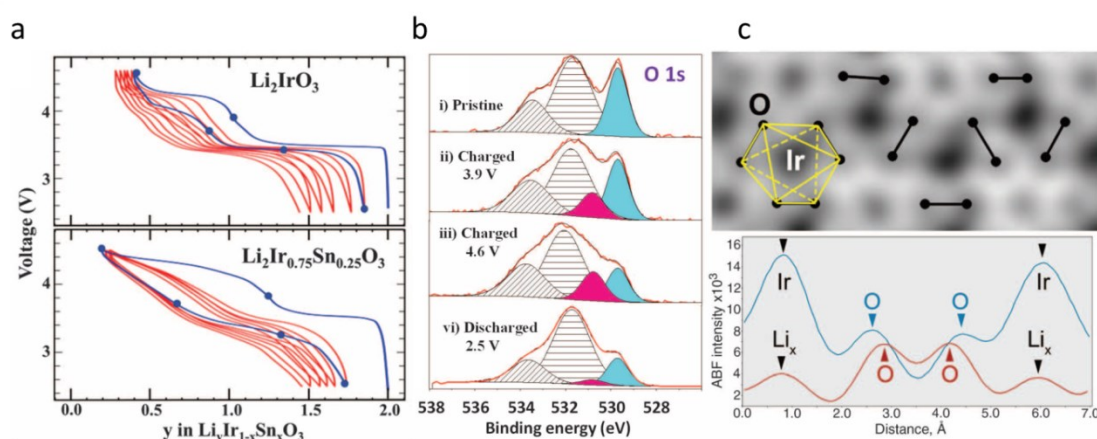


Figure I.5 Evidence and visualization of short O-O distances on fully charged α - Li_2IrO_3 . a) Voltage composition curve of α - Li_2IrO_3 and α - $Li_2Ir_{0.75}Sn_{0.25}O_3$. b) XPS O 1s spectra of α - Li_2IrO_3 at OCV, 3.9 V, 4.6 V and after one charge/discharge cycle. The components obtained by deconvolution of the spectra are as follows: blue for the O^{2-} lattice oxygen, pink for the O^{n-} lattice oxygen, vertically and diagonally hashed for the surface adsorbed species. c) HAADF-STEM image of the fully charged α - Li_2IrO_3 with the integrated intensities shown below evidencing the shortened O-O distances. Reproduced from McCalla *et al.*, *Science* (2015).

This comprehension was then extended to the more complex but useful Li-rich NMC^{51,52} and a plethora of publications on anionic redox as a strategy to increase energy density of oxide cathode materials has been published.^{30,44} However, long term performance decay such as voltage fading^{53,54} and capacity loss over cycling hinder the integration of such Li-rich compounds in batteries for EV applications.

I-5 Origin of performance decay in Li-rich layered oxides

As explained above, the Li-rich layered oxide (LrLO) cathodes display impressive capacities but also steady decay of energy density over cycling coming from both the loss of capacity due to oxygen release on the first cycle at high potential⁴⁰ and the voltage fading⁵³ which origin will now be discussed. Once again, the reason for the diminishing Li^+ de/intercalation potential over cycling was solved through the study of the $\text{Li}_2\text{Ru}_{1-y}\text{M}_y\text{O}_3$ (with $\text{M} = \text{Mn}, \text{Ti}, \text{Sn}$) model compounds. It was observed that the compound containing Ti shows superior voltage decay over cycling compared to the Sn substituted phase (Figure I.6). *Post mortem* TEM images clearly show that a large amount of Ti ions migrate irreversibly to tetrahedral sites within the Li layer in order to stabilize the Li poor structure. While this trapping of small ions is also observed in the Li-rich NMC phases, the substitution of Ru by larger spectator ions such as Sn is found to considerably mitigate the voltage decay and TEM images display substantially less ion migration which can be rationalized by comparing the ionic radii ($r_{\text{Ti}^{4+}} \ll r_{\text{Sn}^{4+}}$).⁴⁶ However, the substitution of active redox centers by inactive ones comes at the expense of energy density and was therefore considered an undesirable strategy although it served its purpose by uncovering the mechanism of voltage decay in Li-rich oxides.⁴⁶ Structural defects as the origin of the loss of lithium extraction potential is now well established^{55–59} and many strategies with varying degrees of success are pursued in order to solve the issue either by substitutions,^{60–65} by controlled formation of oxygen vacancies/cation site defects^{66–68} and by surface doping coating.^{69–74}

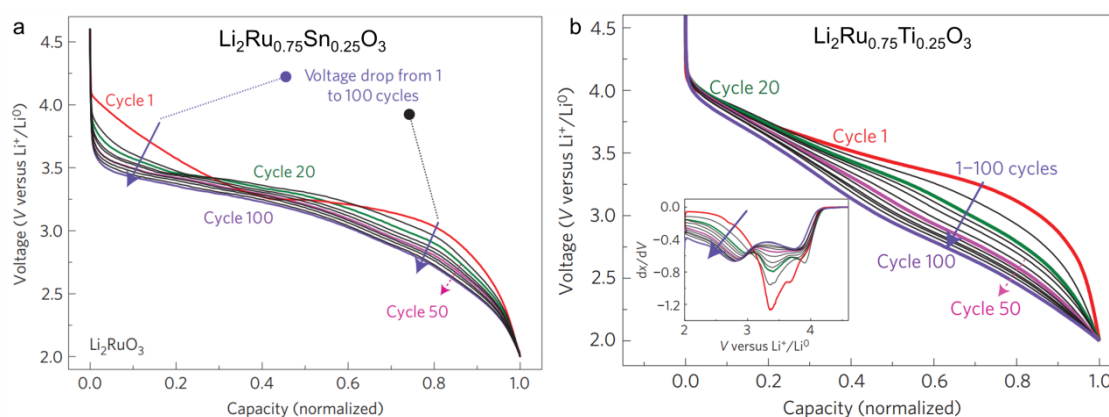


Figure I.6 Voltage composition profiles for the first 100 cycles of a) $\text{Li}_2\text{Ru}_{0.75}\text{Sn}_{0.25}\text{O}_3$ and b) $\text{Li}_2\text{Ru}_{0.75}\text{Ti}_{0.25}\text{O}_3$ showing the voltage decay over cycling (adapted from Sathiya *et al. Nature Materials*, 2013)

While the process of delithiation/lithiation through anionic redox in these LrLOs is well recognized by the community, its crystallographic and electronic structural implications are still not fully resolved and require both theoretical and experimental work in order to paint the complete picture which would allow us to determine its true viability for applications such as portable electronics and EVs. The current understanding of the origin and implications of anionic redox will now be developed.

I-6 Origin of anionic redox

In order to understand the origin of anionic redox, it is essential to have a good description of the electronic structure of the studied oxides. Due to the high covalency of the TM-O bond compared to the Li-O bond, a simplified description of the electronic structure of lithiated oxides can be constructed based solely on the TM-O interactions.^{57–59} The TM orbitals involved in bonding with ligands are the nd orbitals and those for O are the $2p$ orbitals as the $2s$ levels lie too deep for any overlap to take place. In the materials relevant to this discussion, all TM are in octahedral sites and the nd orbitals will be considered as split into stabilized t_{2g} and destabilized e_g orbitals with a gap Δ . In addition, these transition metal oxides are known Mott insulators with a splitting of the TM bands (U) due to electrostatic repulsions between unpaired electrons.

Three different compositions with their structures (excluding Li^+ ions) and band diagrams are depicted in Figure I.7. First we will discuss the case of the classical LiMO_2 structure such as LCO, secondly we will increase the O/M ratio and describe the electronic structure of the LrLOs (Li_2MO_3). Finally we will comment on a yet higher O/M case, the Li_3MO_4 type compound with $M = \text{Ir}$ and/or Ru which has been studied as a model cathode material for pushing the limits of anionic redox.

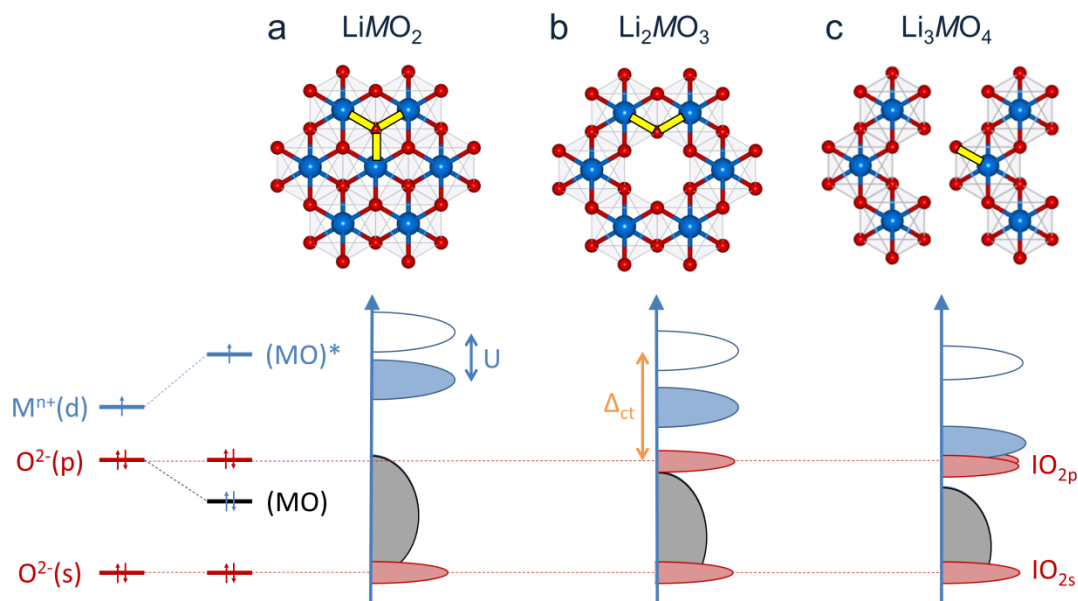


Figure I.7 Structures and simplified band structures of different lithiated TM oxides of compositions a) LiMO_2 , b) Li_2MO_3 and c) Li_3MO_4 . The blue and red spheres represent the TM and oxygen ions respectively and the yellow filled rectangles highlight the O environment with respect to the TM. The Hubbard splitting is shown with a blue double arrow and the charge-transfer gap with an orange double arrow. The bands represented in blue imply orbitals that are mainly localized on the TM, in red on O and in grey both on O and TM.

In the layered LiMO_2 structure, each oxygen anion is bonded to three neighboring TM cations forming (MO) bonding states and $(\text{MO})^*$ antibonding states as depicted in Figure I.7 a). In this scenario, if the nd orbitals of the TM lie much higher in energy than the O $2p$ orbitals as is generally the case, the $(\text{MO})^*$ states are localized on the cation and when the material is oxidized (i.e. lithium is extracted) on charge and electrons are taken from these states, it is called cationic redox as the holes are localized on the TM cation orbitals. When these states are empty, further lithium withdrawal would lead to structural degradation as it would empty the bonding states.

However, in structures where the M/O ratio is higher than $1/2$, such as in the LrLOs (Li_2MO_3), non-bonding oxygen $2p$ states are present as represented by a thin red band at the top of the (MO) band in Figure I.7 b). In this scenario, two cases can be differentiated: (i) if the TM orbitals lie high above the O $2p$ states or in other words $U < \Delta_{\text{ct}}$, the electrons are first withdrawn from the $(\text{MO})^*$ band which is again considered as cationic redox. Once these levels are depleted, the O $2p$ electrons can still be removed

and give rise to what is known as anionic redox. This process is generally thought to entail a distortion of the MO_6 octahedra in order to stabilize the holes on oxygen by the formation of O-O states and which, if pushed too far, can lead to oxygen release. A good example of this degassing is the Li-rich NMC compounds which have been shown to evolve O_2 during the high potential process (anionic redox portion). (ii) If the $(\text{MO})^*$ states lie close to the O 2p non-bonding states, a distortion can give rise to the hybridization of these two states and the formation of $\text{M}(\text{OO})$ σ , π , π^* and σ^* states which should stabilize further the holes on oxygen type states and thus increase reversibility. In both cases, the maximum amount of charge that oxygen is capable of delivering before the release of molecular O_2 in these compounds has been theoretically determined as $1/3 \text{ e}^-/\text{O}$.⁵⁹ Furthermore, structurally this will lead to the formation of distorted octahedra and short O-O distances which have been termed as “peroxo-like” species.⁵⁹ It is important to bear in mind that, while these are considerably shortened O-O distances for these compounds, they are far from the true peroxide bond length and their spectroscopic signatures are not necessarily comparable to Li_2O_2 species as we will see.

As mentioned above, the case of Li_3MO_4 with $\text{M} = \text{Ir}$ and/or Ru were recently studied to attempt to push anionic redox further and assess its limits.^{75,76} In Figure I.7 c), the structure represented is that of Li_3RuO_4 as it has a Li/Ru ordering within the layers whereas in the case of Li_3IrO_4 , Li and Ir are completely disordered and makes the illustration more difficult. It is clear that, while the ordering/disordering will most likely lead to differences in performances, the simplified band structure will most likely be similar with namely the presence of more O 2p non-bonding states as can be deduced by the mean oxygen environment. In this particular case, as Iridium is a 5d TM with a high oxidation state (+V), the $(\text{MO})^*$ states are most likely closer to the O 2p non-bonding states and it has been demonstrated that upon charging (Li^+ extraction) holes are localized mainly, if not solely, on the oxygen state. This anionic redox allows the reversible removal of up to two Li^+ while a third one leads to O_2 evolution and the loss of long range ordering to form an amorphous iridate of composition IrO_3 as deduced by TGA-MS.⁷⁵ In the case of $\text{M} = \text{Ru}$, the dissolution of Ru mitigates the gas evolution but is equally detrimental.⁷⁶ Either way, increasing the O/M ratio seems to favor the extraction of lithium through oxygen redox rather than TM redox and $0.5 \text{ e}^-/\text{O}$ is the highest amount of charge that oxygen is capable of delivering before the release of

molecular O₂ in the case of Li₃IrO₄ which differs significantly from the theoretical limit attributed to the Li₂MO₃ family of compounds (1/3 e⁻/O) suggesting a higher amount of reversibility is attainable by tuning structure and composition.

Another class of materials not mentioned thus far but which has concentrated significant research efforts is the disordered rocksalt Li₂MO₃ compounds. Indeed, while composition is of course the obvious parameter on which chemists have played with in order to increase the capacity of cathode materials, a high degree of order was always desired in order to increase Li⁺ diffusion until the discovery of the surprising yet interesting behavior brought upon by the disordering of cations within the structure of Li₂MO₃ compounds.^{68,77,78} While these display large amounts of reversible anionic redox activity they will not be discussed as of now.

I-7 Na-ion batteries (NIBs)

Sodium based systems have followed a parallel path to Lithium based systems with namely the study of insertion chemistry in the 70's using sulfides and in the 80's using oxides such as NaCoO₂ (see Figure I.8 a). However, the penalty incurred by the lower potential (-2.71 vs SHE) of sodium and its higher molar mass (22.99 g/mol) limited the energy density of insertion compounds compared to those inserting Lithium as illustrated by the cycling profile of LCO compared to NaCoO₂ shown in Figure I.8 a). Furthermore, Na containing compounds tend to exhibit higher reactivity to ambient moisture, making their use more difficult than their lithiated counterparts. In addition, due to the higher solubility of the sodium salts and decomposition products of the electrolyte at low potential, the use of Na metal as anode was impractical and the sodium batteries were not pursued for very long. In fact, research on sodium based systems nearly vanished until recently due to geopolitical and environmental concerns about the limited amounts of Lithium available on earth (see Figure I.8 b) which has boosted considerably the interest in Na-ion batteries.

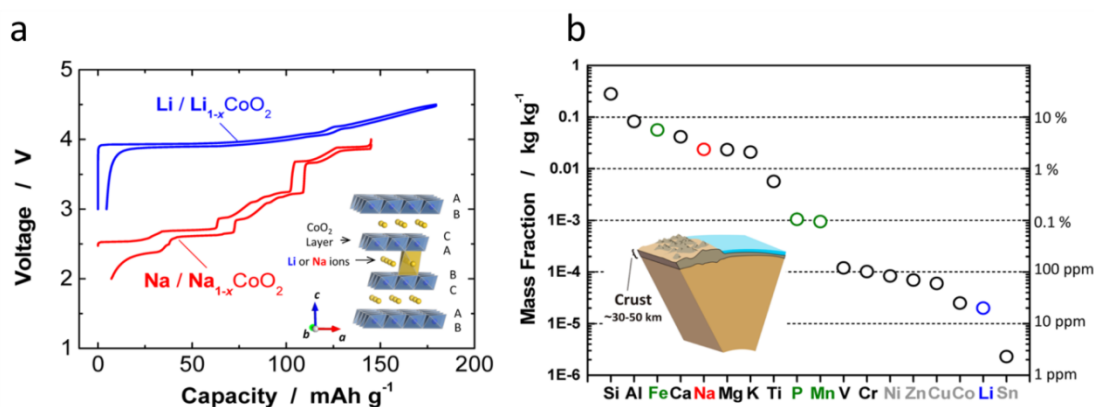


Figure I.8 a) Voltage capacity profiles for LiCoO_2 and NaCoO_2 with the layered ACoO_2 ($A = \text{Li}$ or Na) structure in inset. b) Abundance of elements in earth's crust. Reproduced from Kubota *et al. Chemical Reviews* (2014).⁷⁹

In the early days of research on Na-ion batteries, the major concern was finding a proper negative electrode as graphite could not be used due to its inability to reversibly insert Na. The turning point for these systems was the discovery of a “hard” carbon (that is to say non graphitizable) capable of delivering around 300 mA·h/g of capacity by sodium de/insertion, hence nearing that of graphite in LIBs.^{80,81} While this did not solve the energy density issues (compared to LIBs), it did enable a new wave of enthusiasm for NIBs and today's research is, again similarly to the LIB, focused on developing high energy density cathode materials. Today's stellar material is a polyanionic compound composed of vanadium phosphate of formula $\text{Na}_3\text{V}_2(\text{PO}_4)_2\text{F}_3$ which can deliver up to 110 mA·h/g after 100 cycles.⁸² However, the use of toxic vanadium is undesirable when it comes to large scale applications and finding materials that make use of safer and more environmental-friendly TMs is an important driving force for the materials research community.

Since the NIB community has often been inspired by the LIB research, the recent discovery of anionic redox as a means to increase energy density is of great interest to researchers working on sodium insertion materials. Recent reports of such activity in Na-ion cathode materials have boomed in the past couple of years. However, similarly to the Li insertion compounds, the structural implications of such anionic redox are not well established yet.

Conclusion

In this chapter we have seen the evolution of the Li-ion technology with the different historical events that have led to today's high energy systems. Although the capacities have increased steadily in the past decades, there are still some important limitations that must be pushed back in order to truly earn our independence from fossil fuels and take full advantage of renewable energy sources such as solar or wind.

The Li-ion technology is the most promising for portable electronics and electric transportation and while the automotive industry is pushing hard on the development of electric vehicles, the requirements are still not met in terms of range and lifetime. The Li-rich oxide cathodes represent a significant improvement in energy density compared to the state of the art layered materials but substantial roadblocks still hinder their integration. In recent years, the oxygen redox mechanism has been thoroughly investigated and important efforts are deployed to develop chemical and engineering solutions to mitigate the inherent issues surrounding it. However, questions still remain about the structural implications of anionic redox and the structure/property relationship.

The most studied materials exhibiting a redox active oxygen network mainly crystallize in a layered structure and show very similar electrochemical behaviors. The development and investigation of novel structures could lead to a better understanding of solid state anionic redox and to more stable electrode materials. Interestingly, materials having a disordered structure, meaning that cations are randomly distributed within the oxygen network and therefore increasing the dimensionality of the TM network, have shown some interesting electrochemical properties at 55°C. While the layered structures unanimously display a drastic change of their electrochemistry after the first charge, these completely disordered structures retain their initial electrochemical profile although oxygen redox leads to large polarization issues which exceed those observed in the ordered layered oxides.^{68,77,78,83}

The aim of this thesis is the study of a tridimensional IrO₃ framework which has a redox active oxygen network with an initial voltage profile which is retained over cycling. This framework can accommodate Li⁺ and Na⁺ ions as well as H⁺. While the protonated phase displays poor performances in terms of reversible proton insertion, it

has shown some interesting activity as OER catalyst. The next chapter will describe the work carried out on Li^+ insertion into the IrO_3 framework.

Chapter II. Structural and electronic implications of delithiation for the β -Li₂IrO₃

II-1 Introduction

In this chapter, we will discuss the effect of increasing dimensionality of the host structure on the electrochemical performances of Li-rich layered oxides. Fortunately, the lithiated iridates are an amazing playground in terms of structure and composition. Li_2IrO_3 crystallizes in three different polymorphs^{84,85} named α , β and γ , which are shown in Figure II.1. All derive from the rocksalt structure, with a dense packing of the oxygen layers (ABCABC stacking). The α form is a typical layered structure with alternating layers of composition Li_3 and LiIr_2 . The LiIr_2 layers are organized in a honeycomb type structure with LiO_6 octahedra enclosed in a hexagon formed by IrO_6 octahedra linked together through edge sharing (see Figure II.1). β - Li_2IrO_3 is built on edge-sharing IrO_6 octahedra that form a tridimensional matrix into which Li ions occupy all available octahedral sites as shown in Figure II.3 a. The structure can accommodate Li migration via corrugated interconnected paths as supported by a bond valence landscape calculation shown in Appendix Chapter II. Figure 1.

This chapter is composed of six sections, which are organized as follows. The first will describe the synthesis and structural characterization of the β - Li_2IrO_3 phase, namely through the use of diffraction techniques and electron microscopy. Then the electrochemical behavior of the hyperhoneycomb iridate will be investigated by galvanostatic cycling with potential limitation and we will discuss the effect of different cutoff voltages on its performances. In order to probe the redox active species – Ir or O – during cycling, techniques such as X-ray absorption and X-ray photoelectron spectroscopies have been used and the results will be presented in light of the electrochemical performances. The different structural implications of the delithiation processes will then be explored using *operando* and *ex situ* diffraction measurements using synchrotron X-rays and neutrons as well as EXAFS. Finally, a brief summary of the overall findings with a discussion around the structural and electronic implications of anionic redox during delithiation of the β - Li_2IrO_3 will conclude this chapter.

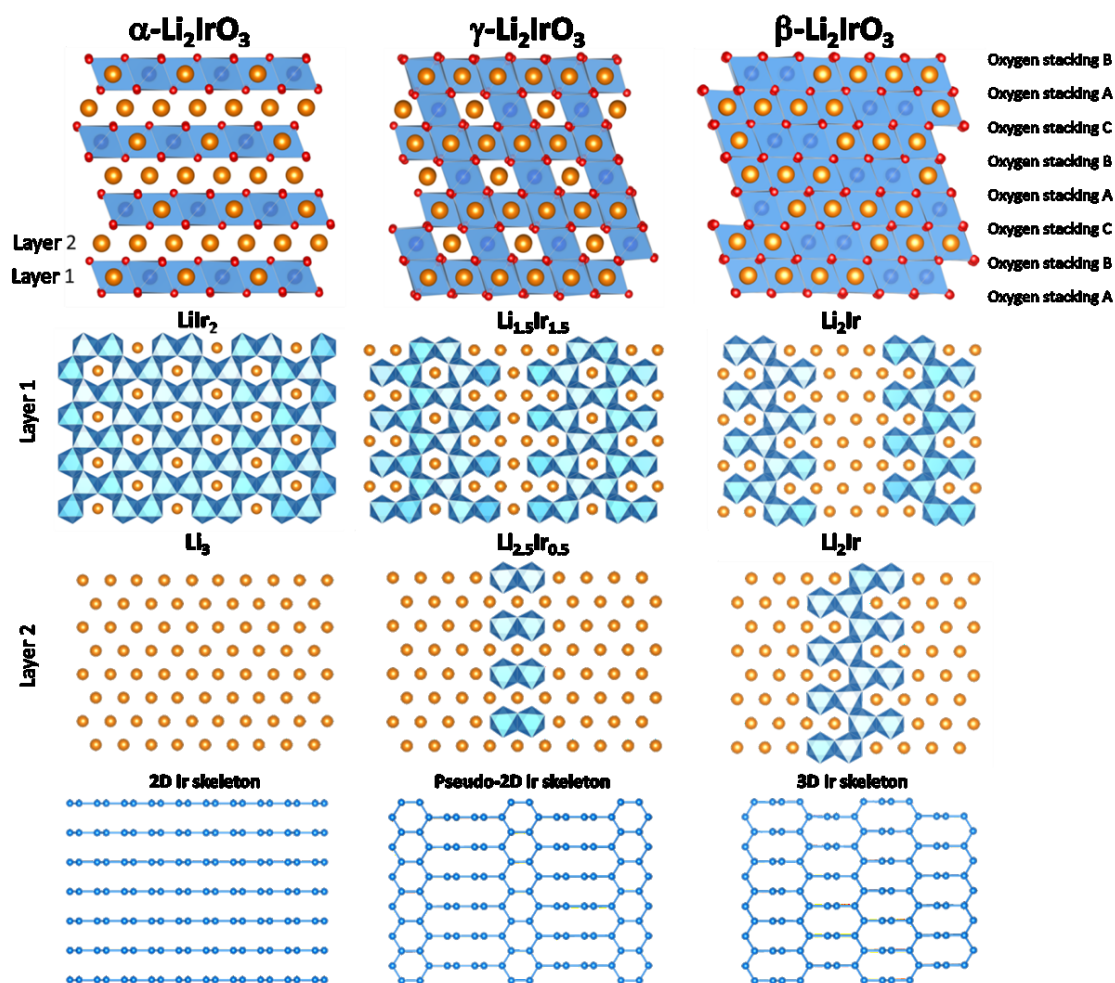


Figure II.1. Structures of the α , γ and β - Li_2IrO_3 polymorphs. From top to bottom: General view of the structure highlighting the ABCABC oxygen dense packing with cations (Li and Ir) sitting in octahedral sites. O is red, Li is orange, and IrO_6 octahedra are colored in blue. The individual layers are shown below with their chemical composition. The bottom part only shows the Ir-Ir bond skeleton to highlight the dimensionality of the polymorphs, and the way Ir atoms are displaced from the α structure to generate the γ and β structures.

II-2 Synthesis and structure

II-2-a Synthesis

In the past, the β - Li_2IrO_3 polymorph has been synthesized by repetitive annealing at temperatures above 1000°C (or prolonged annealing under O_2) of the layered polymorph. However, this synthesis route is both energy intensive and poorly reproducible as annealing times to achieve single-phased materials required either 3 days or one month. In any case, the β - Li_2IrO_3 could only be obtained with particle sizes

above a few microns and the recent report of a new synthesis route for large single crystals of both α - and β - Li_2IrO_3 by a separated educts vapor transport process⁸⁶ was an impetus to design a faster and more reproducible route to synthesize polycrystalline β - Li_2IrO_3 . Indeed, the vapor transport process relies on the formation of gaseous IrO_3 and LiOH which allows the formation of large single crystals. In this logic, the powders were mixed but not compacted into a pellet and Ir was added in excess to increase the IrO_3 vapor pressure.

Hence, different Ir/Li ratios were tested in order to find the optimal synthesis conditions. It was found that an excess of Ir was required to preferentially form large particles of β - Li_2IrO_3 instead of a fine powder composed of α polymorph. After some optimization (see Appendix Chapter II. Figure 2), Ir black and Li_2CO_3 in a 1/0.9 ratio were mixed by hand grinding the powders in an agate mortar, inserted into an alumina (Al_2O_3) crucible. In order to increase the vapor pressure of IrO_3 , an alumina lid was placed on the crucible. To confirm the hypothesis that covering the crucible increases the vapor pressure of both Ir and Li, half of the precursor batch was added to a crucible of same size but without covering. These crucibles were then placed in a box furnace and heated at a rate of $3^\circ/\text{min}$ to 1000°C and held at this temperature for 24 hours after what, the furnace was allowed to cool to room temperature without control of the rate. Visually, both systems showed important differences namely the powder from the covered crucible was glistening with visibly large particles whereas the powder from the uncovered crucible was mat black thin powder. The XRD patterns show a mixture of β - Li_2IrO_3 , IrO_2 and a small impurity of α - Li_2IrO_3 for the sample from the closed crucible and α - Li_2IrO_3 with a bit of IrO_2 for the sample from the open crucible (Appendix Chapter II. Figure 2). The appropriate amount of Li_2CO_3 (0.1 equivalents) was added to the sample that was covered, hand grinded and fired with the same procedure as the previous step to obtain pure β - Li_2IrO_3 with particle sizes $>10\mu\text{m}$ and good crystallinity as evidenced by synchrotron XRD and neutron diffraction which will be described below (Figure II.2 and Figure II.3 c). Our exploration on the synthesis of β - Li_2IrO_3 therefore indicates a strong dependence on the particle size in addition to the temperature: the β phase being easily obtained for particle sizes above a few microns.

II-2-b Structural characterization

The synchrotron X-ray diffraction pattern collected at the MSDP beamline at Alba Synchrotron, Spain, using a wavelength of 0.414 Å was refined using the Rietveld method (Figure II.2), confirming the previously reported $Fddd$ hyperhoneycomb structure (Table II.1)⁸⁴ with lattice parameters $a = 5.905856(8)$ Å, $b = 8.450657(11)$ Å, $c = 17.81199(2)$ Å. Due to the large atomic number of Iridium and therefore its overwhelming contribution to the structure factor, the precision on the positions of Li and O is questionable. NPD, far more sensitive than X-rays to Li and oxygen ($b_{\text{Ir}}=10.6$ fm $b_{\text{Li}}=-1.9$ fm $b_{\text{O}}=5.80$ fm) was carried out and the atomic positions are consistent with the previously reported structure.⁸⁴ The combined Rietveld refinement of both SXRD and NPD patterns is shown in Figure II.2 and the crystallographic data with atomic positions are listed in Table II.1

Table II.1 Crystallographic data and atomic positions of the β -Li₂IrO₃ determined from Rietveld refinement of its neutron diffraction pattern. A bond valence sum analysis (BVS) (using d_0 from Ir⁴⁺) is included.

β -Li ₂ IrO ₃							
Space group $Fddd$							
NPD : $a = 5.91025(6)$ Å, $b = 8.45727(8)$ Å, $c = 17.81218(16)$ Å, $V = 890.334(14)$ Å ³ , $R_{\text{Bragg}} = 3.45\%$, $\chi^2 = 2.31$							
SXRD : $a = 5.905856(8)$ Å, $b = 8.450657(11)$ Å, $c = 17.81199(2)$ Å, $V = 890.353(14)$ Å ³ , $R_{\text{Bragg}} = 5.76\%$, $\chi^2 = 7.82$							
Atom	Wyckoff position	x/a	y/b	z/c	B (Å ²)	Occ.	BVS
Ir	16g	1/8	1/8	0.70821(14)	0.82(2)	1	3.919(12)
Li1	16g	1/8	1/8	0.0489(7)	1.54(16)	1	0.950(7)
Li2	16g	1/8	1/8	0.8738(8)	1.40(13)	1	0.999(10)
O1	16e	0.8596(8)	1/8	1/8	0.86(4)	1	2.034(10)
O2	32h	0.6325(9)	0.36479(17)	0.03830(12)	0.88(2)	1	1.917(10)

In order to further confirm the structure scanning transmission microscopy (STEM) in both high angle annular dark field (HAADF) and annular bright field (ABF) modes have been carried out and the images are shown in Figure II.3 b. These measurements were performed by Dmitry Batuk under the supervision of Artem Abakumov at the University of Antwerp, Belgium. While the HAADF signal, proportional to the atomic number squared, nicely shows the Ir columns, the ABF images clearly display the O and even Li columns in addition to Ir as certain zone axes

are perpendicular to pure atomic columns of each element. These images confirm the structure obtained by SXRD and NPD pattern refinements.

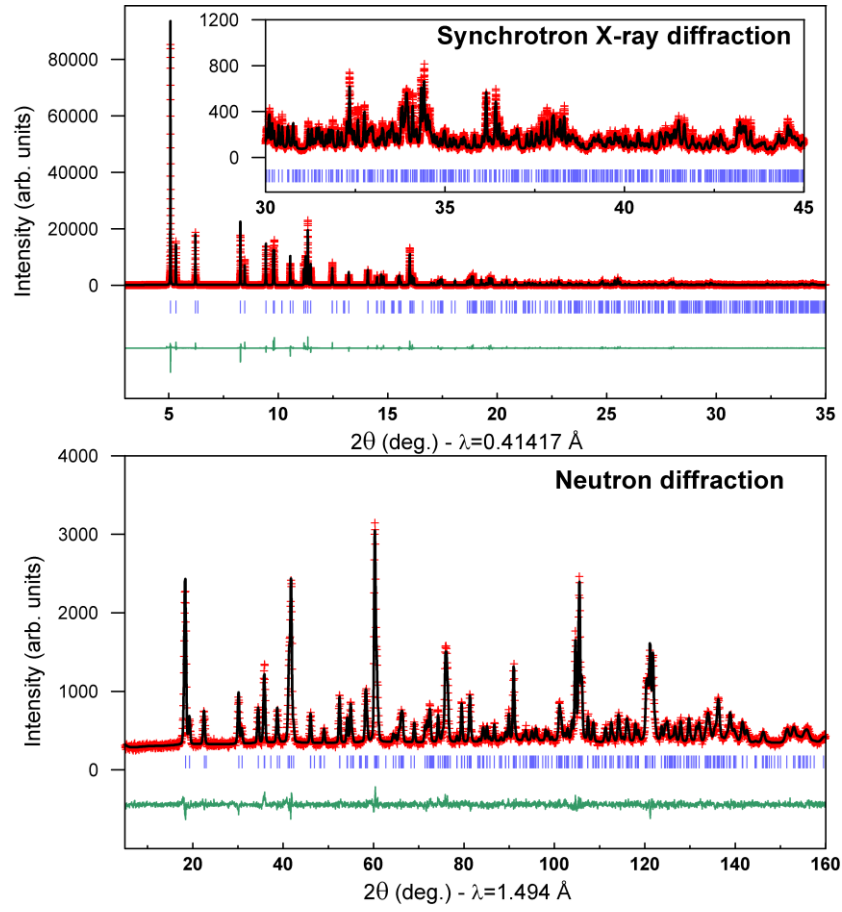


Figure II.2 Rietveld refinement of the Synchrotron X-ray and neutron powder diffraction patterns for β -Li₂IrO₃. In red are the experimental points, in black is the calculated pattern and in green is the difference between the experimental and calculated patterns. The vertical blue ticks beneath the pattern indicate the positions of the Bragg reflections. The data could be fitted in an F-centered orthorhombic cell with lattice parameters $a = 5.905856(8)$ Å, $b = 8.450657(11)$ Å, $c = 17.81199(2)$ Å.

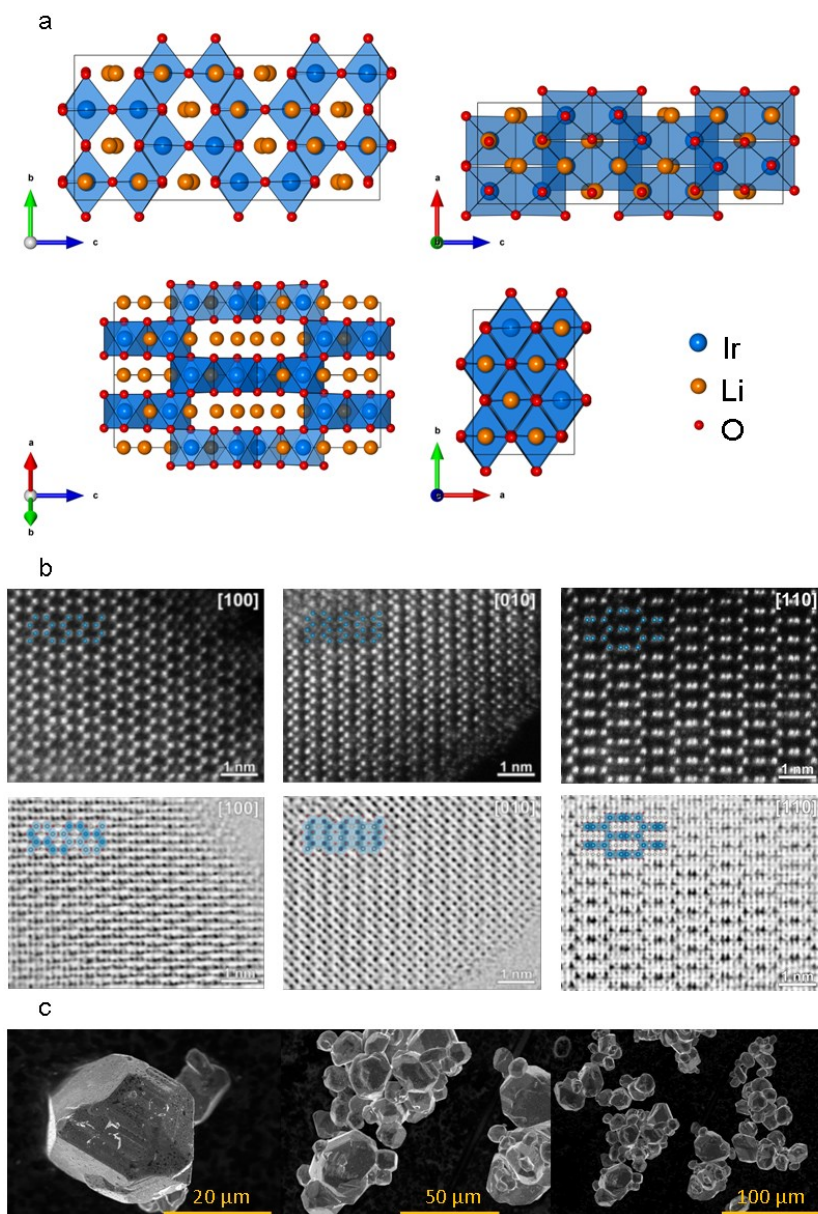


Figure II.3 (a) Structure projections of β - Li_2IrO_3 along the main crystallographic zone axes. Note that the [100] and [110] zone axes provide a clear view of the atomic structure with a separation of the atomic species into individual atomic columns. (b) High angular annular dark field scanning transmission microscopy (HAADF-STEM) and Annular Bright Field (ABF) STEM images of the pristine β - Li_2IrO_3 in the [100], [010] and [110] zone axis. (c) Scanning Electron Microscopy images of β - Li_2IrO_3 after the two step synthesis route.

The structure of the pristine β - Li_2IrO_3 being characterized, its electrochemical performances will be next assessed.

II-3 Electrochemical performances

Figure II.4 a) shows the electrochemical behavior of β - Li_2IrO_3 cycled versus Li in Swagelok cells between 2 and 4.8 V at a C/10 rate. Remarkably, all Li^+ can be removed leading to an “ IrO_3 ” phase which can then uptake nearly 1.8 Li in the following discharge. More specifically, the first charge shows a staircase profile, with the presence of four successive plateaus at 3.45, 3.50, 4.40 and 4.55 V vs Li^+/Li^0 , which can be visualized by four peaks in the dQ/dV plots (Figure II.4 b). Such peaks remain well-defined on the subsequent discharge. This contrasts with the typical behavior of Li-rich oxides: a staircase voltage profile on the first charge that converts to an S-shaped profile on the following discharge which is associated with inter/intra layer cationic migrations.^{45,87} It also differs from the electrochemical behavior of the α - Li_2IrO_3 polymorph which shows only two oxidation plateaus that progressively transform upon cycling into S-shaped profiles.⁵⁰ Figure II.4 b) also shows a weak down shift in voltage of the anodic and cathodic peaks with continued cycling up to 4.8 V which can be avoided by limiting the cutoff voltage to 4.5V. In order to better understand the origin of this voltage decay over cycling, cells cycled over different voltage windows were cycled and the results are described in the following paragraph.

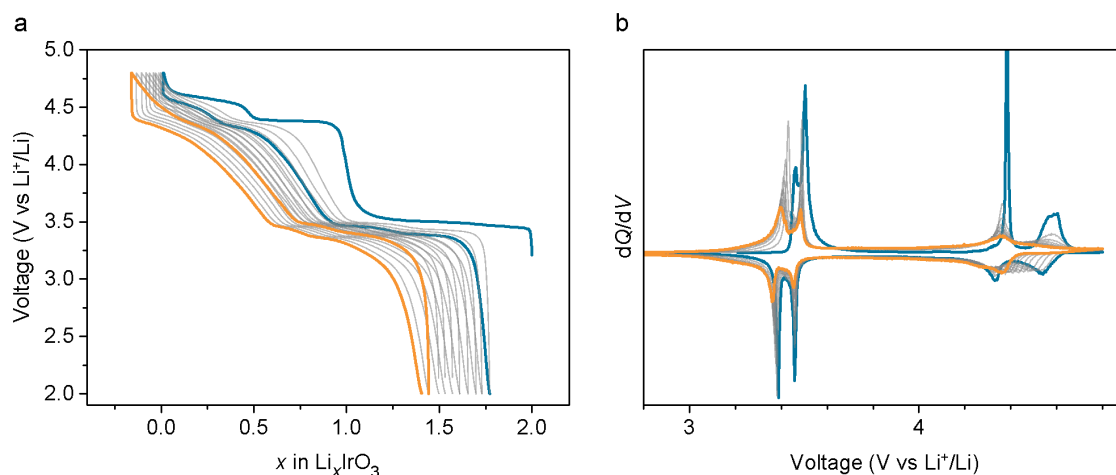


Figure II.4 Electrochemical behavior for β - Li_xIrO_3 . (a) The voltage profiles for cycles 1 (blue) to ten (orange) with (b) the corresponding derivative plots dQ/dV .

Voltage profiles and the corresponding derivative plots for the 1st and 10th cycles of various cells cycled from 2.0 V to either 4.0 V, 4.5 V or 4.8 V which we will refer to as cell A, B and C respectively, are shown in Figure II.5. While no shift in the voltage

plateau can be observed for cell A, a decrease is observed on both low potential processes when the potential window is increased above 4.5 V. Furthermore, the process at 4.45 V also sees its potential decrease in cell C after being cycled up to 4.8V. This is not the case in cell B where only the low potential processes are affected. The downshift voltage is always greater for the anodic peaks than for the cathodic ones. Interestingly, the voltage fade, common to Li-rich compounds, could at first account for this asymmetry based on Bettge et al.⁵³ The authors show that for a Li-rich NMC compound, the oxidation peak near 3.5 V shifts downwards more rapidly than the reduction one, identical to our findings here. However, we believe that the origin is here different as the three dimensional structural framework is unchanged, but we must realize that both Li and O local environments change as deduced by complementary NPD and TEM (discussed in section 4 of this chapter). Turning back to the data we note that the voltage drift observed when cycling to 4.8 V is not present when the higher potential range is avoided. Thus, this voltage drift doesn't occur until after 1.5 Li (50% of cations) are removed, well beyond the point where this occurs in layered NMC materials. As such, we believe that this voltage drift is of kinetic nature and more related to local structural modifications/strains occurring at high potentials as observed by *operando* XRD and ex situ EXAFS analysis which will be discussed in section 4 of this chapter.

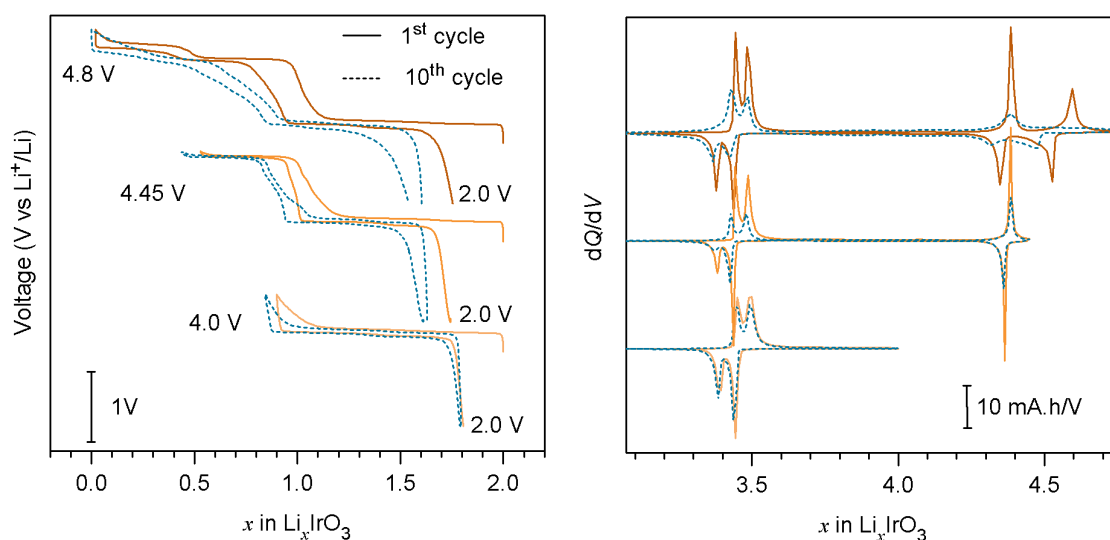


Figure II.5 The left panel shows Voltage composition curves of different cells cycled from 2 V to 4.0 V, 4.45 V and 4.8 V from bottom to top respectively. The right panel shows the corresponding differential curves (dQ/dV). The full orange lines correspond to the first cycles and the dashed blue lines correspond to the tenth cycle.

Interestingly, by discharging the pristine phase *versus* lithium, it appears possible to insert additional Li^+ in the structure. Indeed, two voltage plateaus are observed at potentials of 1.45 V and 1.49 V, each equivalent to 0.25 Li^+ as shown on the voltage capacity and the voltage composition curves in Figure II.6. This process is highly reversible and no voltage fade is observed over cycling as is evidenced by the first ten cycles shown in the left panel. As the pristine material only contains O^{2-} species, it is obvious that this process is accompanied by Ir reduction/oxidation only and is therefore strictly cationic. However, since all octahedral sites are filled in the pristine compound, the question remains: where are these extra Li^+ accommodated? NPD will be discussed and an answer will be formulated in section 4 of this chapter.

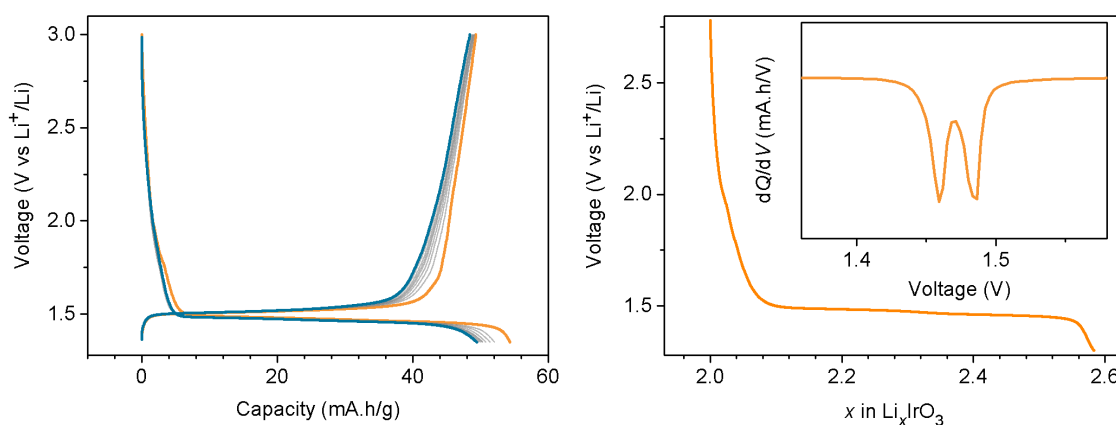


Figure II.6 The voltage capacity profile is shown in the left panel. The orange curve corresponds to the first cycle, the blue curve corresponds to the 10th cycle and the intermediate cycles are shown in grey. The voltage composition curve of the first discharge is shown in the right panel with the inset corresponding to the derivative plot (dQ/dV).

As processes between 1.3 V and 4 V seem highly reversible with no voltage decay and considering it represents 1.5 Li^+ , cells were cycled to observe its behavior over this potential range. Figure II.7 shows (a) the voltage capacity profile alongside (b) the derivative curve over five cycles. Interestingly, a process at 1.8 V on discharge appears after charging to 4V and accounts for the loss of capacity observed initially when the cells are cycled between 2 V and 4.0 V, as described above. This feature is not present when cycling between 1.3 V and 3 V and therefore, must be caused by the processes taking place at 3.45 V and 3.49 V. This type of voltage polarization was previously observed in LiNiO_2 and was attributed to the presence of divalent Ni in the Li interlayer which, upon oxidation to trivalent Ni, decreased the interslab distance thus

impeding the diffusion of Li^+ ions. This slow Li diffusion causes concentration gradients and an overlithiated phase on the surface which leads to high polarization of the cell.^{31,88} The structural transitions occurring during charge are reported further in subsection 4 of this chapter. However, it is important to specify here that the process leading to the voltage jump around $x = 1$ is due to the transition from lithium in octahedral sites to tetrahedral sites as has been determined by Neutron powder diffraction. As Li diffusion is reported to take place through these tetrahedral sites, diffusion issues are likely to occur on discharge, similarly to what is observed for LiNiO_2 .

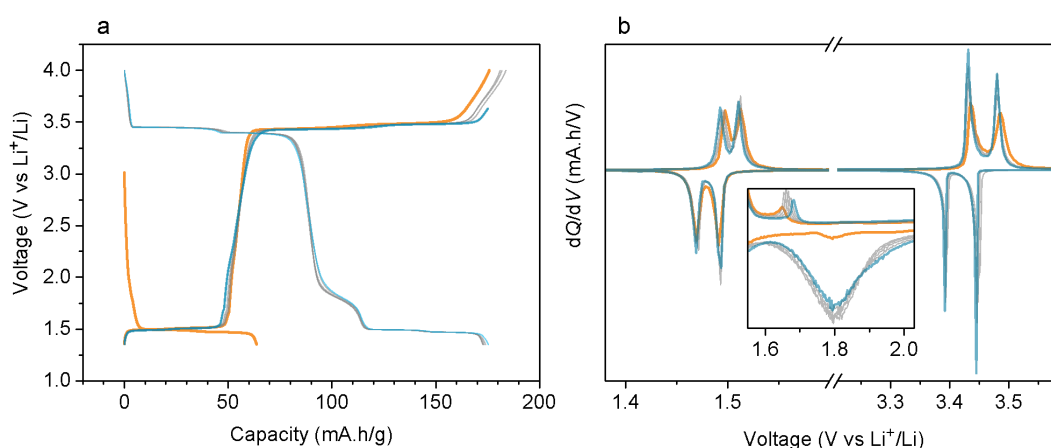


Figure II.7 The voltage capacity profile of a cell cycled between 1.35 and 4.0 V is shown in the left panel. The orange curve corresponds to the first cycle, the blue curve corresponds to the 5th cycle and the intermediate cycles are shown in grey. The corresponding derivative plots (dQ/dV) are shown in the right panel along with a zoom on the region around 1.8 V.

In order to better understand the kinetic limitations of each charge/discharge process, a galvanostatic intermittent titration technique (GITT) was carried out over the whole range of Li content and two large polarization regions are obvious: on charge after the intermediate voltage plateau and on discharge after the same plateau. As discussed above, such polarization may arise when diffusion is hindered and suggests a structural transition which would impede lithium percolation. As we will see further on, Li^+ is found in tetrahedral sites at 4.0 V and as lithium migration takes place through tetrahedral sites; this is a plausible explanation for the polarization and the process appearing at 1.8 V on discharge. While this has not been studied any further, we note that this could be an interesting case study for diffusion limitation modelling. The right panel shows the first three cycles over the total accessible Li content range, however, it

should be noted that limited cycling was achieved and noticeable degradation of the voltage profile arise most likely due to the high potential process in addition to the strain induced by the large variations of Li^+ content.

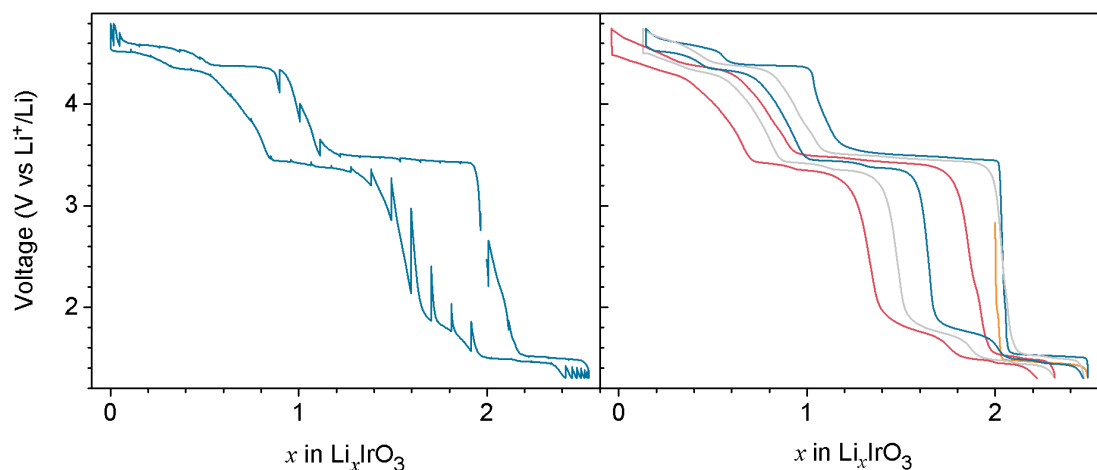


Figure II.8 The voltage composition profile obtained by the galvanostatic intermittent titration technique (GITT) spanning the entire Li^+ content range is shown in the left panel and the first three cycles are shown in the right panel.

In order to ascertain the power/rate capability of the β - Li_2IrO_3 phase and compare it with its layered counterpart, half cells using each polymorph were first charged at a rate of $C/20$ before being successively discharged at different rates starting from fast to slow with rest periods between each discharge steps. This so called “signature process” is a classical way to establish the rate capabilities of cathode materials. Figure II.9 shows the voltage composition curves for each cell in the left panel and the cumulative capacity values for each discharge step in the right panel. In addition to having a higher overall capacity, the β iridate has better rate capability than the α iridate. This is a nice example of the structure/properties relation and the importance of exploring new structures.

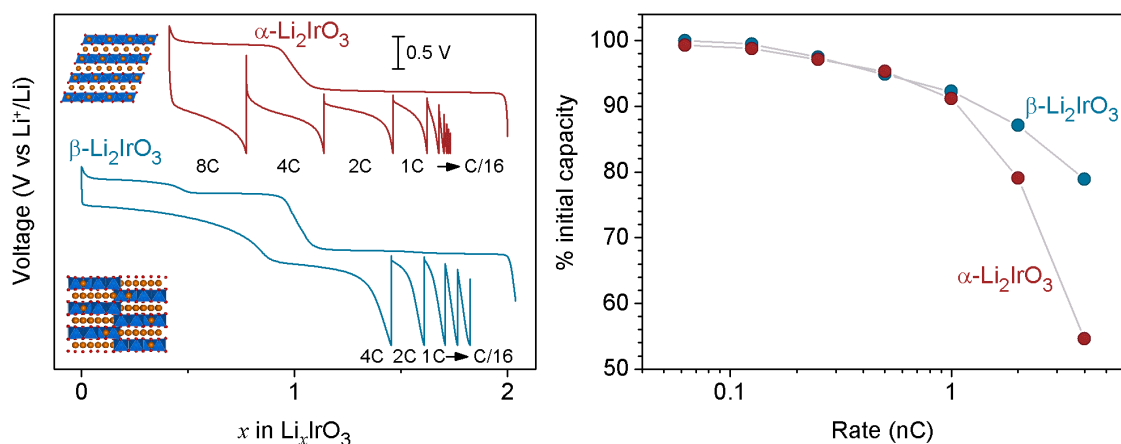


Figure II.9 The power/rate profiles for half cells using either the α or the β iridate as cathode material are shown in the left panel and the discharge capacity values for each discharge step are reported in the right panel.

Now that the electrochemical behavior of the β - Li_2IrO_3 cathode material has been explored over a wide range of composition and voltage, it remains to determine the redox active species for each process via a set of different X-ray spectroscopies.

II-4 Determining anionic and cationic participation during delithiation

II-4-a X-ray Absorption Near Edge Structure (XANES)

In order to probe the contribution of Iridium to the total delithiation path of β - Li_xIrO_3 , *ex situ* ($x = 2.5, 2.25, 2, 1.25, 1.5, 1.25, 1, 0.5$ and 0) Iridium L_3 -edge XAS and more specifically the near edge region (XANES) was used to follow the oxidation state of Ir. The measurements were performed in transmission mode at the ROCK beamline at the SOLEIL synchrotron in France with the valuable help of Antonella Iadecola.⁸⁹ A Si (111) channel-cut quick-XAS monochromator with an energy resolution of 2 eV at 11 keV was used. The intensity of the monochromatic X-ray beam was measured by three consecutive ionization detectors. The *ex situ* samples were prepared as described in the electrochemical section and never exposed to air or moisture. The energy calibration was established with simultaneous absorption measurements on an Iridium metal foil placed between the second and the third ionization chamber.

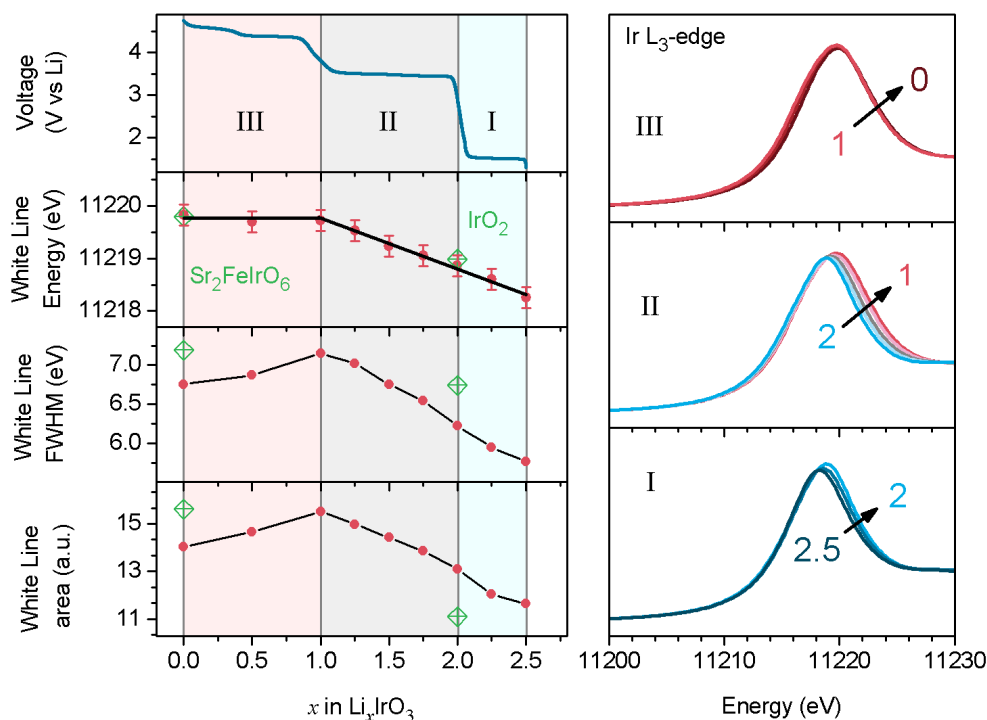


Figure II.10 Electrochemical voltage composition curve with *ex situ* XANES data. a) The voltage composition curve is shown atop the WL energy plot in order to better highlight the different regimes called I, II and III. The WL energy is correlated to the oxidation state of Iridium and is determined by the point of zero crossing of the first derivative of the normalized $\mu(E)$ around E^0 . As comparison, the WL full width at half maximum and its area are also plotted on the two lower plots. b) The XANES portion of the XAS spectra for *ex situ* samples of composition $x = 2.5, 2.25, 2, 1.75, 1.5, 1.25, 1, 0.5$ and 0 are shown in three different plots which correspond to the different regimes observed on panel a). As is illustrated here, Iridium is mostly oxidized during the segments I and II and very little during segment III.

The L_{III} -edge of TM corresponds to transitions from $2p$ to $5d$ states which, in the present case, lead to a large absorption peak commonly known as the White Line or resonant peak. Figure 1 a) shows the electrochemical voltage composition curve on charge of the β - Li_xIrO_3 cathode material in half cell configuration. The cell was initially discharged to 1.35 V in order to observe the full Li range from $x = 2.5$ to 0 (with x in Li_xIrO_3) on charge. While there is a total of 6 distinct plateaus during charge, we will refer, in this paragraph, only to three potential regions: the low potential process from $x = 2.5$ to 2 , the intermediate potential process from $x = 2$ to 1 and the high potential process from $x = 1$ to 0 . This electrochemical curve is shown above the WL energy,

FWHM and area which were all extracted from the XANES spectra shown in panel b) of the same figure as shown in Figure II.11.

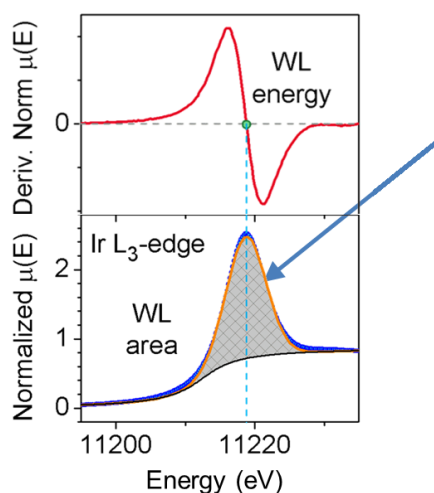


Figure II.11 Analysis of the white line of the Ir L_{III} edge with on top the derivative curve of the absorption coefficient and on the bottom the area extracted by integration of the peak after subtraction of the arctan step function.

The area of the WL is generally associated with the empty 5d states which are indicative of the oxidation state of Ir. However, when comparing the pristine samples' WL area to that of IrO_2 , in which Iridium is in the +IV oxidation state, a large difference is observed. This can simply be attributed to the local environment of Iridium. Indeed, the detailed spectral analysis of the XANES L_{III} -edge for third row TM oxides has been studied to determine the effect of the chemical environment, the M-O covalency and the oxidation state of the TM on the WL shape, magnitude and position.⁹⁰ In the case of an octahedral site, the 5d states are split into t_{2g} and e_g levels according to the crystal field theory. It has been established that the WL can be described as a sum of two Lorentzian peaks which can be assigned to the unoccupied levels of the T_{2g} and e_g states and of an arctangent step which describes the transitions to the continuum.^{91,92} The determination of the e_g and t_{2g} band positions can be carried out by fitting the second derivative of the WL with two Lorentzian functions. Indeed, using the second derivative in this way considerably decreases the contribution of the step function while keeping the Lorentzian peaks intact in position and relative intensities.⁹³ While this is of practical use in cases with known symmetries such as tetrahedral and octahedral sites, it becomes quite complex when these sites are distorted. Nevertheless, the peak shape could be used

as an indicator of the site symmetry and the presence or not of distortions. In fact, while Iridium has a coordination number of 6 in both structures, in rutile IrO_2 there is a rectangular distortion of the base of the IrO_6 octahedra which is not the case in the pristine β - Li_2IrO_3 phase.⁹⁴ This distortion would modify the crystal field which in turn would affect the WL shape – as illustrated by the FWHM plotted in Figure II.10 a) - and could explain the difference between the two peak areas. The XANES of the charged sample was also compared to that of $\text{Sr}_2\text{IrFeO}_6$ in which Iridium is in +V state. Once again, the area of the WL does not correspond to the fully oxidized phase IrO_3 in which Iridium is expected to be at least in the +V state. For this reason and because the environment of Iridium will evolve significantly during the delithiation process, another descriptor must be selected. The peak energy (at which $\mu(E)$ is at its maximum) is in better agreement with the reference materials and has been previously used as a relevant descriptor for Ir oxidation state and will therefore be used for the following discussion.⁹⁵

The evolution of the WL energy clearly displays three different oxidation regimes which we will call I for the low potential process, II for the intermediate potential process and III for the high potential process. References for Ir(IV) and Iridium(V) binding energies are marked by dashed lines and were obtained by measuring IrO_2 and $\text{Sr}_2\text{FeIrO}_6$ respectively.⁹⁶ It is clear from the WL energy plot that there are three different slopes going from sharp for I to flat for III indicating a steady decrease followed by a drop in the cationic participation between I and II then II and III respectively. This can also be observed - albeit in a more qualitative way - directly on the XANES spectra in panel b) of Figure II.10 in which large shifts occur for processes I and II whereas only a slight shift is seen during process III.

These trends are confirmed by *operando* measurements but due to the high energy of the L_3 edge of Iridium and the high intensity of the synchrotron beam, a delay is observed during the intermediate and high potential processes. Nonetheless, the *operando* data is shown in the supporting information Figure II.12. In order to palliate the delay issue, the measurements were carried out on two distinct points of the electrode alternately so as to decrease the time spent under the beam for a given point (Figure II.12). However, while this strategy showed significant improvement compared to the single point experiment, the data still shows significant delays. Nevertheless, as explained above, the general trends observed with *ex situ* measurements are observed

operando. Indeed, the pristine as well as the completely charged materials correspond well between the two experiments and three different electrochemical regimes can be observed on charge in good agreement with regions I, II and III.

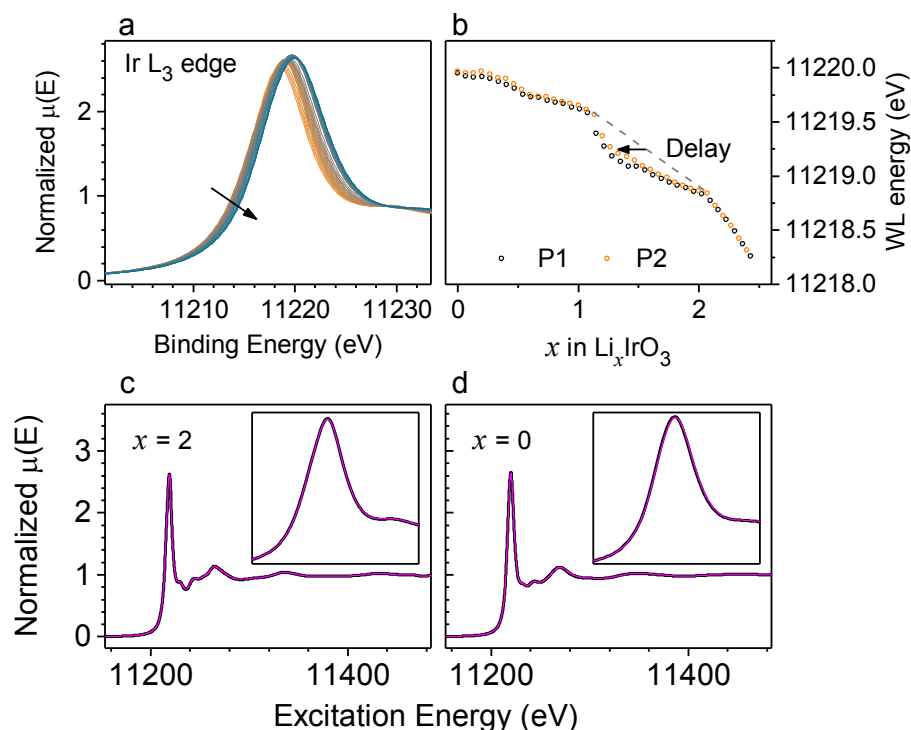


Figure II.12 a, Ir L_{III} -edge XANES spectra recorded *operando* for β - Li_xIrO_3 during charge from $x = 2.5$ to $x = 0$. b, the evolution of the white line energy, in other words the Ir oxidation state, with composition. Note that there are two sets of data (orange and black circles) corresponding to two locations on the electrode on which measurements were taken alternatively in order to limit the exposure of each point to the high photon flux. c and d show the good agreement between spectra of both *ex situ* (black) and *operando* (pink) measurements for compositions $x=2$ and 0 respectively.

II-4-b Hard X-ray Photoelectron Spectroscopy (HAXPES)

The use of HAXPES to probe the bulk of the material is particularly important when looking at the O 1s level because of the presence of surface contaminations which hinder the clean de-convolution of the spectra. This is especially true at low states of charge when the signal of the O^{n-} species at 531 eV is weak. Several samples at different states of charge corresponding to compositions $x = 2, 1, 0.5$ and 0 were prepared and their O 1s, Ir $4f_{5/2}$, $4f_{7/2}$ and $5p_{3/2}$ XP spectra were measured with a photon energy of 6900 eV on the GALAXIES beamline at the Soleil synchrotron facility in France in

collaboration with Gaurav Assat and Rémi Dedryvère. The results are plotted in Figure II.13 and Figure II.14. At this energy, the probe depth is around 22 nm which represents a considerable increase compared to the previous study using lab X-rays with a photon energy of 1486.6 eV for which the probe depth is only around 5 nm. Although this represents only a fraction of each particle, which are several microns wide in the pristine sample, it allows us to decrease the participation of surface species and amplify the signal coming from the bulk of the particles. The O 1s XP spectra will first be discussed in order to ascertain the oxygen participation throughout the charge and then the Ir 4f5/2, 4f7/2 and 5p3/2 XP spectra will be discussed along with the valence band spectra in order to get further confirmation of the Ir L_{III} XANES analysis.

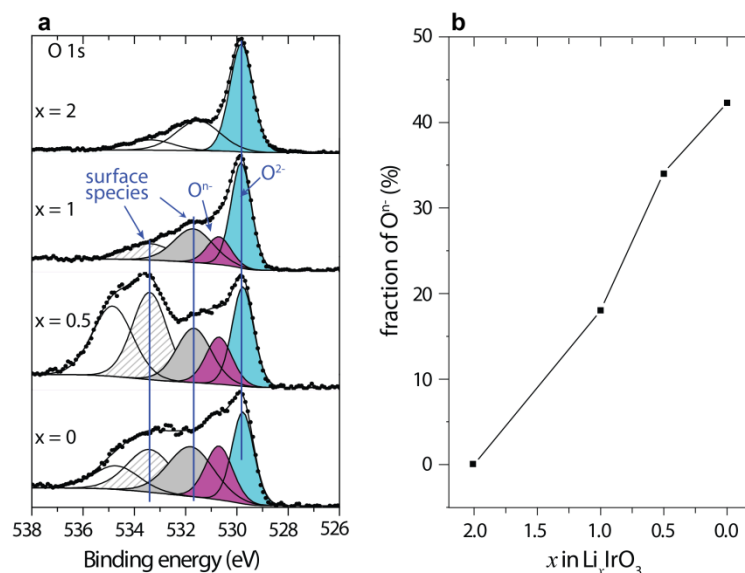


Figure II.13 Hard X-ray photoemission spectroscopy spectra results of different β - Li_xIrO_3 compounds. a) X-ray Photoemission (XP) spectra of the O 1s level with the blue component being the lattice O^{2-} , the pink component being the lattice oxidized oxygen named O^{n-} and in grey, hashed and white the surface contamination as described previously.^{47,48,97,98} b) the fraction of O^{n-} species determined by the surface of the pink peak with respect to the sum of both the pink and blue peaks.

The O 1s spectra for the different samples of compositions $x = 2, 1, 0.5$ and 0 are plotted from top to bottom respectively in Figure II.13 a). The pristine material can be described with three distinct contributions: the lattice oxygen at 529.8 eV and adsorbed species like carbonates at 531.9 eV and 533.5 eV. However, it is clear that even after the first Li^+ is extracted, the peak at 529.8 eV becomes asymmetric and an additional

component must be added at 531 eV which corresponds to what has been previously attributed to the oxidized lattice oxygen (O^{n-}).⁴⁸ By plotting the area of the peak at 531 eV normalized by the sum of the areas of both lattice oxygen peaks (529 and 531 eV), one can obtain the percentage of oxidized oxygen in the material and is here plotted in Figure II.13 b. This allows us to attribute most of the anionic activity to the second Li^+ extracted or the high potential region. This is in good agreement with the XANES results exposed above. Indeed, while Iridium is mostly oxidized during the low and intermediate potential processes it is only slightly so on the high potential one meaning oxygen must be oxidized to compensate for the charge. In order to confirm the cationic activity, the Iridium 4f and 5p core levels as well as the valence band were measured.

Turning to the Ir XP spectra, the scattering amplitude of the Iridium $5p_{1/2}$ becomes non-negligible with respect to the Iridium 4f levels at 6900 eV and a broad contribution is necessary to fully describe the experimental data (Figure II.14 a). A small contribution of the Li 1s level is observed for the pristine sample at 55 eV but is very weak due to the low scattering amplitude of such a light element. This signal disappears in the delithiated phases. Both the $4f_{5/2}$ and $4f_{7/2}$ peaks shift during the extraction of the first Li^+ from 62.6 eV to 63.2 eV and 65.7 eV to 66.3 eV respectively. During the second delithiation, these peaks do not shift any further towards higher binding energies. However, the shape of the peaks changes considerably with namely the loss of asymmetry and the appearance of a clear shoulder at higher binding energies. This shoulder is due to satellite peaks originating from different final states and is most likely symptomatic of a change in the environment of Iridium which we will not speculate on at this moment. Taking a look at the $5p_{3/2}$ level, it is clear that there is a continuous shift towards higher binding energies from $x = 2$ to $x = 0.5$ and for the last 0.5 Li^+ , no shift is observed. These results indicate a strong participation of Iridium during the delithiation of the first Li^+ , a more modest contribution to the following 0.5 Li^+ and a negligible one for the last 0.5 Li^+ .

Finally, the participation of Iridium redox in the delithiation process can also be followed by measuring the valence band which is shown in Figure II.14 b. Thanks to the high photon energy (6900 eV), the Iridium 5d electrons photoexcitation cross section is far greater than that of the O 2p electrons (≈ 550 times larger). Hence, the valence band purely represents the Iridium 5d partial density of states below the Fermi level. This,

contrary to the XANES resonance peak, allows us to follow the evolution of the number of electrons in the 5d orbitals of Iridium and determine when Iridium is oxidized. If the area decreases, this means there are fewer electrons and therefore that Iridium has been oxidized, if it does not change, Iridium is inactive and if the area increases, then it means that Iridium is reduced. During the deintercalation of the first Li^+ , the area is considerably decreased meaning that a strong oxidation has taken place. During the following 0.5 Li^+ , Iridium is further oxidized but to a lesser extent which is expected since the charge to compensate for is half that of the previous delithiation process. Finally, during the final 0.5 Li^+ extraction, Iridium does not seem to be active since the area is unchanged. Once again, this is in good agreement with the results described so far.

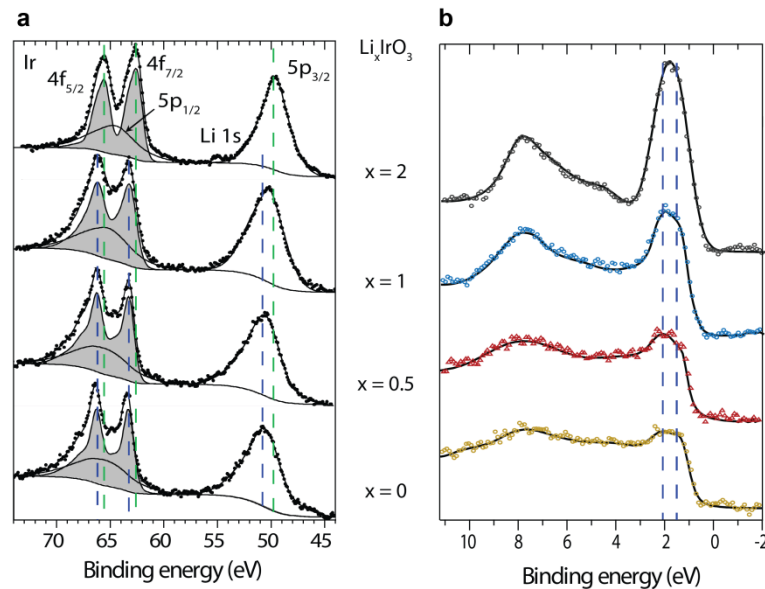


Figure II.14 Hard X-ray photoemission spectroscopy spectra results of different β - Li_xIrO_3 compounds. a) XPS spectra of the Iridium 4f_{5/2}, 4f_{7/2}, 5p_{1/2} and 5p_{3/2}. The grey filled area is the component used for the 4f_{5/2} and 4f_{7/2} at 62.5 eV and 65.7 eV respectively. b) the valence band of the material for the different Li compositions which, at the measurement energy (6900 eV) represents the Iridium participation at the Fermi level.

In conclusion, for $0 \leq x \leq 2$ both spectroscopic techniques point towards three different regimes: (i) a predominantly cationic process for $1 \leq x \leq 2$ with however some participation of oxygen as evidenced by the O 1s XP spectra, (ii) a predominantly anionic process for $0.5 \leq x \leq 1$ with some Ir contribution as evidenced by XANES and the valence band XP spectra and (iii) finally a purely anionic process for $x \leq 0.5$.

Determining the structural implications of the different redox active species during extraction of Li⁺ could help mitigate certain degradation processes observed in anionic active materials during cycling. For this, complementary *operando* SXRD, NPD and EXAFS will be discussed in the next section of this chapter.

II-5 Structural evolution during cycling

II-5-a Synchrotron X-ray diffraction (SXRD)

This next section will focus on the structural evolution during delithiation of the β -Li₂IrO₃ phase using *operando* SXRD which was carried out between $x = 2$ and 0 with the voltage profile shown in Figure II.15 a). This experiment was carried out with the help of François Fauth from the MSPD beamline of the Alba synchrotron in Spain. On this curve are delimited three portions for which the XRD patterns are shown in Figure II.15 d,e and f. All phases which are formed during the delithiation could be described as either orthorhombic cells derived from the pristine material or monoclinic cells. The cell parameters could be obtained by refining the data using the Rietveld method as implemented in the FullProf suite software and the results are shown in Appendix Chapter II. Table 1 along with the crystallographic data in Appendix Chapter II. Table 2-8 and the Rietveld refinements in Appendix Chapter II. Figure 3-8. The cell volumes per formula unit as well as the concentration profile obtained by the refinements are shown in figure 3 b and c. Upon removal of the first 1.15 Li⁺ (Figure II.15 f), three successive biphasic transitions leading to orthorhombic cells with similar volumes to the pristine phase are observed. This illustrates the impressive resolution that can be obtained by the use of synchrotron radiation. Indeed, results using lab X-rays did not allow to isolate the phase of composition Li_{0.85}IrO₃. Interestingly, these intermediate phases have sharp and intense peaks indicating that the structure is well ordered and that no considerable strain is imposed by the delithiation process up to $x = 0.85$.

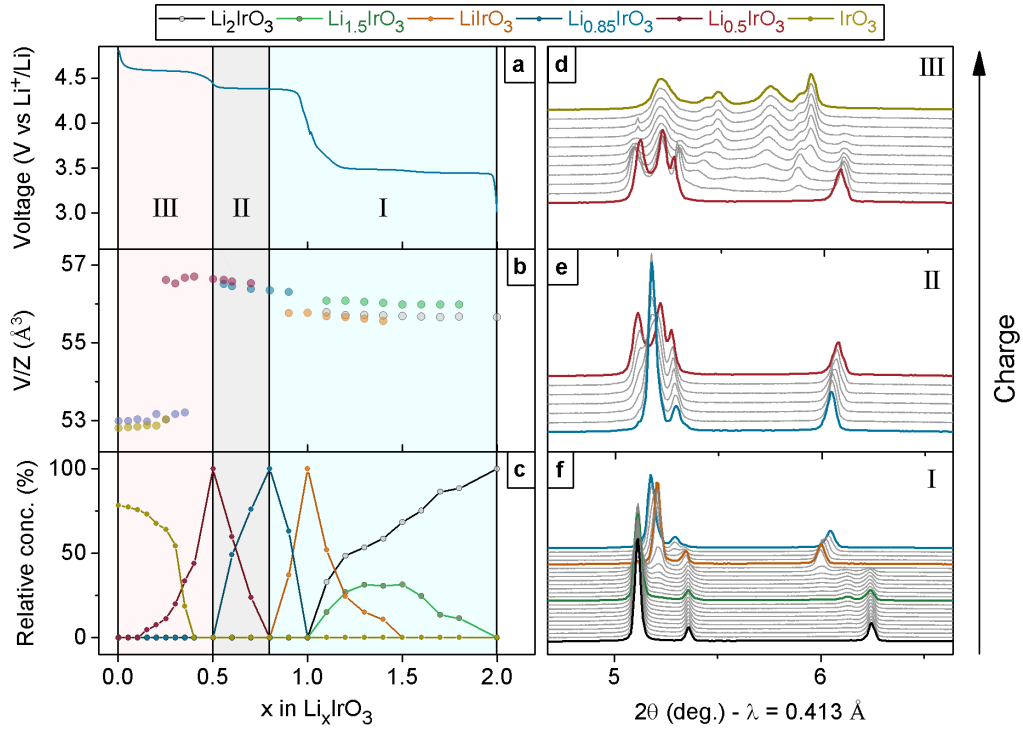


Figure II.15 *Operando* synchrotron XRD. a) The electrochemical curve of β - Li_2IrO_3 on charge starting from the pristine material at $x=2$. b) The cell volume normalized by formula unit of each intermediate phase as determined by Rietveld refinement of selected diffractograms and c) the relative concentration profile. d), e) and f) show the evolution of the diffractograms during charge and corresponding to the portions III, II and I on the electrochemical curve respectively.

However, from $x = 0.85$ to 0.5 a distortion is observed leading to a monoclinic phase with noticeable peak broadening. As delithiation continues, two biphasic transitions leading to monoclinic phases take place. The final phase is a mixture of these two monoclinic phases with a β angle tending towards 90° (94.9° and 93.3°). This corresponds to a large change compared to $\text{Li}_{0.5}\text{IrO}_3$ for which $\beta \approx 105^\circ$. An uneven broadening of peaks arises during this second delithiation which is indicative of strain and/or of the shortening of coherent crystalline domains, which can arise when electrochemical grinding takes place. In the first case, the broadening should be proportional to $\tan(\theta)$ meaning it should be exacerbated at wide angles whereas in the second case it should be proportional to $1/\cos(\theta)$ leading to a larger effect on narrow angles.

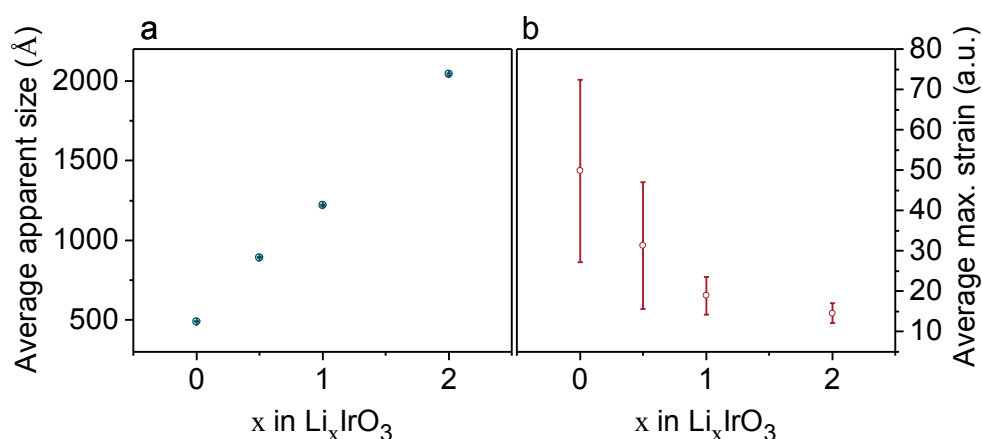


Figure II.16 Broadening parameters obtained from Rietveld refinements. a) The average apparent size which is determined by a lorentzian broadening varying in $1/\cos\theta$. b) The average maximum strain obtained by both Gaussian and Lorentzian broadening varying in $\tan\theta$. The large standard deviation at high states of charge for the strain is due to its anisotropic nature.

Both effects can be modelled and implemented in the refinements. This allows us to discriminate between electrochemical grinding and structural strain at high potential. Figure II.16 shows that while there seems to be a steady electrochemical grinding during charge, there is a substantial increase of anisotropic strain after the first Li^+ is extracted as illustrated in Figure II.16. As described above, this region can be attributed predominantly to anionic redox and while the grinding is not exacerbated during this last Li^+ extraction, the strain is considerably increased. While this strain could coincidentally arise from the fact that a large amount of Li^+ has already been extracted at this point, it is likely due, in no minor part, to the significant distortions induced by anionic redox. In order to confirm this hypothesis and shed light on the effect of delithiation on the oxygen sublattice, NPD was used and will be described in the following section.

II-5-b Neutron powder diffraction

In order to investigate the effect of delithiation on the oxygen network of the β - Li_2IrO_3 , NPD measurements were carried out on samples at different states of charge. For samples of composition $x = 2.5$, 2.25 and 0.5 the measurement were carried out on the D1B beamline at the *Institut Laue Langevin* in Grenoble with a wavelength of 1.288 Å while the samples of composition $x = 2$ and 1 were measured on HRPT high-resolution neutron powder diffractometer of the Swiss Spallation Neutron Source SINQ at the Paul Scherrer Institute, with a wavelength of 1.494 Å. In previous sections, we

have demonstrated that three different regimes could be distinguished during charge. The first one is purely cationic in nature and concerns the insertion/extraction of additional Li^+ in the pristine compound, i.e. for $2.0 \leq x \leq 2.5$. The second one is predominantly cationic with some anionic participation and relates to the extraction of the first Li^+ from the pristine compound, i.e. for $1.0 \leq x \leq 2.0$. The third one is largely anionic with most likely a slight cationic participation and is associated to the last Li^+ extraction, i.e. for $0 \leq x \leq 1.0$. Due to the large broadening of peaks observed for the fully charged state (IrO_3), no accurate refinement could be carried out. We will discuss the results obtained for each regime in the order described above and in light of observations made in previous sections.

Let us consider first the fully discharged compound, which should accommodate 40 Li in its unit cell. In order to determine the most reliable structural model, several configurations in which octahedral and tetrahedral sites were either partially or completely filled were tested. The best fit was obtained for the orthorhombic $Fddd$ cell with a partial filling of the two $16g$ octahedral sites the $16f$ tetrahedral sites. The reason for partially depleting the octahedral sites is the short Li-Li distance between a Li in a tetrahedral and the lithium in the adjacent octahedral site (1.81(9) Å). In addition, this makes more sense in terms of Li^+ diffusion which is likely the reason for the limited insertion of additional Li^+ . The cell parameters and occupancies are listed in Table II.2 and the refinement as well as the structure is shown in Figure II.17. The sample contained a small amount of mid discharged phase ($x = 2.25$) which could be refined as a second phase (orange Bragg reflection ticks). Indeed, a similar approach for the mid-discharged structure leads to the same model with the refined parameters reported in Table II.3.

Table II.2 Crystallographic data and atomic positions of β -Li_{2.5}IrO₃ determined from Rietveld refinement of the neutron powder diffraction pattern.

β -Li _{2.5} IrO ₃						
Space group $F d d d$		$R_{\text{Bragg}} = 5.54 \%$		$\chi^2 = 57.3$		
$a = 6.0101(8) \text{ \AA}$		$b = 8.8127(9) \text{ \AA}$	$c = 17.5885(18) \text{ \AA}$	$V = 931.57(18) \text{ \AA}^3$		
Atom	Wyckoff position	x/a	y/b	z/c	Occupancy	B (\AA^2)
Ir	16g	1/8	1/8	0.7061(5)	1	0.18(12)
Li1	16g	1/8	1/8	0.013(5)	0.92(2)	2.9(9)
Li2	16g	1/8	1/8	0.879(6)	0.98(2)	2.9(9)
Li3	16f	5/8	0.999(14)	5/8	0.60(2)	2.9(9)
O1	16e	0.843(2)	1/8	1/8	1	0.37(13)
O2	32h	0.6057(17)	0.3635(11)	0.0369(6)	1	0.37(13)

Table II.3 Crystallographic data and atomic positions of β -Li_{2.25}IrO₃ determined from Rietveld refinement of the neutron powder diffraction pattern.

β -Li _{2.25} IrO ₃						
Space group $F d d d$		$R_{\text{Bragg}} = 5.27 \%$		$\chi^2 = 21.35$		
$a = 5.9176(6) \text{ \AA}$		$b = 8.7789(7) \text{ \AA}$	$c = 17.4084(16) \text{ \AA}$	$V = 904.35(14) \text{ \AA}^3$		
Atom	Wyckoff position	x/a	y/b	z/c	Occupancy	B (\AA^2)
Ir	16g	1/8	1/8	0.7075(10)	1	0.10(17)
Li1	16g	1/8	1/8	0.036(6)	0.82(2)	0.7(6)
Li2	16g	1/8	1/8	0.868(5)	1(2)	0.7(6)
Li3	16f	5/8	0.989(11)	5/8	0.44(2)	0.7(6)
O1	16e	0.875(4)	1/8	1/8	1	0.39(16)
O2	32h	0.637(3)	0.3644(10)	0.0392(7)	1	0.39(16)

Table II.4 Crystallographic data and atomic positions of the 4 V - charged β -LiIrO₃ - determined from Rietveld refinement of neutron powder diffraction pattern. A bond valence sum analysis (BVS) (using d_0 from Ir⁴⁺) is included.

β -Li ₁ IrO ₃							
Space group $F d d d$				$R_{\text{Bragg}} = 2.64 \%$	$\chi^2 = 1.44$		
$a = 5.62149(6) \text{ \AA}$		$b = 8.88673(10) \text{ \AA}$		$c = 17.8518(2) \text{ \AA}$	$V = 891.815(17) \text{ \AA}^3$		
Atom	Wyckoff position	x/a	y/b	z/c	B (\AA^2)	Occ.	BVS
Ir	16g	1/8	1/8	0.70899(11)	1.54(4)	1	4.555(13)
Li3	16f	1/8	1/8	0.9732(8)	1.84(13)	1	0.974(6)
O1	16e	0.8566(6)	1/8	1/8	1.09(5)	1	1.906(9)
O2	32h	0.6288(7)	0.34651(17)	0.03538(10)	1.42(4)	1	1.812(8)

Table II.5 Crystallographic data and atomic positions of β -Li_{0.5}IrO₃ determined from Rietveld refinement of its neutron diffraction pattern.

β -Li _{0.5} IrO ₃						
Space group $C 2/c$		$R_{\text{Bragg}} = 4.45 \%$			$\chi^2 = 23.71$	
$a = 5.7532(6) \text{ \AA}$, $b = 8.6929(7) \text{ \AA}$, $c = 9.3092(8) \text{ \AA}$, $\beta = 104.604(5)^\circ$, $V = 450.53(7) \text{ \AA}^3$						
Atom	Wyckoff position	x/a	y/b	z/c	Occupancy	B (\AA^2)
Ir	$8f$	0.0823(15)	0.3661(11)	0.4164(9)	1	1.33(14)
Li3b	$4c$	1/2	3/4	3/4	1	2.6(16)
O1	$8f$	0.2045(18)	0.365(2)	0.2451(10)	1	0.93(11)
O2	$8f$	0.402(2)	0.0937(15)	0.0751(13)	1	0.93(11)
O3	$8f$	0.091(2)	0.1484(19)	0.4509(12)	1	0.93(11)

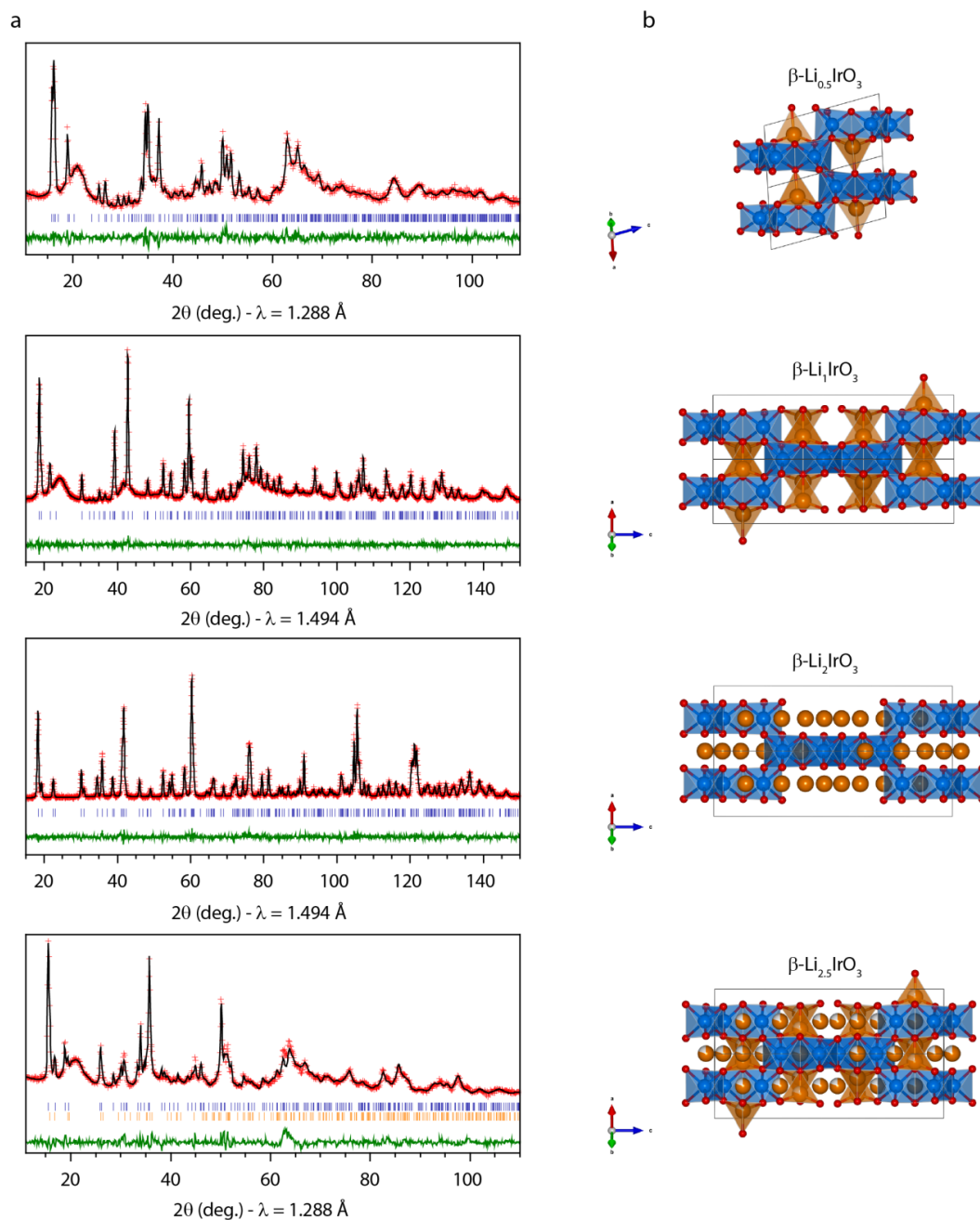


Figure II.17 (a) The Rietveld refinement of the neutron patterns and (b) the resulting structures for β - Li_xIrO_3 with $x = 2.5, 2, 1$ and 0.5 . In red are the experimental points, in black are the calculated patterns and in green are the differences between the experimental and calculated patterns. The vertical blue lines beneath the patterns indicate the positions of the Bragg reflections. In (b), the broad peaks at $2\theta = 25^\circ, 42^\circ, 80^\circ$ are from carbon. For the structural models, Li is orange, Ir is blue, O is red.

An *ex situ* NPD pattern was recorded on the sample charged to 4.0 V (Li_xIrO_3 with $x = 1$). The NPD pattern can be indexed with the *Fddd* orthorhombic space group (Figure II.17.d), with lattice parameters reported in Table II.4. Moreover, Rietveld refinements indicate that the remaining Li occupies a new tetrahedral position (Figure II.17), denoted Li3 in Table II.4. The structure refinement also reveals significant changes in the geometry of the IrO_6 octahedra (Figure II.17). The Ir-Ir and Ir-O distances are given in Table II.6. First, the average Ir-O distance reduces from 2.028(8) Å in the pristine structure to 1.9721(11) Å in the charged sample, concomitantly with the decrease of the ionic radius of the Ir cations from 0.625 Å (Ir^{4+}) to 0.57 Å (Ir^{5+}).⁹⁹ Moreover, the shortest O-O bond in the IrO_6 octahedra is significantly shorter in the charged material (2.53(2) Å, Figure II.18) than in the pristine one (2.75(3) Å, Figure II.18), which is indicative of the formation of peroxo-like species on charge.

Table II.6 Ir-Ir and Ir-O distances obtained by Rietveld refinement of the NPD patterns for compositions $x = 2.5, 2, 1$ and 0.

$x =$	2.5	2	1	0.5
Ir-Ir (Å)	2.858(17)	2.98909(18)	2.999(3)	3.004(10)
	3.078(9)	2.96616(12)	3.0091(14)	3.089(13)
	3.078(9)	2.96616(12)	3.0091(14)	2.939(12)
Ir-O (Å)	1.939(12)	2.04397(11)	1.986(3)	1.908(15)
	1.939(12)	2.04397(11)	1.986(3)	1.946(13)
	2.152(13)	2.00368(11)	1.959(3)	1.996(15)
	2.152(13)	2.00368(11)	1.959(3)	2.006(19)
	2.107(11)	2.03894(12)	1.9712(15)	1.884(17)
	2.107(11)	2.03894(12)	1.9712(15)	1.963(14)

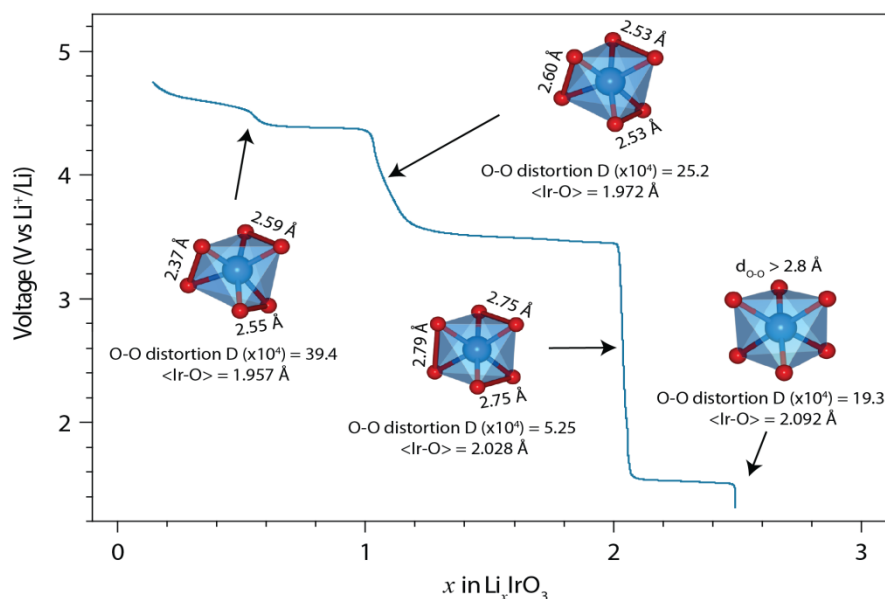


Figure II.18 Voltage composition curve of β - Li_2IrO_3 with the evolution of the IrO_6 octahedra from the fully discharged state with $x = 2.5$ to the high potential phase at $x = 0.5$. The average Ir-O distance is given (indicative of the Ir^{n+} oxidation), and we estimate the O-O distortion with the formula: $\Delta = \frac{1}{12} \sum_{i=1}^{12} \left[\frac{d_i - \langle d \rangle}{\langle d \rangle} \right]^2$ with d_i the individual O-O distances. The shortest O-O distances in the octahedra are highlighted in red with their lengths (Å) reported except for the composition $x = 2.5$ where all distances are above 2.8 Å.

For the sample of composition $x = 0.5$, the small amount of Li in the structure leads to a more difficult analysis of the Li position. In order to obtain the best model, several structural trials were constructed with the Ir-O framework obtained from the synchrotron powder diffraction refinement shown above, and Li atoms being located tetrahedral positions. As a first step, simulations were compared to the experimental data and when possible, distinguishing features were evidenced. As discussed earlier, a monoclinic distortion of the orthorhombic cell is observed at the end of charge. The monoclinic phase at $x = 0.5$ is described in the $C2/c$ space group with Li being likely located in the same tetrahedral sites as the one occupied in the $x = 1$ composition. From $x = 1$ to $x = 0.5$, the symmetry is lowered from $Fddd$ to $C2/c$ and the unique tetrahedral site in the $Fddd$ orthorhombic structure is split in Li3a and Li3b sites in the $C2/c$ cell (Figure II.19). However, these two sites should be only partially occupied, so that the total stoichiometry in Li satisfies the chemical composition. To determine the exact occupancy of these two Li tetrahedral sites, simulations with one of the two sites empty and the other one full and vice versa were compared to the experimental data. The

distinguishing feature is an inversion of relative intensities in the (110) and $(\bar{1}11)$ at values for 2θ of 15.8° and 16.2° , respectively (Figure II.19). This allows the discrimination of one of the two sites and the determination of a delithiation path. The most favorable site is the Li3b site, which is formed by two O1 and two O2 oxygen positions. After refinement, we obtain a Li distribution of 1 for Li3b site and 0 for Li3a, and the refinement is shown Figure II.17 with the structural parameters reported in Table II.5.

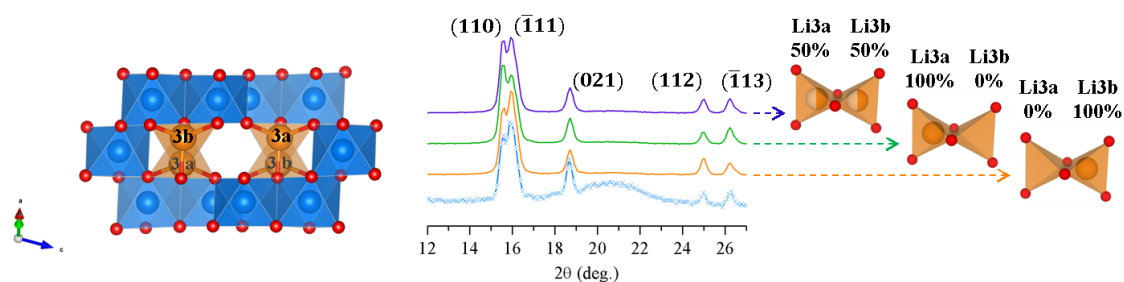


Figure II.19 Characteristic structure view (left) with Ir in blue, O in red and Li in orange. Experimental data in light blue, simulations for Li3b full and Li3a empty in orange, Li3a full and Li3b empty in green and both sites statistically filled in purple.

The concomitant anionic and cationic redox observed in previous sections can be visualized by plotting the shortest O-O distance and the average Ir-O distance. Indeed, Figure II.20 shows the evolution of O-O and Ir-O distances during charge and discharge of β - Li_2IrO_3 and as lithium is extracted from the structure, not only do the IrO_6 octahedrons contract with the oxidation of Ir but the shortest O-O distance also decreases considerably from $2.747(19) \text{ \AA}$ to $2.378(15) \text{ \AA}$. This can be contrasted with the fact that the shortest O-O distance does not change on charge of pristine material where only pure cationic redox is expected. This confirms that the degree of anionic activity can be visualized through the formation of shorter O-O distances leading to the distortion of the IrO_6 octahedrons.

II-5-c Extended X-ray absorption fine structure (EXAFS)

In this next part, we will focus on the EXAFS portion of the XAS data obtained for *ex situ* samples at compositions $x = 2.5, 2, 1.5, 1, 0.5$ and 0 . These have been fitted using the simplest model possible meaning only the first shell consisting of the first oxygen neighbors and the second shell consisting of the first Ir neighbors. The Li, while

part of the second shell, have a negligible contribution to the oscillations as the cross section of such a light element is minimal. Although multiple scatterings can be taken into account to improve the fit, their influence on the Ir-O and Ir-Ir distances is marginal and therefore they have not been included. The extracted distances as well as the Fourier transforms for each intermediate are shown in Figure II.20 with the fitting results, in R and q space, are shown in Figure II.21. Interestingly, the magnitude of the oscillations decreases as the material is charged to high potential. This is most likely due to a certain amount of strain leading to some disorder even at short range.

The distances extracted are shown in Figure II.20 with the O-O distances calculated from the Ir-O and Ir-Ir distances. These results will be described in light of the previous observations. The first section which was attributed to $\text{Ir}^{3+/4+}$ redox concerns the $x = 2.5$ to 2 composition range which is characterized by a shortening of the Ir-O distance but also of the Ir-Ir distance. This is expected for a symmetrical contraction of the IrO_6 octahedra during which, the distances should vary proportionally by the same amount (nearly the case here). This is consistent with the NPD results and can be attributed to $\text{Ir}^{3+/4+}$ oxidation. Previous observations have led to attributing a predominantly cationic process to the first Li extraction and predominantly anionic on the second. However, the distances extracted here do not suggest such a clear-cut picture and a more homogeneous evolution is suggested. Although, the O-O distances clearly decrease steadily during the charge from $x = 2$ to 1, there are no strong indications of separated cationic and anionic redox processes. However, EXAFS might not be sufficiently sensitive to such small variations and it is important to recall that these distances have been calculated based on the assumption that the distortion is somewhat symmetrical around the Ir center. An off-centering of the Ir atom would considerably change these distances. However, the results are very close to the average distances obtained by neutron diffraction with similar trends, validating to some extent the procedure.

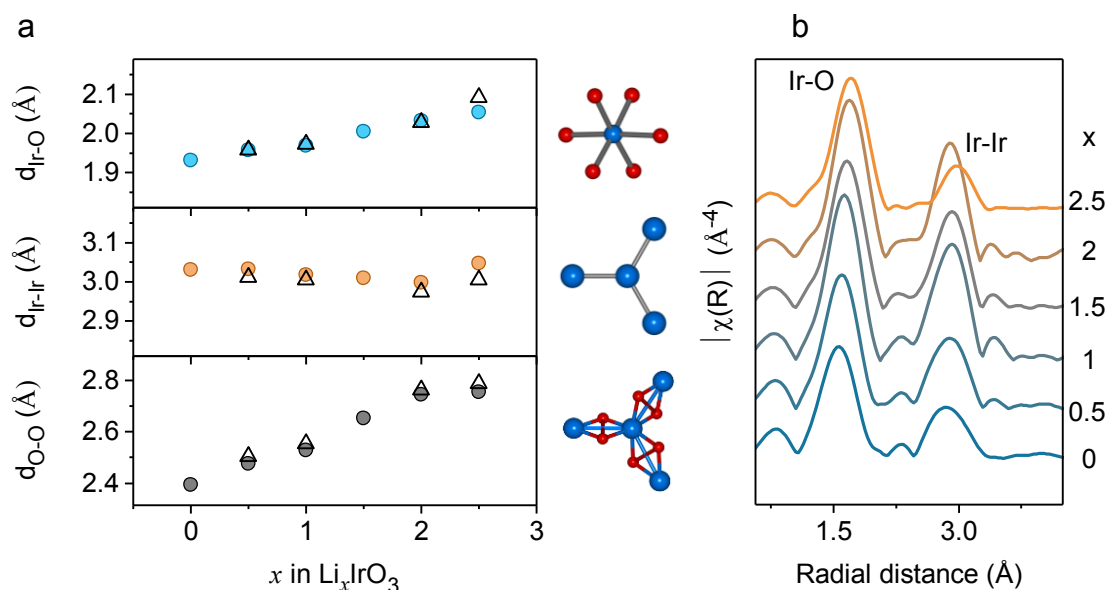


Figure II.20 a) Distances obtained by NPD and EXAFS fitting. From top to bottom are plotted $d_{\text{Ir-O}}$, $d_{\text{Ir-Ir}}$ and $d_{\text{O-O}}$. The distances obtained by NPD represented by black triangles are averaged over all distances in the cases of Ir-O and Ir-Ir and only over the three shortest ones in the case of O-O to compare with the calculated O-O distances obtained by EXAFS. b) The magnitude of the Fourier transforms of the EXAFS oscillations showing the first and second shells.

While it has long been suggested that the degree of O-O distance shortening is a measure of the amount of anionic redox, these results suggest that it might not be straight forward and that other descriptors should be defined. The question of quantification of anionic participation remains delicate in situations where both lattice oxygen and transition metal are involved.

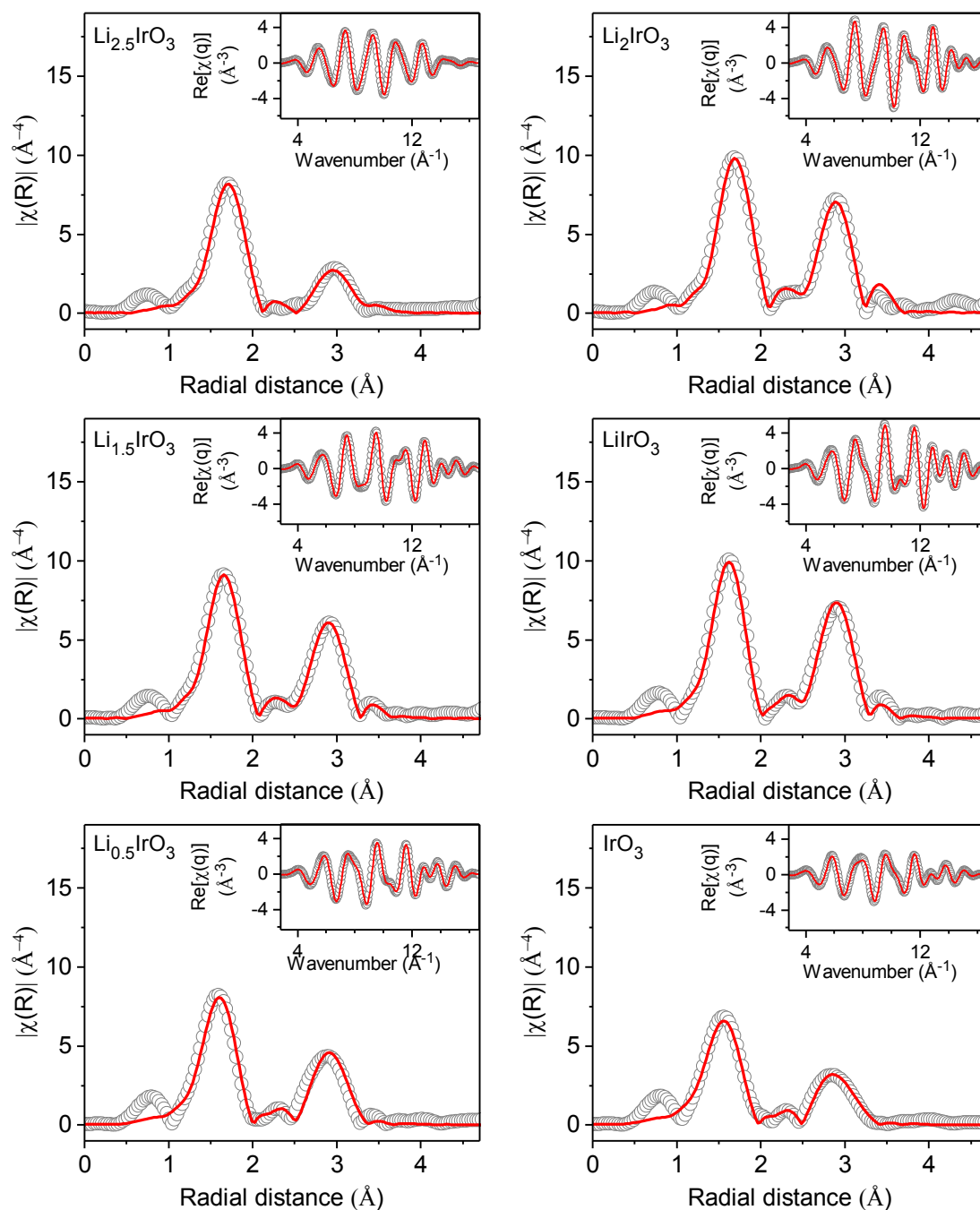


Figure II.21 Magnitude of the Fourier transform of k^3 -weighted EXAFS oscillations for samples of compositions $x = 2.5, 2, 1.5, 1, 0.5$ and 0 (with x in Li_xIrO_3) along with the fitting results in both R- and q-space (The $|\chi(R)|$ plots were not corrected for phase shifts).

Conclusion

In this chapter, we have developed a new and reproducible synthesis route to obtain the hyperhoneycomb β - Li_2IrO_3 structure. A suite of different analytical techniques such as Synchrotron XRD, NPD, STEM and solid state nuclear magnetic resonance spectroscopy were used in order to fully characterize its structure before assessing its electrochemical properties as insertion material for Li^+ .

We demonstrated that this tridimensional structure can be fully delithiated to form IrO_3 and that an additional 0.5 Li^+ could be inserted into the pristine compound to obtain β - $\text{Li}_{2.5}\text{IrO}_3$ which could not be synthesized by solid state reaction. We showed that it was possible to cycle reversibly over $2.5 \text{ Li}^+/\text{Ir}$ and that the voltage profile is composed of well-defined plateaus indicative of biphasic processes over the whole composition range. These are persistent over cycling although they show signs of degradation after a few cycles and eventually, the high potential process tends toward a slope like profile. Nevertheless, we show that by limiting the potential range to 4.0 V, no voltage decay is observed and highly reversible cycling over 1.5 Li^+ can be achieved when setting the low potential cutoff to 1.35 V. Interestingly, a process at 1.8 V appears on discharge after having charged to 4.0 V which is not present if the pristine is discharged to 1.35 V and cycled over only 0.5 Li^+ . This can be explained by the transition of Li^+ from octahedral sites to tetrahedral sites at 4.0 V, as revealed by NPD, which hinders Li^+ diffusion and imposing a large overpotential. This is confirmed by a galvanostatic intermittent titration technique measurement which shows large polarization for the 1.8 V process. This process leads to the recovery of the pristine structure with Li present in octahedral sites. In order to assess the redox active species during the charge process, spectroscopic techniques were used to probe both the Ir and O oxidation states during the delithiation.

The use of the XANES portion of the XA spectra collected at the Ir L_{III} edge on different *ex situ* samples at specific states of charge corresponding to single phase compositions shows that the oxidation of Ir goes through three regimes: I is described as purely cationic in nature and takes place for $2.0 < x < 2.5$; II is mainly cationic but with some anionic participation and takes place of $1.0 < x < 2.0$; III is only slightly cationic and therefore should be mostly anionic and occurs for $0 < x < 1.0$. *Operando*

measurements were also carried out during charge and highlight three main regimes as well with however a delay issue most likely brought about by the beam sensitivity of the material/electrolyte system. This is further confirmed by HAXPES results performed on *ex situ* samples at the Ir $4f_{5/2}$, $4f_{7/2}$, $5p_{1/2}$ and $5p_{3/2}$ as well as on the valence band which, at 6900 eV, can be considered as the Ir occupied states below the Fermi level. Measurements carried out on the O 1s level allowed us to confirm the occurrence of oxygen redox during the charge, mainly on the high potential process although a non-negligible amount is also observed on the intermediate potential processes around 3.4 V. In order to relate these findings with the electrochemical observations, the structural evolution during delithiation of the β - Li_2IrO_3 were determined by complementary SXPd, NPD, STEM and EXAFS.

The *operando* SXRD enabled the determination of the different intermediate phases with more accuracy than what had been previously published using lab XRD. A new phase was spotted and the fully delithiated phase could be more accurately described as two phases. The NPD results show that during the charge, the distortions of the IrO_6 octahedra due to O-O shortening increase and that the intermediate at $x = 0.5$ has one very short (2.37 Å) and two long (~ 2.57 Å) O-O distances. This disproportionation of the oxygen species is well in line with the large strain observed for this phase through the peak broadening. The short distance is also found by EXAFS analysis but the distances are symmetrical and no disproportionation can be spotted. The strong distortions both at long and short range as well as the structural strain, exacerbated during the high potential processes, are consistent with the electrochemical observations and the negative effect of high voltage cycling.

Chapter III. IrO₃ as a Na⁺ host with an active oxygen network

Introduction

As explained in the broader context section of this thesis, the need for high performance electrochemical storage devices is of paramount importance for the transition to renewable energies¹⁰⁰. Today's portable electronics and the automotive industry heavily rely on the Li-ion technology because it shows the highest energy density and a good reliability.¹⁰¹ However, the cost and the limited Li resources have driven research towards alternative battery technologies. Among them, the Na-ion technology was already considered thirty years ago but fell into oblivion because of the incredible soar of LIBs.⁷⁹ Today this technology is gaining considerable interest for applications in which volumetric energy density is of less importance and where high power is required.

As Na-ion batteries have lower energy densities than LIBs, it is imperative to develop new highly performing insertion materials, both for negative and positive electrodes. The recent discovery of anionic redox activity in Li-rich layered phases^{45,50} leading to staggering capacity increases has prompted the study of Na-rich layered compounds with success. Cumulative cationic and anionic redox processes leading to extra-capacities were first reported during Na extraction in Na₂Ru_{1-y}Sn_yO₃ and later in Na₂RuO₃ and Na₂IrO₃.^{98,102,103} These phases, which can be written as Na[Na_{0.33}M_{0.66}]O₂, crystallize in the well-known layered rocksalt-type structure, alike their Li-rich counterparts. Within the structure, pure Na layers alternate with NaM₂ layers (M – TM or spectator cation) for which the NaO₆ octahedra are all edge-shared with MO₆ octahedra to form a honeycomb pattern. This layered structure is prone to gliding of the oxygen close-packed planes as recently observed for Na₂IrO₃ upon removal of 1.5 Na⁺.^{98,103} The same Na removal limitation was observed for Na₂RuO₃ with an additional complexity associated to the feasibility of preparing an ordered or disordered phase depending on the synthesis conditions.¹⁰²

A similar inability to fully remove the alkali ions from the structure was experienced for the layered α -Li₂IrO₃ phase.⁹⁸ This was circumvented by switching to the 3D polymorph β -Li₂IrO₃, as demonstrated in the previous chapter, which also exhibits a rocksalt-type close-packed structure.⁹⁷ However, the distribution of Li and Ir in the structure generates a tridimensional arrangement of edge-sharing IrO₆ octahedra

which is frequently referred to as the “hyperhoneycomb” structure.⁸⁴ Along the same line of thinking, we decided to study the sodium isomorph of β -Li₂IrO₃, which is the object of this chapter.

This chapter is composed of 7 sections, not including this short introduction. In the first section will be described the synthesis of the sodiated iridium hyperhoneycomb through an electrochemical method. The second section will describe the obtained structure as characterized by XRD and TEM. The third section will demonstrate the electrochemical behavior and compare it to the lithiated counterpart. The fourth section will elaborate on the different redox active species during charge as evidenced by XPS. The fifth section will describe the evolution of the structure during the first cycle using *operando* synchrotron XRD. The sixth will describe the long term cycling stability in both half and full cells (vs Na and hard carbon respectively). The seventh and last section will demonstrate the thermal stability of the newly obtained phase. Finally, a short summary of the findings will conclude this chapter.

III-1 Synthesis

The synthesis of the β -Na₂IrO₃ polymorph through solid state methods by playing on several experimental parameters (annealing and cooling rates, annealing and quenching temperatures as well as modifying the heating atmospheres) was unsuccessful, and only the layered α -Na₂IrO₃ phase or the oxidized α -NaIrO₃ phase could be obtained. However, the insertion of 1.7 Na⁺ in the β -IrO₃ framework was successfully achieved. First the iridium trioxide was obtained by total delithiation of β -Li₂IrO₃ in a half cell using 1M LiPF₆ in EC:PC:DMC 1:1:3 as electrolyte and a Li metal disk as the negative electrode (Figure III.1, blue curve). Once recovered and thoroughly washed with DMC, β -IrO₃ was electrochemically discharged versus Na metal in Swagelok cells using 1M NaPF₆ in PC as electrolyte solution in order to obtain “ β -Na_xIrO₃” with x determined by electrochemistry and by quantitative energy-dispersive X-ray (EDX) spectroscopy to be 1.7 (Appendix Chapter III. Table 1). EDX mapping shows homogeneous distribution of Ir and Na as shown in Appendix Chapter III. Figure 1.

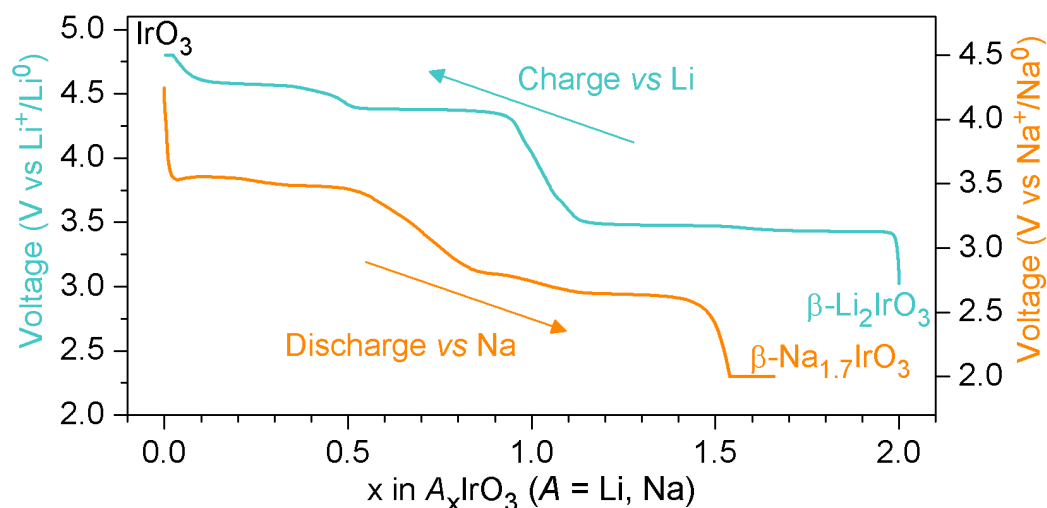


Figure III.1 Voltage-composition curves of $\beta\text{-Li}_2\text{IrO}_3$ versus Li metal on charge (blue) between 3.0 V and 4.6 V (versus Li^+/Li^0) and of the subsequent discharge versus Na metal (orange) between 4.2 V and 2.0 V (versus Na^+/Na^0).

III-2 Structural Characterization

The powder diffraction pattern for the $\beta\text{-Na}_{1.7}\text{IrO}_3$ phase collected on the Materials Science and Powder Diffraction Beamline (MSPD) at ALBA synchrotron with a wavelength of 0.41226 Å was refined using the Rietveld method (Figure III.2 a). All the peaks could be indexed using the same orthorhombic unit cell with Fdd space group as the pristine lithiated compound, however with increased cell parameters: $a = 6.41770(8)$ Å, $b = 8.95987(10)$ Å, $c = 18.5989(2)$ Å for $\text{Na}_{1.7}\text{IrO}_3$ versus $a = 5.90783(7)$ Å, $b = 8.45298(8)$ Å, $c = 17.81094(16)$ Å for Li_2IrO_3 . This corresponds to a large cell expansion compared to the Li counterpart (+ 20% in volume). The structure of $\text{Na}_{1.7}\text{IrO}_3$ was then refined according to the Rietveld method, starting from the structural model of $\beta\text{-Li}_2\text{IrO}_3$ and replacing Li with Na. The Na content was initially fixed to 1.7 per formula unit and the XRD pattern did not evidence any feature that would support some Na/vacancy ordering. The final structural parameters are given in Table III.1 and the resulting refinement is shown in Figure III.2 a).

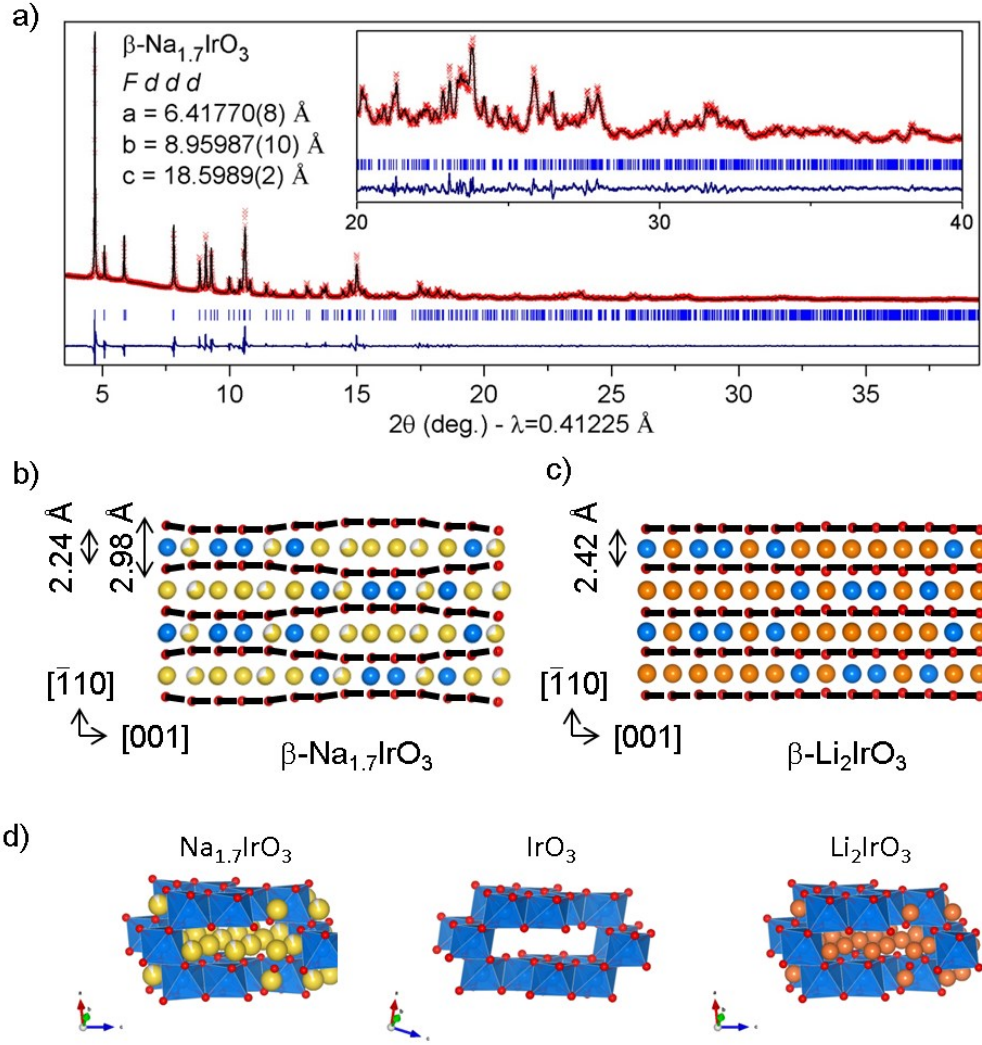


Figure III.2 a) Rietveld refinement of synchrotron data of $\beta\text{-Na}_{1.7}\text{IrO}_3$ with an enlargement of the 20° – 40° region as inset and the extracted cell parameters (observed pattern in red, calculated pattern in black, difference between the observed and calculated patterns in dark blue and the Bragg reflections as blue ticks). b) Structure of $\beta\text{-Na}_{1.7}\text{IrO}_3$ and c) of $\beta\text{-Li}_2\text{IrO}_3$. The black dotted lines highlight the oxygen sublattice and the distances between subsequent oxygen layers are given on the left of each figure. Ir, O, Na and Li are in blue, red, yellow and orange respectively. d) 3D view of $\text{Na}_{1.7}\text{IrO}_3$, IrO_3 and Li_2IrO_3 showing the same IrO_6 connectivity.

Table III.1 Crystallographic data and atomic positions of β -Na_{1.7}IrO₃ determined by Rietveld refinement of synchrotron X-ray powder diffraction pattern.

Atom	Wyckoff position	x/a	y/b	z/c	Occupancy	B (Å ²)
Ir1	16g	1/8	1/8	0.70875(15)	1	0.61(3)
Na1	16g	1/8	1/8	0.0426(13)	1	0.58(12)
Na2	16g	1/8	1/8	0.8834(12)	0.7	0.58(12)
O1	16e	0.833(3)	1/8	1/8	1	0.33(14)
O2	32h	0.644(3)	0.3521(9)	0.0358(6)	1	0.33(14)

Space group $F d d d$. $a = 6.41767(8)$ Å; $b = 8.95985(10)$ Å; $c = 18.5988(2)$ Å; $V = 1069.45(2)$ Å³; $R_{\text{Bragg}} = 2.94$ %; $\chi^2 = 6.904$.

The model obtained from the Rietveld refinement shows strongly distorted oxygen rows along the [001] direction. Indeed, the O2 atom is shifted from the position it occupies in the Li compound. As a result, the oxygen rows running parallel to [001] are considerably displaced outwards, away from each other when they surround Na, while they get closer when they cross Ir (Figure III.2 b). These corrugated oxygen rows can also be observed by high resolution annular bright field scanning transmission electron microscopy (ABF-STEM) when viewing along the [110] direction (Figure III.3 a). A simulation of the ABF-STEM image nicely confirms this observation (Figure III.3 b). It is worth mentioning that such corrugated oxygen rows were also reported for β -Na₂PtO₃ as well as for the high-Tc Bi-based cuprates; the latter were explained in terms of structural strains originating from the mismatch between the two consecutive Bi-O2 and Sr-O layers.^{104–106} We believe that the apparent “waviness” of the O layers in Na_{1.7}IrO₃ is also caused by a geometrical mismatch between the Na-O and the Ir-O distances. Na⁺ being larger than Li⁺, the size of the tunnels pertaining to β -Na_{1.7}IrO₃ must also be larger than in β -Li₂IrO₃. If we estimate the tunnel size as an average distance between the O layers, we get ~ 2.61 Å for Na_{1.7}IrO₃ and 2.42 Å for β -Li₂IrO₃. Although greater, such an enlargement is not sufficient at the center of the tunnels where the O waves move apart, since the local interlayer distance increases to ~ 2.98 Å (Figure III.2 b). However, increasing the O interlayer separation is limited by the Ir-O distances in the Ir₂O₁₀ dimers of the edge-sharing octahedral units going across the layers. As a result, the “normal” Na-O distances are achieved only for Na1 in the center of the tunnels, whereas Na2 at the sides of the tunnels appears over-bonded (BVS = 1.45), thus the Na_{1.7}IrO₃ structure seems to be quite strained. This deformation is also reflected in

larger spread of the O-Ir-O octahedral angles in β -Na_{1.7}IrO₃ (80.6 – 96.1 deg.) compared to that in β -Li₂IrO₃ (85.4 – 92.2 deg.). The strain, associated with the Na2 position, might be at the origin of its fractional occupancy, experimentally observed in the Rietveld refinement.

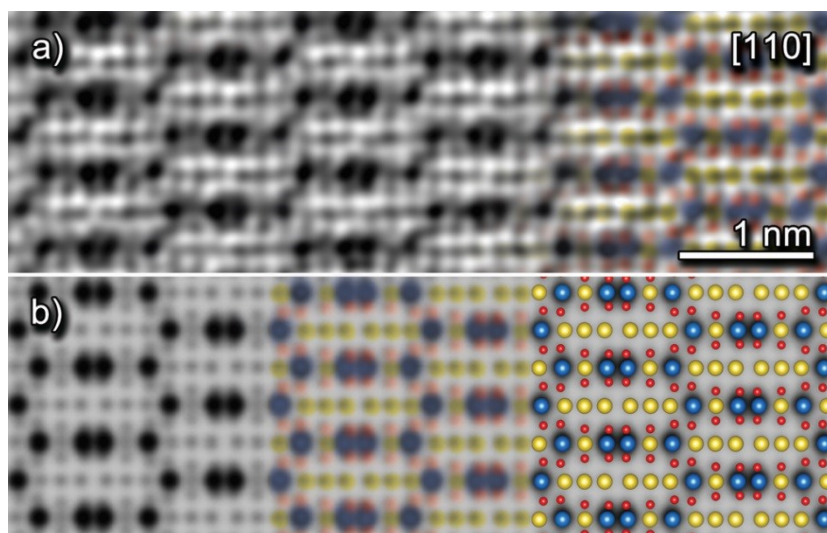


Figure III.3 a) Atomic resolution ABF-STEM image of a β -Na_{1.7}IrO₃ crystal showing the characteristic view of the hyperhoneycomb structure along the [110] axis, highlighting the oxygen sublattice distortion. A low bandpass filter was applied. b) ABF-STEM simulation of the β -Na_{1.7}IrO₃ structure with corresponding atoms (Ir in blue, O in red and Na in yellow) made using QSTEM software.¹⁰⁷

III-3 Electrochemical behavior

The electrochemical discharge profile for the IrO₃/Na cell shown in Figure III.4 a) (blue) is very similar to the one observed when discharging the lithiated counterpart versus lithium, also displayed in Figure III.4 a) (orange). Indeed, four distinct plateaus can be observed and the amount of alkali that can be inserted after full charge is similar (1.7 Na⁺ vs 1.8 Li⁺). Moreover, the voltage trace for the Na cell is, as expected, shifted towards lower potentials because of the lower reducing potential of Na⁺_(aq)/Na_(s) (-2.72 V vs SHE) vs. that of Li⁺_(aq)/Li_(s) (-3.05 V vs SHE). However, if the scales are shifted in order to align the potentials vs SHE as in Figure III.4 a), we can clearly see that the insertion of sodium occurs at much lower potential than for Li. This is often observed in Na-ion insertion materials and the energy density penalty incurred by NIBs is not only due to the lower potential of sodium. It is generally thought that Na insertion occurs

more easily than Li due to its lower solvation energy and higher polarizability which leads to higher rate capabilities which could be the reason for the lower insertion potential as it requires less energy. Lastly, we found that no extra Na^+ can be inserted in $\text{Na}_{1.7}\text{IrO}_3$ by lowering the potential window to 1 V, in contrast to $\beta\text{-Li}_2\text{IrO}_3$ which can uptake 0.5 Li^+ ($\text{Li}_{2.5}\text{IrO}_3$) upon reduction to 1.35 V. Structural hindrance linked to the greater size of Na^+ as compared to Li^+ is most likely at the origin of this difference. Note that the potential of the $\text{Na}_{1.7}\text{IrO}_3$ phase is lower than the stability window of H_2O indicating the sensitivity of this phase to moisture. Consequently, we observe that $\text{Na}_{1.7}\text{IrO}_3$ loses Na when left for a few hours in ambient atmosphere.

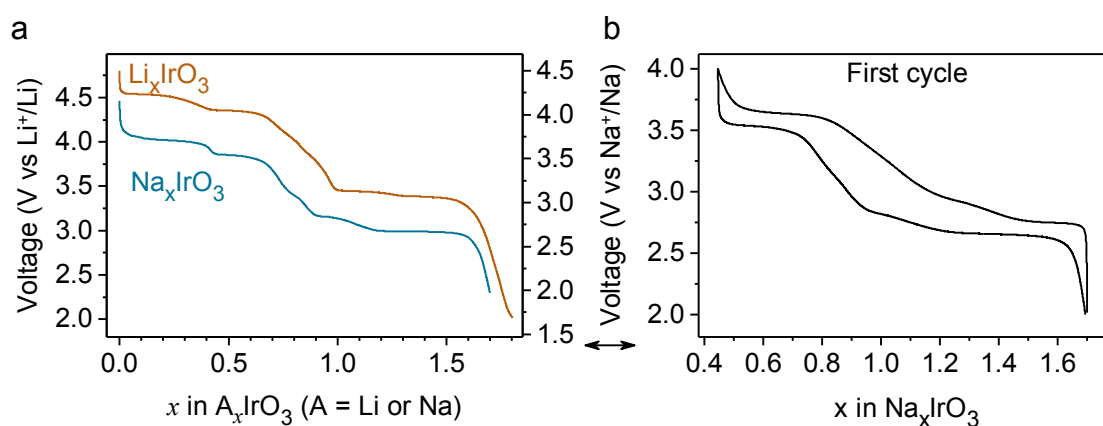


Figure III.4 a) Voltage composition curves on discharge at a C/40 rate of IrO_3 vs Li metal in orange and Na metal in blue. Each curve is plotted vs its respective counter electrode potential but they are shifted in order to be equivalent vs SHE in order to compare them. b) The first cycle after sodiation up to 4.0 V and back to 2.0 V at a C/10 rate.

The first cycle after the initial insertion of Na in IrO_3 is shown in Figure III.4 b). Interestingly, the charge and subsequent discharge only show three voltage plateaus as the high voltage process is never attained. These are retained during subsequent cycles and long term cyclability will be discussed later. It is unfortunate that the desodiation is limited to $\sim 1.2 \text{ Na}^+$ unlike the lithiated counterpart (which can be completely delithiated) especially considering the strong similarities between the two layered compounds. This illustrates both the difference between Li and Na chemistries and the effect of structure on electrochemical properties.

III-4 Anionic redox activity

In order to investigate the charge compensation mechanism within the β -Na_xIrO₃ system, *ex situ* XPS measurements were performed on β -Li₂IrO₃, β -IrO₃, β -Na_{1.7}IrO₃ ("Pristine") and β -Na_{0.4}IrO₃ (fully charged) samples with a special attention to the Ir 4f and O 1s core spectra. The use of XPS has been debated by the community due to the surface sensitivity of the technique.¹⁰⁸ Indeed, XPS can only probe a limited thickness raising the question of bulk vs surface mechanisms. However, the use of bulk sensitive techniques such as electron paramagnetic resonance spectroscopy⁴⁵, and more recently the use of neutron pair distribution functions¹⁰⁹ as well as HAXPES (as described in the previous chapter) have shown that the participation of oxygen to the redox mechanism was not restricted to the surface.⁵²

The XP spectra are shown in Figure III.5. The evolution of the binding energies of the Ir 4f core peaks clearly indicates a reduction of Ir on discharge from IrO₃ to β -Na_{1.7}IrO₃ and an oxidation on charge to β -Na_{0.4}IrO₃. The shift towards lower binding energy observed between β -Li₂IrO₃ and β -Na_{1.7}IrO₃ is most likely due to the different environment (Na⁺ vs Li⁺) rather than a lower oxidation state. Turning to the O 1s binding energy, there is the emergence of a new peak at ~531 eV in going from β -Li₂IrO₃ → β -IrO₃ previously associated to the formation of peroxo-like (O₂)ⁿ⁻ anionic species.^{48,110,111} The intensity of this peak is noted to largely decrease upon reinsertion of Na⁺ into β -IrO₃, but its disappearance is not complete for the composition β -Na_{1.7}IrO₃. We note a regain in intensity of this peak upon removal of Na as shown for the composition β -Na_{0.4}IrO₃ (Figure III.5). Altogether, this clearly indicates that the anionic redox process involving (O₂)ⁿ⁻ species in addition to the reversible cationic activity of Ir is an integral part of the charge compensation mechanism.

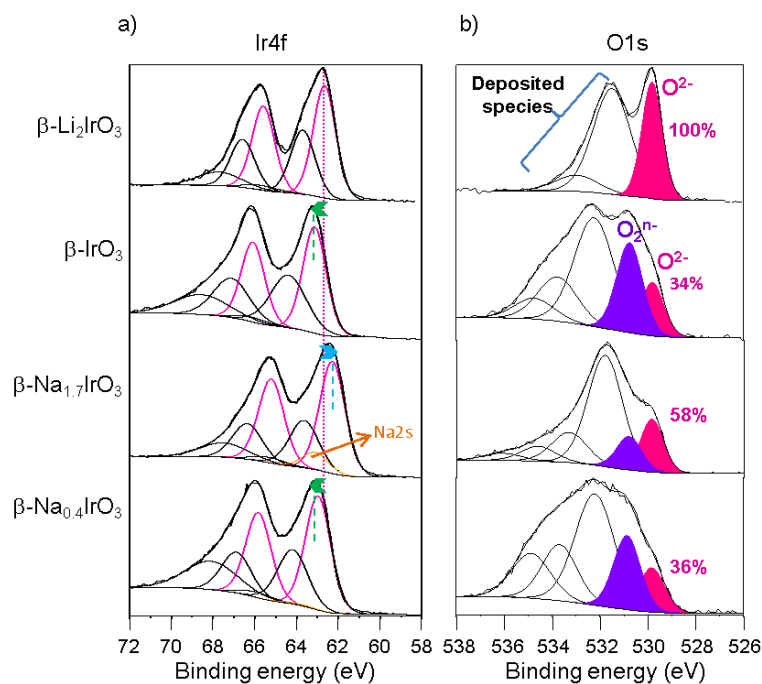


Figure III.5. Ir 4f (a) and O 1s (b) XPS core spectra collected *ex situ* for $\beta\text{-Li}_2\text{IrO}_3$, $\beta\text{-IrO}_3$, $\beta\text{-Na}_{1.7}\text{IrO}_3$ and $\beta\text{-Na}_{0.4}\text{IrO}_3$.

III-5 *Operando* XRD

To grasp further insights into the structural changes associated to the insertion and de-insertion of Na into IrO_3 , *operando* XRD data were further collected at ALBA synchrotron's MSPD beamline with a wavelength of 0.4122 \AA using a home designed cell.¹¹² IrO_3 was first obtained by electrochemical delithiation of $\beta\text{-Li}_2\text{IrO}_3$ as explained above. The *operando* cell was assembled using IrO_3 mixed with 10% carbon SP and Na metal as the positive and negative electrodes, respectively. The electrodes were electronically separated by a borosilicate glass fiber separator soaked with 1M NaClO_4 EC:DMC 1:1 / 1% FEC. This electrolyte composition was tested prior to the experiment and displayed no significant difference on the first cycles. The cell was cycled between 2.0 V and 4.0 V in galvanostatic mode at a C/10 rate with a constant voltage step at the end of discharge and subsequent charge to ensure that a maximum amount of Na^+ is inserted and extracted. Powder XRD patterns were collected with 0.02 steps in the sodium stoichiometry and are shown in Figure III.6. Comparison between electrochemical curve and XRD patterns allows the identification of the different intermediate phases discussed in the following paragraphs and pure phases are isolated

and their pattern refined according to the Rietveld method as implemented in the FullProf suite. The results are shown in Figure III.7 with the crystallographic data and atomic positions in Appendix Chapter III. Table 2-9.

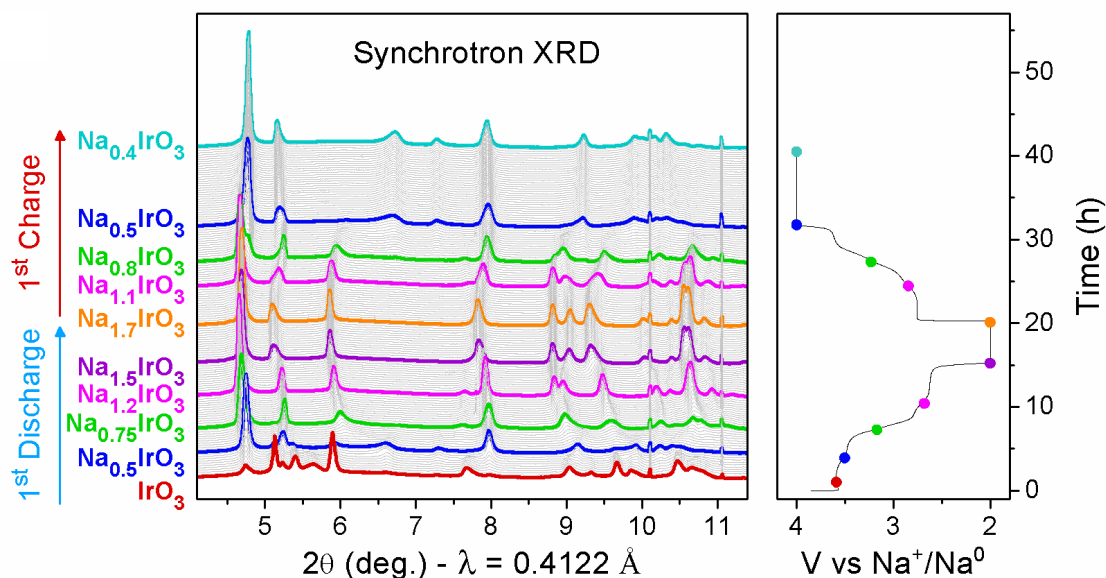


Figure III.6 Synchrotron *operando* XRD patterns of $\beta\text{-IrO}_3$ charged vs Na^+/Na^0 and subsequent charge together with the corresponding charge profile. The markers on the charge profile indicate the points where intermediate phases were isolated and the XRD data were refined. Compositions of pure compounds are indicated on the left of the figure.

When discharging the Na/IrO_3 cell we initially observed, through the first plateau process occurring at 3.6 V, a gradual fade of the peaks corresponding to monoclinic IrO_3 (red pattern) at the expense of a new set of peaks which appears and becomes pure for $x = 0.5$ ($\text{Na}_{0.5}\text{IrO}_3$, blue pattern). This new phase can be indexed with an orthorhombic unit cell (space group $F d d d$) with the following parameters $a = 6.9204(8) \text{ \AA}$, $b = 7.8089(9) \text{ \AA}$, $c = 18.0873(9) \text{ \AA}$. Upon further insertion through the 3.25 V plateau, the peaks corresponding to the $\text{Na}_{0.5}\text{IrO}_3$ phase progressively vanish, at the expense of new ones, which give a well-defined XRD pattern for the $\text{Na}_{0.75}\text{IrO}_3$ composition (green pattern). This phase can also be fully indexed in the $F d d d$ orthorhombic cell with $a = 6.5726(7) \text{ \AA}$, $b = 8.7814(8) \text{ \AA}$ and $c = 18.0034(11) \text{ \AA}$.

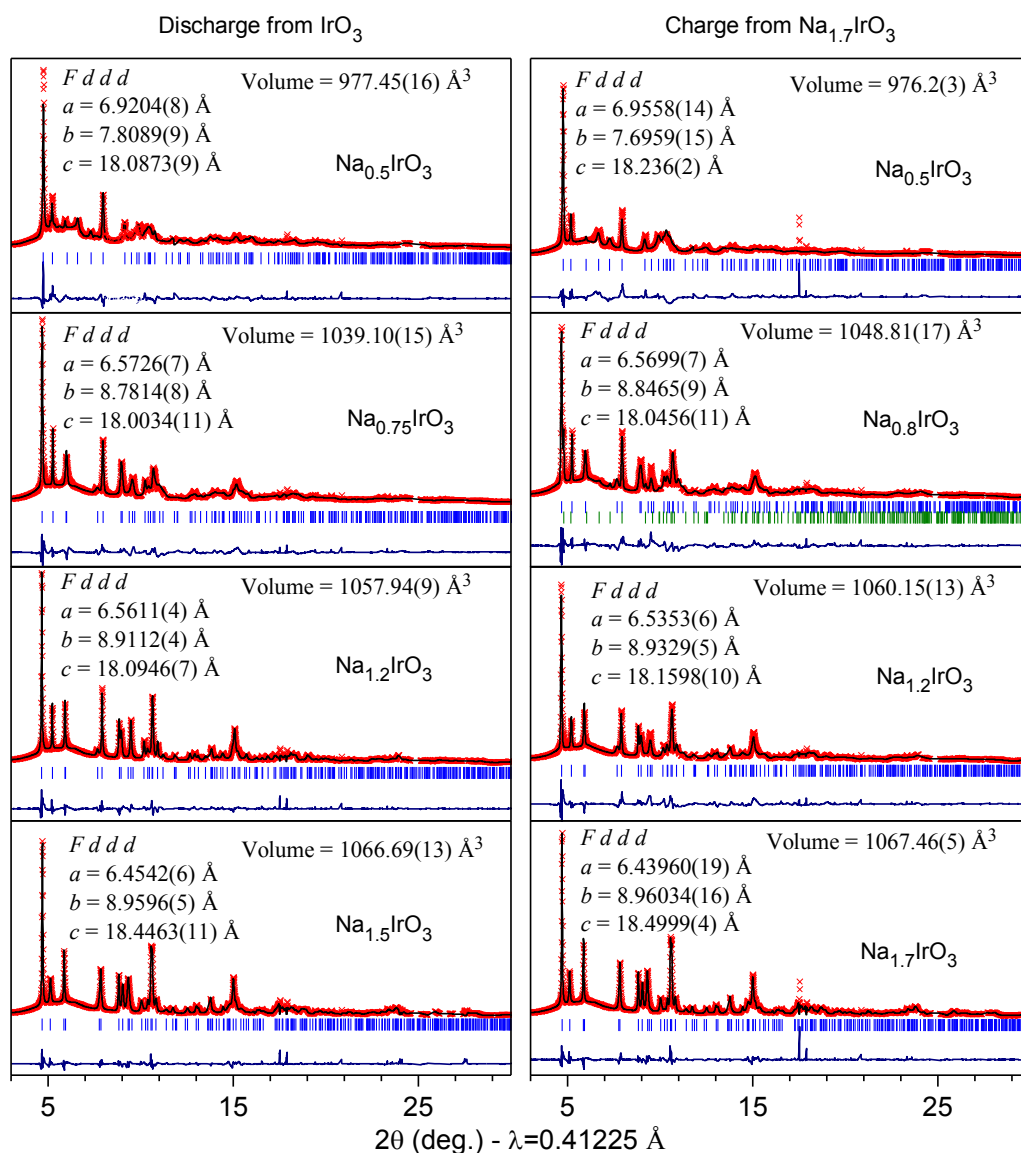


Figure III.7 Rietveld refinements of intermediate phases with on the left the discharge from IrO₃ and on the right the charge from Na_{1.7}IrO₃ to Na_{0.4}IrO₃. In red are the experimental points, in black is the calculated pattern and in blue the difference between the experimental and calculated patterns. The vertical blue lines beneath the patterns indicate the positions of the Bragg reflections. The Na_{0.8}IrO₃ was not obtained pure and some of the x = 1.2 phase was added to the refinement as shown by the green ticks.

The XRD patterns collected while pursuing the discharge to 2 V clearly evidence the successive appearance of two new phases of compositions Na_{1.2}IrO₃ and Na_{1.5}IrO₃ (pink and purple patterns) which form at the end of the 2.5 and 2.2 V plateaus, respectively. Their corresponding lattice cell parameters are $a = 6.5611(4) \text{ \AA}$, $b = 8.9112(4) \text{ \AA}$, $c = 18.0946(7) \text{ \AA}$ and $a = 6.4542(6) \text{ \AA}$, $b = 8.9596(5) \text{ \AA}$, $c = 18.4463(11) \text{ \AA}$. Switching to a constant voltage step on discharge when the potential reaches 2 V

enables the insertion of 0.2 additional Na^+ , hence indicating the poor kinetic of the low voltage Na insertion process. The pattern after this 5 hours process ($\text{Na}_{1.7}\text{IrO}_3$ in orange) presents slightly different lattice parameters and sharpened peaks ($a = 6.43960(19) \text{ \AA}$, $b = 8.96034(16) \text{ \AA}$ and $c = 18.4999(4) \text{ \AA}$).

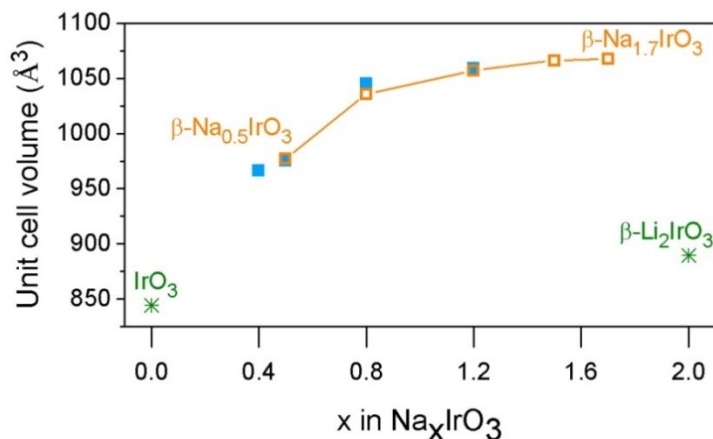


Figure III.8 Orthorhombic cell volume of $\beta\text{-Na}_x\text{IrO}_3$ extracted from XRD data using the Rietveld method for different Na content. In orange is the initial discharge from IrO_3 , in blue the subsequent charge and in green the orthorhombic equivalent volume of IrO_3 and $\beta\text{-Li}_2\text{IrO}_3$ cell volume for reference.

On the subsequent charge (Figure III.6a), all these processes are reversible with the same sequential appearance of the Na_xIrO_3 phases with the exception that the charged composition is then limited to $\text{Na}_{0.4}\text{IrO}_3$ even if a constant voltage is applied at 4.0 V. The evolution of the lattice parameters and unit cell volumes during the whole process are reported in Figure III.9 a) and Figure III.8 respectively. The unit cell volume monotonously increases with the Na content, from 844 \AA^3 for IrO_3 (orthorhombic equivalent volume calculated from the monoclinic cell for comparison) to 1067 \AA^3 for $\text{Na}_{1.7}\text{IrO}_3$ (+26%), and to 977 \AA^3 for the following charge ($\text{Na}_{0.4}\text{IrO}_3$). Such 26% volume increase as compared to solely 5% for the Li system (844 to $\sim 889 \text{ \AA}^3$) further stresses the extraordinary flexibility of the IrO_6 scaffold. An *operando* lab XRD experiment on first charge and subsequent discharge of $\text{Na}_{1.7}\text{IrO}_3$ confirms that these processes are reversible as shown in Figure III.9 b).

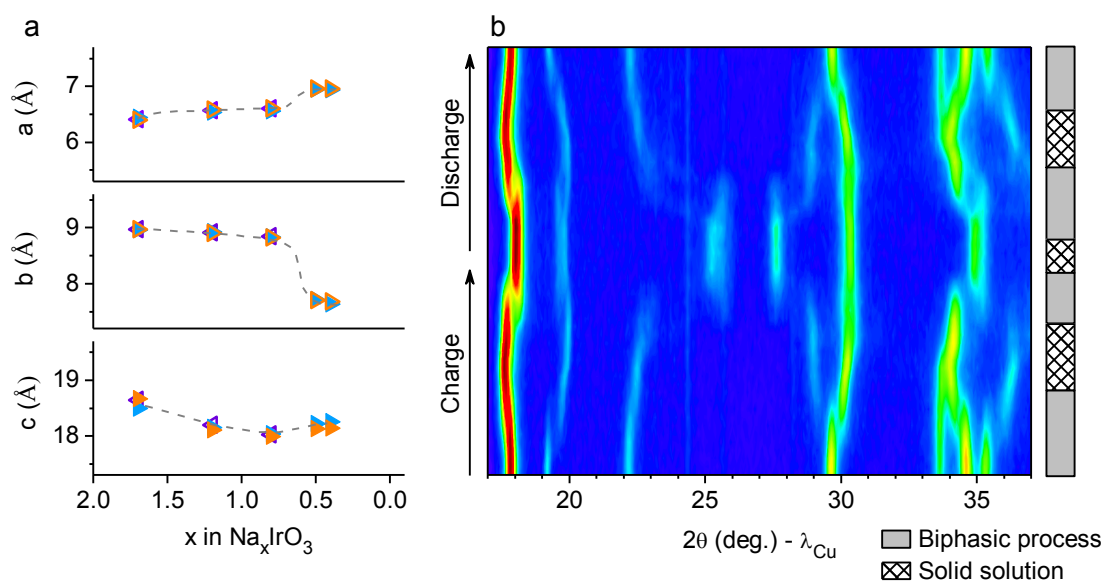


Figure III.9 b) Cell parameters obtained by Rietveld refinement of the different intermediate phases during charge and discharge. In blue and orange are the phases during the 1st charge for two different cells and in purple are the phases during subsequent discharge. c) 2D contour plot of lab source *operando* XRD patterns of $\beta\text{-Na}_{1.7}\text{IrO}_3$ charged and discharged vs Na^+/Na with a schematic describing the transition type, *i.e.* biphasic (grey) vs solid solution (hashed).

Our refinements along with atomic resolution high angular annular dark field STEM (HAADF-STEM) indicate that the IrO_3 scaffold, *i.e.* connectivity between IrO_6 octahedra, remains intact after the insertion of 1.7 Na^+ (Figure III.10). It is important to keep in mind that, due to the considerable difference in mass between Ir and both Na and O, the positions of Na and O from *operando* measurements are difficult to obtain quantitatively even with synchrotron data. This is particularly true for oxygen because of the disorder induced by anionic redox but also for Na when its content is low since the number of scatterers is low.

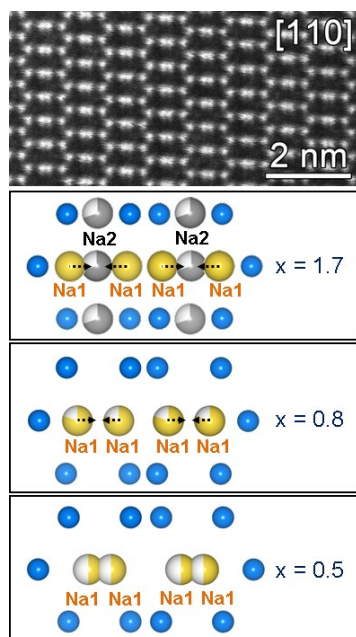


Figure III.10. From top to bottom: Atomic resolution HAADF-STEM image of a $\text{Na}_{1.7}\text{IrO}_3$ particle seen along the $[110]$ direction. Evolution of the Na sites occupation during charge ($\text{Na}_{1.7}\text{IrO}_3$ to $\text{Na}_{0.5}\text{IrO}_3$). Ir atoms are represented in blue, Na1 position in yellow and Na2 position in grey.

Refinements with different models for Na extraction and insertion (preferential extraction/insertion on Na1 or Na2, or a simultaneous extraction/insertion on both crystallographic sites) show that Na2 is preferentially (but not solely) emptied for Na content between $x = 2$ and $x = 1$ (Figure III.10). This does not come as a surprise since Na2 is the more constrained Na in the pristine structure as it occupies the honeycomb-like positions thus being surrounded by five IrO_6 octahedra. Further desodiation leads to an emptying of the remaining Na1, which is accompanied by a shift in the sodium position. Interestingly, this shift in position leads to an off-centered octahedral position with four short Na-O distances and two long ones. The bond valence analysis on Na indicates that despite such an unusual coordination for Na, the average Na-O bond length in NaO_4 is 2.30 Å, in agreement with a bond valence sum of 1. However, for the $\beta\text{-Na}_{0.4}\text{IrO}_3$ compound, the pattern exhibits broad and asymmetric peak profiles so that the positions of the 0.4 remaining Na atoms are difficult to determine with certainty.

III-6 Long term cycling

One of the main issues encountered when testing Na-ion cathode materials is the long term stability, especially when anionic redox is involved since it generally leads to performance decay in LIB cathode materials, as we have seen in the previous chapter.

To investigate the long-term cycling stability of this new compound, half cells composed of IrO₃ mixed with 10% carbon super P as cathodes and Na metal as anodes using 1M NaPF₆ in PC with 1% FEC as electrolyte additive were cycled at a rate of C/10 (1 Na in 10 h). We found a rapid capacity decay upon cycling (Figure III.11 a, b) which can be rooted in either a loss of electronic percolation within the electrode due the electrochemical grinding effect upon cycling resulting from repeated volume contraction/expansion or the growth of a blocking SEI resulting from copious electrolyte degradation in the presence of Na as previously reported for layered α -Na₂IrO₃.⁹⁸

To decipher between the two possibilities, 2032-type coin cells using β -Na_{1.7}IrO₃ mixed with 10% carbon super P as positive electrode, commercial hard carbon as negative electrode and 1M NaPF₆ in PC as electrolyte were assembled and cycled at a C/10 rate between 1 and 4 V (Figure III.11). The first cycle has a high irreversible capacity due to the formation of an SEI on the hard carbon anode. However, the cell retains up to 82 % of its initial capacity after 100 cycles with a coulombic efficiency of around 99.5 %. This implies that the capacity loss observed in Na half cells was mainly due to electrolyte degradation products from the Na metal anode. However, the greater capacity slippage at the discharge endpoint than at the charge endpoint suggests parasitic reactions occurring at the hard carbon anode. This can explain the slight capacity loss observed.

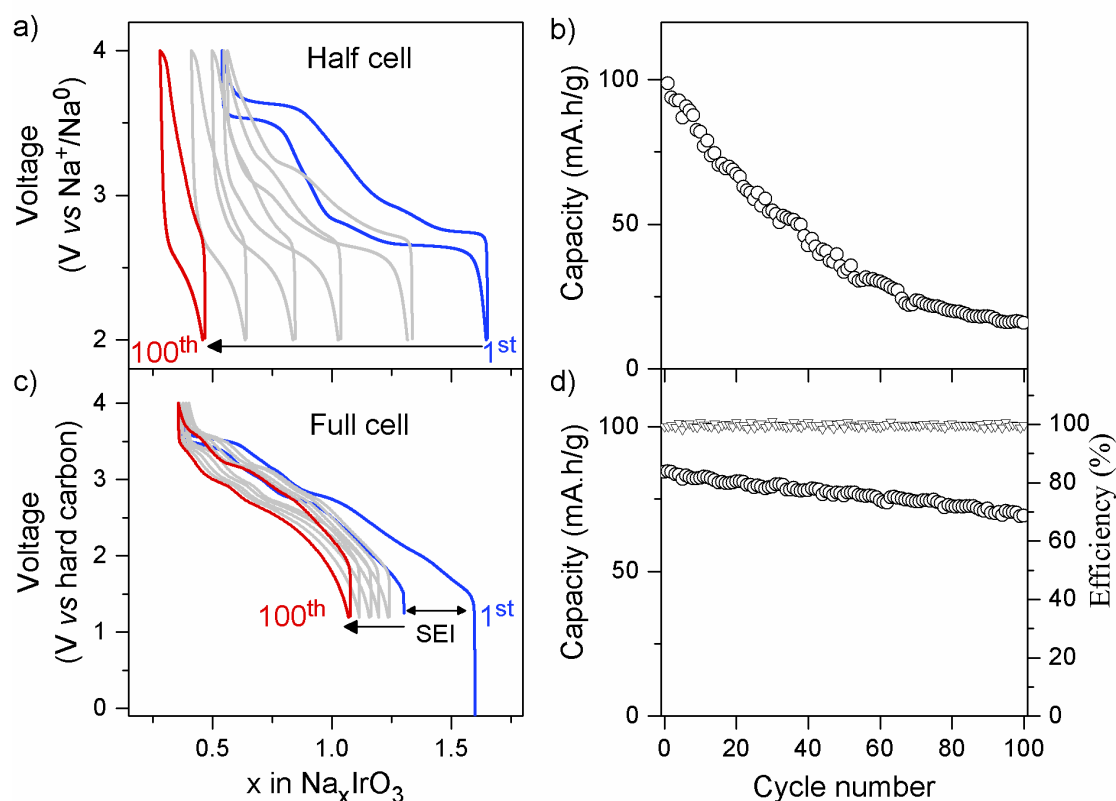


Figure III.11 a) The galvanostatic cycling of $\text{Na}_{1.7}\text{IrO}_3$ in half cell configuration using Na metal as anode and 1M NaPF_6 in PC with 1%FEC as electrolyte solution. The 1st cycle is in blue, the 20th, 40th, 60th and 80th cycles are in grey and 100th cycle is in red. b) The capacity retention upon cycling. c) The galvanostatic cycling of $\text{Na}_{1.7}\text{IrO}_3$ in full cell configuration using hard carbon as anode and 1M NaPF_6 in PC as electrolyte solution. The 1st cycle is in blue, the 20th, 40th, 60th and 80th cycles are in grey and 100th cycle is in red. d) The capacity retention (circles) and coulombic efficiency (triangles) upon cycling (first cycle efficiency is 76%)

III-7 Thermal stability

Our inability to prepare $\beta\text{-Na}_{1.7}\text{IrO}_3$ by high temperature solid state synthesis suggests that this phase is thermodynamically less stable than the layered polymorph. To get further insight into the temperature stability issue, differential scanning calorimetry (DSC) measurements were carried-out for both $\beta\text{-Na}_1\text{IrO}_3$ and $\beta\text{-Na}_{1.7}\text{IrO}_3$ using freshly prepared samples with no carbon as dilithiation as well as sodiation can be carried out without any conductive additives. Since these samples (particularly $\beta\text{-Na}_{1.7}\text{IrO}_3$) are moisture sensitive, they were placed in Al pans that were sealed within the dry box. Prior to being placed in the DSC cavity, the pans were quickly pierced while flushing

under argon and the measurements collected. After the measurement, the Al pan was rapidly returned to the dry-box and the XRD pattern of the recovered powder was collected using an air-tight cell with a Kapton window. Figure III.12 shows the XRD patterns of both β -Na₁IrO₃ and β -Na_{1.7}IrO₃ after the DSC experiment compared to the same composition during *operando* XRD experiment. Both display sharper peaks implying improved crystallinity and negligible peak shifting after annealing step. In addition, no sign of the layered polymorph could be detected meaning that no phase transition occurred during heating. We therefore conclude that these phases are stable at least to 600°C; the maximum we could measure by DSC experiment.

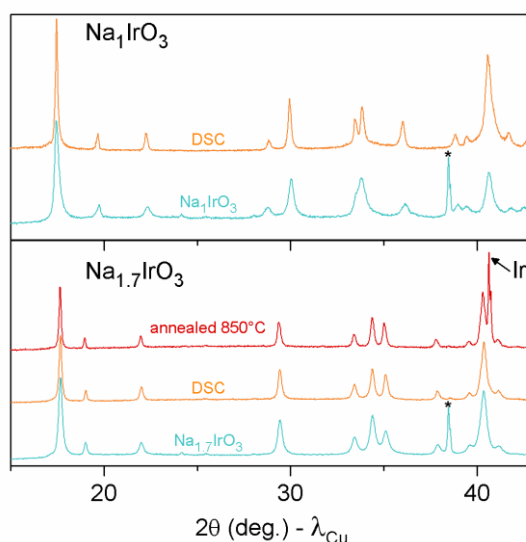


Figure III.12 XRD patterns of β -Na₁IrO₃ and β -Na_{1.7}IrO₃ from in situ measurements (in blue) and after DSC experiment (in orange) and in the case of β -Na_{1.7}IrO₃ the pattern after annealing at 850°C for 6h (in red). Peaks marked by a black star are from the electrochemical cell.

To check the stability towards higher temperatures, β -Na_{1.7}IrO₃ powder was placed in a covered alumina crucible, inserted into an evacuated sealed quartz ampoule and heated to 850°C for 6 hours. After cooling, the ampoule was opened in the dry-box and the powder was recovered for XRD characterization. The collected pattern reveals the existence of two distinct phases, with the dominant one β -Na_xIrO₃ being contaminated by Ir metal ($\approx 35\%$ by Rietveld refinement). To assess the Na content (x) of the main phase, the X-ray diffraction data were refined by the Rietveld method. Surprisingly, the obtained cell parameters ($a = 6.409(3)$ Å, $b = 8.976(7)$ Å, $c = 18.646(8)$ Å) only slightly differ from that of the pristine β -Na_{1.7}IrO₃ ($a = 6.4068(6)$ Å, b

= 8.9590(11) Å, $c = 18.6942(18)$ Å). This implies that the Na composition slightly deviates from $x = 1.7$, implying a slow decomposition process from the particle surface inward with surface decomposing yielding volatile Na₂O and Ir metal. This instability toward Na loss is likely to be the main difficulty to overcome in order to prepare β -Na_{1.7}IrO₃ via a solid state method.

Conclusion

In this chapter, we have seen that the IrO₃ framework obtained by total delithiation of the β -Li₂IrO₃ phase described in Chapter II, could also accommodate larger ions such as Na⁺ for which a composition of $x = 1.7$ could be attained when discharging to 2.0 V vs Na. During the first sodiation, the electrochemical profile is very similar to the one during lithiation with namely the successive appearance of four voltage plateaus. These were determined, by *operando* SXR D measurements, to be caused by four biphasic phase transitions, as expected for such electrochemical features. The subsequent charge shows only three of the plateaus and the forth one could not be reached. Indeed, the full desodiation to IrO₃ was not attained to the contrary of the lithiated compound as only 1.3 Na⁺ could be extracted leading to a lower Na content of $x = 0.4$, this even when the potential was held at 4.0 V.

The structure of Na_{1.7}IrO₃ was determined by SXR D which shows that the IrO₃ framework is retained with however corrugated oxygen rows, further confirmed by HAADF-STEM. The different intermediate phases observed during charge and discharge could be isolated and their SXR D patterns were refined in order to obtain the cell parameters. A large volume expansion/contraction during discharge/charge is observed and highlights the extreme flexibility of this iridium oxide framework. Furthermore, the de/sodiation follows a highly reversible structural evolution with the cell parameters of each intermediate phase on charge and discharge being very close.

As anionic redox has been evidence during charge and discharge for the lithiated compound, XPS measurements were carried out on the discharged and the charged phases in order to probe the activity of oxygen in the sodiated compound. Interestingly, the discharged phase clearly shows that the oxidized oxygen species present in IrO₃ have decreased significantly but have not disappeared. However, on charge the XPS signal associated to the oxidized oxygen species regain intensity, supporting the presence of

anionic activity in this compound. While this is interesting, it is not surprising as anionic redox arises from the non-bonding oxygen states present when oxygen is surrounded by less than three TM cations. In the present case, the Na-O bond is, similarly to the Li-O bond, highly ionic in nature and the orbital overlap is negligible which leads to “non-bonding” like states which can be redox active. While this has been theoretically well established, it is important to bring experimental proofs to these hypothesis, as is the case here.

Finally, the $\beta\text{-Na}_2\text{IrO}_3$ composition was never achieved either by high temperature solid state chemistry or by electrochemistry and while the latter can be explained by sterical hindrance, the former can be better explained by the size difference between Ir and Na which greatly favors a layered structure. However, the hyperhoneycomb IrO_3 framework does not convert to the layered honeycomb at high temperature and decomposes before any structural changes can occur. It could be possible to find a reaction pathway to obtain the stoichiometric compound but this has not been investigated as of yet. Further work should be carried out in order to pinpoint the adequate synthesis conditions which could extend the structure to a more diverse composition and different electrochemical properties.

Chapter IV. A protonated iridium oxide catalyst for water oxidation in acidic media

Introduction

As discussed in the previous chapters, Iridates have been thoroughly investigated as model cathode materials and have been instrumental in understanding the redox mechanisms during Li/Na insertion and extraction in the Li-rich NMC materials. The hyperhoneycomb iridate $\beta\text{-Li}_2\text{IrO}_3$ which is the subject of this thesis has been the first tridimensional framework to exhibit anionic activity and has brought another stone to the field of high energy density insertion cathode materials. Another iridate which has been recently studied and which has brought significant new insights into this field is the Li_3IrO_4 compound.⁷⁵ Not only was this material pivotal for pushing anionic redox to its limit, but it also demonstrated the ability to form a crystalline protonated compound by ion exchange in acidic media, resulting in a protonated iridate $\text{H}_{3.4}\text{IrO}_4$ which displayed significant electrochemical performances in aqueous electrolyte.

In previous work, the exchange of Li^+ for H^+ in the $\beta\text{-Li}_2\text{IrO}_3$ phase was not successful and was attributed to the tridimensional framework.¹¹³ While the exchange did not take place at room temperature, proceeding in hydrothermal conditions at 120°C for 24h enabled the successful synthesis of a crystalline phase which has retained the IrO_3 framework with however, significant changes in the lattice parameters. The structural characterization as well as the insertion properties of this newly formed phase were assessed and are discussed in this chapter.

Furthermore, Iridates have long been studied for their electrocatalytic performances in acidic media for the oxygen evolution reaction (OER). More specifically, questions pertaining to the role of electrophilic oxygen species “ $\text{O}^{\text{n-}}$ ” formed on the surface of iridium based oxide catalysts as well as proton exchange during the OER have lately generated a lot of attention, thus making the study of protonated hyperhoneycomb material of prime interest.

This chapter is composed of four sections, this brief introduction not included. The first section describes the synthesis, the chemical and structural characterizations of the protonated $\beta\text{-H}_2\text{IrO}_3$ compound as well as its proton insertion abilities. The second section will be dedicated to the evaluation of the electrocatalytic performances of this new hydrated iridate and the implication of anionic redox and proton exchange ability for the OER activity in acidic media. The third section will elaborate on the reactivity of

different lithiated intermediates from chapter II and the fate of IrO_3 when in contact with acidic media. The fourth and final section will describe a charge compensation mechanism based on the discussed observations which relies on proton insertion for increased stability. The chapter will be concluded by a short summary of the findings.

IV-1 Synthesis and characterization

IV-1-a Ion exchange

In order to prepare the proton exchanged phase H_2IrO_3 , $\beta\text{-Li}_2\text{IrO}_3$ (synthesized according to the method developed in chapter II) was added to a 1 mol.l^{-1} solution of H_2SO_4 and heated to 120°C for 36 hours in a Teflon-lined steel autoclave. The resulting powder was washed with ultrapure water several times (until pH of the wash water reaches 7) and dried at 55°C in order to remove traces of adsorbed water.

IV-1-b Chemical composition

The composition of the newly obtained compound was determined by thermogravimetric analysis coupled with a mass spectrometer (TGA-MS) in order to determine the gas produced during the decomposition. The TGA-MS measurements were recorded with a STA 449C Netzsch apparatus under argon by applying a heating rate of $5 \text{ K}\cdot\text{min}^{-1}$ from room temperature to 1000°C using around 15-20 mg of material. The TGA curve is shown in Figure IV.1 a) with the MS signals for $m/z = 18$ corresponding to water in orange and $m/z = 32$ corresponding to oxygen in blue.

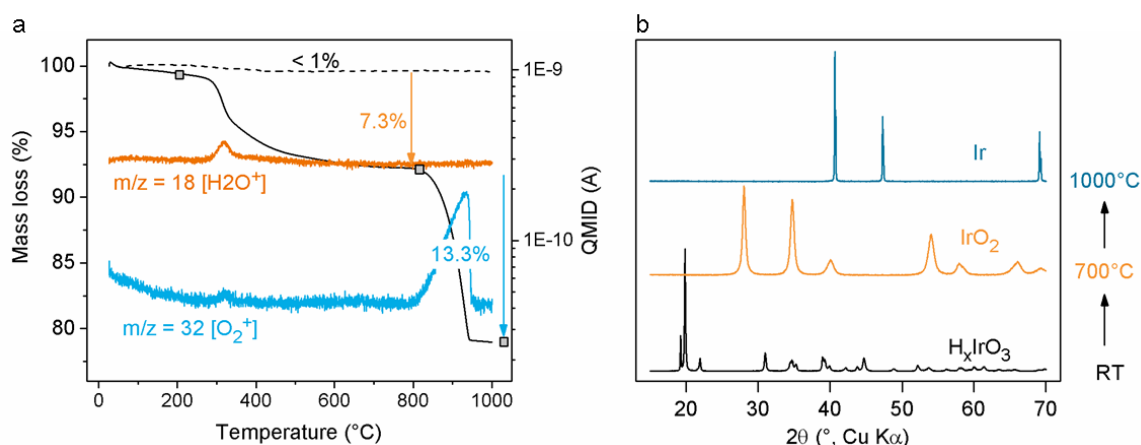
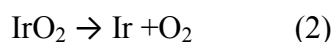
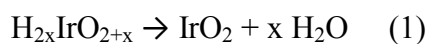


Figure IV.1 a) Thermogravimetric analysis with mass spectrometry data during TGA showing the evolution of $m/z = 18$ and 32 corresponding to H_2O^+ (orange) and O_2^+ (blue) respectively. The dashed line shows the TGA for the pristine $\beta\text{-Li}_2\text{IrO}_3$. b) X-ray diffraction patterns of $\beta\text{-H}_2\text{IrO}_3$ pristine (in black), after heating to 700°C under Ar (in orange) and after heating to 1000°C under Ar (in blue).

Two significant mass losses are observed with one starting around 300°C and the second occurring around 850°C . The MS signal reveals that the first loss is related to water (a small amount of oxygen is released but considering the log scale, this is neglected here) whereas the second can be explained by the loss of oxygen. In order to determine the products obtained after each mass loss, ex situ XRD measurements were carried out and the patterns are shown in Figure IV.1 b). The release of water is accompanied by a phase change to a rutile IrO_2 while the loss of oxygen leads to the formation of metallic Iridium. It is worth mentioning that the pristine $\beta\text{-Li}_2\text{IrO}_3$ was also measured and found to be very stable up to 1000°C with less than 1% mass loss (dashed line in Figure IV.1). Interestingly, there is no sign of a lithiated compound after heating to 1000°C and consequently it is assumed that no Li^+ is present in the compound after acid treatment. This allows us to assign the decomposition process by the following two reactions:



With a loss of 7.3 % of water and assuming that the decomposition follows equation (1), x is determined to be 1 and the chemical formula of the new compound to be H_2IrO_3 .

IV-1-c Structural characterization

The SXRD pattern of the obtained material was collected at ALBA synchrotron's MSPD beamline¹¹⁴ with a wavelength of 0.413 Å. The pattern could be indexed with the same orthorhombic cell as the pristine lithiated structure with however significantly modified cell parameters (Table IV.1), as determined by Rietveld refinement shown in Figure IV.2 a).

Table IV.1 Crystallographic data and atomic positions of $\beta\text{-H}_2\text{IrO}_3$ determined from the combined Rietveld refinement of the synchrotron X-ray and neutron powder diffraction patterns collected on Alba synchrotron's MSPD beamline and on the ILL D20 beamline, respectively.

$\beta\text{-H}_2\text{IrO}_3$							
Space group Fdd							
NPD : $a = 5.40139(18)$ Å, $b = 9.0436(3)$ Å, $c = 18.5007(6)$ Å, $V = 903.56(5)$ Å ³ , $R_{\text{Bragg}} = 2.76\%$, $\chi^2 = 48.9$							
SXRD : $a = 5.39605(7)$ Å, $b = 9.07170(16)$ Å, $c = 18.5488(2)$ Å, $V = 907.986(23)$ Å ³ , $R_{\text{Bragg}} = 2.44\%$, $\chi^2 = 30.8$							
Atom	Wyckoff position	x/a	y/b	z/c	B (Å ²)	Occ.	BVS
Ir	16g	1/8	1/8	0.70629(15)	0.33(6)	1	4.013(17)
H1	32h	0.9931(17)	0.2154(12)	0.1241(10)	0.9(2)	0.245(5)	1.049(8)
H2	32h	0.0533(8)	0.1097(7)	0.97466(19)	0.22(14)	0.520(7)	0.847(4)
O1	16e	0.8731(9)	1/8	1/8	0.40(5)	1	1.735(10)
O2	32h	0.6306(9)	0.3478(3)	0.03820(19)	0.40(5)	1	1.837(10)

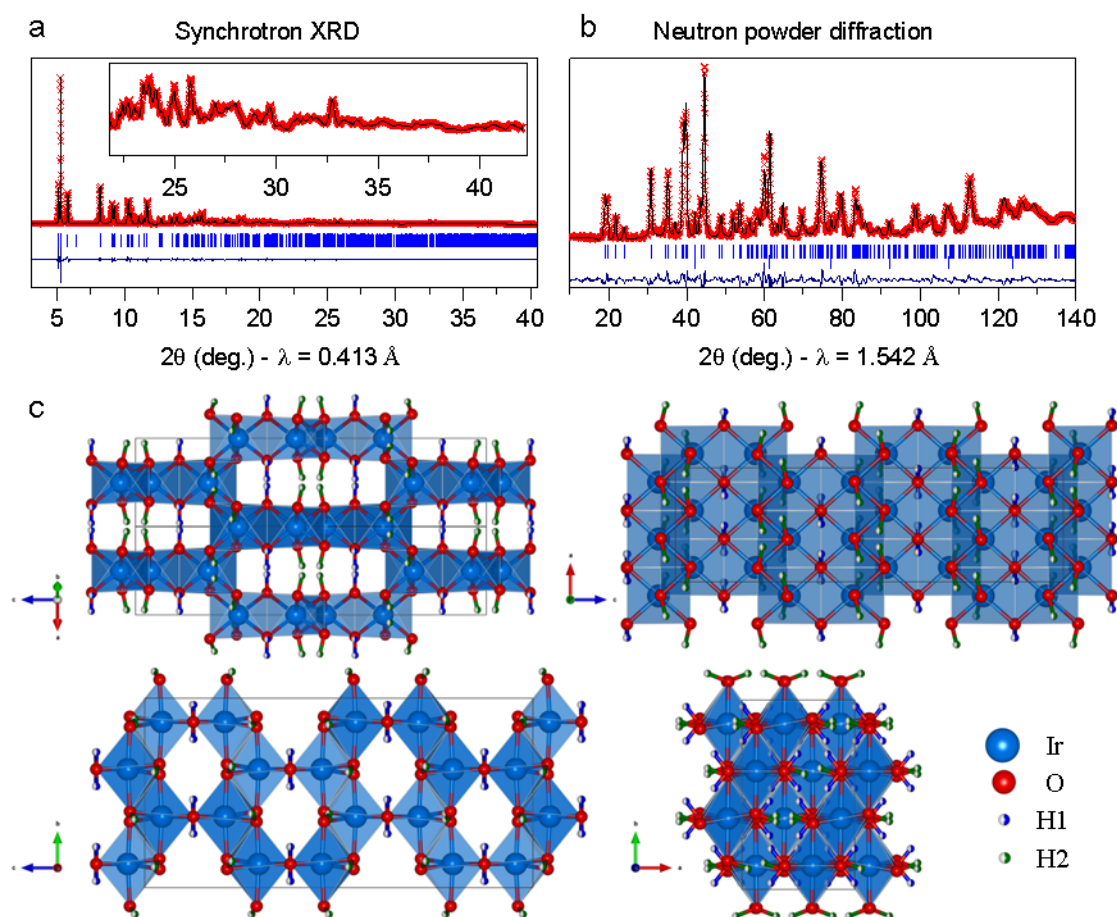


Figure IV.2 a) Rietveld refinement of the Synchrotron X-ray and b) neutron powder diffraction patterns for β -H₂IrO₃. In red are the experimental points, in black is the calculated pattern and in blue is the difference between the experimental and calculated patterns. The vertical blue ticks beneath the pattern indicate the positions of the Bragg reflections. d) Structure projections of β -H₂IrO₃ along the main crystallographic zone axes.

In order to determine the proton sites and the oxygen positions, NPD was measured at the D20 beamline at the ILL neutron facility by J. Rodríguez-Carvajal with a wavelength of 1.542 Å. Hydrogen is a good neutron scatter but its bound incoherent scattering length (25.274(9) fm) and cross section (80.27(6) barn) are very high leading to a low signal/noise ratio and therefore long acquisition times. However, deuterium has significantly smaller bound incoherent scattering length (4.04(3) fm) and cross section (7.64(3) barn).¹¹⁵ The sample was therefore prepared using a deuterated 1M D₂SO₄ in D₂O solution for the ion exchange. The Rietveld refinement is shown in Figure IV.2 and the atomic positions determined by refinement of the NPD powder with the cell parameters determined by refinement of both the NPD and SXRD patterns are given in Table IV.1. Two proton sites could be distinguished with one leading to hydroxyl group

with an O-H distance of 1.091 Å and the other to a H₂O group with an O-H distance of 1.043 Å and an $\widehat{\text{HOH}}$ angle equal to 103.3°, similarly to a free water molecule. The structure is shown along different directions in Figure IV.2 c) with each proton site in a different color and the crystallographic occupancies set to 0.5 for both sites, as expected for a stoichiometric compound. The deuterium content obtained by the neutron refinement is lower than the proton content deduced by TGA-MS, suggesting that the reaction is incomplete with deuterium when compared with proton. This assumption is further supported by our electrochemical data shown in the Appendix Chapter IV. Figure 1 which indicates a slow deuterium diffusion when compared to proton.

IV-1-d Particle morphology

Due to the harsh conditions in which the ion exchange takes place, it is important to verify the effect of such treatment on the particle morphology. For this, scanning electron microscopy was used and the micrographs before and after are shown in Figure IV.3. While severe cracking is observed, no dissolution/precipitation seems to take place as the cracked particles are of same size and overall shape as the pristine material.

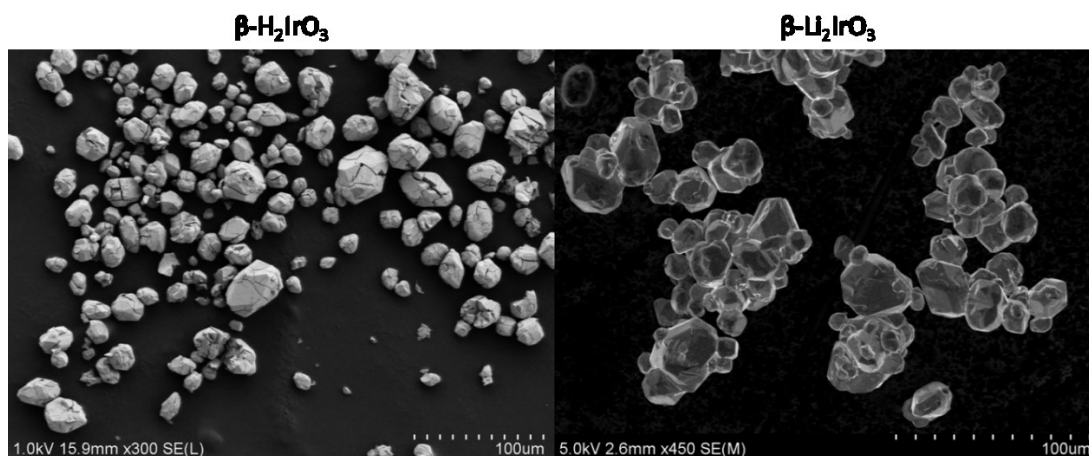


Figure IV.3 Scanning electron micrographs of the $\beta\text{-H}_2\text{IrO}_3$ and the $\beta\text{-Li}_2\text{IrO}_3$. The magnification is slightly different between the two with x300 for the protonated phase and x450 for the lithiated phase.

IV-1-e Ir oxidation state

In order to determine if the protonation process entails a reduction of the material (as what was observed for Li_3IrO_4) and to indirectly confirm the stoichiometry of the

compound, Ir L_{III} edge XAS measurements were carried out on both the pristine β - Li_2IrO_3 and the β - H_2IrO_3 at the Soleil synchrotron's ROCK beamline with the help of A. Iadecola. The results are shown in Figure IV.4 with the lithiated phase in blue and the protonated phase in orange. Interestingly, as discussed in a previous section, the white line area for the Ir L_3 edge is not consistent with the number of unoccupied states in the 5d levels of Ir. The WL energy, meaning the energy of maximum of absorption is more relevant to determining the oxidation state of Ir in these compounds. Here, the WL is centered on the same energy value, indicative of similar oxidation states, which nicely corroborates the composition determined by thermogravimetric analysis described above.

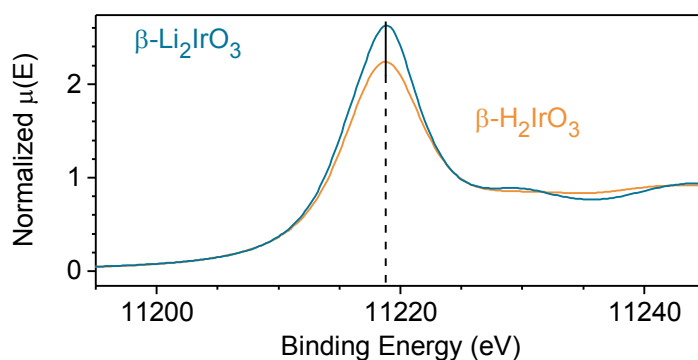


Figure IV.4 The Ir L_{III} edge XANES spectra of the β - Li_2IrO_3 (blue) and β - H_2IrO_3 (orange).

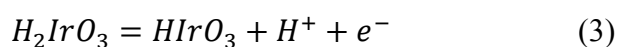
Having established the chemical composition and structural characteristics of this new phase, its proton insertion/extraction abilities will be discussed in the next section.

IV-1-f Proton insertion

As discussed earlier, the interest in the protonated Iridates has stemmed from the previous work on $\text{H}_{3.4}\text{IrO}_4$ which displayed interesting proton insertion abilities.¹¹⁶ In this subsection, the electrochemical activity of the protonated β - H_2IrO_3 will be discussed in aqueous media in order to ascertain its proton insertion properties.

In order to test the electrochemical performances of the β - H_2IrO_3 in acidic conditions, electrodes composed of 80 % active material, 15 % acetylene black (AB) carbon and 5 % polytetrafluoroethylene (PTFE) were prepared by mixing them with

some ethanol and rolling/folding the resulting paste in order to obtain a homogeneous electrode. The electrode could then be cut into smaller electrodes and used as working electrode in a three electrode setup using YP50 carbon (made in a similar fashion using PTFE as binder) as counter electrode and a KCl sat. Ag/AgCl reference electrode. The electrodes were separated by a Whatman GF/D borosilicate glass fiber soaked with a 1M H₂SO₄ solution and the current collectors were glassy carbon rods. In order to confirm the proton involvement, the pH was changed and fixed by using a buffer solution of acetic acid at pH = 4.55 as well as a 1M KCl solution at the same pH. Indeed, the expected reaction can be described by (3) as a proton insertion/extraction:



In order to assess the different electrochemical processes taking place, cyclic voltammetry measurements were performed and the results are shown in Figure IV.5. For the sake of comparison, the cycles shown correspond to the fifth cycle, the current is normalized by the mass of the active material, the rate was set to 5 mV·s⁻¹ and the potential is plotted vs RHE. The CV performed in both sulfuric acid and acetic acid display three processes which are all shifted by -0.059 V per unit of pH. This is consistent with a reaction which entails the exchange of one proton for one electron such as the one described in (3) and the Nernst equation can be written as follows:

$$E = E^\circ + \frac{RT}{F} \ln\left(\frac{a_{H^+} \cdot a_{HIrO_3}}{a_{H_2IrO_3}}\right) \quad (4)$$

$$E = E^\circ + \frac{RT}{F} \ln(a_{H^+}) = E^\circ - 0.059 \cdot pH \quad (5)$$

With E the potential, E° the standard potential, R the perfect gas constant, T the temperature in Kelvin, F the Faraday constant and *a* the activity of the different species. As both H₂IrO₃ and HIrO₃ are solids, their activity is considered equal to unity and while the high proton concentration cannot be considered as a diluted system, we will make the approximation that the activity is equal to the concentration for the sake of explanation. In addition, at 25°C under 1 bar, the term before the natural logarithm is equal to 0.059 for 1 e⁻ and for a decimal log. Under these assumptions, the potential should vary linearly with the value of pH and with a slope of -0.059 V per unit pH.

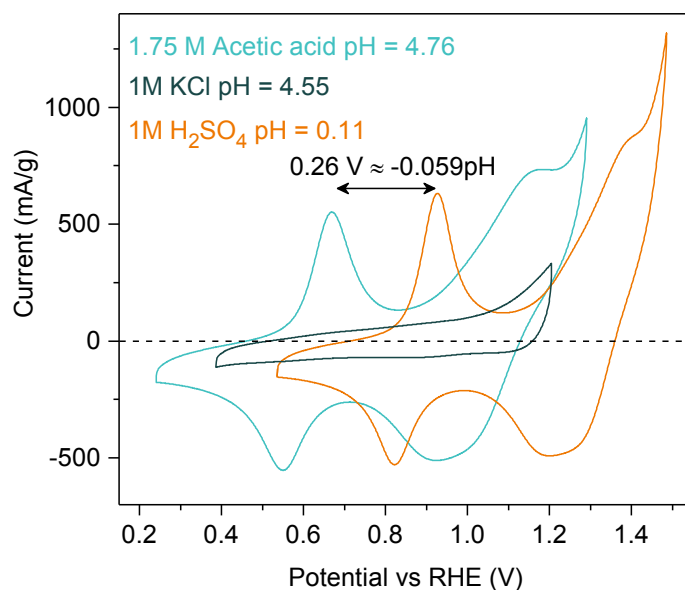


Figure IV.5 Cyclic voltammetry curves of $\beta\text{-H}_2\text{IrO}_3$ in 1 M H_2SO_4 (orange), 1.75 M Acetic acid buffer (blue) and in 1M KCl (dark grey). Three processes can be observed on the orange and blue curves but none on the dark grey curve.

The fact that the peak potential is shifted by such a value when changing the pH from 0.1 to 4.76 is indicative of proton involvement in the overall reaction and points towards an insertion of protons. Furthermore, the same experiment was carried out using a rotating disc electrode with the active material (mixed with tetrahydrofuran and a Nafion suspension) drop casted onto a glassy carbon tip and identical CV were obtained, indicating that the diffusion limitation (a peak instead of a plateau) is most likely originating from the solid state diffusion of protons within the material structure and not from the solution. This assumption is further supported by solid state NMR measurements which show that protons are only slightly mobile within the structure (Appendix Chapter IV. Figure 2), when compared to lithium in the lithiated parent phase. Further evidence for proton insertion is given by the CV carried out in a 1M KCl solution at a pH similar to the one for acetic acid solution and which displays no peak at all. This is quite interesting as it suggests that the acetic acid is the proton donor and that the free protons do not participate in the reaction.

As it has been determined that protons are able to be inserted and extracted from the structure, the capacity of the material is assessed by galvanostatic cycling with potential limitation. While proton exchange was successfully achieved for $\text{H}_{3.4}\text{IrO}_4$ at a potential below the oxidation of water,¹¹⁶ it is not the case for the present phase. Indeed,

as seen Figure IV.6, the first cycle has a large irreversibility which remains, though to a lesser extent, on subsequent cycles. At these potentials, the oxygen evolution reaction (OER) can take place and due to the low current involved, the overpotential is low enough to lead to significant amounts of water oxidation. This is not surprising as Iridates are known for their good electrocatalytic activity towards water oxidation in acidic media.

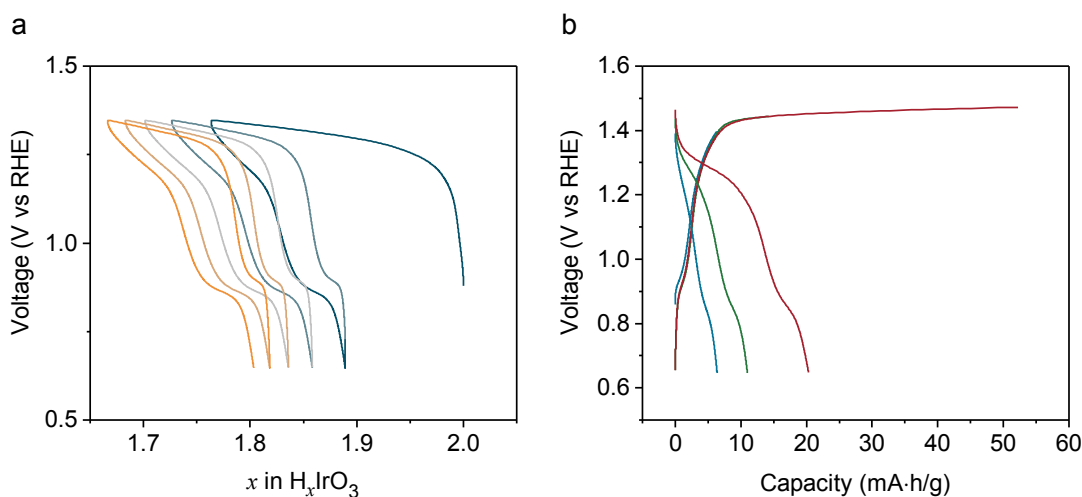


Figure IV.6 Galvanostatic cycling of $\beta\text{-H}_2\text{IrO}_3$ in a 1M H_2SO_4 solution. a) Cycling between 0.65 V and 1.4 V vs RHE at 1C in 1M H_2SO_4 solution. b) Cycling at 10 C in 1M H_2SO_4 with a low voltage cutoff set at 0.65 V and a high voltage cutoff set at 1.4 V, 1.44 V and 1.48 V vs RHE shown in blue, green and red respectively.

Increasing the rate does not prevent the OER reaction as the kinetics of the insertion reaction seem to be comparatively sluggish. However, opening up the voltage window and thus increasing the amount of oxygen evolved, also leads to more discharge capacity (Figure IV.6 b), indicating that the phase is oxidized at a potential concurrent to the OER one. This is further corroborated by the observation that once left at OCV after charging to 1.4 V vs RHE, self-discharge takes place. This is simply explained as the oxidized material has a potential outside the electrochemical window of water, leading to the oxidation of water and the evolution of oxygen counterbalanced by the reduction of the material with proton insertion. While this is well known in the battery field and undesirable, we will see that such charge balance mechanism can be of great interest to design efficient and stable water splitting catalysts.

IV-2 The oxygen evolution reaction

Energy storage via hydrogen production could play a key role in the deployment of renewable energy technologies.^{117,118} Unfortunately, the slow kinetics of the OER leads to high overpotentials and largely limits the current performances of electrolyzers.^{119,120} This is not the case for the cathodic hydrogen evolution reaction (HER) which can occur at almost no overpotential in acidic conditions. Although various TM-based oxides and oxyhydroxides have been developed as efficient electrocatalysts for the OER in neutral and alkaline pH,^{121–126} these catalysts seriously corrode in acidic solutions.^{127–130} Today's stellar electrocatalysts capable of operating in such harsh conditions are composed of Iridium and Ruthenium oxides (IrO_x , RuO_x).^{131–134} However, they still suffer from substantial dissolution and relatively high overpotential for the OER, making them poor choices for long-term use.^{127,135}

Indeed, most materials explored so far as water oxidation electrocatalysts in acidic environment such as Au, IrO_2 , RuO_2 , SrIrO_3 or $\text{La}_2\text{LiIrO}_6$, have demonstrated instability and the formation of an amorphous hydrated MO_x surface layer after prolonged OER tests,^{136–142} this phenomenon being accompanied by cation dissolution.^{128,143} Hence, to suppress the dissolution of precious metals such as Ir, a promising strategy previously investigated is to develop a durable protective surface layer with the formation of a hydrated IrO_x layer. For example, in a co-catalyst system (IrNiO_x), Ni was adopted as a sacrificial metal to be selectively dissolved from the matrix and form an amorphous IrO_x surface layer.^{144–146} In another catalyst with the perovskite structure SrIrO_3 , Sr^{2+} was selectively dissolved during an activation step, thus triggering the formation of a core-shell $\text{IrO}_x/\text{SrIrO}_3$ structure.¹⁴⁷ Despite the relative success of these strategies relying on surface protection, recent understanding pointed towards the existence of a common intermediate responsible for both the enhanced OER activity for iridium-based catalysts as well as their relative instability: electrophilic oxygen formed upon oxidation on the surface of iridium oxides.^{136,148–150} Within this scenario, the electrophilic oxidized oxygen ions serve as active sites and lead to improved reactivity on the surface of the metal oxide. However, increasing the surface reactivity with water leads to a decrease in the coordination number of transition metals on the surface, hence promoting their dissolution into the electrolyte. New strategies to control this surface reactivity are therefore much needed in order to tackle this

activity/stability relationship.^{151–153} In this context, the hydrated iridate $\beta\text{-H}_2\text{IrO}_3$ which as we demonstrated above shows bulk proton intercalation/de-intercalation ability could show promising performances.^{154,155}

IV-2-a Electrochemical performance

Having previously established that structural protons are reversibly exchanged between $\beta\text{-H}_2\text{IrO}_3$ and the electrolyte, its electrochemical OER activity was then compared with the state-of-the-art IrO_2 and $\text{IrO}_x/\text{SrIrO}_3$ electrocatalysts (Figure IV.7 a) and b). When normalized by the oxide surface area, the $\beta\text{-H}_2\text{IrO}_3$ demonstrates a large OER activity with an overpotential as low as ~ 345 mV at a current density of $10 \text{ mA/cm}^2_{\text{oxide}}$ in 1.0 M H_2SO_4 (see BET results in Appendix Chapter IV. Table 2). These metrics outperform the ones measured for micron- (this work, Figure IV.7) and nano-sized IrO_2 ¹³¹ as well as for $\text{La}_2\text{LiIrO}_6$ ¹³⁶ or $\text{Ba}_2\text{PrIrO}_6$ ¹⁵⁶ perovskites and nearly approach the initial activity of today's stellar $\text{IrO}_x/\text{SrIrO}_3$ catalyst. We should however note that in its powder form, $\text{IrO}_x/\text{SrIrO}_3$ catalyst quickly deactivates and finally $\beta\text{-H}_2\text{IrO}_3$, which activity remains relatively stable upon cycling, is found to possess a similar activity after 300 cycles of CVs. Moreover, when normalized by the mass of iridium, $\beta\text{-H}_2\text{IrO}_3$ shows better OER performances than $\text{IrO}_x/\text{SrIrO}_3$ owing to the small particle size which results from chemical grinding during the cationic exchange due to the large cell parameter changes and subsequent grinding in an agate mortar, as shown by the SEM micrographs in Figure IV.3 and Appendix Chapter IV. Figure 4, respectively. Overall, these results make this protonated phase very promising as OER catalyst in acidic conditions.

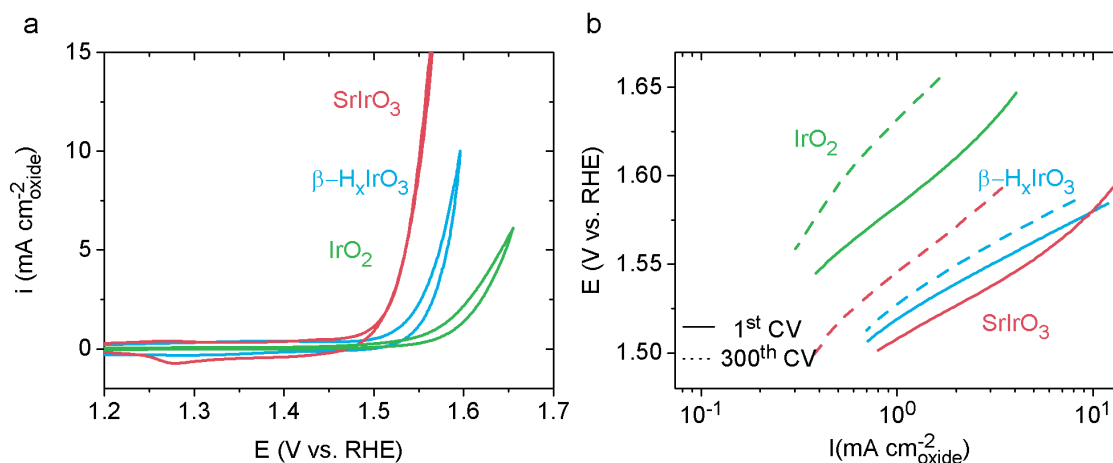


Figure IV.7 Electrochemical activity of the $\beta\text{-H}_2\text{IrO}_3$ phase in 1M H_2SO_4 . (a) Cyclic voltammograms of IrO_2 , $\beta\text{-H}_2\text{IrO}_3$ and SrIrO_3 in 1M H_2SO_4 solution using a rotating disk electrode. (b) Tafel plots of various electrocatalysts in acid media.

IV-2-b Stability during OER

To assess the electrochemical stability of the $\beta\text{-H}_2\text{IrO}_3$ catalyst in acidic condition, ICP-OES measurements were performed on the electrolyte solution over 50 h at a constant potential of 1.55 V vs RHE and the results are compared with $\text{IrO}_x/\text{SrIrO}_3$ (Figure IV.8 a)). Interestingly, the dissolution rate is found reduced for $\beta\text{-H}_2\text{IrO}_3$ when compared to $\text{IrO}_x/\text{SrIrO}_3$. Indeed, less than 0.2 % Ir was found dissolved after 50 hours, while ≈ 0.45 % Ir were detected in solution for $\text{IrO}_x/\text{SrIrO}_3$. This relative stability is further illustrated by the retained electrochemical signature for the potentials below the OER in which three reversible redox peaks at 0.9 V, 1.25 V and 1.35 V vs. RHE corresponding to the bulk oxidation/deprotonation are observed (Figure IV.8 b). Such observation indicates that the bulk retains its proton exchange properties and that no significant increase of the active surface area as well as obvious modification of the surface chemistry occur upon cycling (Figure IV.8 b). This is in direct contrast with previous reports correlating the changes in the capacitive signature of TM oxides to surface modifications.¹⁵⁷ Overall, this low dissolution rate is quite surprising considering the high surface area which, intuitively, should show opposite trends. On the other hand, SrIrO_3 initially displays several sharp redox peaks below 1.5 V, presumably related to a dissolution/re-precipitation process, which quickly disappear after a few cycles to leave only a capacitive current corresponding to the signature of the IrO_x shell.

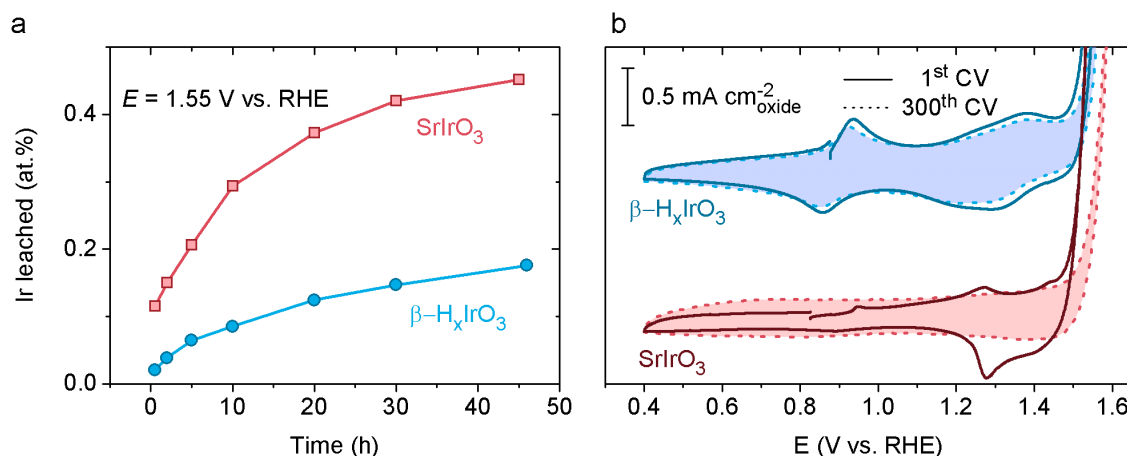


Figure IV.8 Stability of the $\beta\text{-H}_2\text{IrO}_3$ phase in 1M H_2SO_4 during OER. (a) Ir dissolution upon time as measured by ICP-OES for $\beta\text{-H}_2\text{IrO}_3$, SrIrO_3 , IrO_2 . (b) Enlarged CV curves depicting the evolution of capacitance regions for $\beta\text{-H}_2\text{IrO}_3$ (blue) and SrIrO_3 (red) cycled in 1.0 M H_2SO_4 acidic solution for 300 cycles (~20 hours) at a scan rate of 10 mV/s (1st cycle in solid line and 300th cycle in dash line).

We then investigated the evolution of the surface of the catalyst by HAADF-STEM before and after electrochemical cycling. After synthesis, a very thin amorphous layer is found indicating that a surface reconstruction takes place even without any potential bias. Furthermore, this amorphous layer on the surface of the particles shows little to no thickness increase during OER activity, even after 300 CV cycles as evidenced shown in Figure IV.9 b.

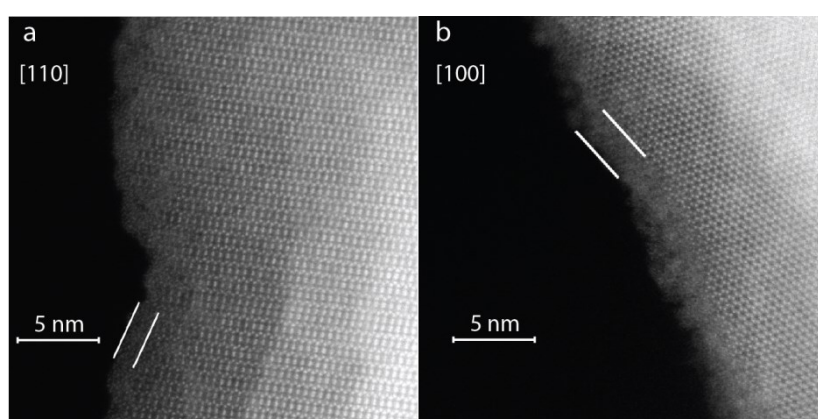


Figure IV.9 HAADF-STEM of a) $\beta\text{-H}_2\text{IrO}_3$ pristine along the [110] zone axis and b) after 300 cycles to 1.65 V vs RHE in 1M H_2SO_4 solution along the [100] zone axis.

IV-2-c *Operando* XRD – β -H₂IrO₃

Having established that β -H_xIrO₃ show promising OER activity combined with a very good stability during oxidation in acidic conditions, the question then arises regarding the redox and structural activity of this protonated phase during OER. To track down the structural evolution of the β -H₂IrO₃ phase upon OER, *operando* XRD was carried out during the anodic scan in 1 M H₂SO₄ solution (Figure IV.10 a and b). Scanning from the OCV to 1.65 V *vs.* RHE at 0.2 mV/s, no drastic structural evolution is observed with the exception of a slight shift of the (004) Bragg diffraction peak to lower angle. This is consistent with the low amount of protons extracted during the three redox processes below the OER region. Nevertheless, when holding the potential in the OER region at 1.65 V *vs.* RHE over 30 minutes, a structural change occurs with the disappearance of the (004) Bragg peak at 19.3° concomitant with the apparition of a new peak at higher angle (\approx 19.45°) (arrows in Figure IV.10 b) and a shift of the main (111) diffraction peak to greater angle. This new phase can be described in the same space group as the pristine β -H₂IrO₃, with nevertheless a modification of the lattice parameters and especially a reduction of the *c* parameter from 18.482(3) Å to 18.314(3) Å, as determined by Rietveld refinement (Appendix Chapter IV. Table 1).

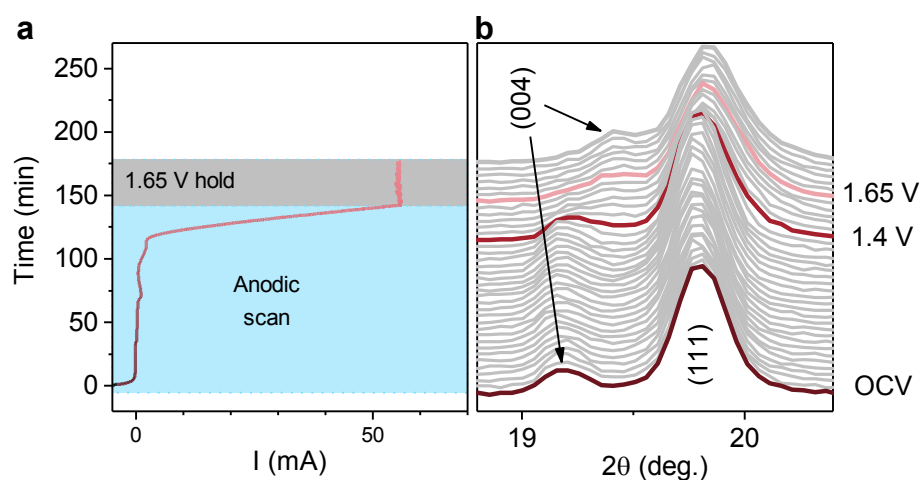


Figure IV.10 Oxidation process of β -H₂IrO₃. a) time dependence and b) structural evolution as characterized by *operando* XRD during OER with corresponding electrochemical curve $t = f(I)$.

IV-2-d Charge compensation during OER

Operando XAS measurements at the Ir L₃-edge using an *operando* cell shown in Appendix Chapter IV. Figure 6 were then performed to track down changes in bulk oxidation state of the protonated iridium catalyst during OER (Figure IV.11 a and b and Appendix Chapter IV. Figure 6). The experiment consists in stepping every five minutes the potential from open circuit voltage (OCV) to 1.65 V *vs.* RHE while monitoring for each step changes of the WL energy for the Ir L₃-edge. During this procedure, a shift of the WL position at higher energy is observed, indicative of the oxidation of the phase all along the capacitive region as well as when entering into the OER potential. Nevertheless, when resting the catalyst at the end of the anodic scan at 1.65 V *vs.* RHE, not only is the potential found to decay towards a value close to 1.3 V *vs.* RHE, but a continuous and slight shift of WL towards lower energy is recorded. This behavior is indicative of the reactivity of the intermediate phase generated at high potential (1.65 V *vs.* RHE) during OER which is slowly reduced when left in contact with the acidic solution via either proton insertion or decomposition, the former being the most likely owing to the evidence of structural transition as demonstrated above.

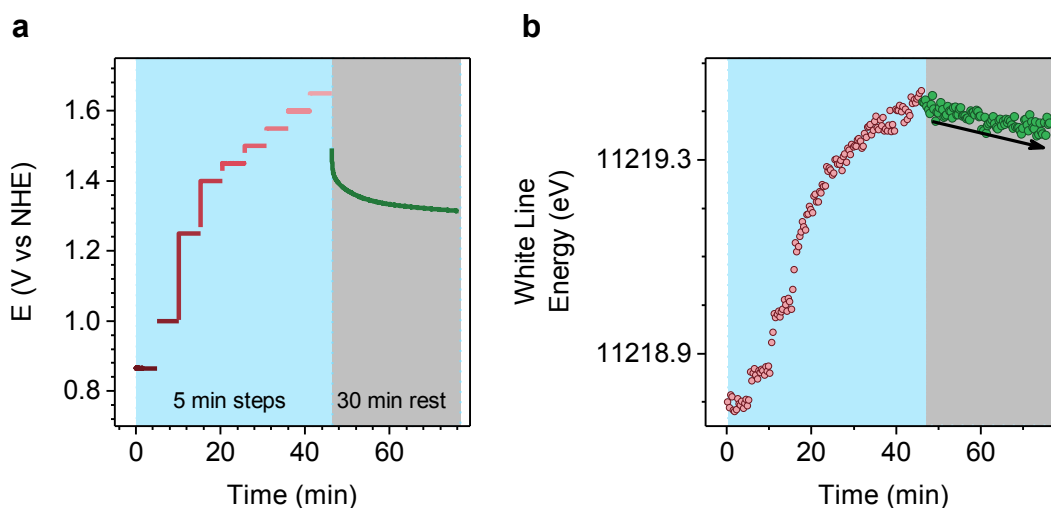


Figure IV.11 Oxidation process of $\beta\text{-H}_2\text{IrO}_3$. a) Applied potential steps during XAS measurement starting at OCV with the first three steps corresponding to the redox peak potentials and from 1.4 V to 1.65 V, the steps are evenly spaced by 50 mV. b) The evolution of the WL energy position of the Ir L₃-edge extracted from the *operando* XAS data.

These two measurements demonstrate that while the amorphous layer formed on the surface of β - H_2IrO_3 is certainly responsible for the electrocatalytic behavior of this new catalyst, the bulk participates to the overall charge balance process. Indeed, the β - H_2IrO_3 phase is gradually deprotonated and oxidized before reaching the OER potential. In fact, our *operando* measurements reveal that the bulk participates to the overall charge balance upon OER with proton diffusing in and out from the phase to counter balance the reactivity of the surface with water in acidic conditions.

In order to further understand the role of the iridate intermediates formed upon oxidation into the reactivity with water, we then carried out a study of different high valence iridates which will be described in the next section. Of particular interest is the reactivity and fate of IrO_3 previously described as the intermediate responsible for both the OER activity and the iridium dissolution upon oxidation.¹⁴⁸

IV-3 Reactivity of lithiated intermediates in acidic media

Recently, the high valence IrO_3 formed upon deprotonation/oxidation of amorphous hydrated iridium oxides was proposed to be the active phase for water to react, owing to the formation of electrophilic oxygen serving as active sites. The enhanced OER activity for iridium-based catalysts as well as their relative instability is attributed to the formation of such a reactive species.^{136,148–150} Indeed, the electrophilic oxygen species undergo nucleophilic attack from water to form O-O bonds which is usually considered to be the rate limiting step of the OER. Therefore, their formation was proposed to be at the origin for the high OER activity. Nevertheless, due to the reactivity of this high valence IrO_3 intermediate with water, it could never be isolated and its electrochemical properties studied independently, preventing us from designing new strategies in order to control its activity and stability.

IV-3-a Sample preparation

In order to probe the reactivity of the different lithiated intermediates which were described in the first chapter, electrochemical delithiation of β - Li_2IrO_3 in Li-ion half-cells in organic electrolytes containing no water was carried out in an argon filed dry box. As the material is a fairly good electronic conductor, this could be done without the addition of conductive carbon. Samples of composition $x = 1, 0.5$ and 0 with x in Li_xIrO_3

were obtained and thoroughly washed with dimethyl carbonate (DMC) and dried under vacuum in the antechamber for 30 minutes. The XRD patterns obtained using an airtight cell (described in the previous chapters for *operando* measurements) confirm that pure intermediates were obtained (Figure IV.12 c)).

IV-3-b *Ex situ* characterization

The Ir oxidation states of these phases was first studied by *ex situ* x-ray absorption spectroscopy (XAS) at the Ir L₃-edge (Figure IV.12 a with the corresponding spectra in Appendix Chapter IV. XANES spectra of the different *ex situ* samples before and after acid treatment. Figure 5). The measurements were carried out at the Soleil synchrotron's ROCK beamline with the help of A. Iadecola. As was discussed in Chapter II of this manuscript, while an increase of the WL energy would indicate the oxidation of iridium upon delithiation, as expected for a classical oxidation event counterbalanced by a cationic redox active center, we instead observed no increase of the WL energy which stays close to the one of Sr₂FeIrO₆ used as Ir⁵⁺ reference.¹⁵⁸ These XAS measurements at the Ir L-edge were then complemented by *ex situ* O 1s x-ray photoelectron (XPS) measurements (Figure IV.12 b), carried out by R. Dédryvère at the Université de Pau et des Pays de l'Adour, which show, in agreement with previous results, the formation of oxidized "O^{x-}" species after complete delithiation and the formation of β-IrO₃. These results indicate that the oxidation of β-Li₂IrO₃ is counterbalanced by the redox activity of the oxygen ligand to "O^{x-}" species for β-Li_yIrO₃ with y ≤ 1, following the so-called anionic redox mechanism discussed in previous chapters.

The reactivity of the different intermediates β-Li_yIrO₃ (with y = 1, 0.5 and 0) with water was then studied upon exposure to a 1M H₂SO₄ solution degassed several hours (t > 4h). Analyzing the *post mortem* samples by XRD (Figure IV.12 c)), β-IrO₃ and β-Li_{0.5}IrO₃ are found to be fully transformed into a new phase. Concomitantly, similar energies of the WL at the Ir L₃-edge and therefore similar oxidation states comprised between Ir⁵⁺ and Ir⁴⁺ (Ir⁴⁺O₂) were found after exposure to H₂SO₄ for these two samples (Figure IV.12 a), indicative of their spontaneous reduction when in contact with acidic media. Furthermore, this chemical reactivity is dependent on the oxidation state of the catalyst and β-Li₁IrO₃ was found by XRD to be only partially transformed into this new phase (Figure IV.12 c) while its oxidation state was found greater than the

one measured for β - IrO_3 and β - $\text{Li}_{0.5}\text{IrO}_3$ after soaking (Figure IV.12 a). Finally, XPS analysis shows after reacting β - IrO_3 with H_2SO_4 the apparition of a new O 1s peak at 531.4 eV which corresponds to the formation of OH^- species (Figure IV.12 b). While the presence of residual “ $\text{O}^{\text{n-}}$ ” oxygen cannot be excluded in IrO_3 after exposure to H_2SO_4 due to energy resolution of the spectrum, their overall weight has largely decreased upon protonation, suggesting their participation to the charge balance process.

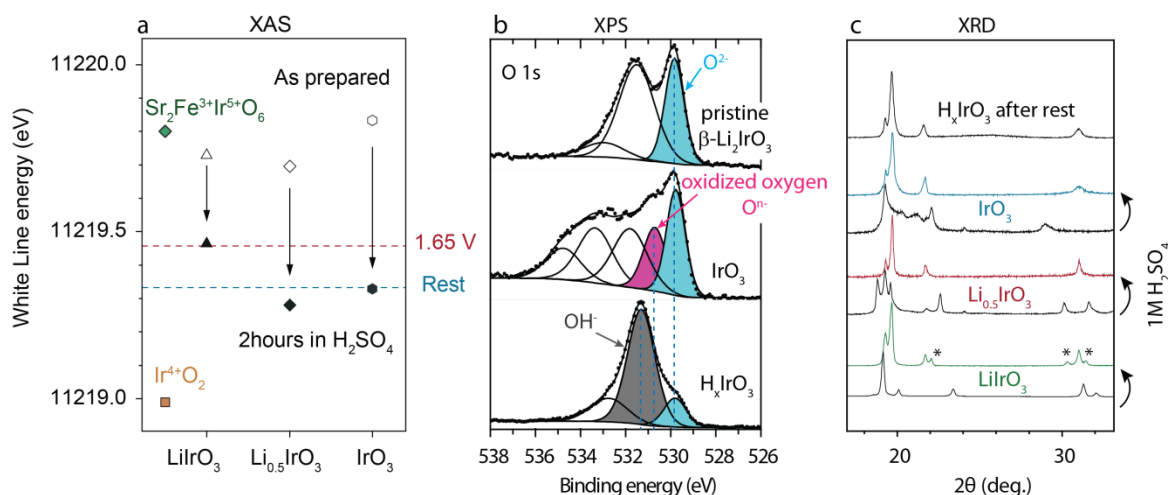


Figure IV.12 Chemical reactivity of oxidized β - Li_2IrO_3 with acid. a) Evolution of the WL energy position of the Ir L_3 -edge XAS for the different compounds before (open symbols) and after acid treatment (filled symbols). IrO_2 (orange square) and $\text{Sr}_2\text{FeIrO}_6$ (green diamond) are shown as references for $\text{Ir}^{+\text{IV}}$ and $\text{Ir}^{+\text{V}}$, respectively. b) O 1s X-ray photoelectron spectra with the pristine β - Li_2IrO_3 phase (top), the fully delithiated IrO_3 phase (middle) and IrO_3 after exposure to 1M H_2SO_4 solution (bottom). The stars indicate surface adsorbed or deposited species. Colored areas indicate oxygen atoms bound to iridium. In order to decrease the intensity of surface components, spectrum (b) was recorded with 6900 eV photon energy on the GALAXIES beamline at the SOLEIL synchrotron (multiplying the probe depth by 4.5). Other spectra were recorded with 1487 eV (standard XPS). c) XRD patterns for each compound before (black) and after acid treatment (colored line) compared to the XRD pattern collected after rest for β - H_xIrO_3 . The stars indicate peaks of a phase that remains partially lithiated.

While we observed a structural transformation for each intermediates when in contact with acidic solution, we then investigated if this transformation is accompanied by the oxidation of water and the evolution of O_2 . For this, on-line mass spectrometry was used and the results are described in the next section.

IV-3-c On-line Mass spectrometry

The reactivity of the samples to acidic media was probed *in situ* by online mass spectrometry (OMS) using a three electrode Swagelok cell body mounted with a stainless-steel plunger inserted into the bottom end on which the sample lies, a rubber stopper in order to inject the acidic solution through a needle on the side connection and finally a pressure sensor with a connection to a HIDEN H1 mass spectrometer system (HIDEN Analytical, UK) which continuously measured the relative amounts of gases present. Before injection of the acidic solution (degassed by bubbling Ar for 24 h), the cell was left to equilibrate at 25°C in a thermostatic chamber. Special care was brought to monitoring the evolution of masses $m = 40$ (Ar), 32 (O_2), 28 (N_2), 18 (H_2O), 16 (O) and 14 (N). This allowed us to follow the tightness of the cell and any evolution of oxygen during the experiment.

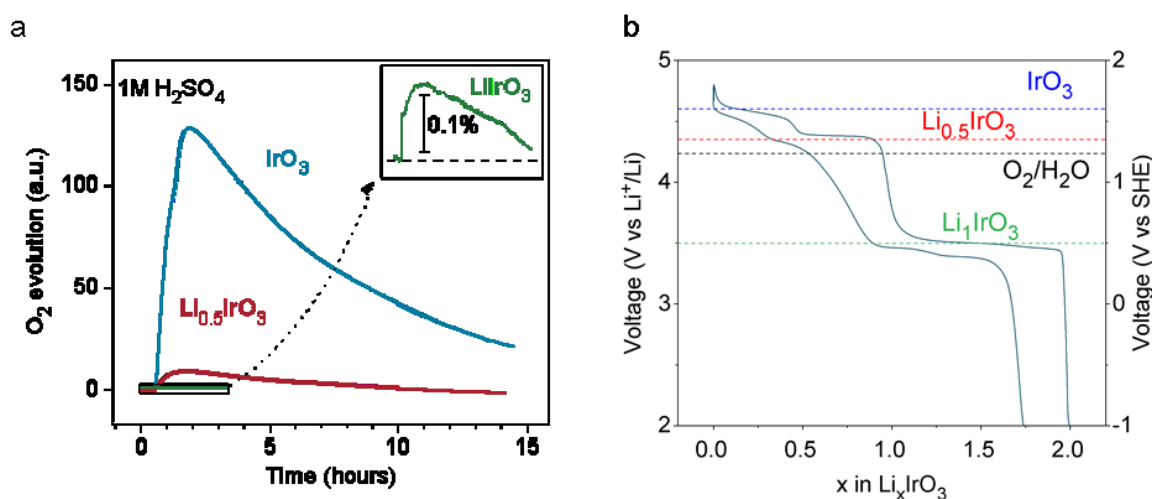


Figure IV.13 Reactivity of lithiated intermediates. a) On-line mass spectrometry signal for $m = 32$ normalized by $m = 40$ for each sample after injection of a 1M H_2SO_4 solution in the cell. b) The electrochemical charge/discharge curve of $\beta-Li_2IrO_3$ with the potentials for each intermediate in colored dashed lines and the oxidation potential of water in black dashed line.

The corresponding results are displayed in Figure IV.13 a) where the blue curve corresponds to IrO_3 , the red curve to $Li_{0.5}IrO_3$ and the green curve, also shown enlarged in the inset, to $LiIrO_3$. While the oxidized active form of the catalyst is reduced in contact with acid as discussed above, we could demonstrate using OMS that this reduction is concomitant with the oxidation of water. Indeed, when exposing $\beta-IrO_3$ and $\beta-Li_{0.5}IrO_3$ to 1M H_2SO_4 , gaseous oxygen is found to be chemically evolved (Figure

IV.13 a)). Interestingly, the amount of oxygen evolved is dependent on the oxidation state of the iridium oxide, with the more oxidized form of the catalyst (β -IrO₃) generating the most oxygen. Almost no oxygen is evolved when exposing β -LiIrO₃ to 1M H₂SO₄ solution.

These observations can be rationalized when looking at the voltage curve and observing that the redox potentials for the formation of β -IrO₃ and β -Li_{0.5}IrO₃ (respectively 4.55 and 4.4 V vs. Li⁺/Li) are above the reversible potential for water oxidation at pH 0 (4.27 V vs. Li⁺/Li, Figure IV.13 b). In contrast, the redox potential for β -Li₁IrO₃ is below the OER potential (3.4 V vs. Li⁺/Li, Figure IV.13 b) and therefore it does not chemically oxidize water. Hence, β -IrO₃ and β -Li_{0.5}IrO₃ are unstable in acidic conditions, therefore acting as an oxidizing agent while H₂O acts as a reducing agent, giving the overall reaction: IrO₃ + H₂O → H₂IrO₃ + ½ O₂. The amount of oxygen generated during this chemical redox reaction is governed by the oxidizing power of the iridium oxide, which is function of the oxidation state and the concentration of active form of the catalyst itself given by the amount of protons in the phase. In other words, the difference between the redox potential of the iridium oxide and E(O₂/H₂O) acts as the driving force for the water oxidation.

IV-3-d Stability

Bearing in mind that electrophilic “Oⁿ⁻” oxygen species were previously reported to be responsible for both the activity but also the instability of Ir-based oxides used as OER catalysts, we then measured by ICP-OES the amount of Ir-leached out during the chemical reactivity of each intermediates with a solution of 1 M H₂SO₄ (Figure IV.14 a). For the pristine β -Li₂IrO₃ compound, a negligible amount of Ir was found leached out during soaking in acid and this amount is found to increase when oxidizing the material from β -Li₂IrO₃ to β -IrO₃. Hence, combining these results with the OMS results previously discussed, we can confirm that the formation of electrophilic “Oⁿ⁻” oxygen species results into an increased reactivity of the surface and the dissolution of iridium.

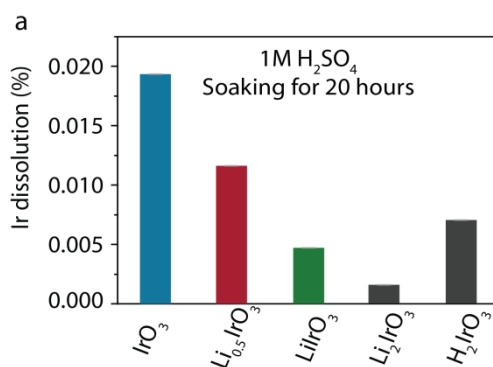


Figure IV.14 Chemical reactivity of oxidized $\beta\text{-Li}_2\text{IrO}_3$ with acid. a) Ir dissolution measured by ICP-OES after soaking the different intermediate phases in a solution of 1M H_2SO_4 .

In summary, electrophilic “ O^{n-} ” oxygen species are formed by the electrochemical oxidation of the iridium oxide catalyst before being consumed by the chemical reaction with H_2O leading to the formation of OH^- groups, as observed by XPS (Figure IV.12 b). This protonation reduces the oxidation state of the iridium oxide and reduces the dissolution of iridium, as the ICP-OES results reveal (Figure IV.14 a).

IV-3-e Operando XRD – $\beta\text{-Li}_2\text{IrO}_3$

In order to better understand the bulk phase transformation previously spotted by *ex situ* XRD (Figure IV.12 c), *operando* XRD was employed to monitor the electrochemical oxidation of $\beta\text{-Li}_2\text{IrO}_3$ in 1 M H_2SO_4 . Starting from $\beta\text{-Li}_2\text{IrO}_3$, several redox processes can be observed below the OER potential (below ≈ 1.55 V vs. RHE, Figure IV.15a). First, the pristine $\beta\text{-Li}_2\text{IrO}_3$ phase disappears below 1.4 V vs. RHE while a second set of peaks appears. This second phase then disappears between 1.4 and 1.65 V vs. RHE where a third one grows. Finally, when holding the electrode at 1.65 V for an hour, a fourth and final phase is completely formed. Analyzing the structural modifications, the second phase can be attributed to the $\beta\text{-LiIrO}_3$ phase, while the third phase does not correspond to the $\beta\text{-Li}_{0.5}\text{IrO}_3$ normally formed when oxidizing $\beta\text{-Li}_2\text{IrO}_3$ in organic electrolyte.⁹⁷ Finally, the last phase which grows when holding the electrode at 1.65 V vs. RHE is related to the protonated phase described in section 1 of this chapter. During the second scan, the oxidation events previously observed below the OER potential are drastically modified and resembles the electrochemistry of the $\beta\text{-H}_2\text{IrO}_3$ while the OER activity is found stable (Figure IV.15 a), indicating that a stable

regime is reached. Overall, this investigation reveals that the whole bulk of $\beta\text{-Li}_2\text{IrO}_3$ is transformed to a protonated phase concomitantly with the OER process.

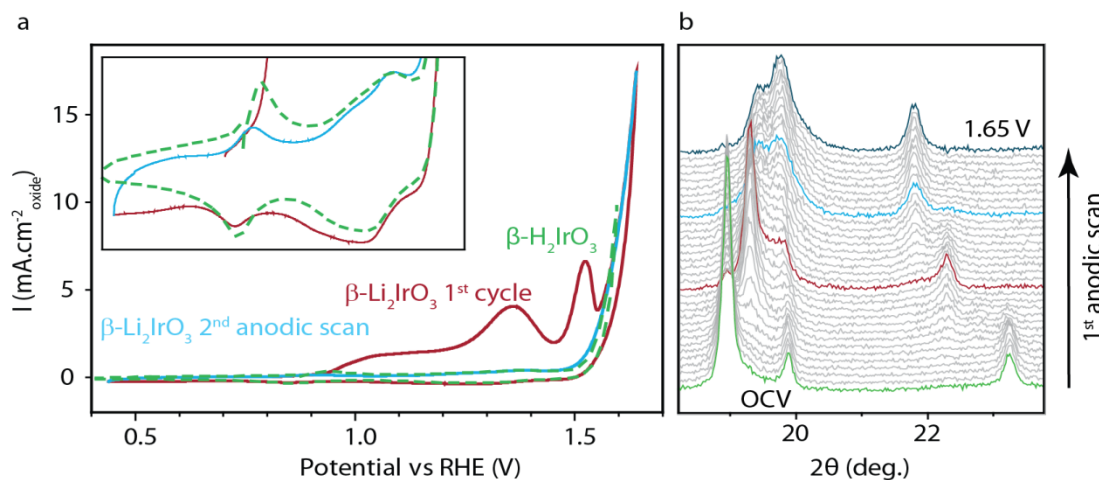


Figure IV.15 a) Cyclic voltammetry for the $\beta\text{-Li}_2\text{IrO}_3$ in 1 M H_2SO_4 (orange) with subsequent anodic scan (blue) compared to the cyclic voltammogram of the $\beta\text{-H}_2\text{IrO}_3$ catalyst (red). (b) The *operando* XRD under the same conditions on charge from $\beta\text{-Li}_2\text{IrO}_3$ to 1.65 V and holding.

IV-4 Proton insertion as charge compensation for stable OER catalysis

Altogether, these results highlight that an OER mechanism for which the bulk of the catalyst is involved into the reaction is possible for protonated iridium oxide. Indeed, upon anodic polarization corresponding to the OER conditions, the surface of the protonated iridium oxide is oxidized (deprotonated), as we uncovered by electrochemistry (Figure IV.5). As we previously described, this 3D iridium oxide possesses an electronic structure in which non-bonding O $2p$ levels are redox active and account for the charge balance upon delithiation for $y \leq 1.5$ in $\beta\text{-Li}_y\text{IrO}_3$.⁹⁷ The electrochemical extraction of protons from the material to the electrolyte raises the redox potential of the catalyst above that of water, thus creating a driving force for the surface to react with water. Second, upon reactivity with water, proton can diffuse back from the solution to the bulk of $\beta\text{-H}_y\text{IrO}_3$; this charge balance mechanism helps stabilize the catalyst and reduces the dissolution of iridium when compared to other iridium based oxides.

While we uncovered this mechanism for the β -H₂IrO₃ protonated catalyst, it is worth mentioning that this result is in line with observations previously made for state-of-the-art protonated IrO_x catalysts or for more complex oxides such as perovskites. Indeed, Minguzzi *et al.* previously observed by *operando* XAS for IrO_x a first oxidation event up to Ir⁵⁺ prior to reaching the OER potential, followed by a reduction of iridium when reaching a potential at which oxygen is generated in acidic environment.¹⁵⁹ Similar reduction of the iridium oxidation state below 4+ was also observed after the OER for La₂LiIrO₆, this reduction being accompanied by the formation of IrO_x-type particles.¹³⁶ This behavior contrasts with the one observed for the thermally prepared IrO₂ catalyst which is found more stable but less active than its protonated IrO_x counterpart.¹⁶⁰

Therefore, designing compounds with the ability to reversibly exchange protons can play a pivotal role in the development of active and stable OER catalysts in acid media. Nevertheless proton diffusion can be slow in some TM oxides. Hence, and to no surprise, the redox peaks observed for the initial delithiation of β -Li₂IrO₃ show greater intensities than those measured for the protonated β -H₂IrO₃ phase (Figure IV.15). This observation suggests that while sufficient to stabilize the mechanism and avoid iridium dissolution, the proton diffusion in this 3D oxide framework is rather slow when compared to the lithium diffusion. This is confirmed by ⁷Li and ¹H NMR spectroscopy which shows exchange between the two Li sites while the chemical exchange between some protons sites were found extremely slow (Appendix Chapter IV. Figure 2 and Appendix Chapter IV. Figure 3). With this in mind, strategies can be proposed in order to design basic oxides with an enhanced proton affinity for OER active surfaces. The first one is the partial substitution of iridium (or ruthenium) by less electronegative 3d TM to create two populations of oxygen: 1) the oxygen ions covalently bonded to iridium and serving as OER active sites and 2) the oxygen ions more ionically bonded to metal cations such as titanium or vanadium and thus more basic, i.e. prone to protonation. Bearing in mind that, following the proposed mechanism, two protons must be exchanged per Ir in order to preserve the charge neutrality of the oxide catalyst upon chemical OER, bulk diffusion such as the one found for the β -H₂IrO₃ phase should be privileged compared to surface protonation which would certainly limit both the activity and the stability of the catalyst. Hence, the wise selection of TM cations will not be

sufficient and it must be coupled with the use of adapted crystallographic structures in order to stabilize this mechanism.

IV-5 Conclusion

In this chapter, we have reported the synthesis of a new crystalline iridate by ion exchange and its characterization combining techniques such as TGA-MS, sXRD, NPD and XAS. The composition of the protonated phase was determined to be H_2IrO_3 with the hyperhoneycomb IrO_3 framework retained. While the compound is able to extract and insert protons reversibly, the kinetics is found relatively slow compared to $\text{H}_{3.4}\text{IrO}_4$. This is in part explained by the high potential at which protons are extracted at which water oxidation occurs. While this phase thus shows limited interest as proton insertion material, it does possess very interesting electrocatalytic properties which we have evaluated.

While the activity of this iridate is comparable to other iridates previously reported as OER catalysts, the compound was found to possess enhanced stability. The stability was assessed electrochemically by observing the retention of the faradaic processes below the OER potential region as well as the capacitive region, indicative that no major surface reconstruction occurred. These observations were confirmed by HRTEM and ICP-OES investigations showing remarkably low dissolution compared to SrIrO_3 so far considered as the stellar OER catalysts in acidic conditions.

We have also demonstrated by the isolation of the $\beta\text{-IrO}_3$ intermediate that the formation of a high valance iridium oxide intermediate is responsible for the high activity of iridium-based catalysts, as well as their limited stability. Coupling XAS and XPS spectroscopic techniques, we could observe that this activity/stability relationship is correlated to the formation of electrophilic “ $\text{O}^{\text{n-}}$ ” oxygen species which chemically react with water to generate gas, while being prone to dissolution, in agreement with previous discussions.^{136,161,148,149} Coupling these measurements with structural characterizations, we demonstrated that upon chemical reactivity with water, protons are inserted into the structure of this intermediate to form the protonated phase following the overall reaction $\text{IrO}_3 + \text{H}_2\text{O} \rightarrow \text{H}_2\text{IrO}_3 + \frac{1}{2} \text{O}_2$. We could further demonstrate that the bulk of this protonated phase is then redox active upon OER and that protons are continuously exchanged with the solution, thus regenerating the catalyst and keeping its

chemical integrity. Furthermore, this ability for the catalyst to accept protons by bulk insertion limits the dissolution of iridium cations which is usually encountered at high potential for iridium oxide OER catalysts. Finally, we believe that this discovery opens up new avenues for designing better and more stable OER catalysts for acidic environment by controlling 1) the protonation state of oxygen through a fine tuning of the iono-covalency of the metal-oxygen bond and 2) the bulk proton diffusivity with a wise choice of crystallographic structures.

General conclusions

This thesis is focused on the study of the hyperhoneycomb IrO_3 framework as a versatile host for Li^+ , Na^+ and H^+ . This flexibility coming from a tridimensional network of edge sharing IrO_6 octahedra is remarkable and presents a playground for the fundamental study of anionic redox processes in Li- and Na-rich materials for battery applications as well as during the oxygen evolution reaction on the surface of iridate catalysts. While the lithiated compound can be obtained by a two-step solid state reaction, the sodiated and hydrated phases could not be obtained directly and were synthesized either electrochemically by full delithiation before electrochemical sodiation or by ion exchange in sulfuric acid in hydrothermal conditions of $\beta\text{-Li}_2\text{IrO}_3$. The two resulting phases, $\beta\text{-Na}_{1.7}\text{IrO}_3$ and H_2IrO_3 , had never been reported prior to this study.

The electrochemical behavior of the $\beta\text{-Li}_2\text{IrO}_3$ is both very similar to the layered $\alpha\text{-Li}_2\text{IrO}_3$ polymorph and completely different. Indeed, both compounds seems to call upon Ir and O for charge compensation during extraction and insertion of Li^+ and the processes take place at very similar potentials. The main difference is that the β iridate can be fully delithiated and recover the pristine material whereas the α polymorph is limited to the extraction of 1.5 Li^+ . This limitation seems to be related to the phase changes during delithiation which hinder the total extraction of Li^+ . The tridimensional framework forbids such drastic structural changes and therefore allows the formation of a crystalline IrO_3 phase. This phase was not previously reported due to its high reactivity with humidity. While the structural transitions during delithiation are numerous, they seem to be very reversible with however, the issues related to high potential cycling. We have shown that the processes that take place at high voltage are associated predominantly to anionic redox, as determined by XAS and HAXPES. These processes seem to entail large amounts of structural strain and long range disorder with namely a shortening of the coherent domains as evidenced by synchrotron XRD. Unfortunately, this has repercussions on the long-term cycling performances as it leads to a slow voltage decay and loss of the staircase profile.

The sodiation process of IrO_3 is fairly simple with only four main processes which resemble the lithiation at a lower overall potential. However, the desodiation is

limited to around 0.8 Na^+ contrary to the lithiated phase. The oxygen is active during both charge and discharge as evidenced by XPS on the O 1s peak. This new compound is shown to be quite stable at high temperature which suggests a thermodynamically stable structure with a formation energy close to that of the layered counterpart. However, the inability to synthesize the material by solid state chemistry could be linked to the decomposition of the material at a lower temperature than that necessary to its formation. Indeed, at high temperature, the material decomposes to form Ir and most likely Na_2O . This could be solved by finding an alternative to high temperature synthesis to obtain different polymorphs. The structure/property relationship is of great consequence to the field of energy storage and could allow the discovery of materials with superior performances. However, it is evidenced here that what is understood for Li-ion insertion cannot simply be transposed to the Na-ion field. In the present case, increasing the dimensionality comes at a cost and leads to inferior performances.

In this work, the anionic redox activity has been probed directly by XPS and HAXPES and indirectly by the Ir L_{III} Edge XANES data. While many examples have been given to validate these techniques, there is still much debate around the true nature of the anionic species formed during these redox processes. Recently, resonant inelastic X-ray spectroscopy (RIXS) has been suggested as a reliable technique to investigate the presence of anionic redox in several known materials.¹⁶² Indeed, while the oxygen K-edge spectra oxygen active materials have been thoroughly studied, the overwhelming contribution of the M-O orbitals to the signal makes an unambiguous attribution questionable.¹⁶³ RIXS allows the separation of the different processes that arise at one excitation energy but have different emission energies, i.e. different amounts of energy lost, similarly to electron energy loss spectroscopy (EELS). It is claimed that a 2p-2p intraband exciton leads to a sharp peak at an emission energy of 523.7 eV which is only possible if holes are present in pure non-bonding 2p orbitals.¹⁶² While this is a reasonable explanation, it is still uncertain if the absence of such a peak necessarily means the absence of holes on oxygen type orbitals. This returns the question of the nature of anionic redox and its ubiquity. It is conceivable that the participation of oxygen to the redox processes during delithiation might take place in different manners depending on the structure and composition of the materials.

A recent review of the different possible mechanisms by which lattice oxygen can participate in charge compensation and their implications on the electronic structure and stability of high energy density cathode materials, nicely describes this issue.⁵⁹ The covalency of the M-O bond is of great importance in the determination of the redox process since it will dictate the orbital mixing and relative contributions of each element to the electronic structure. In more ionic cases such as 3d TM oxides, it can be expected that the TM-O antibonding states, localized mainly on the TM, will first be emptied completely, leaving the O 2p non-bonding levels next in line for oxidation. This mechanism generally tends towards irreversible loss of oxygen and structure densification by cationic migrations. However, increasing the covalency such as in the ruthenates or better even in the iridates leads to a possible mixing of the O 2p non-bonding levels with the antibonding TM-O levels accompanied by a distortion of the MO₆ octahedra to form peroxo-like species and TM(O-O) bonding and antibonding states. The withdrawal of electrons from these states results in the formation of oxygen type holes and is therefore enabled by a form of anionic redox with minimal oxygen loss and structural degradations. This second mechanism would not result in a sharp peak in the RIXS spectra due to the formation of hybridized states and therefore the absence of possible 2p-2p intraband excitons. Although this is more of a cautionary remark, it is also a possible explanation to a recent paper stating that the layered iridate does not present any sign of anionic redox based on RIXS data.¹⁰⁸ It is crucial to develop a robust theoretical foundation which could unambiguously explain the appearance of this signal and its relation to what is known as anionic redox activity. The debate is clearly still open.

There is still much to understand about the interactions between cations and anions in oxides and the implications of structure or composition on the electrochemical performances of insertion materials. Anionic redox, while a promising direction for increasing energy density of cathode materials, still has major intrinsic drawbacks which must be addressed in order to make use of the Li-rich materials. This thesis evidences the structural strains induced by large amounts of anionic participation and its effects on the cycling performances of a tridimensional structure. This structure has remarkable properties but it still suffers from performance decay although the Ir-O bond is highly covalent compared to 3d TM. This work also highlights the importance of structure on

the performances of materials and the importance of exploring polymorphism by low temperature conditions allowing the synthesis of metastable phases.

Finally, anionic redox has long been studied in the field of catalysis with namely pure oxygen redox as counter reaction for hydrogen production. Indeed, the oxygen evolution reaction is of great importance to the hydrogen economy as it is the counter reaction in water splitting and requires large overpotentials due to its sluggish kinetics. Iridates are widely studied for OER in acidic media but due to the reactivity of the intermediates, they could never be isolated and studied. Thanks to the β - Li_2IrO_3 phase which can be fully delithiated, IrO_3 and its reactivity could be assessed and a new hydrated crystalline iridate could be synthesized. This has proven valuable to the comprehension of the charge compensation mechanism during OER on the surface of iridates in acidic media. Indeed, the bulk protonation and deprotonation allows the formation of a stable high valence iridate which can chemically react with water to form oxygen and insert protons to stabilize the structure. This was inspired by observations made on the layered iridate in alkaline solution for which potassium intercalation counterintuitively seems to increase the activity while stabilizing the structure. Preliminary work on LiCoO_2 in alkaline media has also shown a strong cation dependency and the formation of a K_xCoO_2 phase after going to OER potential as evidence by *ex situ* XRD measurements. As insertion chemistry is not well known in the field of catalysis, the bulk properties of the catalysts studied thus far seems to have been widely overlooked. More work on the charge compensation mechanism, the activity/stability relationship and the role of cations must be carried out to fully elucidate these surprising observations.

Appendix

Appendix – Chapter II

Methods

Electrochemistry

For electrochemical testing, the powders were cast into free-standing Bellcore-type electrodes by a methodology described previously.^{13,36} To obtain a good signal-to-noise ratio at the Ir L_{III}-edge, the active material loading in the electrode was set to $\sim 6 \text{ mg}\cdot\text{cm}^{-2}$. Circular discs of $\sim 7 \text{ mm}$ in diameter were used in each cell. The cycling was carried out using two electrode Swagelok type cells with a lithium counter electrode separated from the working electrode by two layers of Whatman GF/D borosilicate glass fiber sheets soaked with a mixture of ethylene carbonate (EC), propylene carbonate (PC) and dimethyl carbonate (DMC) in a 1/1/3 weight ratio containing 1 M lithium hexafluorophosphate (LiPF₆) as electrolyte. The cells were assembled in an Ar-filled glovebox and were cycled at a C/5 rate (1 Li⁺ eq. removed in 5h) if not specified otherwise.

HAXPES

For photoemission measurements, the electrodes were prepared by mixing the pristine material with 20 wt% carbon Super-P by ball-milling for 20 min prior to cycling, in order to avoid the polymer binder disturbing the analyses. Hard X-ray photoemission spectroscopy (HAXPES) was carried out at the GALAXIES^{37,38} beamline of SOLEIL synchrotron with $h\nu = 6.9 \text{ keV}$ photon energy (third order reflection of the Si(111) double-crystal monochromator). Photoelectrons were analyzed by a SCIENTA EW4000 spectrometer, and the obtained energy resolution from the Au Fermi edge was 0.14 eV. No charge neutralizer was used. The analysis chamber pressure was maintained around 10^{-8} mbar during the measurements. The binding energy scale was calibrated by comparison with the in-house XPS spectra carried out on the same samples.

XAS

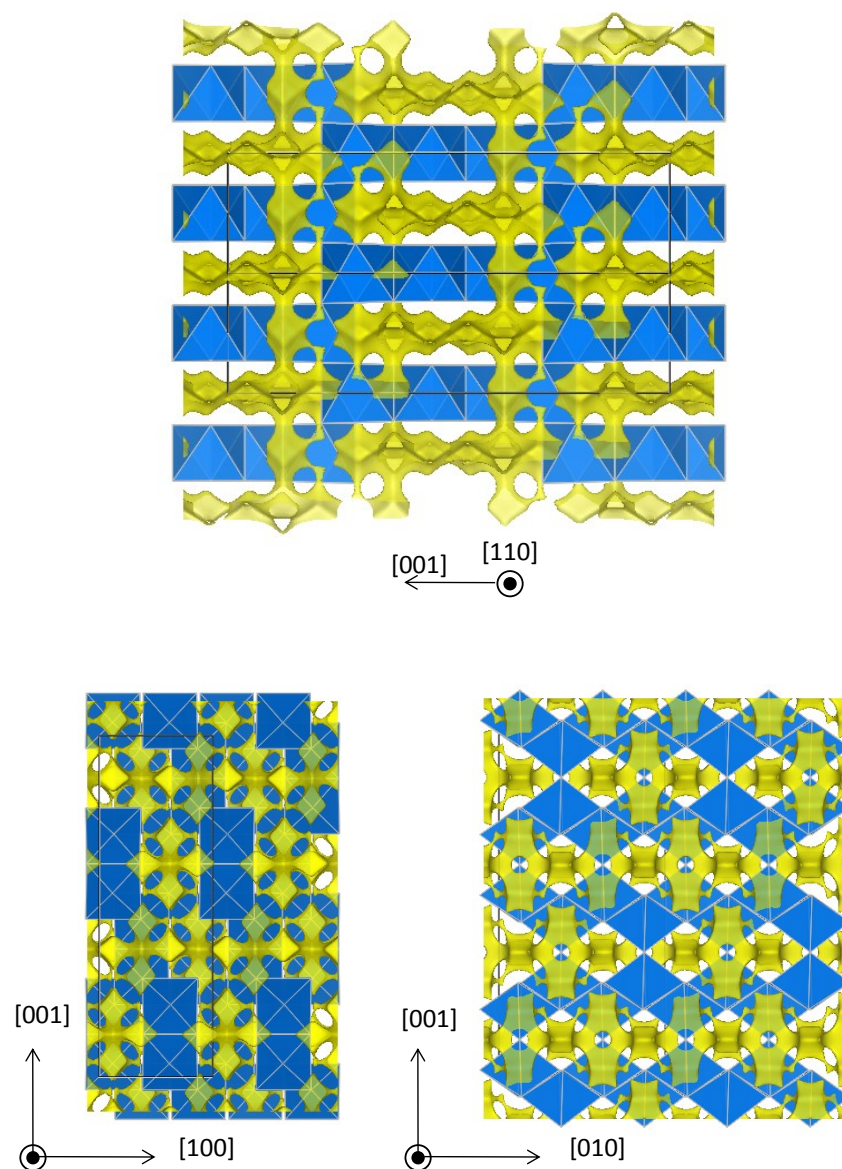
Ex situ XAS measurements at the Iridium L_{III}-edge were carried out in transmission mode at the ROCK beamline at the SOLEIL synchrotron in France.³⁹ A Si (111) channel-cut quick-XAS monochromator with an energy resolution of 2 eV at 11 keV was used. The intensity of the monochromatic X-ray beam was measured by three consecutive ionization detectors. The *ex situ* samples were prepared as described in the electrochemical section and never exposed to air nor moisture as described before.³³ *Operando* XAS spectra were collected continuously at a rate of 2 Hz and averaged out over periods of 20 seconds. The energy calibration was established with simultaneous absorption measurements on Iridium metal foil placed between the second and the third ionization chamber. The data was treated using the python routine described elsewhere for energy calibration and normalization.⁴⁰ The white line (WL) energy position was obtained as the zero of the first derivative of the XAS spectrum. The WL area was obtained by integrating the peak after subtracting an arctangent background as reported in our previous paper [20]. The fitting of the EXAFS oscillations was carried out using the Demeter package. The EXAFS oscillations were extracted at the Ir L₃-edge and weighted by k^3 in the k range [3.7 \AA^{-1} - 15.9 \AA^{-1}]. The back-Fourier transform was done in the R -range [1 \AA - 3.3 \AA]. All parameters except the radial distances R_i and the mean-square relative displacements σ_i^2 were fixed during the fitting procedure ($S_0^2 = 0.8$, $N_{\text{Ir}} = 3$, $N_{\text{O1}} = 6$, $N_{\text{O2}} = 24$). The value of E_0 was checked for each sample.

Diffraction

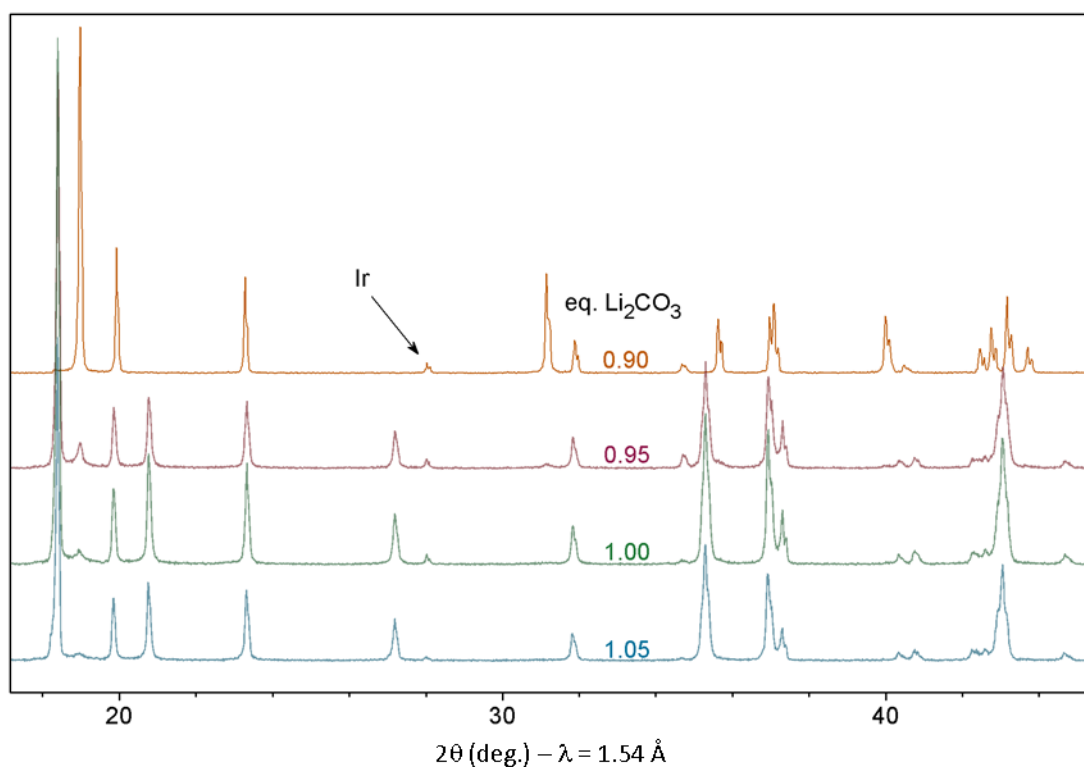
Operando X-ray powder diffraction (XRD) measurements were carried out using an airtight electrochemical cell equipped with a Be window.¹¹² Synchrotron XRD measurements were performed on the materials science and powder diffraction beamline (MSPD) at Alba synchrotron, with a wavelength of 0.412 \AA .¹¹⁴

Neutron powder diffraction (NPD) patterns for the sample at $x = 0.5$ and 2.5 were measured on the D1B High resolution neutron two-axis powder diffractometer at the Laue-Langevin Institute, with a wavelength of 1.288 \AA .

Figures



Appendix Chapter II. Figure 1 Visualization of the Li diffusion paths in $\beta\text{-Li}_2\text{IrO}_3$ (yellow domains), via the bond valence energy landscape approach.¹⁶⁸ The value chosen for the plot is 2.3 eV above the minimum energy. IrO_6 octahedra are colored in blue.



Appendix Chapter II. Figure 2 Synthesis optimization. XRD patterns of powder after annealing with different equivalents of Li_2CO_3 . The bottom pattern corresponds to the α polymorph whereas the top pattern corresponds to the β polymorph.

Appendix Chapter II. Table 1 Space group and unit cell parameters of the $\beta\text{-Li}_x\text{IrO}_3$ ($x = 2, 1.5, 1, 0.5$ and 0) phases as obtained from Rietveld refinement of the *operando* synchrotron X-ray powder diffraction data.

Composition	Space group	a (Å)	b (Å)	c (Å)	θ (°)	Vol (Å ³)
Li_2IrO_3	$Fddd$	5.90709(7)	8.45673(9)	17.82779(16)	90	890.581(16)
$\text{Li}_{1.5}\text{IrO}_3$	$Fddd$	5.8279(3)	8.6685(4)	17.7380(9)	90	896.11(7)
Li_1IrO_3	$Fddd$	5.61885(6)	8.87546(9)	17.8926(3)	90	892.300(18)
$\text{Li}_{0.85}\text{IrO}_3$	$Fddd$	5.69115(15)	8.77962(17)	18.0435(4)	90	901.50(4)
$\text{Li}_{0.5}\text{IrO}_3$	$C2/c$	5.73738(20)	8.71946(19)	9.36504(18)	104.6815(14)	453.207(20)
IrO_3	$C2/c$	5.3493(4)	9.0662(3)	8.7203(4)	93.200(5)	422.26(4)
	$C2/c$	5.2822(4)	9.1414(4)	8.8473(5)	94.882(7)	425.66(4)

Appendix Chapter II. Table 2 Crystallographic data and atomic positions of β -Li₂IrO₃ determined from Rietveld refinement of the *operando* synchrotron X-ray powder diffraction data. B_{iso} was fixed to 1 for Li.

β -Li ₂ IrO ₃						
Space group $Fddd$		$R_{\text{Bragg}} = 6.83 \%$		$\chi^2 = 10.91$		
$a = 5.90709(7) \text{ \AA}$		$b = 8.45673(9) \text{ \AA}$	$c = 17.82779(16) \text{ \AA}$	$V = 890.581(16) \text{ \AA}^3$		
Atom	Wyckoff position	x/a	y/b	z/c	Occupancy	$B (\text{\AA}^2)$
Ir	16g	1/8	1/8	0.70824(8)	1	0.38(2)
Li1	16g	1/8	1/8	0.04167	1	1
Li2	16g	1/8	1/8	0.875	1	1
O1	16e	0.850(4)	1/8	1/8	1	0.64(14)
O2	32h	0.647(4)	0.3644(11)	0.0372(6)	1	0.64(14)

Appendix Chapter II. Table 3 Crystallographic data and atomic positions of β -Li_{1.5}IrO₃ determined from Rietveld refinement of the *operando* synchrotron X-ray powder diffraction data. B_{iso} was fixed to 1 for O and Li.

β -Li _{1.5} IrO ₃						
Space group $Fddd$		$R_{\text{Bragg}} = 5.12 \%$		$\chi^2 = 9.83$		
$a = 5.8279(3) \text{ \AA}$		$b = 8.6685(4) \text{ \AA}$	$c = 17.7380(9) \text{ \AA}$	$V = 896.11(7) \text{ \AA}^3$		
Atom	Wyckoff position	x/a	y/b	z/c	Occupancy	$B (\text{\AA}^2)$
Ir	16g	1/8	1/8	0.70824(8)	1	0.38(2)
Li1	16g	1/8	1/8	0.04167	0.75	1
Li2	16g	1/8	1/8	0.875	0.75	1
O1	16e	0.850	1/8	1/8	1	1
O2	32h	0.647	0.3644	0.0372	1	1

Appendix Chapter II. Table 4 Crystallographic data and atomic positions of β -LiIrO₃ determined from Rietveld refinement of the *operando* synchrotron X-ray powder diffraction data. B_{iso} was fixed to 1 for O and Li.

β -LiIrO ₃						
Space group $Fddd$		$R_{\text{Bragg}} = 5.96 \%$		$\chi^2 = 12.1$		
$a = 5.61885(6) \text{ \AA}$		$b = 8.87546(9) \text{ \AA}$	$c = 17.8926(3) \text{ \AA}$	$V = 892.300(18) \text{ \AA}^3$		
Atom	Wyckoff position	x/a	y/b	z/c	Occupancy	$B (\text{\AA}^2)$
Ir	16g	1/8	1/8	0.70892(9)	1	0.50(2)
Li3	16g	1/8	0.973200	1/8	1	1
O1	16e	0.8566	1/8	1/8	1	1
O2	32h	0.6288	0.34651	0.03538	1	1

Appendix Chapter II. Table 5 Crystallographic data and atomic positions of β -Li_{0.85}IrO₃ determined from Rietveld refinement of the *operando* synchrotron X-ray powder diffraction data. B_{iso} was fixed to 1 for O and Li.

β -Li _{0.85} IrO ₃						
Space group $Fddd$		$R_{\text{Bragg}} = 8.74 \%$		$\chi^2 = 14.8$		
$a = 5.69115(15) \text{ \AA}$		$b = 8.77962(17) \text{ \AA}$	$c = 18.0435(4) \text{ \AA}$	$V = 901.50(4) \text{ \AA}^3$		
Atom	Wyckoff position	x/a	y/b	z/c	Occupancy	B (\AA^2)
Ir	16g	1/8	1/8	0.70788(10)	1	0.77(4)
Li3	16g	1/8	0.973200	1/8	0.85	1
O1	16e	0.8566	1/8	1/8	1	1
O2	32h	0.6288	0.34651	0.03538	1	1

Appendix Chapter II. Table 6 Crystallographic data and atomic positions of β -Li_{0.5}IrO₃ determined from Rietveld refinement of the *operando* synchrotron X-ray powder diffraction data. B_{iso} was fixed to 1 for O and Li.

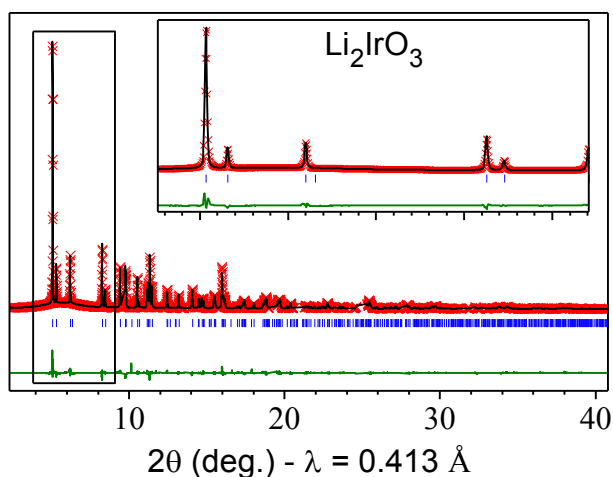
β -Li _{0.5} IrO ₃						
Space group $C2/c$		$R_{\text{Bragg}} = 5.89 \%$		$\chi^2 = 10.00$		
$a = 5.73738(20) \text{ \AA}$		$b = 8.71946(19) \text{ \AA}$	$c = 9.36504(18) \text{ \AA}$	$\beta = 104.6815(14)^\circ$	$V = 453.207(20) \text{ \AA}^3$	
Atom	Wyckoff position	x/a	y/b	z/c	Occupancy	B (\AA^2)
Ir	8f	0.0814(3)	0.3706(2)	0.41577(19)	1	0.46(3)
Li3b	4c	0.5	0.771910	0.75	1	1
O1	8f	0.208060	0.365940	0.245430	1	1
O2	8f	0.412510	0.094730	0.076140	1	1
O3	8f	0.094880	0.151200	0.449710	1	1

Appendix Chapter II. Table 7 Crystallographic data and atomic positions of β -IrO₃ phase 1 determined from Rietveld refinement of the *operando* synchrotron X-ray powder diffraction data. B_{iso} was fixed to 1 for O and constrained for Ir to be equal to that of Ir in the second phase.

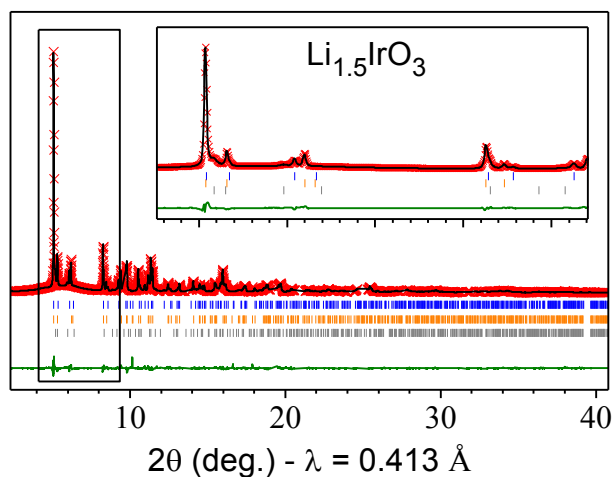
β -IrO ₃ phase 1						
Space group $C2/c$		$R_{\text{Bragg}} = 6.56 \%$		$\chi^2 = 4.29$		
$a = 5.3493(4) \text{ \AA}$		$b = 9.0662(3) \text{ \AA}$	$c = 8.7203(4) \text{ \AA}$	$\beta = 93.200(5)^\circ$	$V = 422.26(4) \text{ \AA}^3$	
Atom	Wyckoff position	x/a	y/b	z/c	Occupancy	B (\AA^2)
Ir	8f	0.0883(7)	0.3645(3)	0.4171(3)	1	1.060(13)
O1	8f	0.208060	0.365940	0.245430	1	1
O2	8f	0.412510	0.094730	0.076140	1	1
O3	8f	0.094880	0.151200	0.449710	1	1

Appendix Chapter II. Table 8 Crystallographic data and atomic positions of β - IrO_3 phase 2 determined from Rietveld refinement of the *operando* synchrotron X-ray powder diffraction data. B_{iso} was fixed to 1 for O and constrained for Ir to be equal to that of Ir in the first phase.

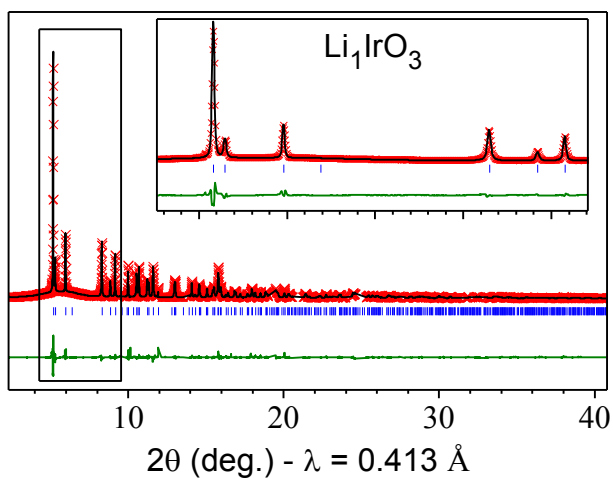
β - IrO_3 phase 2						
Space group $C2/c$		$R_{\text{Bragg}} = 4.53 \%$		$\chi^2 = 4.29$		
$a = 5.2822(4) \text{ \AA}$		$b = 9.1414(4) \text{ \AA}$	$c = 8.8473(5) \text{ \AA}$	$\beta = 94.882(7)^\circ$	$V = 425.66(4) \text{ \AA}^3$	
Atom	Wyckoff position	x/a	y/b	z/c	Occupancy	$B (\text{\AA}^2)$
Ir	$8f$	0.0720(9)	0.3697(5)	0.4231(4)	1	1.060(13)
O1	$8f$	0.208060	0.365940	0.245430	1	1
O2	$8f$	0.412510	0.094730	0.076140	1	1
O3	$8f$	0.094880	0.151200	0.449710	1	1



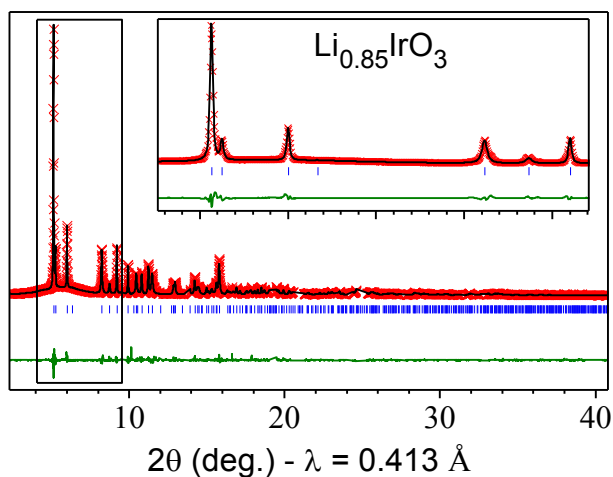
Appendix Chapter II. Figure 3 Rietveld refinement of the *in situ* synchrotron X-ray powder diffraction patterns for β - Li_2IrO_3 . In red are the experimental points, in black is the calculated pattern and in green is the difference between the experimental and calculated patterns. The vertical blue ticks beneath the pattern indicate the positions of the Bragg reflections.



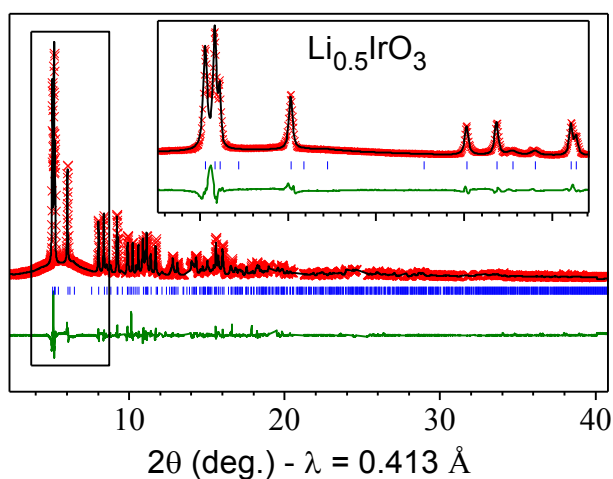
Appendix Chapter II. Figure 4 Rietveld refinement of the *in situ* synchrotron X-ray powder diffraction patterns for β - $\text{Li}_{1.5}\text{IrO}_3$. In red are the experimental points, in black is the calculated pattern and in green is the difference between the experimental and calculated patterns. The vertical blue ticks beneath the pattern indicate the positions of the Bragg reflections. This refinement was carried out using three phases of composition $x = 2, 1.5$ and 1 which are shown by the blue, orange and grey ticks respectively.



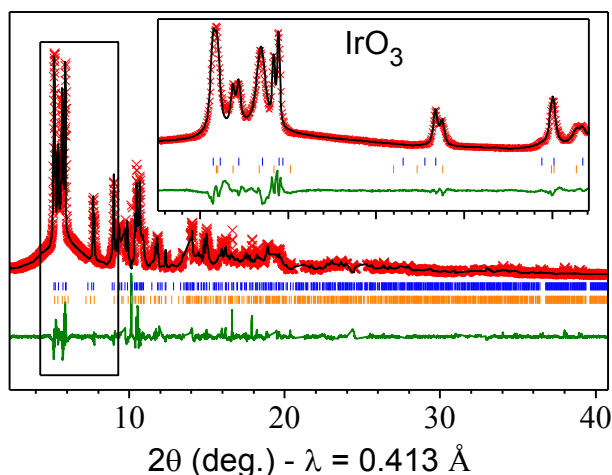
Appendix Chapter II. Figure 5 Rietveld refinement of the *in situ* synchrotron X-ray powder diffraction patterns for β - Li_1IrO_3 . In red are the experimental points, in black is the calculated pattern and in green is the difference between the experimental and calculated patterns. The vertical blue ticks beneath the pattern indicate the positions of the Bragg reflections.



Appendix Chapter II. Figure 6 Rietveld refinement of the *in situ* synchrotron X-ray powder diffraction patterns for $\beta\text{-Li}_{0.5}\text{IrO}_3$. In red are the experimental points, in black is the calculated pattern and in green is the difference between the experimental and calculated patterns. The vertical blue ticks beneath the pattern indicate the positions of the Bragg reflections.



Appendix Chapter II. Figure 7 Rietveld refinement of the *in situ* synchrotron X-ray powder diffraction patterns for $\beta\text{-Li}_{0.35}\text{IrO}_3$. In red are the experimental points, in black is the calculated pattern and in green is the difference between the experimental and calculated patterns. The vertical blue ticks beneath the pattern indicate the positions of the Bragg reflections.



Appendix Chapter II. Figure 8 Rietveld refinement of the *in situ* synchrotron X-ray powder diffraction patterns for β - IrO_3 which was only obtained as a mixture of two phases of compositions $x = 0.35$ and 0, in orange and blue respectively. In red are the experimental points, in black is the calculated pattern and in green is the difference between the experimental and calculated patterns. The vertical blue ticks beneath the pattern indicate the positions of the Bragg reflections. The blue and orange ticks correspond to the phases 2 and 1 respectively.

Appendix Chapter II. Table 9 Fitting results of EXAFS measured on ex situ samples at different lithium contents for β - Li_2IrO_3 .

x	IrO_6 (first shell)			IrIr_3 (second shell)			Calculated O-O distance (Å)
	CN	R (Å)	σ^2 (Å ²)	CN	R (Å)	σ^2 (Å ²)	
2.5	6	2.054 (2)	0.0033 (2)	3	3.047 (4)	0.0068 (3)	2.754 (4) R-factor = 0.0118
2	6	2.033 (1)	0.0024 (1)	3	2.998 (1)	0.00291 (8)	2.746 (2) R-factor = 0.0031
1.5	6	2.006 (2)	0.0030 (2)	3	3.010 (1)	0.0035 (1)	2.652 (2) R-factor = 0.0040
1	6	1.968 (2)	0.0026 (2)	3	3.018 (2)	0.0026 (1)	2.528 (3) R-factor = 0.0077
0.5	6	1.958 (1)	0.0039 (5)	3	3.034 (3)	0.0043 (3)	2.476 (3) R-factor = 0.0160
0	6	1.930 (2)	0.005 (2)	3	3.030 (2)	0.0053 (2)	2.391 (3) R-factor = 0.0164

Appendix – Chapter III

Methods

Synthesis

β -Na_{1.7}IrO₃ was obtained by a two-step electrochemical process. The first is the total delithiation of β -Li₂IrO₃ to obtain IrO₃. This is done by charging the powder vs Li metal in a Swagelok type cell using 1M lithium hexafluorophosphate (LiPF₆) in ethylene carbonate/propylene carbonate/dimethyl carbonate (EC/PC/DMC) in a 1/1/3 ratio as electrolyte and a Whatman GF/D borosilicate glass fiber membrane as electronic separator. The IrO₃ powder is then retrieved and thoroughly washed with DMC and dried under vacuum. The second step is the electrochemical sodiation of IrO₃ to obtain β -Na_{1.7}IrO₃. Similarly to the first step, this is done by discharging the IrO₃ powder vs Na metal in a Swagelok type cell using 1M sodium hexafluorophosphate (NaPF₆) in PC as electrolyte and the same glass fiber separator as previous step. The powder is then retrieved and thoroughly washed with DMC and dried under vacuum.

Electrochemistry

Electrochemical testing was done in Swagelok or 2032 type coin cells as specified, using Na_{1.7}IrO₃ mixed with 10% carbon super P as positive electrode and either Na metal or hard carbon as negative electrode. A Whatman GF/D borosilicate glass fiber membrane soaked with 1M NaPF₆ in PC was used as separator and electrolyte. For half cells, 1% fluoroethylene carbonate (FEC) was used as electrolyte additive. The cells were assembled in an Ar-filled glovebox and were cycled at a rate of C/10 (1 Na⁺ removed in 10h) if not specified otherwise.

X-ray Diffraction

Operando and *ex situ* XRD measurements were performed at ALBA synchrotron's MSPD beamline¹¹⁴ with a wavelength of 0.4122 Å and in a BRUKER D8 Advance diffractometer with Cu K α radiation ($\lambda_{K\alpha 1} = 1.540$ Å, $\lambda_{K\alpha 2} = 1.544$ Å) using a home designed cell equipped with beryllium windows.¹¹² For the pristine β -Na_{1.7}IrO₃

sample, the XRD pattern was collected at the MSPD beamline using a sealed quartz capillary (prepared in an Ar-filled glovebox) inserted in a 0.3 mm Kapton capillary.

X-ray Photoelectron Spectroscopy

XPS measurements were carried out with a Kratos Axis Ultra spectrometer, using focused monochromatic Al K α radiation ($h\nu = 1486.6$ eV). The analyzed area of the samples was $300 \times 700 \mu\text{m}^2$ and peaks were recorded with constant pass energy of 20 eV. Under the recording conditions, the Ag 3d $_{5/2}$ line appeared at 368.3 eV and its full width at half-maximum (FWHM) was 0.58 eV. The pressure in the analysis chamber was around 5×10^{-9} mbar. Short acquisition time spectra were recorded before and after each normal experiment to check that the samples did not suffer from degradation during the measurements. The binding energy scale was calibrated using the C 1s peak at 285.0 eV from the hydrocarbon contamination invariably present. To avoid any error on the calibration choice and for more precision, binding energy difference between the O1s lattice and metal core peaks was also examined. Core peaks were analyzed using a nonlinear Shirley-type background¹⁶⁹. The peak positions and areas were optimized by a weighted least-squares fitting method using 70% Gaussian, 30% Lorentzian line shapes. Quantification was performed on the basis of Scofield's relative sensitivity factors.¹⁷⁰ The curves fit for core peaks were obtained using a minimum number of components in order to fit the experimental curves. The XPS spectrometer was directly connected through a transfer chamber to an argon dry box in which the samples are handled, in order to avoid moisture/air exposure of the samples.

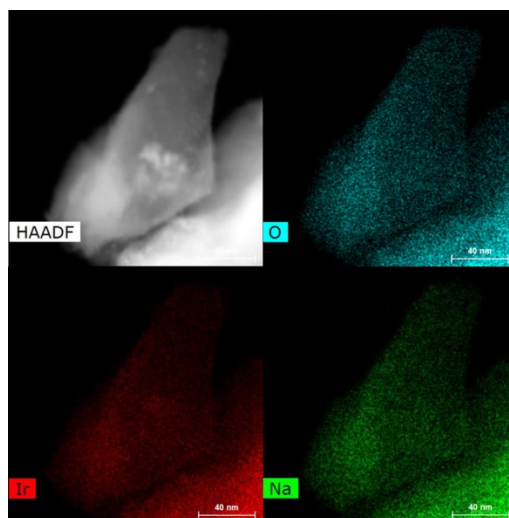
Scanning Transmission Electron Microscopy

The samples were prepared by dipping a Cu TEM grid covered with a holey carbon layer in the powder. No solvent was used. A Gatan vacuum transfer holder was used to protect the specimen from air. The TEM study was performed at a FEI Titan³ cubed microscope operated at 300 kV.

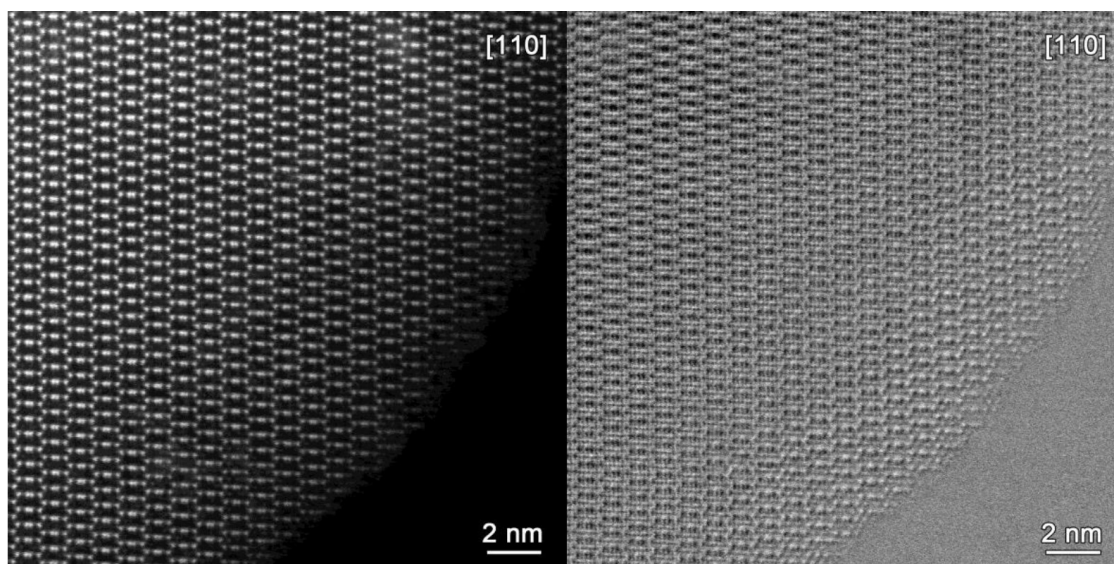
Figures

Appendix Chapter III. Table 1 Na and Ir in $\text{Na}_{1.7}\text{IrO}_3$ particles. Numbers are presented in atomic %. Na K-line and Ir M-line were used for quantification. Due to software underestimation, a correction factor was applied to compensate for Ir.

Region	Na measured	Ir measured	Na/Ir measured	Na/Ir corrected
1	75.3	24.7	3.04	1.69
2	74.1	25.9	2.87	1.59
3	77.5	22.5	3.45	1.92
4	75.2	24.8	3.04	1.69
5	73.1	26.9	2.71	1.51
6	76.3	23.7	3.21	1.79
7	74.2	25.8	2.87	1.59
8	75.0	25.0	2.99	1.66
9	76.6	23.4	3.28	1.82
10	76.1	23.9	3.18	1.77
11	72.5	27.5	2.64	1.47
12	72.1	27.9	2.58	1.43
13	78.4	21.6	3.63	2.02
Average	75.1	24.9	3.04	1.69
Standard deviation	1.8	1.8	0.30	0.17



Appendix Chapter III. Figure 1 HAADF-STEM image and individual element maps Na/Ir/O presented in counts and showing that Ir and Na are homogeneously distributed.



Appendix Chapter III. Figure 2 Atomic resolution HAADF-STEM and ABF-STEM images of a $\text{Na}_{1.7}\text{IrO}_3$ particle. The crystallite is viewed along the $[110]$ direction.

Appendix Chapter III. Table 2 Crystallographic data and atomic positions of $\beta\text{-Na}_{0.5}\text{IrO}_3$ during sodiation of IrO_3 determined by Rietveld refinement of synchrotron X-ray powder diffraction pattern. Occupancies were fixed to correspond to the stoichiometry determined by electrochemistry. Oxygen positions were fixed to the values obtained for the fully sodiated compound as determined by Rietveld refinement of the synchrotron XRD pattern.

Atom	Wyckoff position	x/a	y/b	z/c	Occupancy
Ir1	16g	1/8	1/8	0.71342(13)	1
Na1	16g	1/8	1/8	0.1009(19)	0.5
O1	16e	0.822	1/8	1/8	1
O2	32h	0.661	0.3481	0.0329	1
Space group $Fdd\bar{d}$. $a = 6.9204(8) \text{ \AA}$; $b = 7.8089(9) \text{ \AA}$; $c = 18.0873(9) \text{ \AA}$; $V = 977.45(16) \text{ \AA}^3$; $R_{\text{Bragg}} = 14.11\%$; $\chi^2 = 32.20$.					

Appendix Chapter III. Table 3 Crystallographic data and atomic positions of β - $\text{Na}_{0.75}\text{IrO}_3$ during sodiation of IrO_3 determined by Rietveld refinement of synchrotron X-ray powder diffraction pattern. Occupancies were fixed to correspond to the stoichiometry determined by electrochemistry. Oxygen positions were fixed to the values obtained for the fully sodiated compound as determined by Rietveld refinement of the synchrotron XRD pattern.

Atom	Wyckoff position	x/a	y/b	z/c	Occupancy
Ir1	16g	1/8	1/8	0.71326(18)	1
Na1	16g	1/8	1/8	0.0814(12)	0.75
O1	16e	0.822	1/8	1/8	1
O2	32h	0.661	0.3481	0.0329	1
Space group $F d d d$. $a = 6.5726(7) \text{ \AA}$; $b = 8.7814(8) \text{ \AA}$; $c = 18.0034(11) \text{ \AA}$; $V = 1039.10(15) \text{ \AA}^3$; $R_{\text{Bragg}} = 19.87\%$; $\chi^2 = 100.5$.					

Appendix Chapter III. Table 4 Crystallographic data and atomic positions of β - $\text{Na}_{1.2}\text{IrO}_3$ during sodiation of IrO_3 determined by Rietveld refinement of synchrotron X-ray powder diffraction pattern. Occupancies were fixed to correspond to the stoichiometry determined by electrochemistry. Oxygen positions were fixed to the values obtained for the fully sodiated compound as determined by Rietveld refinement of the synchrotron XRD pattern.

Atom	Wyckoff position	x/a	y/b	z/c	Occupancy
Ir1	16g	1/8	1/8	0.71171(15)	1
Na1	16g	1/8	1/8	0.1925(12)	0.8
Na2	16g	1/8	1/8	0.873640	0.4
O1	16e	0.822	1/8	1/8	1
O2	32h	0.661	0.3481	0.0329	1
Space group $F d d d$. $a = 6.5611(4) \text{ \AA}$; $b = 8.9112(4) \text{ \AA}$; $c = 18.0946(7) \text{ \AA}$; $V = 1057.94(9) \text{ \AA}^3$; $R_{\text{Bragg}} = 24.50\%$; $\chi^2 = 132.3$.					

Appendix Chapter III. Table 5 Crystallographic data and atomic positions of β -Na_{1.5}IrO₃ during sodiation of IrO₃ determined by Rietveld refinement of synchrotron X-ray powder diffraction pattern. Occupancies were fixed to correspond to the stoichiometry determined by electrochemistry. Oxygen positions were fixed to the values obtained for the fully sodiated compound as determined by Rietveld refinement of the synchrotron XRD pattern.

Atom	Wyckoff position	x/a	y/b	z/c	Occupancy
Ir1	16g	1/8	1/8	0.7096(2)	1
Na1	16g	1/8	1/8	0.2049(19)	0.9
Na2	16g	1/8	1/8	0.889450	0.6
O1	16e	16e	0.822	1/8	1
O2	32h	32h	0.661	0.3481	1

Space group $Fdd\bar{d}$. $a = 6.4542(6)$ Å; $b = 8.9596(5)$ Å; $c = 18.4463(11)$ Å; $V = 1066.69(13)$ Å³;
 $R_{\text{Bragg}} = 26.62$ %; $\chi^2 = 245.5$.

Appendix Chapter III. Table 6 Crystallographic data and atomic positions of β -Na_{1.7}IrO₃ during sodiation of IrO₃ determined by Rietveld refinement of synchrotron X-ray powder diffraction pattern. Occupancies were fixed to correspond to the stoichiometry determined by electrochemistry.

Atom	Wyckoff position	x/a	y/b	z/c	Occupancy
Ir1	16g	1/8	1/8	0.71010(15)	1
Na1	16g	1/8	1/8	0.2020(10)	0.9
Na2	16g	1/8	1/8	0.8736(15)	0.8
O1	16e	0.822(4)	1/8	1/8	1
O2	32h	0.661(3)	0.3506(9)	0.0430(6)	1

Space group $Fdd\bar{d}$. $a = 6.43960(19)$ Å; $b = 8.96034(16)$ Å; $c = 18.4999(4)$ Å; $V = 1067.46(4)$ Å³;
 $R_{\text{Bragg}} = 2.94$ %; $\chi^2 = 47.07$.

Appendix Chapter III. Table 7 Crystallographic data and atomic positions of β -Na_{1.2}IrO₃ during desodiation of Na_{1.7}IrO₃ determined by Rietveld refinement of synchrotron X-ray powder diffraction pattern. Occupancies were fixed to correspond to the stoichiometry determined by electrochemistry. Oxygen positions were fixed to the values obtained for the fully sodiated compound as determined by Rietveld refinement of the synchrotron XRD pattern.

Atom	Wyckoff position	x/a	y/b	z/c	Occupancy
Ir1	16g	1/8	1/8	0.71268(19)	1
Na1	16g	1/8	1/8	0.1893(12)	0.8
Na2	16g	1/8	1/8	0.873610	0.4
O1	16e	0.822	1/8	1/8	1
O2	32h	0.661	0.3481	0.0329	1
Space group $Fdd\bar{d}$. $a = 6.5353(6)$ Å; $b = 8.9329(5)$ Å; $c = 18.1598(10)$ Å; $V = 1060.15(13)$ Å ³ ; $R_{\text{Bragg}} = 22.47$ %; $\chi^2 = 134.5$.					

Appendix Chapter III. Table 8 Crystallographic data and atomic positions of β -Na_{0.8}IrO₃ during desodiation of Na_{1.7}IrO₃ determined by Rietveld refinement of synchrotron X-ray powder diffraction pattern. Occupancies were fixed to correspond to the stoichiometry determined by electrochemistry. Oxygen positions were fixed to the values obtained for the fully sodiated compound as determined by Rietveld refinement of the synchrotron XRD pattern.

Atom	Wyckoff position	x/a	y/b	z/c	Occupancy
Ir1	16g	1/8	1/8	0.71405(19)	1
Na1	16g	1/8	1/8	0.1806(11)	0.8
O1	16e	0.822	1/8	1/8	1
O2	32h	0.661	0.3481	0.0329	1
Space group $Fdd\bar{d}$. $a = 6.5699(7)$ Å; $b = 8.8465(9)$ Å; $c = 18.0456(11)$ Å; $V = 1048.81(17)$ Å ³ ; $R_{\text{Bragg}} = 19.40$ %; $\chi^2 = 98.09$.					

Appendix Chapter III. Table 9 Crystallographic data and atomic positions of β -Na_{0.4}IrO₃ during desodiation of Na_{1.7}IrO₃ determined by Rietveld refinement of synchrotron X-ray powder diffraction pattern. Occupancies were fixed to correspond to the stoichiometry determined by electrochemistry. Oxygen positions were fixed to the values obtained for the fully sodiated compound as determined by Rietveld refinement of the synchrotron XRD pattern.

Atom	Wyckoff position	x/a	y/b	z/c	Occupancy
Ir1	16g	1/8	1/8	0.71076(13)	1
Na1	16g	1/8	1/8	0.144(3)	0.4
O1	16e	0.822	1/8	1/8	1
O2	32h	0.661	0.3481	0.0329	1
Space group $F d d d$. $a = 6.9230(5)$ Å; $b = 7.6354(8)$ Å; $c = 18.2565(9)$ Å; $V = 965.03(13)$ Å ³ ; $R_{\text{Bragg}} = 8.86$ %; $\chi^2 = 70.8$.					

Appendix – Chapter IV

Methods

Electrochemical measurements

Working electrode preparation: Electrodes were prepared by drop-casting ink containing oxide catalyst powder on a round glassy carbon electrode (5 mm diameter) or a large glassy carbon plate ($2 \times 2 \text{ cm}^2$).¹⁷¹ The glassy carbon electrode was loaded with $0.5 \text{ mg}_{\text{catalyst}} \text{ cm}^{-2}_{\text{disk}}$ and a mass ratio of 5:1:1 of Ir-oxide catalyst to acetylene black carbon to Nafion®. Oxygen evolution reaction (OER) measurements were performed using rotating disk electrode (RDE) on a biologic MPG-30 potentiostat (PINE Inc, US). The OER activities of different Ir-based catalysts were evaluated by the RDE experiments in a three-electrode configuration. The glassy carbon electrode loaded with catalyst is used as working electrode, and a KCl-saturated Ag/AgCl reference electrode and a Pt wire were adopted as reference electrode (RE) and counter electrode (CE), respectively. The Ag/AgCl reference electrode is calibrated by using a reversible hydrogen reference electrode (HydroFlex®, from Gaskatel, Germany) before and after each experiment. Potentials were then converted to the RHE scale. A scan rate of 10 mV/s was used for all cyclic voltammetry (CV) and rotation was set to 1600 rpm. Oxygen was bubbled into the electrolyte before the CV and potentiostatic measurements of OER activity. CVs scanned in broad potential ranges between 0.3 to 1.6 V vs. RHE were measured in Ar-saturated sulfuric acid solutions. H_2SO_4 (96-98%, Sigma-Aldrich) solutions with different concentrations were prepared using Milli-Q® ultrapure water. All electrochemical measurements were conducted at room temperature (25 °C).

Ir dissolution during OER: Ir dissolution during OER for different Ir-based catalysts, including SrIrO_3 and $\beta\text{-H}_{2+x}\text{IrO}_3$, was compared by chronoamperometry using inductively coupled plasma optical emission spectrometry (ICP-OES) on a ThermoFisher iCAP 6000 device. Chronoamperometry was conducted by holding the electrode at 1.55 V vs. RHE ($\eta_{\text{OER}} = 320 \text{ mV}$) in a 40 ml of 1.0 M H_2SO_4 solution continuously for 50 hours.

Physical characterizations

Diffraction measurements: Operando and ex situ XRD measurements were performed in a BRUKER D8 Advance diffractometer with Cu K α radiation ($\lambda_{K\alpha1} = 1.54056$ Å, $\lambda_{K\alpha2} = 1.54439$ Å) using a home designed cell. A three-electrode configuration is adopted using carbon paper loaded with $\sim 5\text{--}8$ mg cm $^{-2}_{\text{geo}}$ of $\beta\text{-H}_2\text{IrO}_3$ catalyst as working electrode, a KCl-saturated Ag/AgCl reference electrode and a Pt wire as counter electrode. For the pristine material, the synchrotron XRD pattern was measured at ALBA synchrotron's MSPD beamline¹¹⁴ using a 0.3 mm Kapton capillary with a wavelength of 0.41226 Å. The Neutron Powder Diffraction (NPD) measurements were performed on the D20 beamline at the Institut Laue Langevin in Grenoble (France) using a Vanadium can with a wavelength of 1.5419 Å.

Operando XAS: Operando XAS measurements at the Ir L $_3$ -edge were performed in transmission mode at the ROCK beamline⁸⁹ of synchrotron SOLEIL (France). A Si (111) channel-cut quick-XAS monochromator with an energy resolution of 2 eV at 11 keV was used. The intensity of the monochromatic X-ray beam was measured by three consecutive ionization detectors. The *in situ* 3-electrodes cell was placed between the first and the second ionization chambers. Operando XAS spectra were collected continuously at a rate of 2 Hz and averaged out over periods of 20 seconds. The energy calibration was established with simultaneous absorption measurements on an Ir metal foil placed between the second and the third ionization chamber. The data was treated using the Demeter package for energy calibration and normalization. The WL energy position was obtained as the value for which the first derivative of the XANES portion of each spectrum is null. The WL intensity was obtained by fitting the XANES spectra using an Arctan function for the step and a Gaussian function to fit the WL.

Solid-state NMR (ssNMR): ssNMR spectra were recorded on a Bruker 4.7 T Avance III spectrometer mounted with a 1.3 mm double-resonance probehead tuned to ^1H at 200 MHz and ^7Li at 77.8 MHz. The 1.3 mm rotor, packed with $\beta\text{-Li}_2\text{IrO}_3$ or $\beta\text{-H}_2\text{IrO}_3$, was spinning at a 64 kHz MAS rate under nitrogen at room temperature, with no temperature regulation, assuming that the internal rotor temperature is around 60–70°C due to friction effects. The chemical shifts were referenced at 0 ppm with respect to TMS for ^1H and 1M LiCl for ^7Li , and the RF field strength was set to 250 kHz for

^7Li and 287 kHz for ^1H . All 1D spectra were obtained with a rotor synchronized Hahn echo sequence, with a total echo time of 2 rotor periods (31.25 μs). The 2D EXSY and RFDR sequence have been described in previous works.¹⁷²

X-ray photoelectron spectroscopy: Standard XPS measurements (in-house) were performed with a Kratos Axis Ultra spectrometer (monochromatized Al K α radiation $h\nu = 1486.6$ eV). The analyzed area of the samples was 300 $\mu\text{m} \times 700$ μm . Peaks were recorded with constant pass energy of 20 eV. For the Ag 3d $_{5/2}$ line, the full width at half maximum (FWHM) was 0.58 eV under the recording conditions. Hard X-ray photoemission spectroscopy (HAXPES) was carried out at the GALAXIES^{166,167} beamline of SOLEIL synchrotron with $h\nu = 6.9$ keV photon energy (third order reflection of the Si(111) double-crystal monochromator). Photoelectrons were analyzed by a SCIENTA EW4000 spectrometer, and the obtained energy resolution from the Au Fermi edge was 0.14 eV.

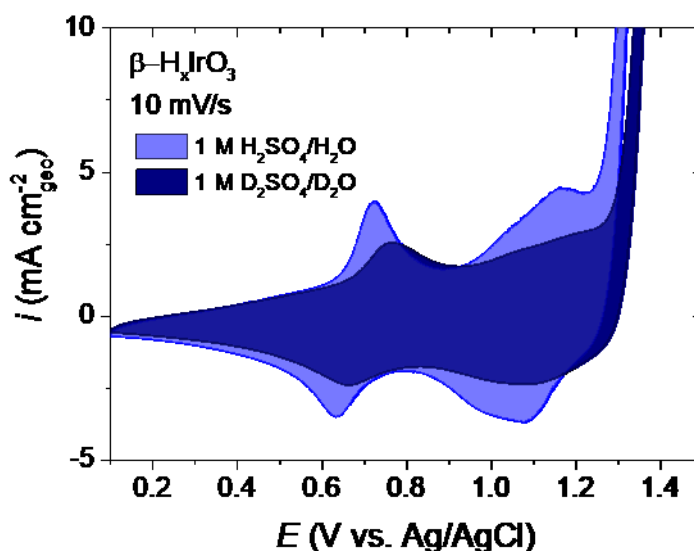
Thermogravimetric analysis coupled with differential scanning calorimetry (TGA-MS): TGA-MS measurements were recorded with a STA 449C Netzsch apparatus under argon by applying a heating rate of 5 K min⁻¹ from room temperature to 1000 °C using around 15-20 mg of material.

Scanning Electron Microscopy: The morphology of the particles was observed by scanning electron microscopy (SEM) performed in Hitachi S-3400N and FEI Quanta FEG 250 microscopes. Energy dispersive X-ray (EDX) analysis was performed using an Oxford X-Max detector (accelerating voltage: 10 keV) to evaluate the atomic ratio of K to Ir.

Online Mass spectrometry (OMS) gas-analysis: OMS was performed using a HIDEN H1 mass spectrometer system (HIDEN Analytical, UK). A three-neck Swagelok-type cell was used as the reaction container with one neck connecting to the mass spectrometer for gas analysis, two necks sealed by a stainless steel rod and a silicone rubber stopper. ~100 mg of as-prepared IrO₃ powder was sealed in the Swagelok cell in the Ar-glovebox. The Swagelok cell was then connected to the HIDEN mass spectrometer through a flexible 1 m capillary inlet and two porous stainless steel membrane filters (~2 μm pore diameter, Valco Instruments Co. Inc.) for *online* gas analysis. 2 ml of Ar-saturated 1 M H₂SO₄ solution was injected using a

syringe through the silicon stopper into the Swagelok cell. Blank test was conducted by injecting H_2SO_4 solution into a sealed Swagelok cell without the IrO_3 powder.

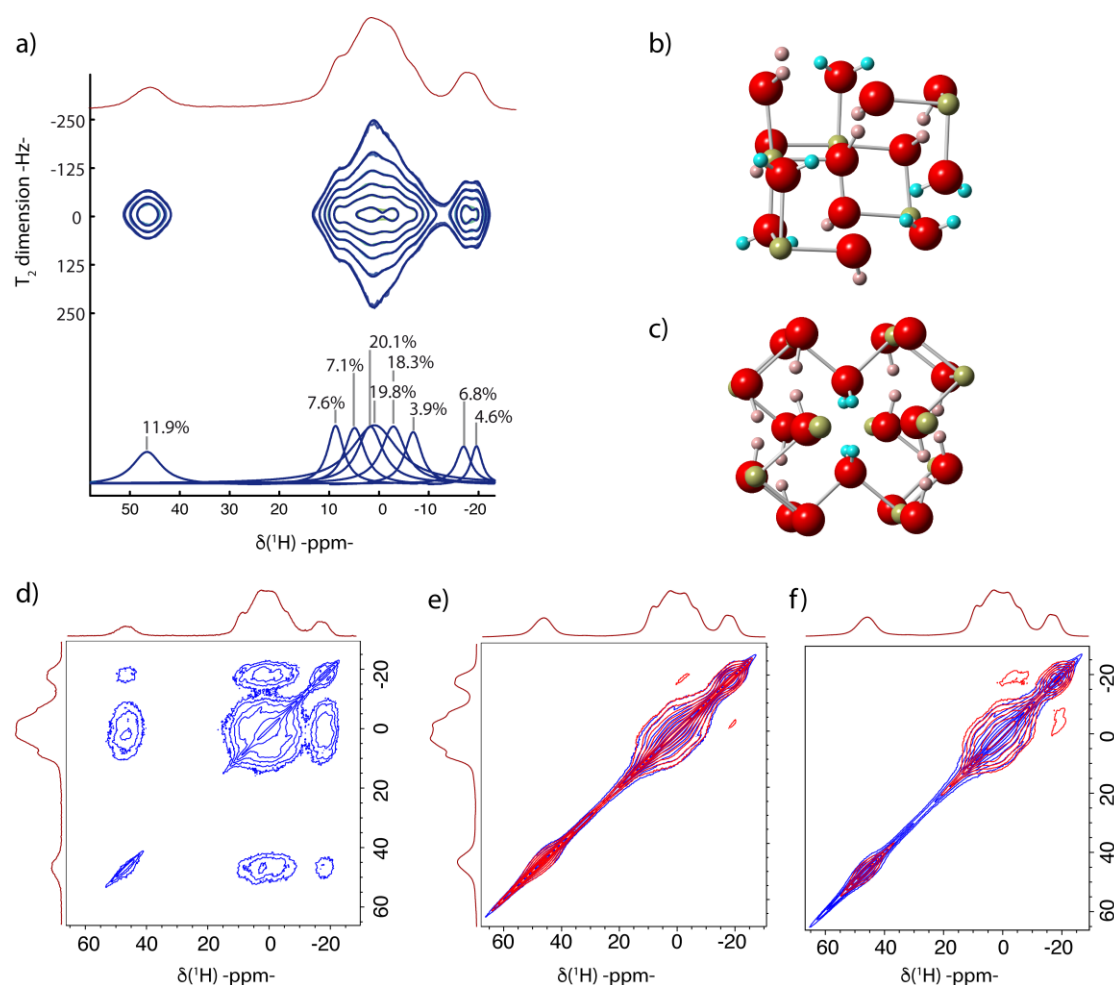
Figures



Appendix Chapter IV. Figure 1 H/D isotope effect for the OER activity and surface redox properties of $\beta\text{-H}_2\text{IrO}_3$. CVs conducted in 1.0 M $\text{H}_2\text{SO}_4/\text{H}_2\text{O}$ and $\text{D}_2\text{SO}_4/\text{D}_2\text{O}$ solutions are compared. The slow deuterium transfer kinetics in $\text{D}_2\text{SO}_4/\text{D}_2\text{O}$ solution suppresses the OER activity, as well as the redox of Ir for $\beta\text{-H}_2\text{IrO}_3$.

For ^1H NMR on $\beta\text{-H}_2\text{IrO}_3$ (see Appendix Chapter IV. Figure 2), the 1D Hahn echo spectrum displays many sites, and a 2D Hahn echo was used to distinguish the different sites based on T_2 variations leading to different linewidths in the indirect dimension. A minimum of 9 sites were necessary to model Appendix Chapter IV. Figure 2 a) correctly. As the adjacent H1 and H2 sites are unlikely to be protonated at the same time due to their occupancies, we expect the shortest H-H distance to be around 2.7 Å, which would give rise to a dipolar coupling of roughly 6 kHz which should be averaged by ultra-fast MAS. The longitudinal relaxation times (T_1) varied between 52 ms for the left hand side of the spectrum to 164 ms for the peaks in the middle and 332 ms for the two peaks on the right hand side. The 2D RFDR shows that all sites are correlated to each other, and therefore belong to the same -homogeneous-phase (Appendix Chapter IV. Figure 2 d). The EXSY experiment shown in e (5 ms) and f (50 ms) both feature cross-peaks between the peaks located in left hand side of

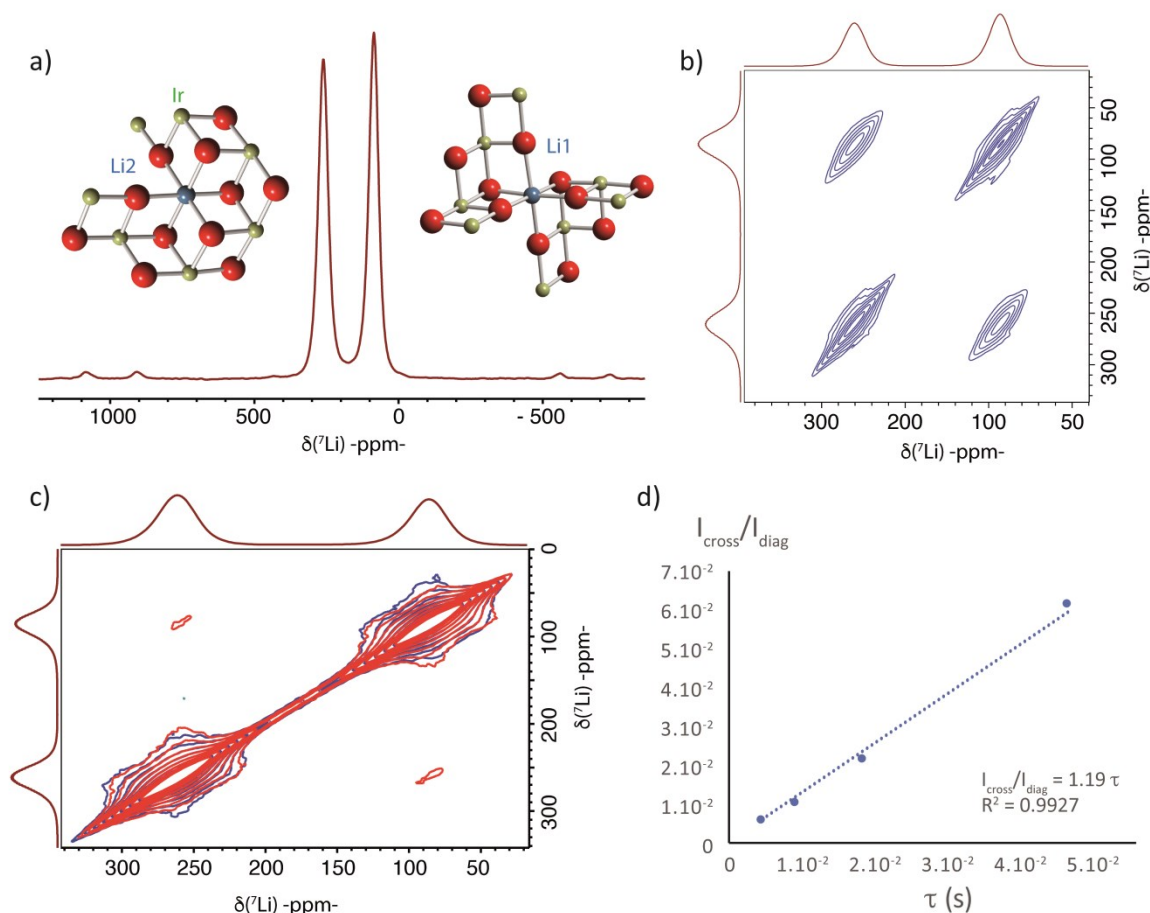
the spectrum. Spin diffusion is expected to be reduced by ultra-fast spinning and the relatively long distances between the hydrogen atoms. A faint and nearly undetectable cross-peak between the site at 48 ppm and the peaks on the left is observed (not shown), and confirms that chemical exchange between hydrogen sites is observed but is extremely slow between some of the environments. Precise quantification of the exchange rate was impossible due to the multiplicity of sites and further studies will be needed to fully understand the ^1H MAS-NMR spectra.



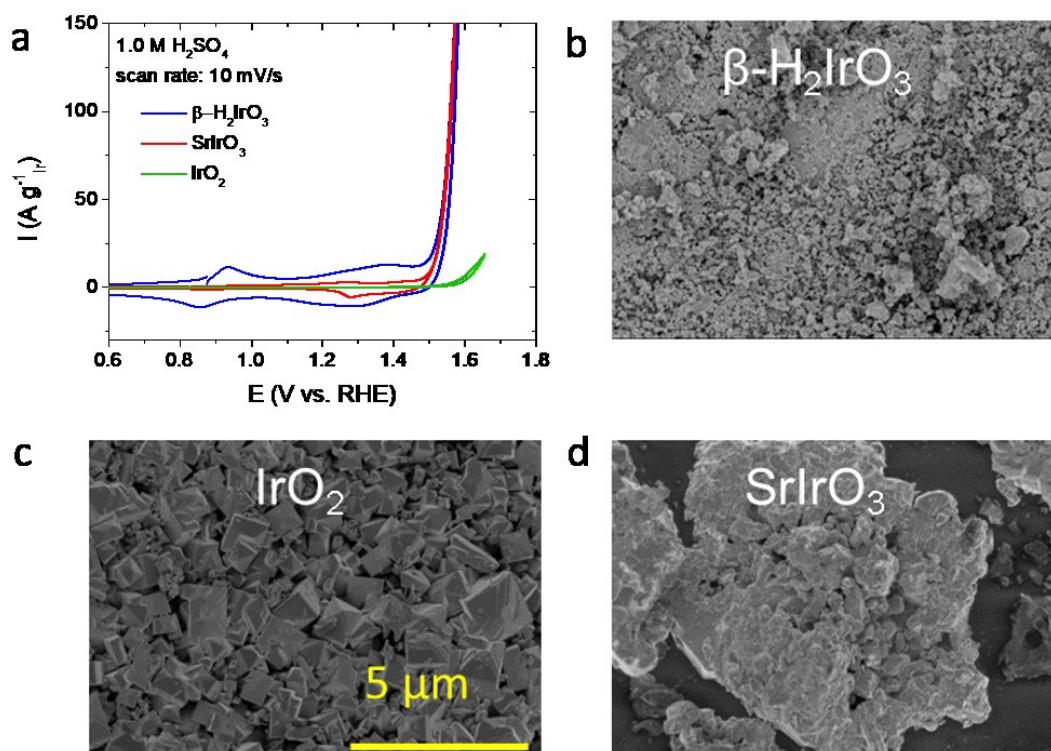
Appendix Chapter IV. Figure 2 ^1H NMR. a) 1D ^1H MAS-NMR Hahn echo spectrum of $\beta\text{-H}_2\text{IrO}_3$ recorded at 4.7 T and a 64 kHz MAS rate, with below the 2D Hahn echo spectrum obtained after the real Fourier transform against the echo time in the indirect dimension and the corresponding fit in blue (obtained with dmfit¹⁷³). The 9 detected environments with their respective weights in the 1D spectrum are shown at the bottom, and the T_2 's ranged between 2 and 4 ms, except for the broad peak in the center, which has a $T_2 = 0.06$ ms; b)-c) atomic environments for H1 (pink) and H2 (blue), where H1 sites have a roughly a 50% occupancy and H2 sites a 25% occupancy. The disorder in H1/H2 occupancies give rise to the multiplicity of sites in the ^1H spectrum. D) 2D-RFDR homonuclear correlation spectrum obtained with a 2 ms dipolar recoupling using a XY-16 RFDR train of rotor synchronized 180° pulses. All the peaks belong to the same phase. e) and f) EXSY spectra obtained with a mixing time of 1 rotor period (15.6 μs) -in blue- compared with a 5 ms mixing time (e) and 50 ms mixing time (f), both in red.

To further confirm the lithium sites in the $\beta\text{-Li}_2\text{IrO}_3$, ^7Li solid state nuclear magnetic resonance (see Appendix Chapter IV. Figure 3) was carried out. This study

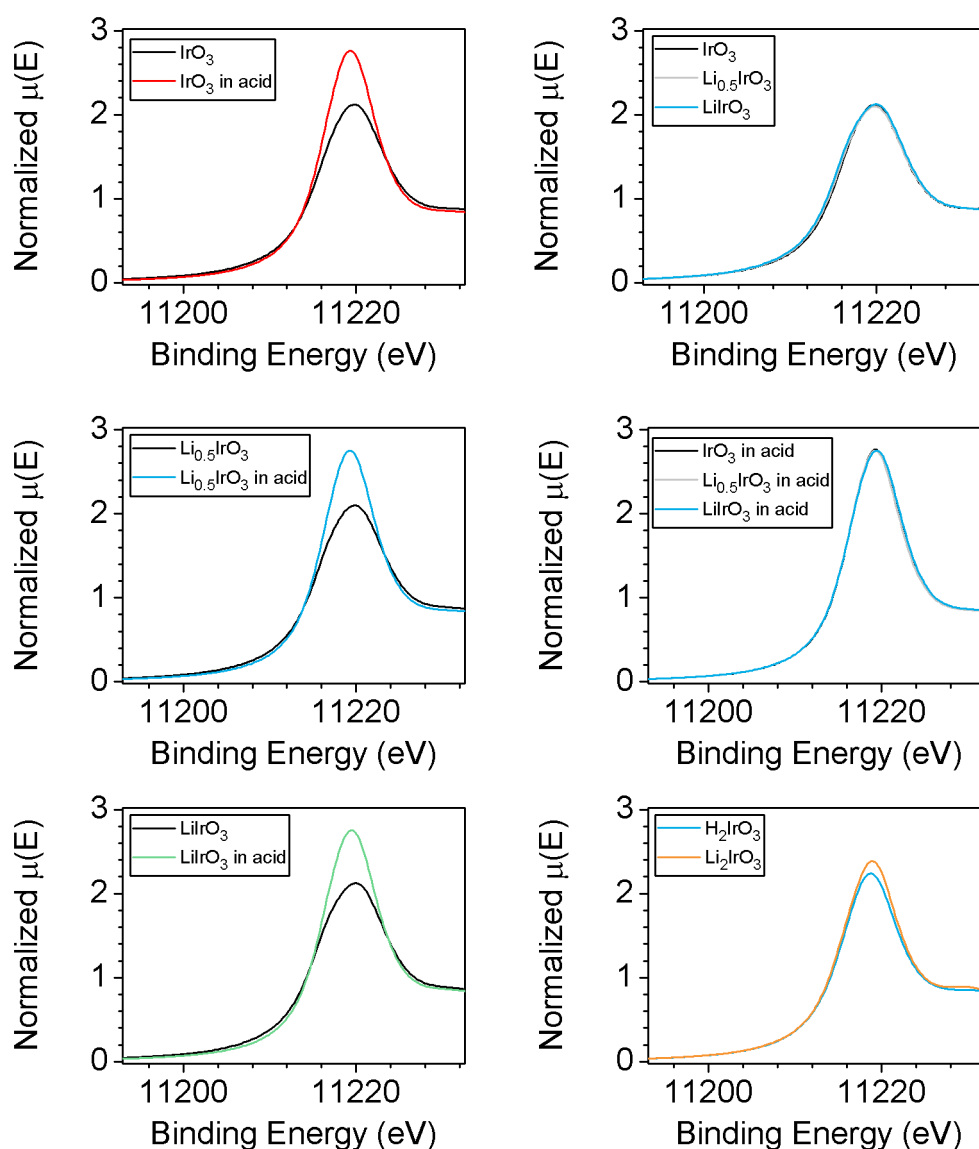
was performed in collaboration with Michael Deschamps from the University of Orleans and the results presented here have been measured and extracted by him. Two sites of nearly equal intensities (49/51%) were detected with very weak sidebands, as expected from the structure. We account for the observed shifts with the model for paramagnetic Fermi contact (FC) shifts developed by Grey et al.,¹⁷⁴ for lithium oxides containing paramagnetic metals with octahedral geometry. The observed shifts can be interpreted using the sum of the individual contributions of all paramagnetic Ir–O–Li bonds, each bond contributing to a positive or a negative shift depending on the Ir–O–Li bond angle and the electronic configuration. The FC shift is expected to be dominant here, as the chemical shift range is negligible compared to the FC shift. Assuming a low spin configuration, Grey's model indicates that the 90° Ir–O–Li bonds will give rise to a positive FC shift through delocalization, while the 180° Ir–O–Li is expected to lead to a negative shift on ^7Li by a polarization mechanism. Therefore, as Li1 is bound to four O–Ir with a 180° angle and four at 90°, while Li2 is bound to 2 and 5 O–Ir at 180° and 90°, respectively, we expect Li1 to have the lowest shift. Therefore, we assigned the 261 ppm peak to Li2 and the peak at 86 ppm to Li1. The longitudinal relaxation times (T_1) were measured at 49 and 107 ms for Li2 and Li1, respectively. Therefore, the 2D RFDR experiment is possible and clearly confirms the proximity between the two lithium sites which belong to the same phase. The rather long T_1 allowed us to run a 2D-EXSY experiment, and for a 5 ms mixing time, we found a weak cross-peak indicating magnetization exchange. Previous experiments, such as those run by Messinger et al. showed that spin diffusion at such high MAS rate is expected to quench significant spin diffusion, and therefore, we can confirm that chemical exchange occur between the two sites. The plot of the ratio between the areas of the cross peak and of the diagonal peak has a linear dependence with the mixing time (from 5 to 50 ms), allowing us to retrieve the rather slow exchange rate constant at 1.19 s^{-1} .



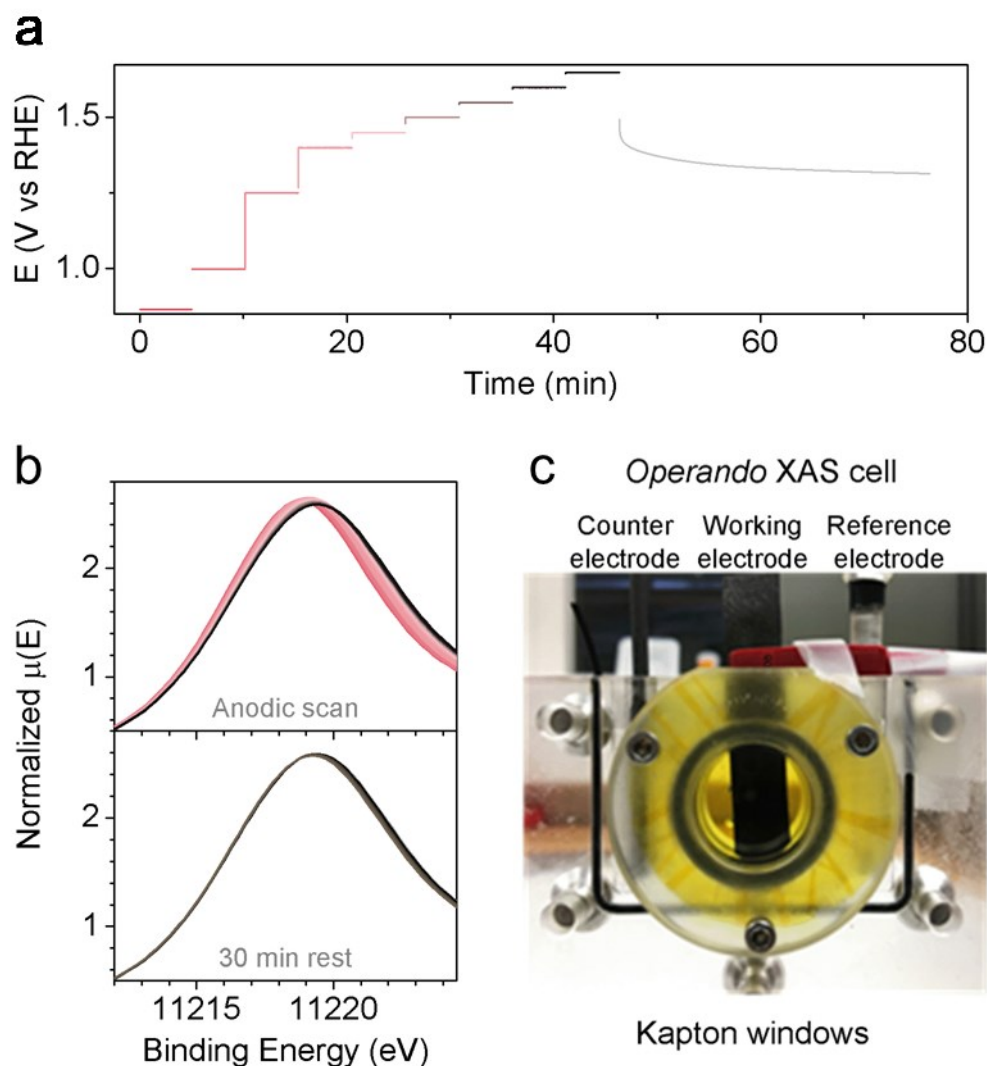
Appendix Chapter IV. Figure 3 Li NMR. a) ^7Li MAS-NMR spectrum of $\beta\text{-Li}_2\text{IrO}_3$ recorded at 4.7 T and 64 kHz MAS, featuring the environments of the two lithium sites (blue) in term of oxygen (red) and iridium (green) atoms; b) 2D-RFDR spectrum, using a 4 ms long XY-16 RFDR train of rotor synchronized 180° pulses for dipolar recoupling, showing the proximity in space of the two detected sites; c) 2D-EXSY experiment with the reference spectrum (1 rotor period mixing time) in blue and the 2D EXSY obtained with 5 ms mixing time in red, displaying weak cross-peaks indicating an exchange between the two sites; d) measuring the ratio between the areas of the cross peak and the diagonal peak leads to the exchange rate constant, measured at 1.19 s^{-1} at $60\text{-}70^\circ\text{C}$.



Appendix Chapter IV. Figure 4 Comparison of the OER activities normalized by Ir mass. (a) Cyclic voltammograms of IrO_2 , $\beta\text{-H}_x\text{IrO}_3$ and SrIrO_3 in 1M H_2SO_4 solution using a rotating disk electrode. The current is normalized by Ir mass loaded on the electrode. (b-d) SEM micrographs of $\beta\text{-H}_2\text{IrO}_3$, IrO_2 and SrIrO_3 catalysts, respectively.



Appendix Chapter IV. XANES spectra of the different *ex situ* samples before and after acid treatment. Figure 5 left column from top to bottom: XANES spectra for the samples of initial compositions $x = 0, 0.5$ and 1 before (black line) and after (colored line) acid treatment. Right column from top to bottom: the XANES spectra of the three samples before acid treatment, after acid treatment and the XANES spectra of the pristine H_2IrO_3 compared to that of the pristine Li_2IrO_3 .



Appendix Chapter IV. Figure 6 a) electrochemical curve during operando XAS measurements. b) XANES spectra obtained operando. c) Picture of the home-made electrochemical cell for operating operando XAS experiments, using carbon paper loaded with 5-8 mg/cm²_{geo} of β -H₂IrO₃ catalyst as working electrode, porous graphitic carbon rod as counter electrode, and Ag/AgCl (KCl sat.) as reference electrode.

Appendix Chapter IV. Table 1 Crystallographic data of β -Li₂IrO₃, β -Na_{1.7}IrO₃, β -H₂IrO₃ obtained by refining synchrotron data and β -H_xIrO₃ after charging to 1.65 V vs RHE obtained by refining lab XRD data.

Composition	a (Å)	b (Å)	c (Å)	Vol (Å ³)
β -Li ₂ IrO ₃	5.90709(7)	8.45673(9)	17.82779(16)	890.581(16)
β -Na _{1.7} IrO ₃	6.41767(8)	8.95985(10)	18.5988(2)	1069.45(2)
β -H ₂ IrO ₃	5.39605(7)	9.07170(16)	18.5488(2)	907.99(2)
β -H _x IrO ₃	5.3660(10)	9.1163(15)	18.314(3)	895.8(3)

Appendix Chapter IV. Table 2 BET surface area for the different catalysts studied.

Composition	specific area (m ² /g)
RuO ₂	7.32
IrO ₂	0.263
H ₂ IrO ₃	2.4
SrIrO ₃	0.45
β -Li ₂ IrO ₃	0.085

References

- (1) Volta Alessandro. XVII. On the Electricity Excited by the Mere Contact of Conducting Substances of Different Kinds. In a Letter from Mr. Alexander Volta, F. R. S. Professor of Natural Philosophy in the University of Pavia, to the Rt. Hon. Sir Joseph Banks, Bart. K.B. P. R. S. *Philosophical Transactions of the Royal Society of London* **1800**, 90, 403–431. <https://doi.org/10.1098/rstl.1800.0018>.
- (2) Berzelius. Ein Neues Mineralisches Alkali Und Ein Neues Metall. *Journal für Chemie und Physik* **1817**, 21, 44–48.
- (3) Brande, W. T. *A Manual of Chemistry*, 2nd edition.; John Murray: London, 1821; Vol. II.
- (4) Lewis, G. N.; Keyes, F. G. The Potential of the Lithium Electrode. *J. Am. Chem. Soc.* **1913**, 35 (4), 340–344. <https://doi.org/10.1021/ja02193a004>.
- (5) Anson, F. C. Common Sources of Confusion; Electrode Sign Conventions. *J. Chem. Educ.* **1959**, 36 (8), 394–395. <https://doi.org/10.1021/ed036p394>.
- (6) Harris, W. S. [Univ. of C., Berkeley, CA (United States)]. Electrochemical Studies in Cyclic Esters, United States, 1958. <https://doi.org/10.2172/4305596>.
- (7) Peled, E. The Electrochemical Behavior of Alkali and Alkaline Earth Metals in Nonaqueous Battery Systems—The Solid Electrolyte Interphase Model. *J. Electrochem. Soc.* **1979**, 126 (12), 2047–2051. <https://doi.org/10.1149/1.2128859>.
- (8) Vincent, C. Lithium Batteries: A 50-Year Perspective, 1959–2009. *Solid State Ionics* **2000**, 134 (1–2), 159–167. [https://doi.org/10.1016/S0167-2738\(00\)00723-2](https://doi.org/10.1016/S0167-2738(00)00723-2).
- (9) Whittingham, M. S. Chemistry of Intercalation Compounds: Metal Guests in Chalcogenide Hosts. *Progress in Solid State Chemistry* **1978**, 12 (1), 41–99. [https://doi.org/10.1016/0079-6786\(78\)90003-1](https://doi.org/10.1016/0079-6786(78)90003-1).
- (10) Mizushima, K.; Jones, P. C.; Wiseman, P. J.; Goodenough, J. B. Li_xCoO_2 ($0 < x < 1$): A New Cathode Material for Batteries of High Energy Density. *Materials Research Bulletin* **1980**, 15 (6), 783–789. [https://doi.org/10.1016/0025-5408\(80\)90012-4](https://doi.org/10.1016/0025-5408(80)90012-4).
- (11) Cheng, K.; Stanleywhittingham, M. Lithium Incorporation in Tungsten Oxides. *Solid State Ionics* **1980**, 1 (1–2), 151–161. [https://doi.org/10.1016/0167-2738\(80\)90030-2](https://doi.org/10.1016/0167-2738(80)90030-2).

- (12) Armand, M. B. Intercalation Electrodes. In *Materials for Advanced Batteries*; Murphy, D. W., Broadhead, J., Steele, B. C. H., Eds.; Springer US: Boston, MA, 1980; pp 145–161. https://doi.org/10.1007/978-1-4684-3851-2_7.
- (13) Lazzari, M.; Scrosati, B. A Cyclable Lithium Organic Electrolyte Cell Based on Two Intercalation Electrodes. *J. Electrochem. Soc.* **1980**, *127* (3), 773–774. <https://doi.org/10.1149/1.2129753>.
- (14) Di Pietro, B.; Patriarca, M.; Scrosati, B. On the Use of Rocking Chair Configurations for Cyclable Lithium Organic Electrolyte Batteries. *J. Power Sources* **1982**, *8* (2), 289–299. [https://doi.org/10.1016/0378-7753\(82\)80062-1](https://doi.org/10.1016/0378-7753(82)80062-1).
- (15) Ohzuku, T.; Ueda, A.; Nagayama, M. Electrochemistry and Structural Chemistry of LiNiO_2 (R3m) for 4 Volt Secondary Lithium Cells. *J. Electrochem. Soc.* **1993**, *140* (7), 1862–1870. <https://doi.org/10.1149/1.2220730>.
- (16) Auborn, J. J.; Barberio, Y. L. Lithium Intercalation Cells Without Metallic Lithium. *J. Electrochem. Soc.* **1987**, *134* (3), 638–641. <https://doi.org/10.1149/1.2100521>.
- (17) Ohzuku, T.; Ueda, A.; Yamamoto, N. Zero-Strain Insertion Material of $\text{Li}[\text{Li}_{1/3}\text{Ti}_{5/3}]\text{O}_4$ for Rechargeable Lithium Cells. *J. Electrochem. Soc.* **1995**, *142* (5), 1431–1435. <https://doi.org/10.1149/1.2048592>.
- (18) Fong, R.; Von Sacken, U.; Dahn, J. R. Studies of Lithium Intercalation into Carbons Using Nonaqueous Electrochemical Cells. *J. Electrochem. Soc.* **1990**, *137* (7), 2009–2013. <https://doi.org/10.1149/1.2086855>.
- (19) Thackeray, M. M.; David, W. I. F.; Bruce, P. G.; Goodenough, J. B. Lithium Insertion into Manganese Spinels. *Materials Research Bulletin* **1983**, *18* (4), 461–472. [https://doi.org/10.1016/0025-5408\(83\)90138-1](https://doi.org/10.1016/0025-5408(83)90138-1).
- (20) Padhi, A. K.; Nanjundaswamy, K. S.; Goodenough, J. B. Phospho-Olivines as Positive-Electrode Materials for Rechargeable Lithium Batteries. *J. Electrochem. Soc.* **1997**, *144* (4), 1188–1194. <https://doi.org/10.1149/1.1837571>.
- (21) Dahn, J. R.; Fuller, E. W.; Obrovac, M.; Sacken, U. von. Thermal Stability of Li_xCoO_2 , Li_xNiO_2 and $\lambda\text{-MnO}_2$ and Consequences for the Safety of Li-Ion Cells. *Solid State Ionics* **1994**, *69* (3), 265–270. [https://doi.org/10.1016/0167-2738\(94\)90415-4](https://doi.org/10.1016/0167-2738(94)90415-4).
- (22) Armstrong, A. R.; Bruce, P. G. Synthesis of Layered LiMnO_2 as an Electrode for Rechargeable Lithium Batteries. *Nature* **1996**, *381* (6582), 499–500. <https://doi.org/10.1038/381499a0>.
- (23) Zhaolin Liu; Aishui Yu; Jim Y. Lee. Synthesis and Characterization of $\text{LiNi}_{(1-x-y)}\text{Co}_x\text{Mn}_y\text{O}_2$ as the Cathode Materials of Secondary Lithium Batteries. *J. Power Sources* **1999**, *81*–82, 416–419. [https://doi.org/10.1016/S0378-7753\(99\)00221-9](https://doi.org/10.1016/S0378-7753(99)00221-9).

- (24) Gao, Y.; Yakovleva, M. V.; Ebner, W. B. Novel $\text{LiNi}_{1-x}\text{Ti}_{x/2}\text{Mg}_{x/2}\text{O}_2$ Compounds as Cathode Materials for Safer Lithium-Ion Batteries. *Electrochemical and Solid-State Letters* **1998**, *1* (3), 117–119. <https://doi.org/10.1149/1.1390656>.
- (25) Chang, C.-C.; Kim, J. Y.; Kumta, P. N. Divalent Cation Incorporated $\text{Li}_{(1+x)}\text{MMg}_x\text{O}_{2(1+x)}$ ($\text{M} = \text{Ni}_{0.75}\text{Co}_{0.25}$): Viable Cathode Materials for Rechargeable Lithium-Ion Batteries. *J. Power Sources* **2000**, *89* (1), 56–63. [https://doi.org/https://doi.org/10.1016/S0378-7753\(00\)00393-1](https://doi.org/https://doi.org/10.1016/S0378-7753(00)00393-1).
- (26) Huang, H.; Rao, G. V. S.; Chowdari, B. V. R. $\text{LiAl}_x\text{Co}_{1-x}\text{O}_2$ as 4 V Cathodes for Lithium Ion Batteries. *Journal of Power Sources* **1999**, *81–82*, 690–695. [https://doi.org/https://doi.org/10.1016/S0378-7753\(99\)00249-9](https://doi.org/https://doi.org/10.1016/S0378-7753(99)00249-9).
- (27) Ohzuku, T.; Makimura, Y. Layered Lithium Insertion Material of $\text{LiCo}_{1/3}\text{Ni}_{1/3}\text{Mn}_{1/3}\text{O}_2$ for Lithium-Ion Batteries. *Chem. Lett.* **2001**, *30* (7), 642–643. <https://doi.org/10.1246/cl.2001.642>.
- (28) Lu, Z.; MacNeil, D. D.; Dahn, J. R. Layered $\text{Li}[\text{Ni}_x\text{Co}_{(1-2x)}\text{Mn}_x]\text{O}_2$ Cathode Materials for Lithium-Ion Batteries. *Electrochem. Solid-State Lett.* **2001**, *4* (12), A200–A203. <https://doi.org/10.1149/1.1413182>.
- (29) Noh, H.-J.; Youn, S.; Yoon, C. S.; Sun, Y.-K. Comparison of the Structural and Electrochemical Properties of Layered $\text{Li}[\text{Ni}_x\text{Co}_y\text{Mn}_z]\text{O}_2$ ($x = 1/3, 0.5, 0.6, 0.7, 0.8$ and 0.85) Cathode Material for Lithium-Ion Batteries. *J. Power Sources* **2013**, *233*, 121–130. <https://doi.org/10.1016/j.jpowsour.2013.01.063>.
- (30) Rozier, P.; Tarascon, J.-M. Review—Li-Rich Layered Oxide Cathodes for Next-Generation Li-Ion Batteries: Chances and Challenges. *J. Electrochem. Soc.* **2015**, *162* (14), A2490–A2499. <https://doi.org/10.1149/2.0111514jes>.
- (31) Rougier, A.; Gravereau, P.; Delmas, C. Optimization of the Composition of the $\text{Li}_{1-x}\text{Ni}_{1+x}\text{O}_2$ Electrode Materials: Structural, Magnetic, and Electrochemical Studies. *J. Electrochem. Soc.* **1996**, *143* (4), 1168–1175. <https://doi.org/10.1149/1.1836614>.
- (32) Olivetti, E. A.; Ceder, G.; Gaustad, G. G.; Fu, X. Lithium-Ion Battery Supply Chain Considerations: Analysis of Potential Bottlenecks in Critical Metals. *Joule* **2017**, *1* (2), 229–243. <https://doi.org/10.1016/j.joule.2017.08.019>.
- (33) Amatucci, G. G.; Tarascon, J. M.; Klein, L. C. CoO_2 , the End Member of the Li_xCoO_2 Solid Solution. *J. Electrochem. Soc.* **1996**, *143* (3), 1114–1123.
- (34) Ceder, G.; Chiang, Y.-M.; Sadoway, D. R.; Aydinol, M. K.; Jang, Y.-I.; Huang, B. Identification of Cathode Materials for Lithium Batteries Guided by First-Principles Calculations. *Nature* **1998**, *392* (6677), 694–696. <https://doi.org/10.1038/33647>.
- (35) Aydinol, M. K.; Kohan, A. F.; Ceder, G.; Cho, K.; Joannopoulos, J. *Ab Initio* Study of Lithium Intercalation in Metal Oxides and Metal Dichalcogenides.

- Physical Review B* **1997**, *56* (3), 1354–1365. <https://doi.org/10.1103/PhysRevB.56.1354>.
- (36) Tarascon, J. M.; Vaughan, G.; Chabre, Y.; Seguin, L.; Anne, M.; Strobel, P.; Amatucci, G. In Situ Structural and Electrochemical Study of $\text{Ni}_{1-x}\text{Co}_x\text{O}_2$ Metastable Oxides Prepared by Soft Chemistry. *Journal of Solid State Chemistry* **1999**, *147* (1), 410–420. <https://doi.org/10.1006/jssc.1999.8465>.
- (37) James, A. C. W. P.; Goodenough, J. B. Structure and Bonding in Lithium Ruthenate, Li_2RuO_3 . *Journal of Solid State Chemistry* **1988**, *74* (2), 287–294. [https://doi.org/10.1016/0022-4596\(88\)90357-X](https://doi.org/10.1016/0022-4596(88)90357-X).
- (38) James, A. C. W. P.; Goodenough, J. B. Structure and Bonding in Li_2MoO_3 and $\text{Li}_{2-x}\text{MoO}_3$ ($0 \leq x \leq 1.7$). *Journal of Solid State Chemistry* **1988**, *76* (1), 87–96. [https://doi.org/10.1016/0022-4596\(88\)90194-6](https://doi.org/10.1016/0022-4596(88)90194-6).
- (39) Lu, Z.; Dahn, J. R. Understanding the Anomalous Capacity of $\text{Li}/\text{Li}[\text{Ni}_x\text{Li}_{(1/3-2x/3)}\text{Mn}_{(2/3-x/3)}]\text{O}_2$ Cells Using In Situ X-Ray Diffraction and Electrochemical Studies. *J. Electrochem. Soc.* **2002**, *149* (7), A815–A822. <https://doi.org/10.1149/1.1480014>.
- (40) Armstrong, A. R.; Holzapfel, M.; Novák, P.; Johnson, C. S.; Kang, S.-H.; Thackeray, M. M.; Bruce, P. G. Demonstrating Oxygen Loss and Associated Structural Reorganization in the Lithium Battery Cathode $\text{Li}[\text{Ni}_{0.2}\text{Li}_{0.2}\text{Mn}_{0.6}]\text{O}_2$. *J. Am. Chem. Soc.* **2006**, *128* (26), 8694–8698.
- (41) Jiang, J.; Dahn, J. R. Insignificant Impact of Designed Oxygen Release from High Capacity $\text{Li}[(\text{Ni}_{1/2}\text{Mn}_{1/2})_x\text{Co}_y(\text{Li}_{1/3}\text{Mn}_{2/3})_{1/3}]\text{O}_2$ ($X+y = 2/3$) Positive Electrodes during the Cycling of Li-Ion Cells. *Electrochim. Acta* **2006**, *51* (17), 3413–3416. <https://doi.org/10.1016/j.electacta.2005.10.006>.
- (42) Thackeray, M. M.; Kang, S.-H.; Johnson, C. S.; Vaughey, J. T.; Hackney, S. A. Comments on the Structural Complexity of Lithium-Rich $\text{Li}_{1+x}\text{M}_{1-x}\text{O}_2$ Electrodes (M=Mn, Ni, Co) for Lithium Batteries. *Electrochem. Commun.* **2006**, *8* (9), 1531–1538. <https://doi.org/10.1016/j.elecom.2006.06.030>.
- (43) Deng, C.; Zhang, S.; Fu, B. L.; Yang, S. Y.; Ma, L. Synthetic Optimization of Nanostructured $\text{Li}[\text{Ni}_{1/3}\text{Mn}_{1/3}\text{Co}_{1/3}]\text{O}_2$ Cathode Material Prepared by Hydroxide Coprecipitation at 273 K. *Journal of Alloys and Compounds* **2010**, *496* (1–2), 521–527. <https://doi.org/10.1016/j.jallcom.2010.02.094>.
- (44) Assat, G.; Tarascon, J.-M. Fundamental Understanding and Practical Challenges of Anionic Redox Activity in Li-Ion Batteries. *Nat. Energy* **2018**, *3* (5), 373–386. <https://doi.org/10.1038/s41560-018-0097-0>.
- (45) Sathiya, M.; Rousse, G.; Ramesha, K.; Laisa, C. P.; Vezin, H.; Sougrati, M. T.; Doublet, M.-L.; Foix, D.; Gonbeau, D.; Walker, W.; et al. Reversible Anionic Redox Chemistry in High-Capacity Layered-Oxide Electrodes. *Nat. Mater.* **2013**, *12* (9), 827–835. <https://doi.org/10.1038/nmat3699>.

- (46) Sathiya, M.; Abakumov, A. M.; Foix, D.; Rousse, G.; Ramesha, K.; Saubanère, M.; Doublet, M. L.; Vezin, H.; Laisa, C. P.; Prakash, A. S.; et al. Origin of Voltage Decay in High-Capacity Layered Oxide Electrodes. *Nat. Mater.* **2014**, *14* (2), 230–238. <https://doi.org/10.1038/nmat4137>.
- (47) Sathiya, M.; Ramesha, K.; Rousse, G.; Foix, D.; Gonbeau, D.; Prakash, A. S.; Doublet, M. L.; Hemalatha, K.; Tarascon, J.-M. High Performance $\text{Li}_2\text{Ru}_{1-y}\text{Mn}_y\text{O}_3$ ($0.2 \leq y \leq 0.8$) Cathode Materials for Rechargeable Lithium-Ion Batteries: Their Understanding. *Chem. Mater.* **2013**, *25* (7), 1121–1131. <https://doi.org/10.1021/cm400193m>.
- (48) Foix, D.; Sathiya, M.; McCalla, E.; Tarascon, J.-M.; Gonbeau, D. X-Ray Photoemission Spectroscopy Study of Cationic and Anionic Redox Processes in High-Capacity Li-Ion Battery Layered-Oxide Electrodes. *J. Phys. Chem. C* **2016**, *120* (2), 862–874. <https://doi.org/10.1021/acs.jpcc.5b10475>.
- (49) Assat, G.; Iadecola, A.; Delacourt, C.; Dedryvère, R.; Tarascon, J.-M. Decoupling Cationic–Anionic Redox Processes in a Model Li-Rich Cathode via Operando X-Ray Absorption Spectroscopy. *Chem. Mater.* **2017**, *29* (22), 9714–9724. <https://doi.org/10.1021/acs.chemmater.7b03434>.
- (50) McCalla, E.; Abakumov, A. M.; Saubanère, M.; Foix, D.; Berg, E. J.; Rousse, G.; Doublet, M.-L.; Gonbeau, D.; Novák, P.; Van Tendeloo, G.; et al. Visualization of O-O Peroxo-like Dimers in High-Capacity Layered Oxides for Li-Ion Batteries. *Science* **2015**, *350* (6267), 1516–1521. <https://doi.org/10.1126/science.aac8260>.
- (51) Koga, H.; Croguennec, L.; Ménétrier, M.; Douhil, K.; Belin, S.; Bourgeois, L.; Suard, E.; Weill, F.; Delmas, C. Reversible Oxygen Participation to the Redox Processes Revealed for $\text{Li}_{1.20}\text{Mn}_{0.54}\text{Co}_{0.13}\text{Ni}_{0.13}\text{O}_2$. *J. Electrochem. Soc.* **2013**, *160* (6), A786–A792. <https://doi.org/10.1149/2.038306jes>.
- (52) Assat, G.; Foix, D.; Delacourt, C.; Iadecola, A.; Dedryvère, R.; Tarascon, J.-M. Fundamental Interplay between Anionic/Cationic Redox Governing the Kinetics and Thermodynamics of Lithium-Rich Cathodes. *Nat. Commun.* **2017**, *8* (1), 2219. <https://doi.org/10.1038/s41467-017-02291-9>.
- (53) Bettge, M.; Li, Y.; Gallagher, K.; Zhu, Y.; Wu, Q.; Lu, W.; Bloom, I.; Abraham, D. P. Voltage Fade of Layered Oxides: Its Measurement and Impact on Energy Density. *J. Electrochem. Soc.* **2013**, *160* (11), A2046–A2055. <https://doi.org/10.1149/2.034311jes>.
- (54) Croy, J. R.; Kim, D.; Balasubramanian, M.; Gallagher, K.; Kang, S.-H.; Thackeray, M. M. Countering the Voltage Decay in High Capacity $\text{XLi}_2\text{MnO}_3 \cdot (1-x)\text{LiMO}_2$ Electrodes (M = Mn, Ni, Co) for Li^+ -Ion Batteries. *J. Electrochem. Soc.* **2012**, *159* (6), A781–A790. <https://doi.org/10.1149/2.080206jes>.
- (55) Myeong, S.; Cho, W.; Jin, W.; Hwang, J.; Yoon, M.; Yoo, Y.; Nam, G.; Jang, H.; Han, J.-G.; Choi, N.-S.; et al. Understanding Voltage Decay in Lithium-

- Excess Layered Cathode Materials through Oxygen-Centred Structural Arrangement. *Nat. Commun.* **2018**, 9 (1), 3285. <https://doi.org/10.1038/s41467-018-05802-4>.
- (56) Singer, A.; Zhang, M.; Hy, S.; Cela, D.; Fang, C.; Wynn, T. A.; Qiu, B.; Xia, Y.; Liu, Z.; Ulvestad, A.; et al. Nucleation of Dislocations and Their Dynamics in Layered Oxide Cathode Materials during Battery Charging. *Nat. Energy* **2018**, 3 (8), 641–647. <https://doi.org/10.1038/s41560-018-0184-2>.
- (57) Seo, D.-H.; Lee, J.; Urban, A.; Malik, R.; Kang, S.; Ceder, G. The Structural and Chemical Origin of the Oxygen Redox Activity in Layered and Cation-Disordered Li-Excess Cathode Materials. *Nat. Chem.* **2016**, 8, 692–697. <https://doi.org/10.1038/nchem.2524>.
- (58) Saubanère, M.; McCalla, E.; Tarascon, J.-M.; Doublet, M.-L. The Intriguing Question of Anionic Redox in High-Energy Density Cathodes for Li-Ion Batteries. *Energy Environ. Sci.* **2016**, 3 (9), 984–991. <https://doi.org/10.1039/C5EE03048J>.
- (59) Ben Yahia, M.; Vergnet, J.; Saubanère, M.; Doublet, M.-L. Unified Picture of Anionic Redox in Li/Na-Ion Batteries. *Nat. Mater.* **2019**, 18, 496–502. <https://doi.org/10.1038/s41563-019-0318-3>.
- (60) Laisa, C. P.; Nanda Kumar, A. K.; Selva Chandrasekaran, S.; Murugan, P.; Lakshminarasimhan, N.; Govindaraj, R.; Ramesha, K. A Comparative Study on Electrochemical Cycling Stability of Lithium Rich Layered Cathode Materials $\text{Li}_{1.2}\text{Ni}_{0.13}\text{M}_{0.13}\text{Mn}_{0.54}\text{O}_2$ Where M = Fe or Co. *J. Power Sources* **2016**, 324, 462–474. <https://doi.org/10.1016/j.jpowsour.2016.05.107>.
- (61) Nayak, P. K.; Grinblat, J.; Levi, M.; Levi, E.; Kim, S.; Choi, J. W.; Aurbach, D. Al Doping for Mitigating the Capacity Fading and Voltage Decay of Layered Li and Mn-Rich Cathodes for Li-Ion Batteries. *Adv. Energy Mater.* **2016**, 6 (8), 1502398. <https://doi.org/10.1002/aenm.201502398>.
- (62) Ku, K.; Hong, J.; Kim, H.; Park, H.; Seong, W. M.; Jung, S.-K.; Yoon, G.; Park, K.-Y.; Kim, H.; Kang, K. Suppression of Voltage Decay through Manganese Deactivation and Nickel Redox Buffering in High-Energy Layered Lithium-Rich Electrodes. *Adv. Energy Mater.* **2018**, 8 (21), 1800606. <https://doi.org/10.1002/aenm.201800606>.
- (63) Dahiya, P. P.; Ghanty, C.; Sahoo, K.; Basu, S.; Majumder, S. B. Suppression of Voltage Decay and Improvement in Electrochemical Performance by Zirconium Doping in Li-Rich Cathode Materials for Li-Ion Batteries. *J. Electrochem. Soc.* **2018**, 165 (13), A3114–A3124. <https://doi.org/10.1149/2.0751813jes>.
- (64) Liu, Y.; Ning, D.; Zheng, L.; Zhang, Q.; Gu, L.; Gao, R.; Zhang, J.; Franz, A.; Schumacher, G.; Liu, X. Improving the Electrochemical Performances of Li-Rich $\text{Li}_{1.20}\text{Ni}_{0.13}\text{Co}_{0.13}\text{Mn}_{0.54}\text{O}_2$ through a Cooperative Doping of Na^+ and PO_4^{3-} with Na_3PO_4 . *Journal of Power Sources* **2018**, 375, 1–10. <https://doi.org/10.1016/j.jpowsour.2017.11.042>.

- (65) Wu, F.; Li, Q.; Bao, L.; Zheng, Y.; Lu, Y.; Su, Y.; Wang, J.; Chen, S.; Chen, R.; Tian, J. Role of LaNiO₃ in Suppressing Voltage Decay of Layered Lithium-Rich Cathode Materials. *Electrochimica Acta* **2018**, *260*, 986–993. <https://doi.org/10.1016/j.electacta.2017.12.034>.
- (66) Qiu, B.; Zhang, M.; Wu, L.; Wang, J.; Xia, Y.; Qian, D.; Liu, H.; Hy, S.; Chen, Y.; An, K.; et al. Gas–Solid Interfacial Modification of Oxygen Activity in Layered Oxide Cathodes for Lithium-Ion Batteries. *Nat Commun* **2016**, *7* (1), 12108. <https://doi.org/10.1038/ncomms12108>.
- (67) Guo, H.; Wei, Z.; Jia, K.; Qiu, B.; Yin, C.; Meng, F.; Zhang, Q.; Gu, L.; Han, S.; Liu, Y.; et al. Abundant Nanoscale Defects to Eliminate Voltage Decay in Li-Rich Cathode Materials. *Energy Storage Materials* **2019**, *16*, 220–227. <https://doi.org/10.1016/j.ensm.2018.05.022>.
- (68) Zhao, E.; Li, Q.; Meng, F.; Liu, J.; Wang, J.; He, L.; Jiang, Z.; Zhang, Q.; Yu, X.; Gu, L.; et al. Stabilizing the Oxygen Lattice and Reversible Oxygen Redox Chemistry through Structural Dimensionality in Lithium-Rich Cathode Oxides. *Angew. Chem., Int. Ed. Engl.* **2019**, *58* (13), 4323–4327. <https://doi.org/10.1002/anie.201900444>.
- (69) Zheng, F.; Yang, C.; Xiong, X.; Xiong, J.; Hu, R.; Chen, Y.; Liu, M. Nanoscale Surface Modification of Lithium-Rich Layered-Oxide Composite Cathodes for Suppressing Voltage Fade. *Angew. Chem. Int. Ed.* **2015**, *54* (44), 13058–13062. <https://doi.org/10.1002/anie.201506408>.
- (70) Chong, S.; Chen, Y.; Yan, W.; Guo, S.; Tan, Q.; Wu, Y.; Jiang, T.; Liu, Y. Suppressing Capacity Fading and Voltage Decay of Li-Rich Layered Cathode Material by a Surface Nano-Protective Layer of CoF₂ for Lithium-Ion Batteries. *Journal of Power Sources* **2016**, *332*, 230–239. <https://doi.org/10.1016/j.jpowsour.2016.09.028>.
- (71) He, X.; Wang, J.; Wang, R.; Qiu, B.; Frielinghaus, H.; Niehoff, P.; Liu, H.; Stan, M. C.; Paillard, E.; Winter, M.; et al. A 3D Porous Li-Rich Cathode Material with an in Situ Modified Surface for High Performance Lithium Ion Batteries with Reduced Voltage Decay. *J. Mater. Chem. A* **2016**, *4* (19), 7230–7237. <https://doi.org/10.1039/C6TA01448H>.
- (72) Zhang, X.-D.; Shi, J.-L.; Liang, J.-Y.; Yin, Y.-X.; Zhang, J.-N.; Yu, X.-Q.; Guo, Y.-G. Suppressing Surface Lattice Oxygen Release of Li-Rich Cathode Materials via Heterostructured Spinel Li₄Mn₅O₁₂ Coating. *Adv. Mater.* **2018**, *30* (29), 1801751. <https://doi.org/10.1002/adma.201801751>.
- (73) Huang, J.; Liu, H.; Hu, T.; Meng, Y. S.; Luo, J. Enhancing the Electrochemical Performance of Li-Rich Layered Oxide Li_{1.13}Ni_{0.3}Mn_{0.57}O₂ via WO₃ Doping and Accompanying Spontaneous Surface Phase Formation. *Journal of Power Sources* **2018**, *375*, 21–28. <https://doi.org/10.1016/j.jpowsour.2017.11.048>.
- (74) Shang, H.; Ning, F.; Li, B.; Zuo, Y.; Lu, S.; Xia, D. Suppressing Voltage Decay of a Lithium-Rich Cathode Material by Surface Enrichment with Atomic

- Ruthenium. *ACS Appl. Mater. Interfaces* **2018**, *10* (25), 21349–21355. <https://doi.org/10.1021/acsami.8b06271>.
- (75) Perez, A. J.; Jacquet, Q.; Batuk, D.; Iadecola, A.; Saubanère, M.; Rousse, G.; Larcher, D.; Vezin, H.; Doublet, M.-L.; Tarascon, J.-M. Approaching the Limits of Cationic and Anionic Electrochemical Activity with the Li-Rich Layered Rocksalt Li_3IrO_4 . *Nat. Energy* **2017**, *2* (12), 954–962. <https://doi.org/10.1038/s41560-017-0042-7>.
- (76) Jacquet, Q.; Iadecola, A.; Saubanère, M.; Lemarquis, L.; Berg, E. J.; Alves Dalla Corte, D.; Rousse, G.; Doublet, M.-L.; Tarascon, J.-M. Competition between Metal Dissolution and Gas Release in Li-Rich $\text{Li}_3\text{Ru}_y\text{Ir}_{1-y}\text{O}_4$ Model Compounds Showing Anionic Redox. *Chem. Mater.* **2018**, *30* (21), 7682–7690. <https://doi.org/10.1021/acs.chemmater.8b02955>.
- (77) Yabuuchi, N.; Takeuchi, M.; Nakayama, M.; Shiiba, H.; Ogawa, M.; Nakayama, K.; Ohta, T.; Endo, D.; Ozaki, T.; Inamasu, T.; et al. High-Capacity Electrode Materials for Rechargeable Lithium Batteries: Li_3NbO_4 -Based System with Cation-Disordered Rocksalt Structure. *Proc. Natl. Acad. Sci.* **2015**, *112* (25), 7650–7655. <https://doi.org/10.1073/pnas.1504901112>.
- (78) Lee, J.; Urban, A.; Li, X.; Su, D.; Hautier, G.; Ceder, G. Unlocking the Potential of Cation-Disordered Oxides for Rechargeable Lithium Batteries. *Science* **2014**, *343* (6170), 519–522. <https://doi.org/10.1126/science.1246432>.
- (79) Yabuuchi, N.; Kubota, K.; Dahbi, M.; Komaba, S. Research Development on Sodium-Ion Batteries. *Chem. Rev.* **2014**, *114* (23), 11636–11682. <https://doi.org/10.1021/cr500192f>.
- (80) Stevens, D. A.; Dahn, J. R. High Capacity Anode Materials for Rechargeable Sodium-Ion Batteries. *J. Electrochem. Soc.* **2000**, *147* (4), 1271–1273. <https://doi.org/10.1149/1.1393348>.
- (81) Stevens, D. A.; Dahn, J. R. An In Situ Small-Angle X-Ray Scattering Study of Sodium Insertion into a Nanoporous Carbon Anode Material within an Operating Electrochemical Cell. *J. Electrochem. Soc.* **2000**, *147* (12), 4428–4431. <https://doi.org/10.1149/1.1394081>.
- (82) Yan, G.; Mariyappan, S.; Rousse, G.; Jacquet, Q.; Deschamps, M.; David, R.; Mirvaux, B.; Freeland, J. W.; Tarascon, J.-M. Higher Energy and Safer Sodium Ion Batteries via an Electrochemically Made Disordered $\text{Na}_3\text{V}_2(\text{PO}_4)_2\text{F}_3$ Material. *Nat. Commun.* **2019**, *10* (1), 585. <https://doi.org/10.1038/s41467-019-08359-y>.
- (83) Lee, J.; Papp, J. K.; Clément, R. J.; Sallis, S.; Kwon, D.-H.; Shi, T.; Yang, W.; McCloskey, B. D.; Ceder, G. Mitigating Oxygen Loss to Improve the Cycling Performance of High Capacity Cation-Disordered Cathode Materials. *Nat. Commun.* **2017**, *8* (1). <https://doi.org/10.1038/s41467-017-01115-0>.

- (84) Biffin, A.; Johnson, R. D.; Choi, S.; Freund, F.; Manni, S.; Bombardi, A.; Manuel, P.; Gegenwart, P.; Coldea, R. Unconventional Magnetic Order on the Hyperhoneycomb Kitaev Lattice in β - Li_2IrO_3 : Full Solution via Magnetic Resonant x-Ray Diffraction. *Phys. Rev. B* **2014**, *90* (20), 205116. <https://doi.org/10.1103/PhysRevB.90.205116>.
- (85) Modic, K. A.; Smidt, T. E.; Kimchi, I.; Breznay, N. P.; Biffin, A.; Choi, S.; Johnson, R. D.; Coldea, R.; Watkins-Curry, P.; McCandless, G. T.; et al. Realization of a Three-Dimensional Spin–Anisotropic Harmonic Honeycomb Iridate. *Nat. Commun.* **2014**, *5*, 4203. <https://doi.org/10.1038/ncomms5203>.
- (86) Freund, F.; Williams, S. C.; Johnson, R. D.; Coldea, R.; Gegenwart, P.; Jesche, A. Single Crystal Growth from Separated Educts and Its Application to Lithium Transition-Metal Oxides. *Scientific Reports* **2016**, *6* (35362), 35362. <https://doi.org/10.1038/srep35362>.
- (87) Thackeray, M. M.; Kang, S.-H.; Johnson, C. S.; Vaughey, J. T.; Benedek, R.; Hackney, S. A. Li_2MnO_3 -Stabilized LiMO_2 (M = Mn, Ni, Co) Electrodes for Lithium-Ion Batteries. *Journal of Materials Chemistry* **2007**, *17* (30), 3112–3125. <https://doi.org/10.1039/b702425h>.
- (88) Peres, J. P.; Delmas, C.; Rougier, A.; Broussely, M.; Pertion, F.; Biensan, P.; Willmann, P. The Relationship between the Composition of Lithium Nickel Oxide and the Loss of Reversibility during the First Cycle. *J. Phys. Chem. Solids* **1996**, *57* (6–8), 1057–1060. [https://doi.org/10.1016/0022-3697\(95\)00395-9](https://doi.org/10.1016/0022-3697(95)00395-9).
- (89) Briois, V.; La Fontaine, C.; Belin, S.; Barthe, L.; Moreno, T.; Pinty, V.; Carcy, A.; Girardot, R.; Fonda, E. ROCK: The New Quick-EXAFS Beamline at SOLEIL. *Journal of Physics: Conference Series* **2016**, *712*, 012149. <https://doi.org/10.1088/1742-6596/712/1/012149>.
- (90) Joly, Y.; Grenier, S. Theory of X-Ray Absorption Near Edge Structure. In *X-Ray Absorption and X-Ray Emission Spectroscopy*; Van Bokhoven, J. A., Lamberti, C., Eds.; John Wiley & Sons, Ltd: Chichester, UK, 2016; pp 73–97. <https://doi.org/10.1002/9781118844243.ch4>.
- (91) Horsley, J. A. Relationship between the Area of $L_{2,3}$ X-ray Absorption Edge Resonances and the d Orbital Occupancy in Compounds of Platinum and Iridium. *The Journal of Chemical Physics* **1982**, *76* (3), 1451–1458. <https://doi.org/10.1063/1.443105>.
- (92) Choy, J.-H.; Kim, D.-K.; Demazeau, G.; Jung, D.-Y. L_{III} -Edge XANES Study on Unusually High Valent Iridium in a Perovskite Lattice. *J. Phys. Chem.* **1994**, *98* (25), 6258–6262. <https://doi.org/10.1021/j100076a005>.
- (93) Lytle, F. W.; Greegor, R. B. Investigation of the “Join” between the near Edge and Extended X-ray Absorption Fine Structure. *Applied Physics Letters* **1990**, *56* (2), 192–194. <https://doi.org/10.1063/1.103282>.

- (94) Bolzan, A. A.; Fong, C.; Kennedy, B. J.; Howard, C. J. Structural Studies of Rutile-Type Metal Dioxides. *Acta Crystallogr., Sect. B: Struct. Sci.* **1997**, *53* (3), 373–380. <https://doi.org/10.1107/S0108768197001468>.
- (95) Laguna-Marco, M. A.; Kayser, P.; Alonso, J. A.; Martínez-Lope, M. J.; van Veenendaal, M.; Choi, Y.; Haskel, D. Electronic Structure, Local Magnetism, and Spin-Orbit Effects of Ir(IV)-, Ir(V)-, and Ir(VI)-Based Compounds. *Phys. Rev. B* **2015**, *91* (214433), 214433. <https://doi.org/10.1103/PhysRevB.91.214433>.
- (96) Kayser, P.; Martínez-Lope, M. J.; Alonso, J. A.; Retuerto, M.; Croft, M.; Ignatov, A.; Fernández-Díaz, M. T. Crystal Structure, Phase Transitions, and Magnetic Properties of Iridium Perovskites Sr_2MIrO_6 (M = Ni, Zn). *Inorg. Chem.* **2013**, *52* (19), 11013–11022. <https://doi.org/10.1021/ic401161d>.
- (97) Pearce, P. E.; Perez, A. J.; Rousse, G.; Saubanère, M.; Batuk, D.; Foix, D.; McCalla, E.; Abakumov, A. M.; Van Tendeloo, G.; Doublet, M.-L.; et al. Evidence for Anionic Redox Activity in a Tridimensional-Ordered Li-Rich Positive Electrode $\beta\text{-Li}_2\text{IrO}_3$. *Nat. Mater.* **2017**, *16* (5), 580–586. <https://doi.org/10.1038/nmat4864>.
- (98) Perez, A. J.; Batuk, D.; Saubanère, M.; Rousse, G.; Foix, D.; McCalla, E.; Berg, E. J.; Dugas, R.; H. W. van den Bos, K.; Doublet, M.-L.; et al. Strong Oxygen Participation in the Redox Governing the Structural and Electrochemical Properties of Na-Rich Layered Oxide Na_2IrO_3 . *Chem. Mater.* **2016**, *28* (22), 8278–8288. <https://doi.org/10.1021/acs.chemmater.6b03338>.
- (99) Shannon, R. D. Revised Effective Ionic-Radii and Systematic Studies of Interatomic Distances in Halides and Chalcogenides. *Acta Crystallographica Section A* **1976**, *32*, 751–767.
- (100) Larcher, D.; Tarascon, J.-M. Towards Greener and More Sustainable Batteries for Electrical Energy Storage. *Nat. Chem.* **2014**, *7* (1), 19–29. <https://doi.org/10.1038/nchem.2085>.
- (101) Etacheri, V.; Marom, R.; Elazari, R.; Salitra, G.; Aurbach, D. Challenges in the Development of Advanced Li-Ion Batteries: A Review. *Energy Environ. Sci.* **2011**, *4* (9), 3243–3262. <https://doi.org/10.1039/c1ee01598b>.
- (102) Rozier, P.; Sathiya, M.; Paulraj, A.-R.; Foix, D.; Desautay, T.; Taberna, P.-L.; Simon, P.; Tarascon, J.-M. Anionic Redox Chemistry in Na-Rich $\text{Na}_2\text{Ru}_{1-y}\text{Sn}_y\text{O}_3$ Positive Electrode Material for Na-Ion Batteries. *Electrochem. Commun.* **2015**, *53*, 29–32. <https://doi.org/10.1016/j.elecom.2015.02.001>.
- (103) Mortemard de Boisse, B.; Liu, G.; Ma, J.; Nishimura, S.; Chung, S.-C.; Kiuchi, H.; Harada, Y.; Kikkawa, J.; Kobayashi, Y.; Okubo, M.; et al. Intermediate Honeycomb Ordering to Trigger Oxygen Redox Chemistry in Layered Battery Electrode. *Nat. Commun.* **2016**, *7*, 11397. <https://doi.org/10.1038/ncomms11397>.

- (104) Tarascon, J.-M.; Le Page, Y.; Barboux, P.; Bagley, B. G.; Greene, L. H.; McKinnon, W. R.; Hull, G. W.; Giroud, M.; Hwang, D. M. Crystal Substructure and Physical Properties of the Superconducting Phase $\text{Bi}_4(\text{Sr}, \text{Ca})_6\text{Cu}_4\text{O}_{16+x}$. *Phys. Rev. B* **1988**, 37 (16), 9382–9389.
- (105) Urland, W.; Hoppe, R. The Oxoplatinates Na_2PtO_2 , Na_2PtO_3 , „ K_2PtO_3 ” Und „ Rb_2PtO_3 ”. *Zeitschrift für anorganische und allgemeine Chemie* **1972**, 392 (1), 23–36.
- (106) Zandbergen, H. W.; Groen, W. A.; Mijlthoff, F. C.; van Tendeloo, G.; Amelinckx, S. Models for the Modulation in $\text{A}_2\text{B}_2\text{Ca}_n\text{Cu}_{1+n}\text{O}_{6+2n}$, A, B = Bi, Sr or Tl, Ba and $n = 0, 1, 2$. *Physica C: Superconductivity* **1988**, 156 (3), 325–354. [https://doi.org/10.1016/0921-4534\(88\)90756-3](https://doi.org/10.1016/0921-4534(88)90756-3).
- (107) Christoph Koch. Determination of Core Structure Periodicity and Point Defect Density along Dislocations. PhD, Arizona State University, 2002.
- (108) Gent, W. E.; Lim, K.; Liang, Y.; Li, Q.; Barnes, T.; Ahn, S.-J.; Stone, K. H.; McIntire, M.; Hong, J.; Song, J. H.; et al. Coupling between Oxygen Redox and Cation Migration Explains Unusual Electrochemistry in Lithium-Rich Layered Oxides. *Nature Communications* **2017**, 8 (1). <https://doi.org/10.1038/s41467-017-02041-x>.
- (109) Rong, X.; Liu, J.; Hu, E.; Liu, Y.; Wang, Y.; Wu, J.; Yu, X.; Page, K.; Hu, Y.-S.; Yang, W.; et al. Structure-Induced Reversible Anionic Redox Activity in Na Layered Oxide Cathode. *Joule* **2018**, 2 (1), 125–140. <https://doi.org/10.1016/j.joule.2017.10.008>.
- (110) Dahéron, L.; Dedryvère, R.; Martinez, H.; Ménétrier, M.; Denage, C.; Delmas, C.; Gonbeau, D. Electron Transfer Mechanisms upon Lithium Deintercalation from LiCoO_2 to CoO_2 Investigated by XPS. *Chem. Mater.* **2008**, 20 (2), 583–590. <https://doi.org/10.1021/cm702546s>.
- (111) Shimoda, K.; Minato, T.; Nakanishi, K.; Komatsu, H.; Matsunaga, T.; Tanida, H.; Arai, H.; Ukyo, Y.; Uchimoto, Y.; Ogumi, Z. Oxidation Behaviour of Lattice Oxygen in Li-Rich Manganese-Based Layered Oxide Studied by Hard X-Ray Photoelectron Spectroscopy. *J. Mater. Chem. A* **2016**, 4 (16), 5909–5916. <https://doi.org/10.1039/C6TA01152G>.
- (112) Leriche, J. B.; Hamelet, S.; Shu, J.; Morcrette, M.; Masquelier, C.; Ouvrard, G.; Zerrouki, M.; Soudan, P.; Belin, S.; Elkaïm, E.; et al. An Electrochemical Cell for Operando Study of Lithium Batteries Using Synchrotron Radiation. *J. Electrochem. Soc.* **2010**, 157 (5), A606–A610. <https://doi.org/10.1149/1.3355977>.
- (113) Arnaud Perez. Energy Storage Properties of Iridium Oxides: Model Materials for the Study of Anionic Redox, Université Pierre et Marie Curie - Paris VI, 2017.
- (114) Fauth, F.; Boer, R.; Gil-Ortiz, F.; Popescu, C.; Vallcorba, O.; Peral, I.; Fullà, D.; Benach, J.; Juanhuix, J. The Crystallography Stations at the Alba Synchrotron.

- The European Physical Journal Plus* **2015**, *130* (8), 160.
<https://doi.org/10.1140/epjp/i2015-15160-y>.
- (115) Sears, V. F. Neutron Scattering Lengths and Cross Sections. *Neutron News* **1992**, *3* (3), 26–37. <https://doi.org/10.1080/10448639208218770>.
- (116) Perez, A. J.; Beer, R.; Lin, Z.; Salager, E.; Taberna, P.-L.; Abakumov, A. M.; Simon, P.; Tarascon, J.-M. Proton Ion Exchange Reaction in $\text{Li}_{3-x}\text{IrO}_4$: A Way to New $\text{H}_{3+x}\text{IrO}_4$ Phases Electrochemically Active in Both Aqueous and Nonaqueous Electrolytes. *Adv. Energy Mater.* **2018**, 1702855. <https://doi.org/10.1002/aenm.201702855>.
- (117) Lewis, N. S.; Nocera, D. G. Powering the Planet: Chemical Challenges in Solar Energy Utilization. *Proc. Natl. Acad. Sci.* **2006**, *103* (43), 15729–15735. <https://doi.org/10.1073/pnas.0603395103>.
- (118) Stamenkovic, V. R.; Strmcnik, D.; Lopes, P. P.; Markovic, N. M. Energy and Fuels from Electrochemical Interfaces. *Nat. Mater.* **2017**, *16* (1), 57–69. <https://doi.org/10.1038/nmat4738>.
- (119) Hong, W. T.; Risch, M.; Stoerzinger, K. A.; Grimaud, A.; Suntivich, J.; Shao-Horn, Y. Toward the Rational Design of Non-Precious Transition Metal Oxides for Oxygen Electrocatalysis. *Energy Environ. Sci.* **2015**, *8* (5), 1404–1427. <https://doi.org/10.1039/C4EE03869J>.
- (120) Montoya, J. H.; Seitz, L. C.; Chakthranont, P.; Vojvodic, A.; Jaramillo, T. F.; Nørskov, J. K. Materials for Solar Fuels and Chemicals. *Nat. Mater.* **2017**, *16* (1), 70–81. <https://doi.org/10.1038/nmat4778>.
- (121) Kanan, M. W.; Nocera, D. G. In Situ Formation of an Oxygen-Evolving Catalyst in Neutral Water Containing Phosphate and Co^{2+} . *Science* **2008**, *321* (5892), 1072–1075. <https://doi.org/10.1126/science.1162018>.
- (122) Grimaud, A.; May, K. J.; Carlton, C. E.; Lee, Y.-L.; Risch, M.; Hong, W. T.; Zhou, J.; Shao-Horn, Y. Double Perovskites as a Family of Highly Active Catalysts for Oxygen Evolution in Alkaline Solution. *Nat. Commun.* **2013**, *4*, 2439. <https://doi.org/10.1038/ncomms3439>.
- (123) Suntivich, J.; May, K. J.; Gasteiger, H. A.; Goodenough, J. B.; Shao-Horn, Y. A Perovskite Oxide Optimized for Oxygen Evolution Catalysis from Molecular Orbital Principles. *Science* **2011**, *334* (6061), 1383–1385. <https://doi.org/10.1126/science.1212858>.
- (124) Mefford, J. T.; Rong, X.; Abakumov, A. M.; Hardin, W. G.; Dai, S.; Kolpak, A. M.; Johnston, K. P.; Stevenson, K. J. Water Electrolysis on $\text{La}_{1-x}\text{Sr}_x\text{CoO}_{3-\delta}$ Perovskite Electrocatalysts. *Nat. Commun.* **2016**, *7*, 11053. <https://doi.org/10.1038/ncomms11053>.
- (125) Fabbri, E.; Haberer, A.; Waltar, K.; Kötter, R.; Schmidt, T. J. Developments and Perspectives of Oxide-Based Catalysts for the Oxygen Evolution Reaction.

- Catal. Sci. Technol.* **2014**, *4* (11), 3800–3821. <https://doi.org/10.1039/C4CY00669K>.
- (126) Fabbri, E.; Nachtegaal, M.; Binninger, T.; Cheng, X.; Kim, B.-J.; Durst, J.; Bozza, F.; Graule, T.; Schaublin, R.; Wiles, L.; et al. Dynamic Surface Self-Reconstruction Is the Key of Highly Active Perovskite Nano-Electrocatalysts for Water Splitting. *Nat. Mater.* **2017**, *16* (9), 925–931. <https://doi.org/10.1038/nmat4938>.
- (127) Cherevko, S.; Zeradjanin, A. R.; Topalov, A. A.; Kulyk, N.; Katsounaros, I.; Mayrhofer, K. J. J. Dissolution of Noble Metals during Oxygen Evolution in Acidic Media. *ChemCatChem* **2014**, *6* (8), 2219–2223. <https://doi.org/10.1002/cctc.201402194>.
- (128) Geiger, S.; Kasian, O.; Ledendecker, M.; Pizzutilo, E.; Mingers, A. M.; Fu, W. T.; Diaz-Morales, O.; Li, Z.; Oellers, T.; Fruchter, L.; et al. The Stability Number as a Metric for Electrocatalyst Stability Benchmarking. *Nature Catalysis* **2018**, *1* (7), 508–515. <https://doi.org/10.1038/s41929-018-0085-6>.
- (129) Pourbaix, M. *Atlas of Electrochemical Equilibria in Aqueous Solutions*; National Association of Corrosion Engineers, 1974.
- (130) Ng, J. W. D.; García-Melchor, M.; Bajdich, M.; Chakthranont, P.; Kirk, C.; Vojvodic, A.; Jaramillo, T. F. Gold-Supported Cerium-Doped NiO_x Catalysts for Water Oxidation. *Nat. Energy* **2016**, *1*, 16053. <https://doi.org/10.1038/nenergy.2016.53>.
- (131) Lee, Y.; Suntivich, J.; May, K. J.; Perry, E. E.; Shao-Horn, Y. Synthesis and Activities of Rutile IrO₂ and RuO₂ Nanoparticles for Oxygen Evolution in Acid and Alkaline Solutions. *J. Phys. Chem. Lett.* **2012**, *3* (3), 399–404. <https://doi.org/10.1021/jz2016507>.
- (132) Lettenmeier, P.; Wang, L.; Golla-Schindler, U.; Gazdzicki, P.; Cañas, N. A.; Handl, M.; Hiesgen, R.; Hosseiny, S. S.; Gago, A. S.; Friedrich, K. A. Nanosized IrO_x-Ir Catalyst with Relevant Activity for Anodes of Proton Exchange Membrane Electrolysis Produced by a Cost-Effective Procedure. *Angew. Chem.* **2016**, *128* (2), 752–756. <https://doi.org/10.1002/ange.201507626>.
- (133) Reier, T.; Nong, H. N.; Teschner, D.; Schlögl, R.; Strasser, P. Electrocatalytic Oxygen Evolution Reaction in Acidic Environments - Reaction Mechanisms and Catalysts. *Adv. Energy Mater.* **2017**, *7* (1), 1601275. <https://doi.org/10.1002/aenm.201601275>.
- (134) Rao, R. R.; Kolb, M. J.; Halck, N. B.; Pedersen, A. F.; Mehta, A.; You, H.; Stoerzinger, K. A.; Feng, Z.; Hansen, H. A.; Zhou, H.; et al. Towards Identifying the Active Sites on RuO₂ (110) in Catalyzing Oxygen Evolution. *Energy Environ. Sci.* **2017**, *10* (12), 2626–2637. <https://doi.org/10.1039/C7EE02307C>.
- (135) Spöri, C.; Kwan, J. T. H.; Bonakdarpour, A.; Wilkinson, D. P.; Strasser, P. The Stability Challenges of Oxygen Evolving Catalysts: Towards a Common

- Fundamental Understanding and Mitigation of Catalyst Degradation. *Angew. Chem., Int. Ed. Engl.* **2017**, *56* (22), 5994–6021. <https://doi.org/10.1002/anie.201608601>.
- (136) Grimaud, A.; Demortière, A.; Saubanère, M.; Dachraoui, W.; Duchamp, M.; Doublet, M.-L.; Tarascon, J.-M. Activation of Surface Oxygen Sites on an Iridium-Based Model Catalyst for the Oxygen Evolution Reaction. *Nat. Energy* **2016**, *2*, 16189.
- (137) Li, T.; Kasian, O.; Cherevko, S.; Zhang, S.; Geiger, S.; Scheu, C.; Felfer, P.; Raabe, D.; Gault, B.; Mayrhofer, K. J. J. Atomic-Scale Insights into Surface Species of Electrocatalysts in Three Dimensions. *Nat. Catalysis* **2018**, *1* (4), 300–305. <https://doi.org/10.1038/s41929-018-0043-3>.
- (138) Diaz-Morales, O.; Calle-Vallejo, F.; De Munck, C.; Koper, M. T. M. Electrochemical Water Splitting by Gold: Evidence for an Oxide Decomposition Mechanism. *Chemical Science* **2013**, *4* (6), 2334–2343. <https://doi.org/10.1039/c3sc50301a>.
- (139) Wohlfahrt-Mehrens, M.; Heitbaum, J. Oxygen Evolution on Ru and RuO₂ Electrodes Studied Using Isotope Labelling and On-Line Mass Spectrometry. *J. Electroanal. Chem. Interfacial Electrochem.* **1987**, *237* (2), 251–260. [https://doi.org/10.1016/0022-0728\(87\)85237-3](https://doi.org/10.1016/0022-0728(87)85237-3).
- (140) Pfeifer, V.; Jones, T. E.; Velasco Vélez, J. J.; Arrigo, R.; Piccinin, S.; Hävecker, M.; Knop-Gericke, A.; Schlögl, R. In Situ Observation of Reactive Oxygen Species Forming on Oxygen-Evolving Iridium Surfaces. *Chemical Science* **2017**, *8* (3), 2143–2149. <https://doi.org/10.1039/c6sc04622c>.
- (141) Abbott, D. F.; Lebedev, D.; Waltar, K.; Povia, M.; Nachtegaal, M.; Fabbri, E.; Copéret, C.; Schmidt, T. J. Iridium Oxide for the Oxygen Evolution Reaction: Correlation between Particle Size, Morphology, and the Surface Hydroxo Layer from Operando XAS. *Chem. Mater.* **2016**, *28* (18), 6591–6604. <https://doi.org/10.1021/acs.chemmater.6b02625>.
- (142) Minguzzi, A.; Locatelli, C.; Lugaresi, O.; Achilli, E.; Cappelletti, G.; Scavini, M.; Coduri, M.; Masala, P.; Sacchi, B.; Vertova, A.; et al. Easy Accommodation of Different Oxidation States in Iridium Oxide Nanoparticles with Different Hydration Degree as Water Oxidation Electrocatalysts. *ACS Catal.* **2015**, *5* (9), 5104–5115. <https://doi.org/10.1021/acscatal.5b01281>.
- (143) Costentin, C.; Nocera, D. G. Self-Healing Catalysis in Water. *Proc. Natl. Acad. Sci.* **2017**, *114* (51), 13380–13384. <https://doi.org/10.1073/pnas.1711836114>.
- (144) Reier, T.; Pawolek, Z.; Cherevko, S.; Bruns, M.; Jones, T.; Teschner, D.; Selve, S.; Bergmann, A.; Nong, H. N.; Schlögl, R.; et al. Molecular Insight in Structure and Activity of Highly Efficient, Low-Ir Ir–Ni Oxide Catalysts for Electrochemical Water Splitting (OER). *J. Am. Chem. Soc.* **2015**, *137* (40), 13031–13040. <https://doi.org/10.1021/jacs.5b07788>.

- (145) Nong, H. N.; Oh, H.-S.; Reier, T.; Willinger, E.; Willinger, M.-G.; Petkov, V.; Teschner, D.; Strasser, P. Oxide-Supported IrNiO_x Core-Shell Particles as Efficient, Cost-Effective, and Stable Catalysts for Electrochemical Water Splitting. *Angew. Chem., Int. Ed. Engl.* **2015**, *54* (10), 2975–2979. <https://doi.org/10.1002/anie.201411072>.
- (146) Sanchez Casalongue, H. G.; Ng, M. L.; Kaya, S.; Friebel, D.; Ogasawara, H.; Nilsson, A. In Situ Observation of Surface Species on Iridium Oxide Nanoparticles during the Oxygen Evolution Reaction. *Angew. Chem.* **2014**, *126* (28), 7297–7300. <https://doi.org/10.1002/ange.201402311>.
- (147) Seitz, L. C.; Dickens, C. F.; Nishio, K.; Hikita, Y.; Montoya, J.; Doyle, A.; Kirk, C.; Vojvodic, A.; Hwang, H. Y.; Norskov, J. K. A Highly Active and Stable IrO_x/SrIrO₃ Catalyst for the Oxygen Evolution Reaction. *Science* **2016**, *353* (6303), 1011–1014. <https://doi.org/10.1126/science.aaf5050>.
- (148) Kasian, O.; Grote, J.-P.; Geiger, S.; Cherevko, S.; Mayrhofer, K. J. J. The Common Intermediates of Oxygen Evolution and Dissolution Reactions during Water Electrolysis on Iridium. *Angew. Chem., Int. Ed. Engl.* **2018**, *57* (9), 2488–2491. <https://doi.org/10.1002/anie.201709652>.
- (149) Saveleva, V. A.; Wang, L.; Teschner, D.; Jones, T.; Gago, A. S.; Friedrich, K. A.; Zafeirotas, S.; Schlögl, R.; Savinova, E. R. Operando Evidence for a Universal Oxygen Evolution Mechanism on Thermal and Electrochemical Iridium Oxides. *J. Phys. Chem. Lett.* **2018**, *9* (11), 3154–3160. <https://doi.org/10.1021/acs.jpcclett.8b00810>.
- (150) Willinger, E.; Massué, C.; Schlögl, R.; Willinger, M. G. Identifying Key Structural Features of IrO_x Water Splitting Catalysts. *J. Am. Chem. Soc.* **2017**, *139* (34), 12093–12101. <https://doi.org/10.1021/jacs.7b07079>.
- (151) Feng, Z.; Hong, W. T.; Fong, D. D.; Lee, Y. L.; Yacoby, Y.; Morgan, D.; Shao-Horn, Y. Catalytic Activity and Stability of Oxides: The Role of Near-Surface Atomic Structures and Compositions. *Accounts of Chemical Research* **2016**, *49* (5), 966–973. <https://doi.org/10.1021/acs.accounts.5b00555>.
- (152) Cherevko, S.; Geiger, S.; Kasian, O.; Kulyk, N.; Grote, J.-P.; Savan, A.; Shrestha, B. R.; Merzlikin, S.; Breitbach, B.; Ludwig, A.; et al. Oxygen and Hydrogen Evolution Reactions on Ru, RuO₂, Ir, and IrO₂ Thin Film Electrodes in Acidic and Alkaline Electrolytes: A Comparative Study on Activity and Stability. *Catal. Today* **2016**, *262*, 170–180. <https://doi.org/10.1016/j.cattod.2015.08.014>.
- (153) Kim, Y.-T.; Lopes, P. P.; Park, S.-A.; Lee, A.-Y.; Lim, J.; Lee, H.; Back, S.; Jung, Y.; Danilovic, N.; Stamenkovic, V.; et al. Balancing Activity, Stability and Conductivity of Nanoporous Core-Shell Iridium/Iridium Oxide Oxygen Evolution Catalysts. *Nat. Commun.* **2017**, *8* (1). <https://doi.org/10.1038/s41467-017-01734-7>.

- (154) Costentin, C.; Porter, T. R.; Savéant, J.-M. Conduction and Reactivity in Heterogeneous-Molecular Catalysis: New Insights in Water Oxidation Catalysis by Phosphate Cobalt Oxide Films. *J. Am. Chem. Soc.* **2016**, *138* (17), 5615–5622. <https://doi.org/10.1021/jacs.6b00737>.
- (155) Dau, H.; Limberg, C.; Reier, T.; Risch, M.; Roggan, S.; Strasser, P. The Mechanism of Water Oxidation: From Electrolysis via Homogeneous to Biological Catalysis. *ChemCatChem* **2010**, *2* (7), 724–761. <https://doi.org/10.1002/cctc.201000126>.
- (156) Diaz-Morales, O.; Raaijman, S.; Kortlever, R.; Kooyman, P. J.; Wezendonk, T.; Gascon, J.; Fu, W. T.; Koper, M. T. M. Iridium-Based Double Perovskites for Efficient Water Oxidation in Acid Media. *Nat. Commun.* **2016**, *7*, 12363. <https://doi.org/10.1038/ncomms12363>.
- (157) Grimaud, A.; Diaz-Morales, O.; Han, B.; Hong, W. T.; Lee, Y.-L.; Giordano, L.; Stoerzinger, K. A.; Koper, M. T. M.; Shao-Horn, Y. Activating Lattice Oxygen Redox Reactions in Metal Oxides to Catalyse Oxygen Evolution. *Nat. Chem.* **2017**, *9* (5), 457–465. <https://doi.org/10.1038/nchem.2695>.
- (158) Zhang, R.; Dubouis, N.; Ben Osman, M.; Yin, W.; Sougrati, M. T.; Corte, D. A. D.; Giaume, D.; Grimaud, A. A Dissolution/Precipitation Equilibrium on the Surface of Iridium-Based Perovskites Controls Their Activity as Oxygen Evolution Reaction Catalysts in Acidic Media. *Angew. Chem., Int. Ed. Engl.* **2019**, *58* (14), 4571–4575. <https://doi.org/10.1002/anie.201814075>.
- (159) Minguzzi, A.; Lugaresi, O.; Achilli, E.; Locatelli, C.; Vertova, A.; Ghigna, P.; Rondinini, S. Observing the Oxidation State Turnover in Heterogeneous Iridium-Based Water Oxidation Catalysts. *Chem. Sci.* **2014**, *5* (9), 3591–3597. <https://doi.org/10.1039/C4SC00975D>.
- (160) Geiger, S.; Kasian, O.; Shrestha, B. R.; Mingers, A. M.; Mayrhofer, K. J.; Cherevko, S. Activity and Stability of Electrochemically and Thermally Treated Iridium for the Oxygen Evolution Reaction. *J. Electrochem. Soc.* **2016**, *163* (11), F3132–F3138. <https://doi.org/10.1149/2.0181611jes>.
- (161) Pfeifer, V.; Jones, T. E.; Velasco Vélez, J. J.; Arrigo, R.; Piccinin, S.; Hävecker, M.; Knop-Gericke, A.; Schlögl, R. In Situ Observation of Reactive Oxygen Species Forming on Oxygen-Evolving Iridium Surfaces. *Chem. Sci.* **2017**, *8* (3), 2143–2149. <https://doi.org/10.1039/C6SC04622C>.
- (162) Wu, J.; Li, Q.; Sallis, S.; Zhuo, Z.; Gent, W.; Chueh, W.; Yan, S.; Chuang, Y.; Yang, W. Fingerprint Oxygen Redox Reactions in Batteries through High-Efficiency Mapping of Resonant Inelastic X-Ray Scattering. *Condens. Matter* **2019**, *4* (1), 5. <https://doi.org/10.3390/condmat4010005>.
- (163) de Groot, F. M. F.; Grioni, M.; Fuggle, J. C.; Ghijsen, J.; Sawatzky, G. A.; Petersen, H. Oxygen *1 s* x-Ray-Absorption Edges of Transition-Metal Oxides. *Phys. Rev. B* **1989**, *40* (8), 5715–5723. <https://doi.org/10.1103/PhysRevB.40.5715>.

- (164) Tarascon, J.-M.; Gozdz, A. S.; Schmutz, C.; Shokoohi, F.; Warren, P. C. Performance of Bellcore's Plastic Rechargeable Li-Ion Batteries. *Solid State Ionics* **1996**, 86–88, 49–54. [https://doi.org/10.1016/0167-2738\(96\)00330-X](https://doi.org/10.1016/0167-2738(96)00330-X).
- (165) Assat, G.; Delacourt, C.; Corte, D. A. D.; Tarascon, J.-M. Editors' Choice—Practical Assessment of Anionic Redox in Li-Rich Layered Oxide Cathodes: A Mixed Blessing for High Energy Li-Ion Batteries. *J. Electrochem. Soc.* **2016**, 163 (14), A2965–A2976. <https://doi.org/10.1149/2.0531614jes>.
- (166) Rueff, J.-P.; Ablett, J. M.; Céolin, D.; Prieur, D.; Moreno, T.; Balédent, V.; Lassalle-Kaiser, B.; Rault, J. E.; Simon, M.; Shukla, A. The GALAXIES Beamline at the SOLEIL Synchrotron: Inelastic X-Ray Scattering and Photoelectron Spectroscopy in the Hard X-Ray Range. *Journal of Synchrotron Radiation* **2015**, 22 (1), 175–179. <https://doi.org/10.1107/S160057751402102X>.
- (167) Rueff, J.-P.; Rault, J. E.; Ablett, J. M.; Utsumi, Y.; Céolin, D. HAXPES for Materials Science at the GALAXIES Beamline. *Synchrotron Radiation News* **2018**, 31 (4), 4–9. <https://doi.org/10.1080/08940886.2018.1483648>.
- (168) Adams, S. From Bond Valence Maps to Energy Landscapes for Mobile Ions in Ion-Conducting Solids. *Solid State Ionics* **2006**, 177 (19–25), 1625–1630. <https://doi.org/10.1016/j.ssi.2006.03.054>.
- (169) Shirley, D. A. High-Resolution X-Ray Photoemission Spectrum of the Valence Bands of Gold. *Phys. Rev. B* **1972**, 5 (12), 4709–4714. <https://doi.org/10.1103/PhysRevB.5.4709>.
- (170) Scofield, J. H. Hartree-Slater Subshell Photoionization Cross-Sections at 1254 and 1487 eV. *Journal of Electron Spectroscopy and Related Phenomena* **1976**, 8 (2), 129–137. [https://doi.org/10.1016/0368-2048\(76\)80015-1](https://doi.org/10.1016/0368-2048(76)80015-1).
- (171) Suntivich, J.; Gasteiger, H. A.; Yabuuchi, N.; Shao-Horn, Y. Electrocatalytic Measurement Methodology of Oxide Catalysts Using a Thin-Film Rotating Disk Electrode. *Journal of The Electrochemical Society* **2010**. <https://doi.org/10.1149/1.3456630>.
- (172) Messinger, R. J.; Ménétrier, M.; Salager, E.; Boulineau, A.; Duttine, M.; Carlier, D.; Ateba-Mba, J. M.; Croguennec, L.; Masquelier, C.; Massiot, D.; et al. Revealing Defects in Crystalline Lithium-Ion Battery Electrodes by Solid-State NMR: Applications to LiVPO₄F. *Chem. Mater.* **2015**, 27 (15), 5212–5221. <https://doi.org/10.1021/acs.chemmater.5b01234>.
- (173) Massiot, D.; Fayon, F.; Capron, M.; King, I.; Le Calvé, S.; Alonso, B.; Durand, J.-O.; Bujoli, B.; Gan, Z.; Hoatson, G. Modelling One- and Two-Dimensional Solid-State NMR Spectra: Modelling 1D and 2D Solid-State NMR Spectra. *Magnetic Resonance in Chemistry* **2002**, 40 (1), 70–76. <https://doi.org/10.1002/mrc.984>.

- (174) Grey, C. P.; Dupré, N. NMR Studies of Cathode Materials for Lithium-Ion Rechargeable Batteries. *Chem. Rev.* **2004**, *104* (10), 4493–4512. <https://doi.org/10.1021/cr020734p>.

Résumé étendu :

Introduction générale

La production d'énergie propre et renouvelable est essentielle pour atténuer le réchauffement climatique et la crise énergétique à venir. Des efforts importants sont investis dans le développement de technologies telles que le photovoltaïque et les éoliennes, qui permettent la conversion de l'énergie solaire et éolienne en électricité. Ces technologies sont de nature intermittente, leur intégration au réseau est donc difficile. Afin de remédier à ce problème, les systèmes de stockage d'énergie doivent être développés en parallèle. La batterie à ion lithium (BIL) est une technologie qui gagne en popularité grâce à sa polyvalence et à son coût décroissant. La capacité de stocker de grandes quantités d'énergie et de disposer de capacités de puissance raisonnables constitue un avantage considérable pour les applications de réseau. De plus, cela permet aux systèmes d'alimentation isolés qui reposent sur des panneaux solaires ou des éoliennes mais n'ont pas accès au réseau. De plus, développer des alternatives aux combustibles fossiles pour la mobilité est crucial pour la transition vers une planète plus verte. Bien que la densité énergétique et la fiabilité des BIL se soient considérablement améliorées depuis leur première commercialisation en 1991 par Sony, les exigences actuelles ne sont toujours pas satisfaites et de nouvelles améliorations s'imposent. Par ailleurs, des préoccupations au sujet de l'abondance limitée du lithium ont été à l'origine du développement de technologies de batteries alternatives, notamment la technologie à ion sodium. Bien qu'elle n'ait pas encore atteint la maturité des BIL, les matériaux utilisés pour de tels systèmes à base de sodium ont été considérablement améliorés.

Le développement des nouveaux matériaux d'électrodes positives à haute densité d'énergie pour les technologies de batteries a été bouleversé par un nouveau paradigme : la participation de l'oxygène du réseau cristallin dans les processus redox lors de l'insertion et de l'extraction des ions alcalins dans une certaine famille d'oxydes. Cela permet aux matériaux présentant une telle activité d'augmenter leur capacité réversible à haut potentiel, augmentant ainsi leur densité d'énergie. Cependant, cela a généralement un prix sur la durée de vie en cyclage et une dégradation importante des performances au cours du temps est observée. Alors que le premier chapitre approfondira ce sujet, le

but de cette thèse est d'étudier les implications structurales et électroniques du rédox anionique dans un matériau d'insertion $A_x\text{IrO}_3$, avec $A = \text{Li}$ ou Na . L'utilisation de techniques analytiques de pointe, telles que la diffraction des rayons X en synchrotron et de la diffraction de neutrons sur poudre, ainsi que l'absorption des rayons X ou la spectroscopie de photoémission X, permet de sonder les différents aspects d'un processus aussi subtil. Obtenir une bonne compréhension des répercussions structurales et électroniques de l'oxydation de l'oxygène du réseau est cruciale pour aider la communauté scientifique à trouver des solutions et rendre ces matériaux viables sur le plan industriel.

Alors que les technologies de batterie sont des systèmes de stockage d'énergie prometteurs et sont devenues dominantes dans le secteur des transports et de l'électronique portable, le paysage énergétique de demain se composera vraisemblablement de toute une gamme de technologies différentes, dont les piles à hydrogène. En effet, utiliser l'hydrogène comme carburant et contrôler sa recombinaison avec l'oxygène pour former de l'eau tout en fournissant de grandes quantités d'énergie semble être une solution idéale. Cependant, des efforts considérables ont été déployés pour développer des systèmes efficaces capables de produire de l'hydrogène à partir d'eau en utilisant uniquement des énergies renouvelables, mais les progrès ont été rares au cours des dernières décennies. L'un des principaux obstacles est la cinétique lente de la réaction d'oxydation de l'eau (*oxygen evolution reaction* en anglais, soit OER) - réaction opposée à l'évolution de l'hydrogène - qui se traduit par de lourdes pénalités en énergie. La production d'hydrogène peut être effectuée dans des environnements acides et alcalins, mais les surtensions les plus faibles sont obtenues à des pH très bas. Dans ces conditions difficiles, les matériaux catalyseurs de l'OER composés d'oxydes de métaux de transition se dissolvent généralement lors de la polarisation anodique. Les meilleurs matériaux sont aujourd'hui composés d'Iridium ou de Ruthénium, les derniers étant moins stables et les premiers moins actifs. L'iridate décrit dans cette thèse présente des propriétés intéressantes pour la catalyse de l'OER. En effet, sa capacité à absorber et à délivrer des protons a permis de mieux comprendre le mécanisme de compensation de charge d'un oxyde d'iridium hydraté longtemps suspecté. En outre, la possibilité de former IrO_3 par oxydation du $\beta\text{-Li}_2\text{IrO}_3$ dans un milieu organique a permis l'étude d'un iridate de haute valence soupçonné d'être l'intermédiaire actif lors de la catalyse de l'OER à la surface d'oxydes d'iridium. Il est important de poursuivre la recherche de

catalyseurs efficaces capables d'abaisser les surtensions élevées rencontrés lors de la réaction de dissociation de l'eau afin de permettre la production de dihydrogène à moindre coûts et l'utilisation à grande échelle des piles à combustible.

Le sujet de cette thèse est l'étude de l'oxydoréduction de l'oxygène du réseau de l'hôte IrO_3 lors de l'insertion et de l'extraction de Li et de Na, ainsi que sur la surface de la phase protonée en milieu acide. Les domaines concernés par ces travaux sont les technologies de batteries à ion Li et Na et l'électrocatalyse de la réaction d'oxydation de l'eau. Ce manuscrit est divisé en quatre chapitres, sans compter cette courte introduction générale.

Chapitre I. Introduction aux batteries

La technologie à ion lithium est caractérisée par l'utilisation de deux matériaux d'insertion comme électrode négative et positive.^{4,5} Dans ce cas, le problème des dendrites inhérent à l'utilisation du lithium métallique comme électrode négative est contourné mais la densité énergétique s'en voit considérablement diminuée. En effet, la capacité théorique du lithium est de $3862 \text{ mA}\cdot\text{h/g}$ alors que le graphite, matériau qui le remplace communément aujourd'hui, a une capacité théorique de $372 \text{ mA}\cdot\text{h/g}$, soit dix fois inférieure. De plus, la formation d'une couche de passivation à sa surface due à la dégradation de l'électrolyte à bas potentiel et qui permet le bon fonctionnement de la batterie à long terme, mène néanmoins à une importante perte de capacité lors de la première charge.

Malgré ces pertes à l'électrode négative, la densité énergétique reste limitée principalement par l'utilisation d'oxydes de métaux de transitions lourds à l'électrode positive. Les matériaux d'insertions les plus utilisés sont des phosphates de fer ou bien des oxydes mixtes à base de cobalt, de nickel, de manganèse et/ou d'aluminium. Le composé utilisé dans les premières batteries Li-ion commercialisées en 1991 par Sony était LiCoO_2 qui possède une structure lamellaire avec le cobalt et le lithium en sites octaédriques dans un empilement compact d'oxygène. Les ions cobalt et lithium sont arrangés de façon à former des couches alternées ce qui permet des chemins de diffusion du lithium en deux dimensions. La capacité de ce matériau est de $140 \text{ mA}\cdot\text{h/g}$ à des potentiel autour de $4 \text{ V vs Li}^+/\text{Li}$ et reste couramment utilisé.²

Afin d'augmenter la densité d'énergie et d'améliorer la stabilité du composé, les chercheurs ont substitué le cobalt par du nickel et/ou du manganèse pour obtenir des composés de formule $\text{Li}(\text{Ni}_x\text{Mn}_y\text{Co}_{1-x-y})\text{O}_2$ qui constitue la famille de composés couramment utilisée aujourd'hui et connue sous le nom de NMC.⁶ Différents ratio des métaux de transitions apportent différentes propriétés mais c'est le nickel qui apporte le plus de capacité et la tendance d'aujourd'hui est de peu à peu augmenter sa concentration. Le premier à être implémenter dans les batteries commerciales était le NMC 111, i.e. avec un rapport 1/1/1 de Ni/Mn/Co. Désormais, l'industrie cherche à utiliser des composés plus riches en nickel tel que les NMC 622 et 811 pour atteindre des capacités supérieur à 200 mA.h/g.^{7,8} Malheureusement cette augmentation de capacité s'accompagne d'une forte instabilité et de risques d'explosions accrues. Il est donc nécessaire de mettre au point des stratégies permettant de pallier ces problèmes de stabilité thermique.

Récemment, de nouveaux matériaux oxydes dérivées des NMC dans lesquels les métaux de transitions sont substitués par du Li pour donner des composés de formule $\text{Li}_{1+x}\text{M}_{1-x}\text{O}_2$ avec $x \leq 1/3$ ($M = \text{Ni}, \text{Mn}$ and/or Co) pouvant aussi s'écrire Li_2MO_3 pour $x = 1/3$.^{9,10} Ces composés forment ainsi des structures lamellaires dans lesquelles du lithium est présent dans les couches de métaux de transition avec un arrangement des métaux de transition en nid d'abeille et le lithium au centre. La possibilité d'atteindre des capacités bien supérieures à la capacité théorique que peut apporter les métaux de transition a provoqué un fort engouement de la part de la communauté scientifique. En effet, classiquement l'insertion et la désinsertion du lithium sont contrebalancées par la réduction et l'oxydation du cation métallique à des degrés d'oxydation bien définis. Cependant, dans ces nouveaux matériaux, une capacité supplémentaire est observée ce qui provoquât bien des discussions sur son origine. La complexité apporté par la présence de plusieurs centres redox ne permis pas de déterminer clairement le mécanisme mis en jeu. Ce n'est qu'en développant des matériaux dit « modèles » de formule Li_2MO_3 avec $M = \text{Ru}$ ou Ir , ayant une structure et une électrochimie similaire que les chercheurs ont pu mettre en évidence la participation des oxygènes du réseau aux processus redox d'insertion/désinsertion du lithium.

Malheureusement, cette augmentation de la capacité s'accompagne généralement d'un dégagement d'oxygène à haut potentiel et de migrations cationiques qui mènent à

une densification de la surface des particules.^{11,12} Cette densification est irréversible et se manifeste par (i) une augmentation de la résistance qui mène à une polarisation et (ii) à une perte de capacité.^{13–17} Comprendre les implications structurales et électroniques de ce nouveau mécanisme de compensation de charge lors du cyclage est essentielle à l'intégration de ces matériaux dans le marché. Cette compréhension passe par l'étude systématique d'une variété de matériaux ayant la capacité de faire appel au réseau d'oxygène et au développement de techniques analytiques robustes qui permettent d'observer *in situ* et même *operando* les évolutions structurales et électroniques. Ce nouveau paradigme a d'autre part été généralisé aux matériaux d'insertion du Na^+ avec néanmoins les mêmes problématiques de pertes de performances.

Chapitre II. Les implications structurales et électroniques de la délithiation de la $\beta\text{-Li}_2\text{IrO}_3$

Le composé Li_2IrO_3 peut cristalliser en trois polymorphes reportés. La phase α qui possède la même structure que les Li-rich NMC avec notamment des couches de lithium alternées avec des couches de métaux de transition arrangés en nid d'abeille avec le lithium au centre des hexagones formés par les octaèdres de métaux de transition. La phase β qui possède une structure différente par son arrangement cationique avec la moitié des métaux de transitions qui sont dans la couche de lithium formant une structure dite « *hyperhoneycomb* ». La phase γ qui possède une structure intermédiaire avec seulement un quart des métaux de transition qui sont présents dans la couche de lithium. Cette dernière phase n'a pas encore été étudiée pour ses propriétés électrochimiques en raison de la difficulté de sa synthèse.

Le comportement électrochimique de ce composé a été évalué et présente quatre plateaux successifs en charges à 3.45 V, 3.55 V, 4.45 V et 4.6 V vs Li^+/Li signifiant quatre processus biphasiques s'opérant chaque 0.5 Li^+ extrait et menant à une phase totalement délithiée de composition IrO_3 . Ces plateaux sont conservés lors de la décharge avec cependant la nécessité de pousser le potentiel jusqu'à 1.6 V pour observer un plateau autour de 1.8 V qui permet de retrouver le composé d'origine. Ce nouveau plateau est d'origine cinétique comme en atteste les résultats du titrage galvanostatique intermittent où une large polarisation est observée. Il est par ailleurs possible d'insérer 0.5 Li^+ supplémentaires dans la structure si on décharge le matériau jusqu'à 1.35 V.

Cette insertion s'opère via deux plateaux successifs à 1.55 V et 1.45 V. Il est possible de cycliser le matériau sur toute sa composition, i.e. entre $\text{Li}_{2.5}\text{IrO}_3$ et IrO_3 mais il semble que les processus s'opérant à haut potentiel aient un fort impact sur la tenue en cyclage de la capacité et du voltage. Chaque processus a été caractérisé par des techniques de diffraction des rayons X *operando* et de neutrons *ex situ* ainsi que par spectroscopies d'absorption et de photoémission X *ex situ*.

La diffraction des rayons X permet de constater qu'il y a de multiples processus biphasiques et que les processus à haut potentiel mènent à une diminution de la longueur de cohérence ainsi qu'à de fortes tensions cristallographique qui se manifestent par un élargissement des pics de Bragg. Chaque intermédiaire a pu être isolé et sa structure déterminée par affinement des diffractogrammes par la méthode de Rietveld. Des mesures de diffraction de neutrons sur poudre sur les intermédiaires de composition $x = 2.5, 2.0, 1$ et 0.5 avec x dans Li_xIrO_3 ont permis de déterminer que l'oxydation de la phase initiale provoque une distorsion des octaèdres IrO_6 et une diminution de certaines distances O-O, notamment entre les iridium, alors que la réduction mène à une croissance homogène des octaèdres IrO_6 . La diminution des distances O-O et ainsi la distorsion qui en découle, a été attribuée à la formation d'espèces dites « peroxy-like » dont l'origine est la rédox anionique. Il est donc intéressant de voir qu'a priori, l'oxygène serait actif en charge entre $x = 2$ et 0 . Il est par ailleurs cohérent que l'oxygène ne participe pas au processus de décharge entre $x = 2$ et 2.5 puisqu'il se trouve déjà sous sa forme réduite.

Afin de vérifier que l'oxygène participe bien au processus de compensation de charge lors de la désinsertion de Li^+ de la phase $\beta\text{-Li}_2\text{IrO}_3$, la spectroscopie d'absorption X a été utilisée au seuil L_3 de l'iridium afin de suivre le degré d'oxydation du cation métallique lors de la charge. Ces expériences ont été menées sur la ligne ROCK du synchrotron soleil en France. Les résultats montrent que l'iridium est oxydé selon trois régimes différents. L'iridium est oxydé de façon plus significative entre $x = 2.5$ et 2 , puis un peu moins entre $x = 2$ et 1 et de façon négligeable entre $x = 1$ et 0 . Il serait donc aisé de penser que l'iridium compense la charge principalement jusqu'à $x = 1$ puis l'oxygène compense la charge entre $x = 1$ et 0 . La portion du spectre étendue aux hautes énergies permet d'obtenir des informations sur l'environnement local de l'iridium et indirectement d'obtenir les distances O-O entre deux atomes d'iridium voisins. Il est

intéressant de voir que les résultats obtenus par diffraction de neutrons sur poudre sont retrouvés ici.

D'autre part, le degré d'oxydation de l'oxygène peut être suivi par spectroscopie de photoémission X au niveau 1s de l'oxygène. Afin d'augmenter la profondeur d'analyse, l'utilisation de rayons X de haute énergie (6900 eV) a été utilisée grâce à la ligne GALAXIES du synchrotron Soleil en France. Cette spectroscopie est l'une des premières techniques qui a permis de mettre en évidence la présence d'oxygènes oxydés dans les matériaux de batterie. Le signal de ces espèces « O^{n-} » dites « peroxo-like » sort à 531 eV alors que les oxygènes O^{2-} ont un signal à 529.8 eV.¹⁸⁻²⁰ Étonnamment, un signal à 531 eV apparaît dès l'extraction du premier lithium, soit de $x = 2$ à 1. Ce signal augmente considérablement quand la charge est poursuivie jusqu'à $x = 0$. Ce signal disparaît lors de la décharge, attestant de la réversibilité du processus. Il n'est pas surprenant de voir que le composé déchargé à $x = 2.5$ ne possède qu'un signal d'oxygène à 529.8 eV, signifiant que tous les oxygènes sont au degré d'oxydation $-II$.

Ces résultats nous mènent à conclure que l'extraction de Li^+ du composé β - Li_2IrO_3 se fait grâce à une compensation de la charge qui dans un premier temps est majoritairement portée par l'iridium et qui dans un second temps est majoritairement portée par le réseau d'oxygène. Hors, comme expliqué plus haut, les processus s'opérant à haut potentiel semblent avoir un fort impact sur la cyclabilité du matériau. Ceci pointe vers un effet néfaste de la rédox anionique similairement à ce qui est observé dans les composés lamellaires riches en lithium lorsque de trop hauts potentiels sont atteints et ce malgré une structure tridimensionnelle supposée plus robuste. En revanche, la diminution des distances O-O semble être linéaire durant tout le processus de charge, supposant une contribution constante de l'oxygène au mécanisme de compensation de charge. Cependant, les résultats de spectroscopie indiquent autrement, ce qui supposerait que la distance O-O n'est pas un indicateur correct du degré de participation du réseau d'oxygène. La question de l'origine de cette distorsion et son implication dans le processus de rédox anionique reste ouverte.

Chapitre III. IrO_3 comme structure hôte d'ions Na^+ ayant un réseau d'oxygène actif

Le composé Na_2IrO_3 est bien connu et sa capacité à dé/insérer du Na^+ a été rigoureusement caractérisée. Cependant, d'autres polymorphes de ce composé n'ont pas encore été reportés. La synthèse céramique classique n'ayant pas permis l'obtention d'autres polymorphes, une autre stratégie a été ici implémentée. En effet, au vu de la possibilité d'obtenir le composé IrO_3 par délithiation électrochimique de la phase $\beta\text{-Li}_2\text{IrO}_3$ sans ajout d'additifs conducteurs, il est alors possible d'envisager une sodiation électrochimique de la même manière. Cependant, alors qu'une sodiation partielle jusqu'à 1.7 Na^+ a été obtenue, le composé stœchiométrique n'a pas été obtenu même en déchargeant jusqu'à 1.0 V vs Na^+/Na .

Grâce à la diffraction des rayons X *operando* menée sur la ligne MSDP au synchrotron Alba en Espagne, les changements structuraux qui prennent place durant la première décharge et la charge qui suit ont été caractérisés. La première décharge suit un comportement similaire à celle vs Li^+/Li avec notamment quatre plateaux successifs entre 4.5 V et 2.0 V vs Na^+/Na . Les intermédiaires sodiés possèdent tous une structure de géométrie orthorhombique avec cependant des paramètres de mailles (obtenues par affinement des diffractogrammes de composés purs par la méthode Rietveld) qui diffèrent et un volume de cellule qui augmente considérablement tout au long de la décharge. Tous ces processus à l'exception de celui à haut potentiel, qui compte pour 0.5 Na^+ , sont réversibles en charge et en décharge avec des paramètres de mailles des composés intermédiaires qui se superposent, attestant de la réversibilité des processus.

La spectroscopie de photoémission X a été utilisée pour évaluer la contribution de l'oxygène aux processus d'insertion et de désinsertion du sodium dans le composé $\text{Na}_{1.7}\text{IrO}_3$. Une nette diminution de l'intensité du pic à 531 eV après première sodiation de IrO_3 atteste de la réduction de l'oxygène et de sa participation au processus mais sa persistance indique que tous les oxygènes ne sont pas réduits et qu'il y a donc une participation partielle de l'oxygène. Lors de la charge qui suit, l'oxygène est de nouveau oxydé pour atteindre le même rapport entre $\text{O}^{\cdot-}$ et O^{2-} que pour IrO_3 , indiquant une forte participation de l'oxygène aux processus redox du composé $\text{Na}_{1.7}\text{IrO}_3$. Cette activité anionique pourrait avoir un effet néfaste sur les performances du matériau au

long terme mais le cyclage obtenu en cellule complète (utilisant du carbone non graphitisable comme électrode négative) atteste que le voltage moyen est maintenu et que la capacité est maintenue au-dessus de 80% après 100 cycles.

La stabilité thermique du matériau est évaluée par analyse thermogravimétrique et la phase semble stable jusqu'à 800 degrés où des pertes de sodium semble mener à la décomposition en Ir métallique du composé. Il semblerait que cette décomposition soit la principale difficulté à surmonter pour obtenir ce polymorphe.

Chapitre IV. Un iridate protoné pour la catalyse de la réaction d'oxydation de l'eau en milieu acide

Ce dernier chapitre porte sur la synthèse, la caractérisation structurale et électrochimique d'un iridate protoné cristallin obtenu par échange cationique de la phase β - Li_2IrO_3 . Ses propriétés d'insertion des protons ont été établies et son activité en tant que catalyseur de la réaction d'oxydation de l'eau a été évaluée.

La synthèse se fait sous conditions hydrothermal dans une solution 1M d'acide sulfurique à 120°C dans un autoclave. Le matériau qui en résulte a été caractérisé par diffraction des rayons X au synchrotron Alba sur la ligne MSDP et par diffraction des neutrons sur poudre sur la ligne D1b de l'institut Laue Langevin de Grenoble. La charpente dessinée par les octaèdres IrO_6 est maintenue et deux sites de protons sont déterminés. La composition est obtenue par analyse thermogravimétrique comme étant H_2IrO_3 . Le degré d'oxydation de l'iridium est identique à celui de la phase lithiée d'origine comme déterminé par spectroscopie d'absorption X, ce qui confirme la composition de deux protons par unité formulaire.

Des mesures de voltamétrie cyclique dans une solution de 1M H_2SO_4 montre trois pics rédox réversibles. Ces pics sont décalés de 260 mV lorsque la mesure est effectuée dans une solution tampon acide acétique à un $\text{pH} = 4.76$, ce qui revient à 60 mV par unité pH et qui confirme l'implication du proton dans l'équation bilan. De plus, que l'électrode soit tournante ou non, la forme du voltammogram reste inchangé et pointe vers un processus limité par la diffusion dans le solide. Malheureusement, la diffusion du proton semble être déterminante et le potentiel franchi rapidement le potentiel d'oxydation de l'eau qui se fait à une surtension relativement basse. En effet,

lorsque le matériau est soumis à un courant constant, seule une très faible capacité ne peut être obtenue avant d'atteindre le mur du solvant. L'intérêt du matériau comme électrode d'insertion de proton est limitée. Cependant, il présente des caractéristiques intéressantes pour l'oxydation de l'eau.

Son activité est comparable à l'état de l'art mais semble présenter une stabilité accrue comme déterminé par spectrométrie à plasma à couplage inductif. L'étude de la réactivité des intermédiaires délithiés Li_xIrO_3 avec $x = 1, 0.5$ et 0 montre qu'il y a une oxydation chimique de l'eau suivi d'une insertion de protons pour compenser la charge. De ces observations, un mécanisme intégrant l'insertion de protons lors de l'activité d'électrocatalyse de la réaction d'oxydation de l'eau est décrit et permet de rationaliser la stabilité apparente du matériau. En effet, le matériau est oxydé lors du balayage anodique comme démontré par des mesures *operando* de spectroscopie d'absorption X jusqu'à former une phase réactive qui peut alors oxyder l'eau en se réduisant par insertion de protons sans biais électrochimique. Contrairement à ce qui avait été proposé par d'autres équipes, le composé IrO_3 ne se décompose donc pas en O_2 et IrO_2 mais forme une phase protonée.

Conclusions générales

Cette thèse est centrée sur l'étude du composé A_xIrO_3 en tant qu'hôte polyvalent pour Li^+ , Na^+ et H^+ . La flexibilité du squelette d'octaèdres d' IrO_6 qui forment une structure tridimensionnelle représente un terrain intéressant pour l'étude fondamentale de l'oxydoréduction du réseau anionique dans les oxydes pour les batteries à ions Li^+ et Na^+ . La phase lithiée peut être obtenue par synthèse céramique à haute température selon deux étapes alors que la phase sodiée n'a pu être obtenue que par voie électrochimique en passant par IrO_3 . La phase protonée peut être obtenue par échange cationique de la phase lithiée ou par réaction de l'eau avec IrO_3 . Ces deux dernières phases n'avaient encore pas été reportées auparavant.

Les processus d'insertion du lithium et sodium ont été caractérisés par diverses techniques telles que la diffraction des rayons X et des neutrons et par spectroscopies d'absorption et de photoémission X afin de déterminer les changements structuraux associés aux processus d'oxydoréduction cationique et anionique. Dans le cas du lithium, les processus de nature anionique semblent être nuisibles aux performances au

long terme comme dans les matériaux lamellaires riches en lithium. Ceci peut s'expliquer par la tension structurale induite par les distorsions des octaèdres d' IrO_6 qui peuvent être rationalisées par l'oxydation des oxygènes pour former des espèces $\text{O}_2^{\text{n-}}$.

Le nouvel iridate ainsi que l'étude de la réactivité d' IrO_3 avec un milieu acide a permis de décrire un mécanisme de catalyse de la réaction d'oxydation de l'eau à la surface des oxydes d'iridium. Il a notamment été montré qu' IrO_3 pouvait être stabilisé et qu'il ne se décompose pas en IrO_2 et O_2 mais réagit avec l'eau pour former de l'eau et la nouvelle phase protonée. Ceci apporte des pistes pour le développement de nouveaux électrocatalyseurs à base d'iridium avec une haute activité et une stabilité accrue.

Résumé :

Cette thèse est centrée sur l'étude du composé $A_x\text{IrO}_3$ en tant qu'hôte polyvalent pour Li^+ , Na^+ et H^+ . Sa structure tridimensionnelle représente un terrain intéressant pour l'étude fondamentale de l'oxydoréduction du réseau anionique dans les oxydes pour les batteries à ions Li^+ et Na^+ . La phase lithiée peut être obtenue par synthèse céramique à haute température selon deux étapes alors que la phase sodiée n'a pu être obtenue que par voie électrochimique en passant par IrO_3 . La phase protonée peut être obtenue par échange cationique de la phase lithiée ou par réaction de l'eau avec IrO_3 . Ces deux dernières phases n'avaient encore pas été reportées auparavant. Les processus d'insertion ont été caractérisés par diverses techniques telles que la diffraction des rayons X et des neutrons et par spectroscopies d'absorption et de photoémission X afin de déterminer les changements structuraux associés aux processus d'oxydoréduction cationique et anionique. Les résultats obtenus permettent d'approfondir notre compréhension d'un mécanisme de compensation de charge encore mal compris. De plus, l'étude de la réactivité d' IrO_3 avec un milieu aqueux acide a permis de décrire un mécanisme de catalyse de la réaction d'oxydation de l'eau à la surface des oxydes d'iridium et apporte des pistes pour le développement de nouveaux électrocatalyseurs à base d'iridium.

Mots-clés : Batteries Li-ion, Batteries Na-ion, électrochimie, Redox anionique, spectroscopie, diffraction

$A_x\text{IrO}_3$ (A = Li, Na or H) for the electrochemical storage and conversion of energy

Abstract:

This thesis focuses on the study of the compound $A_x\text{IrO}_3$ as a versatile host for Li^+ , Na^+ and H^+ . Its three-dimensional structure represents an interesting playing field for the fundamental study of the redox activity of the anionic network in oxides for Li^+ and Na^+ ion batteries. The lithiated phase can be obtained by high temperature ceramic synthesis in two stages whereas the sodiated phase could only be obtained electrochemically via IrO_3 . The protonated phase can be obtained by cation exchange of the lithiated phase or by reaction of water with IrO_3 . These last two phases had not been previously reported. The insertion processes were characterized by various techniques

such as X-ray and neutron diffraction as well as X-ray absorption and photoemission spectroscopies to determine the structural changes associated with cationic and anionic oxidation processes. The results obtained allow us to deepen our understanding of a charge compensation mechanism that is still poorly understood. In addition, the study of the reactivity of IrO_3 with an acidic aqueous media has made it possible to describe a mechanism for the electrocatalysis of the oxygen evolution reaction on the surface of iridium oxides and provides avenues for the development of new electrocatalysts based on iridium.

Key words : Li-ion Battery, Na-ion battery, Oxygen evolution reaction